

AN ABSTRACT OF THE THESIS OF


Gary Brian Sidder for the degree of Doctor of Philosophy in
Geology presented on November 21, 1984

Title: Ore Genesis at the Monterrosas Deposit in the Coastal

Batholith, Ica, Peru

Redacted for privacy

Abstract approved: _

 Cyrus W. Field

Monterrosas is a hydrothermal deposit of copper and iron that is hosted by gabbro-diorites of the Upper Cretaceous Patap Superunit within the Coastal Batholith of central Peru. The orebody is localized by fractures and splays related to a nearby regional fault and is composed of massive chalcopyrite, magnetite, and pyrite. Ore and alteration minerals such as actinolite, sodic scapolite, epidotes, sphene, magnetite, apatite, tourmaline, chlorites, hematite, and quartz formed dominantly as replacements of magmatic diopside, labradorite-andesine, and ilmenite. Hydrothermal mineralization was characterized by the exchange of major, minor, and trace elements between hot saline fluids and gabbro-diorite wall rocks. Metasomatism involved the addition of FeO_t , K_2O , MgO , and the ore-forming metals (Cu, Co, Au, Ag, and Mo) to the host rocks, and the concomitant depletion of SiO_2 , CaO , Na_2O , and TiO_2 . The losses and gains of these major oxide components in samples of gabbro-diorite may be used to define an alteration index that is correlative with the distance to ore, the intensity of hydrothermal alteration, and the concentration of copper. Geochemical data suggest

that the ore and gangue minerals were deposited at high temperatures from saline fluids derived from a magma. The evidence includes fluid inclusions within gangue quartz that exhibit homogenization temperatures of 400° to 500°C, salinities of 32 to 56 wt percent NaCl, and the halite trend, and magmatic-like sulfur isotopic compositions that range from 1.6 to 3.3 permil in pyrite and chalcopyrite. Ore-bearing fluids evolved as a consequence of progressive crystallization of labradorite-andesine, diopside, and ilmenite from gabbro-diorite magma, which resulted in the residual concentration of iron, water, chlorine, and other volatiles and metals. These components were subsequently exsolved as a discrete fluid that migrated upward along faults and fractures. Deposition of the ore and alteration minerals resulted from decreases of temperature and (or) acidity in the fluids because of reactions between the hydrothermal fluids and early-formed gabbro-diorite host rocks.

Ore Genesis at the Monterrosas Deposit
in the Coastal Batholith, Ica, Peru

by

Gary Brian Sidder

A THESIS

submitted to

Oregon State University

in partial fulfillment of
the requirements for the
degree of

Doctor of Philosophy

Completed November 21, 1984

Commencement June 1985

APPROVED: **Redacted for privacy**

Professor of the Department of Geology in charge of major

Redacted for privacy

Head of the Department of Geology

Redacted for privacy

Dean of Graduate School

Date thesis is presented November 21, 1984

Typed by Gayla Badovick for Gary Brian Sidder

ACKNOWLEDGEMENT

I would like to thank Dr. Cyrus W. Field for his guidance throughout my graduate program. Cy always found time to meet with me, and I greatly appreciated all our conversations about research, classes, employment, business, family, babies, and many other topics. This dissertation would not have been possible without Cy. I would also like to thank Guillermo Abele, Luis Sassarini, Alberto Caballero, Cesar Rios, Lorgio Maguina, and others at Centromin Peru for their warm hospitality and logistical and technical support for this project. Dr. Field, The Geological Society of America (Grant No. 3063-82), Conoco Minerals Co., and a Graduate Fellowship from the ASARCO Foundation provided funds for parts of this dissertation.

I would also like to acknowledge several people who made my years of graduate study at OSU a pleasurable experience. Rich Fifarek, Alan Wallace, Max Rosenberg, Bob Walker, and Mike McCulla have all been good friends and counselors. Drs. Taubeneck, Enlows, Senechal, and Frenkel provided constructive suggestions throughout this project. My typist, Gayla Badovick, did yeoman service for this paper, and Ed Howes and Tony Selle did fine work on the drafting. My parents have been steadfast in their much needed praise and support. Finally, I would like to express my deepest appreciation to my wife, Francie Steinzeig, who endured this entire project and still managed to offer encouragement and love throughout. This degree is dedicated to my newborn son, Aaron.

TABLE OF CONTENTS

INTRODUCTION	1
Location and Accessibility	1
Purpose of the Investigation	3
Methods of Study	3
REGIONAL GEOLOGIC SETTING	7
The Coastal Batholith of Peru	7
Regional Metallogeny	12
Regional Tectonics	18
THE MONTERROSAS MINE	23
Mine History	23
The Monterrosas Deposit	25
PLUTONIC ROCKS	30
The Patap Superunit	30
The Linga Superunit	37
Chemistry of the Plutonic Rocks	42
The Patap Superunit	42
The Linga Superunit	47
Discussion	49
METALLIZATION	59
Ore Mineralogy	59
Distribution of Metals	68
ALTERATION	73
Mineralogy of the Alteration Assemblage	74
Geochemistry of Alteration	80
FLUID INCLUSIONS	94
Methodology	94
Homogenization Temperatures	100
Salinities	110
Interpretation of the Fluid Inclusion Data	116
ORE GENESIS	131
Conditions and Processes of Mineralization	131
Similarities to Other Deposits	142
SUMMARY AND CONCLUSIONS	147
REFERENCES	151
APPENDICES	166

LIST OF FIGURES

<u>Figure</u>	<u>Page</u>
1. Regional Location Map of Ica, Peru	2
2. Local Location Map of the Monterrosas Mine	4
3. Simplified Physiographic Map of Peru	8
4. The Segments of the Coastal Batholith of Peru	9
5. Metallogenic Belts of South America	14
6. Schematic Cross-Section of the Monterrosas Mine	24
7. Schematic Diagram of Mineralization in the Subsurface of the Monterrosas Mine	27
8. Electron Microprobe Analyses of Clinopyroxenes	35
9. QAP (quartz-alkali feldspar-plagioclase feldspar) Diagram (after Streckeisen, 1973) of Modal Compositions of the Patap and Linga Superunits in the Monterrosas area	38
10. Ternary AFM Diagram	46
11. Ternary NKC Diagram	48
12. Variation Diagrams of Wt Percent MgO vs. Fe' and La _N vs. Fe'	53
13. T-x _{H₂O} Section at 5 kb for Mt. Hood Andesite	56
14. Photomicrograph of Chalcopyrite-Cubanite-Pyrrhotite Bleb in Pyrite	65
15. Cumulative Frequency Diagram for Copper	71
16. Alteration Index Versus Distance from the Ore Zone (a) and Versus Concentration of Copper (b)	92
17. Type III Inclusions in Samples of Ore from the Monterrosas Mine	98
18. Histogram of the Temperatures of Vapor Homogenization in Type I Inclusions	106

<u>Figure</u>		<u>Page</u>
19.	Histogram of the Temperatures of Vapor Disappearance in Type III Inclusions	108
20.	Histogram of the Temperatures of Halite Disappearance in Type III Inclusions	109
21.	Histogram of the Salinity for Types I (stippled) and III (open) Inclusions	111
22.	Salinity vs. Temperature of Homogenization for Type I and Type III Inclusions	113
23.	Phase Relations in the System NaCl-KCl-H ₂ O	114
24.	Location of the Halite Trends Observed at the Naica Pb-Zn-Ag, Limestone Replacement Deposit (Erwood et al., 1979), and at the Panguna (Eastoe, 1978, 1982), and Granisle and Bell (Wilson et al., 1980) Porphyry Copper Deposits	118
25.	Plane of Constant Composition (isopleth) at 52 Wt Percent NaCl in the NaCl-H ₂ O System	119
26.	Phase Relations in the NaCl-KCl-H ₂ O System at 50 and 60 Percent Combined NaCl + KCl	120
27.	Possible Path Followed by Saline Fluids in Type III Inclusions at the Monterrosas Mine	122
28.	Some Phase Relations in the Central Portion of the Cu-Fe-S System at 600°C	137

LIST OF TABLES

<u>Table</u>	<u>Page</u>
1. Modal Compositions of the Least Altered Rocks of the Patap and Linga Superunits in the Monterrosas Area	32
2. Means, Standard Deviations, and Ranges of Major Oxide and Minor and Trace Element Constituents in the Least Altered Samples of the Patap and Linga Superunits of the Monterrosas Area.	43
3. Comparison of the Average Concentrations of Major Oxides and Selected Trace Elements in the Least Altered Gabbro-Diorites from the Monterrosas Area and Basaltic Andesites from the Oregon Cascades	51
4. Electron Microprobe Average Compositions of Chalcopyrite in Ore from the Monterrosas Mine	60
5. Electron Microprobe Average Compositions of Pyrite in Ore from the Monterrosas Mine	62
6. Electron Microprobe Average Compositions of Magnetite in Ore from the Monterrosas Mine	64
7. Electron Microprobe Average Compositions of Cubanite and Pyrrhotite in Ore from the Monterrosas Mine	66
8. Range and Threshold Values of Trace Elements in Samples of Ore and Country Rocks at Monterrosas (in ppm)	69
9. Exchanges of Elements in the Gabbro-Diorites from a Summary Reaction of Alteration	88
10. Chemical Changes Between Relatively Unaltered and Altered Patap Gabbro-Diorites (in wt % and g/100 cm ³)	90
11. Fluid Inclusion Data for the Monterrosas Deposit	102
12. Sulfur Isotope Data for Sulfides of the Monterrosas Deposit (in permil)	139

LIST OF PLATES

<u>Plate</u>		<u>Page</u>
1.	Geologic Map of the Monterrosas Mine	in pocket
2.	Cross-Section A-A' and Plan View of the Underground Levels, with Sample Locations	in pocket
3.	Location Map of Surface Samples	in pocket

ORE GENESIS AT THE MONTERROSAS DEPOSIT IN THE COASTAL BATHOLITH, ICA, PERU

INTRODUCTION

The Monterrosas Mine is a fracture controlled vein-like deposit of copper and iron within the Coastal Batholith of central Peru. Gabbros and diorites of the middle Cretaceous Patap Superunit host the orebody. The ores, although hosted by plutonic rocks, are typical of skarn assemblages in that they consist of chalcopyrite, magnetite, pyrite, and actinolite in variable proportions. Secondary minerals such as amphiboles, scapolite, epidotes, tourmaline, sphene, apatite, magnetite, chlorites, and quartz formed dominantly as replacements of magmatic clinopyroxene and plagioclase feldspar in the Patap units. Mineralization at the Monterrosas Mine is manifested by bimetasomatic exchange of major, minor, and trace element components between hot aqueous fluids and dioritic wall rocks along major fractures. It is postulated that the hydrothermal fluids were heated by and possibly derived from a unit of the Patap magma series as it cooled and underwent crystallization to form gabbros and diorites.

Location and Accessibility

The Monterrosas Mine is about 20 km northeast of Ica, Peru, at 14°00' South latitude and 75°37' West longitude, as shown in Figure 1. Ica is in the Peruvian Coastal Desert approximately 300 km south of Lima and about 60 km inland from the Pacific Ocean. It is accessible by car from the north and south via the Pan American Highway. The mine, which is at an altitude of about 1100 m in the western foothills

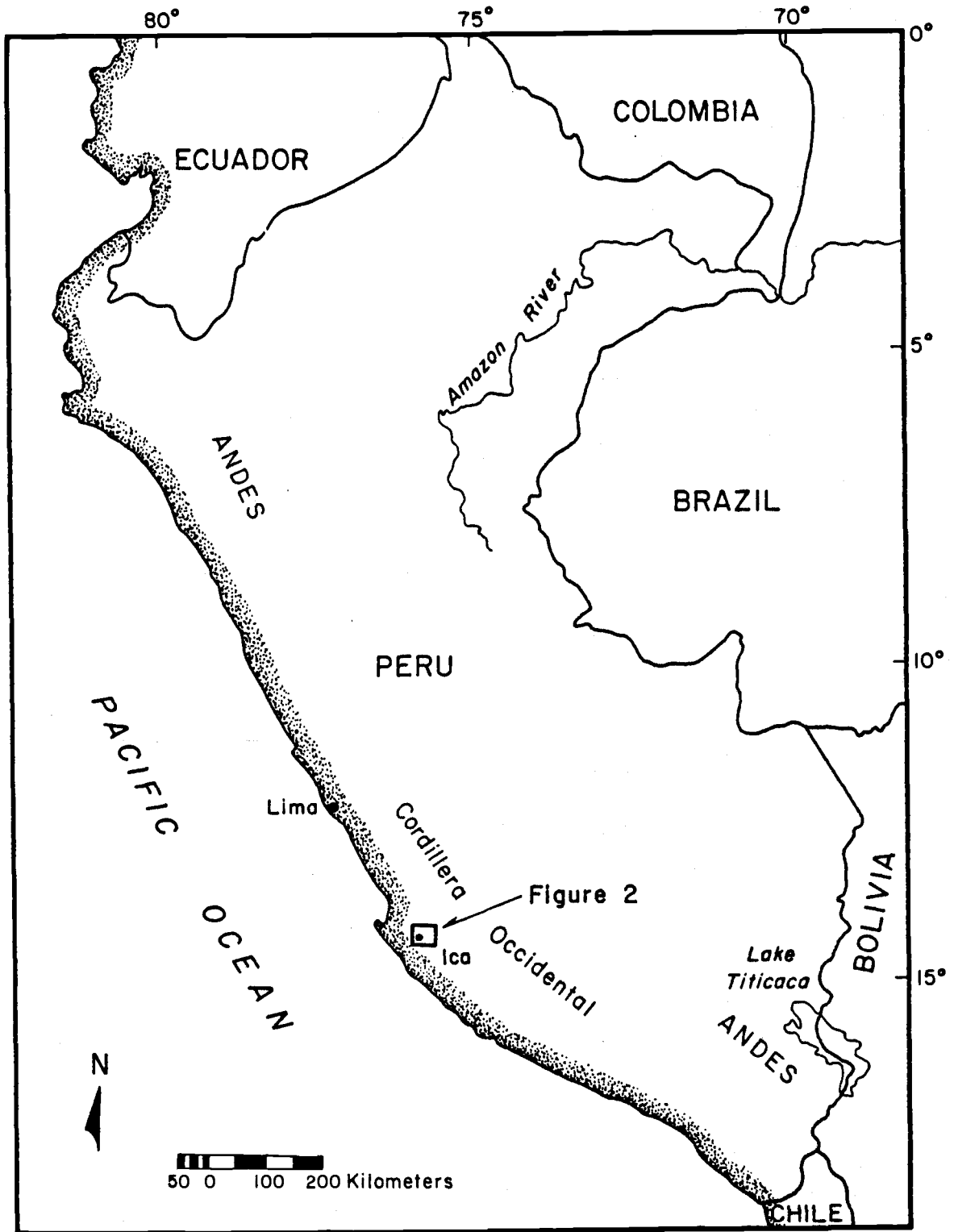


Figure 1. Regional Location Map of Ica, Peru.

of the Andean Cordillera Occidental, may be reached by an improved gravel road that extends across the desert from Ica as depicted in Figure 2.

Purpose of the Investigation

The Monterrosas deposit has several unusual and perhaps unique characteristics. For example, hydrothermal mineralization is associated with intermediate to mafic plutonic rocks of the Coastal Batholith. Furthermore, the ore and alteration mineral assemblages resemble most closely a skarn-type replacement deposit hosted commonly by limestones. Also, metals such as copper, iron, cobalt, molybdenum, gold, and silver found in the ore present an unusually interesting association. Thus, the purpose of this investigation was to study the petrology and petrochemistry of the ore and host rocks. A careful documentation of the distribution of elements and minerals in the ore zone and in altered wall rocks was considered essential to better understand the environment of mineralization. The ultimate goal of this study was to formulate a model for the genesis of this deposit that will help to refine metallogenic concepts for this and related submagmatic-hydrothermal types of ore deposits.

Methods of Study

The study of the Monterrosas Mine incorporates both field and laboratory examinations. Field work was done in December, 1979, and June to August, 1981. Reconnaissance mapping of the surface geology was conducted on a scale of 1:10,000. Detailed mapping underground of the mineralized and altered zones was carried out at a scale of 1:100

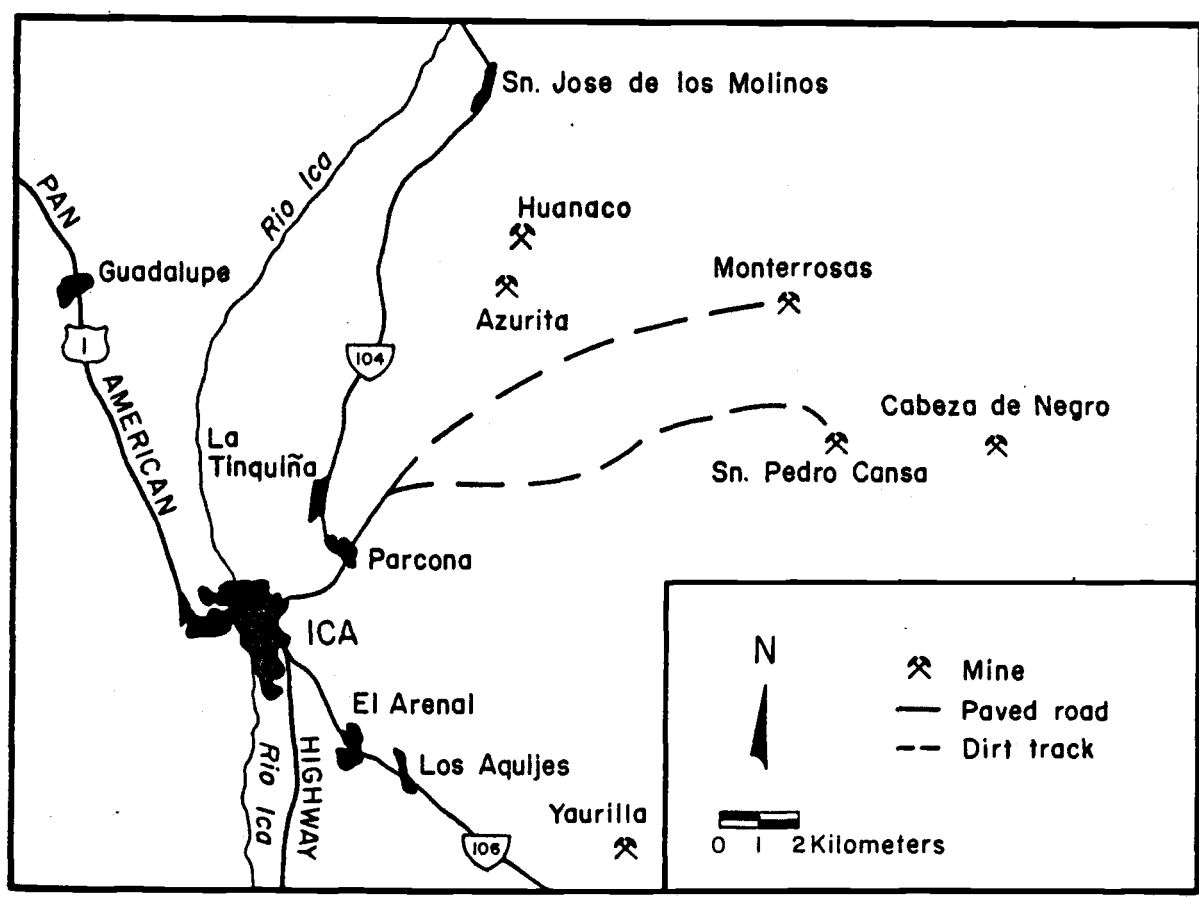


Figure 2. Local Location Map of the Monterrosas Mine.

and 1:200. Field studies concentrated on the host rocks, alteration zones, and ore. Samples collected were used for petrographic, mineralogic, and chemical studies. Over 200 thin sections, polished thin sections, and polished sections were examined optically with transmitted and reflected light. The electron beam microprobe (ARL) at the University of Oregon was used to verify mineral identifications and provide quantitative analyses of mineral species.

Whole rock major oxide analyses of Si, Al, Ti, total Fe, Ca, and K were obtained by X-ray fluorescence spectrometry, and Na and Mg oxide values were collected via atomic absorption spectrophotometry at Oregon State University. Total iron was also analyzed with plasma spectrometry, and ferric iron was obtained by titration methods at Skyline Laboratories. Values of Cu, Mo, Pb, Zn, Ag, and Co were determined by atomic absorption spectrophotometry, and samples with greater than 1000 ppm were quantified with wet chemical assay techniques by Chemical and Mineralogical Services. Preliminary analyses for additional trace elements were acquired via X-ray fluorescence spectrometry at the University of Nottingham, England.

Fluid inclusion studies were conducted on selected samples of quartz. The fluid inclusions in doubly polished sections were first studied optically and described. A Chaixmeca heating and freezing stage was then used to determine freezing and homogenization temperatures for the inclusions. This information provides estimates of the salinity and temperatures of fluids that circulated through the Monterrosas area.

The sulfur isotopic ratios of pyrite and chalcopyrite from the ore zone were obtained by standard techniques of mass spectrometry at the U.S. Geological Survey, Branch of Isotope Geochemistry in Denver, Colorado. Two K-Ar whole rock age dates were determined on samples provided to Richard L. Armstrong at the University of British Columbia.

REGIONAL GEOLOGIC SETTING

The Monterrosas deposit is within the western margin of the Coastal Batholith of Peru. The batholith forms the core of the Cordillera Occidental, or Western Cordillera, in the central part of the Andean Orogen (Figure 3). Near Ica, the batholith is flanked to the west by the Rio Canete eugeosynclinal basin (Cobbing, 1978). The Coastal Cordillera, which is farther west, contains the Lower Devonian San Nicholas Batholith (Shackleton et al., 1979) and a Precambrian metamorphic massif of the granulite facies (Dalmayrac et al., 1977; Cobbing, Ozard, and Snelling, 1977).

The Coastal Batholith of Peru

The Coastal Batholith of Peru is exposed as a continuous body for a length of 2000 km from 4° to 18° South latitudes and is subparallel to the continental margin. The batholith consists of as many as 1000 separate plutons that were emplaced over a 70 million year (m.y.) interval from 100 m.y. to 30 m.y. ago (Cobbing et al., 1981). It includes five compositionally distinct segments, as illustrated in Figure 4, and each segment of this batholith is composed of a specific assemblage of intrusive rocks which represent a petrologically and geochemically unique magma series (Cobbing, Pitcher, and Taylor, 1977). These assemblages, or superunits, consist of a consanguineous suite of associated plutonic units that are spatially and temporally related, and that have similar chemical and petrological characteristics. Each successively younger superunit in the batholith exhibits a more restricted areal distribution, and thus it may be inferred that each

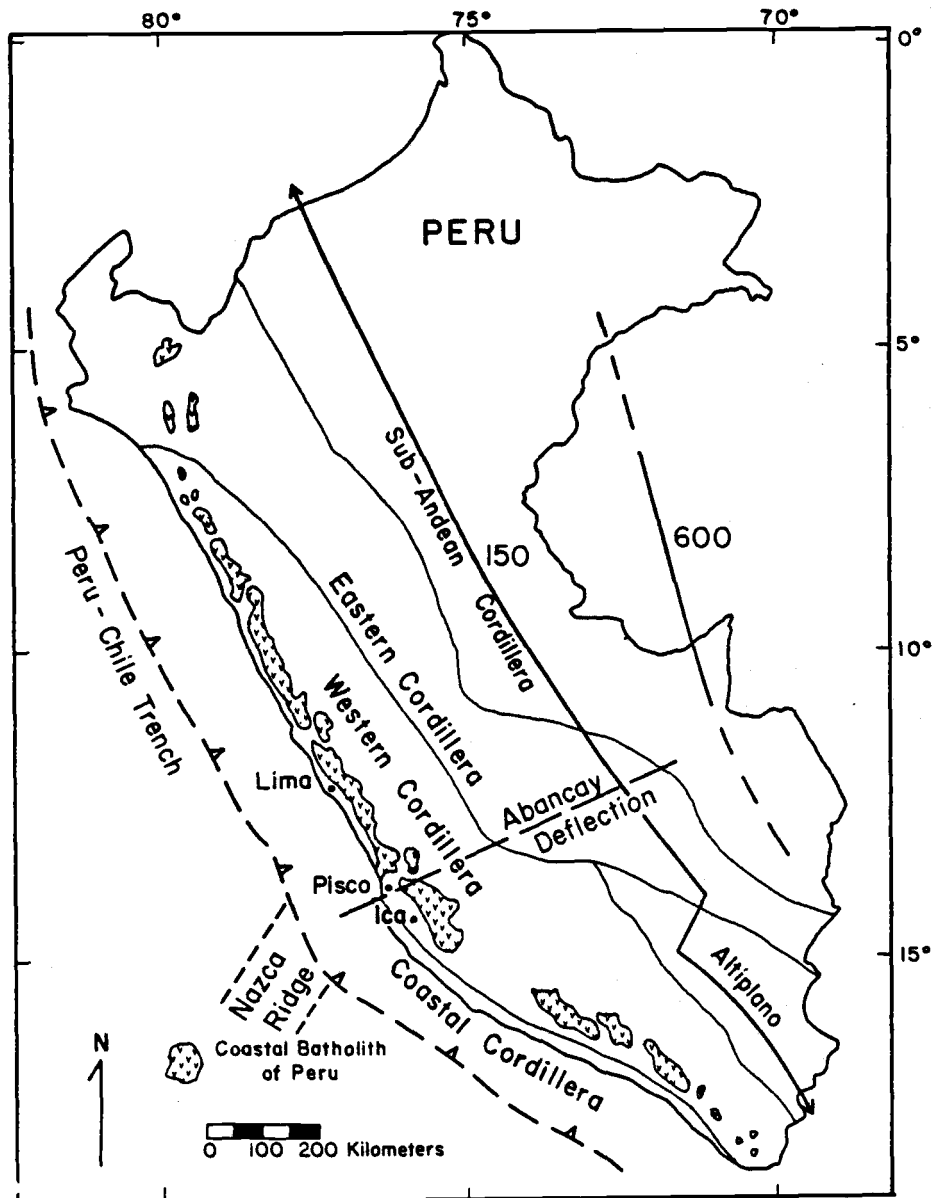


Figure 3. Simplified Physiographic Map of Peru. This map shows the general distribution of the Coastal Batholith and regional tectonic features. Contours of the depth to the Benioff zone at 150 km and 600 km are also shown (after Isacks and Barazangi, 1977). Note the change in dip of subduction near 15°S.

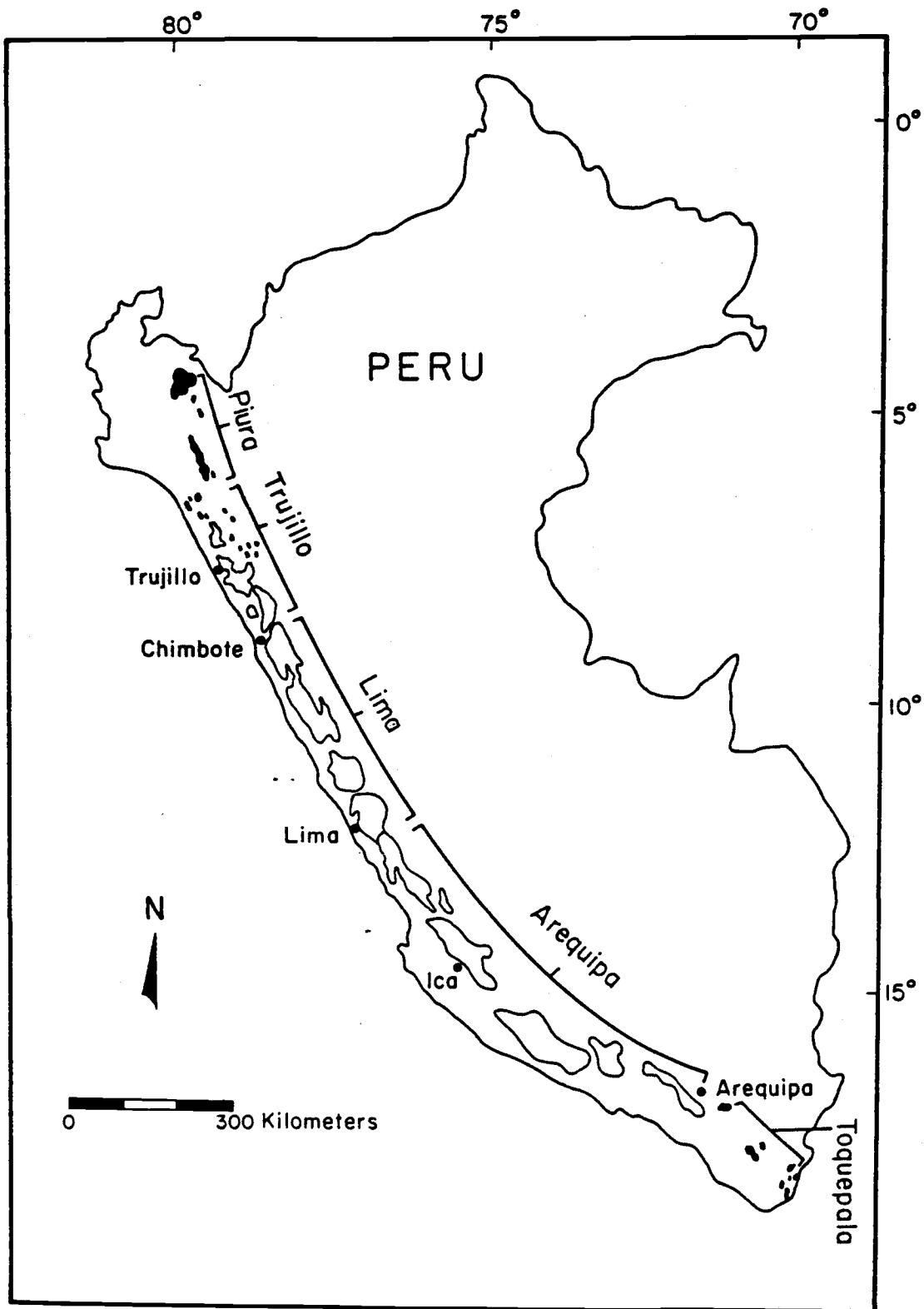


Figure 4. The Segments of the Coastal Batholith of Peru
(after Cobbing and Pitcher, 1983, Figure 2, p. 279).

successive pulse of magma generation in the batholith became volumetrically smaller (Cobbing, Pitcher, and Taylor, 1977).

Plutonic rocks in the Monterrosas area occupy the central portion of the Arequipa segment of the batholith. Two of the five superunits in the Arequipa segment are present at Monterrosas. The oldest rocks belong to the Patap Superunit. The Patap represents the earliest phase of batholithic activity about 100 m.y. ago (Atherton et al., 1979). Magmas of the Patap Superunit were probably derived from the mantle wedge above the descending oceanic plate as primitive melts and were intruded along extension fractures at the outer edge of the South American continent (Cobbing, 1982; Bussell, 1983). These tholeiitic magmas were emplaced as small widely dispersed plutons within a eugeosynclinal sequence that has a maximum thickness of 10 km or less. Mullan and Bussell (1977) have recognized four primary types of gabbro in the Coastal Batholith: (1) olivine-plagioclase-augite (troctolitic) gabbro; (2) olivine-plagioclase-augite-orthopyroxene (troctolitic-noritic) gabbro; (3) augite-plagioclase gabbro; and (4) hornblende gabbro. However, repeated alternations of injection and deformation give the Patap rocks a chaotic appearance, and post-crystallization metamorphism, metasomatism, and hybridization contribute to the complexity of these rocks (Mullan and Bussell, 1977; McCourt, 1981). Clinopyroxene-plagioclase[±]hornblende gabbros and diorites characterize units of the Patap Superunit in the Monterrosas area. An anomalously young whole rock K-Ar age date of 82 ± 3 m.y. for the least altered sample of gabbro-diorite exposed in the Monterrosas area presumably reflects some of these changes in rocks of the Patap Superunit.

Intrusions of the Linga Superunit about 97 m.y. ago were emplaced during the granitoid cycle of the batholith in the Arequipa segment (Cobbing and Pitcher, 1983). Monzonitic rocks of the Linga and younger superunits reveal a primary, calc-alkaline compositional trend. A subsidiary rhythm, which is superimposed on the primary trend, is also calc-alkaline, and it denotes in-situ mafic to felsic differentiation within individual plutons (Cobbing and Pitcher, 1972; Pitcher, 1978). A K-Ar whole rock age date of 92 ± 3 m.y. was obtained from a granodiorite of the Linga Superunit at Monterrosas.

Overall, the batholith is characterized as an I-type granitoid body (Chappell and White, 1974), accompanied by significant volumes of gabbro and coeval extrusions of basaltic and andesitic rocks (Pitcher, 1979). Mafic and intermediate rocks constitute the largest proportion of the batholith. Tonalites account for 55 percent of the Arequipa segment; 32 percent is granodiorite and adamellite (quartz monzonite); 9 percent is gabbro and diorite, and granites constitute 4 percent of the rocks exposed in this segment (Cobbing and Pitcher, 1972; Jenks and Harris, 1953). Initial $^{87}\text{Sr}/^{86}\text{Sr}$ ratios exhibit a narrow range of values (0.7040 to 0.7050) for the batholith as a whole (Pitcher, 1979), and an initial $^{87}\text{Sr}/^{86}\text{Sr}$ ratio of 0.7043 has been reported by Stewart et al. (1974) for a granodiorite several kilometers east of the Monterrosas deposit.

Pitcher (1978, 1979) and Cobbing et al. (1981) have provided a comprehensive discussion of the generation and emplacement of the

Coastal Batholith of Peru. This so-called cauldron batholith¹ (Pitcher, 1979, pp. 648-649) was passively emplaced into predominantly eugeosynclinal volcanic and volcanoclastic rocks. Intrusion was along a major lineament parallel to the South American plate boundary, and emplacement occurred at a high level in the crust. These events took place in a tensional stress regime that was related to subduction processes, at the close of a principal phase of deformation known as the Subhercynian orogeny in the Andean Orogen (Pitcher, 1979; Cobbing and Pitcher, 1983). Pitcher (1979) favored a partial melting process of equilibrium fusion, as described by Presnall and Bateman (1973), for the origin of the granitoid magmas of the Coastal Batholith. In this model, melts are generated in the lower crust as a result of the transfer of heat from rising basaltic and gabbroic melts generated in the subduction zone. Magmatic differentiation accounts for the mafic to felsic trend seen in batholiths and their individual plutons (Presnall and Bateman, 1973).

Regional Metallogeny

The Arequipa segment, in which the Monterrosas deposit is situated, represents the most mineralized part of the Coastal Batholith. Pitcher (1978) has recognized a marked contrast in the composition and intensity of mineralization between the weakly mineralized Lima segment and the more productive Arequipa segment, which contains numerous mineral deposits of several genetic types. The boundary between the

¹ A cauldron batholith is one in which the granitoid magmas remain highly mobile and are capable of being rapidly injected into the crust along fractures, faults, and other potential voids, in contrast to diapir batholiths, which intrude the crust by forcibly shouldering it aside.

two is located near the Abancay deflection (Figure 3). Many important deposits of copper lie to the south of this boundary, whereas to the north mineralization is sparse (Sillitoe, 1976). The Monterrosas deposit is located immediately south of the Abancay deflection, as shown in Figure 5.

Sillitoe (1974) has suggested that segments of the Andean Orogen have distinctive metallic characteristics. Although the same types of deposits have formed in nearly all segments (Sillitoe, 1976), the deposits differ in age, size, and grade of contained metals from one tectonic segment to another (Sillitoe, 1974; Petersen, 1972). Regardless of such variations, metal distribution patterns form a series of narrow metallogenic subprovinces that are elongated parallel to the continental margin and exhibit a general west to east zonation that is perpendicular to the regional trend of the Andes (Figure 5). These subprovinces, from west to east, are characterized by: (1) iron \pm phosphorous as apatite; (2) copper \pm gold \pm silver \pm molybdenum; (3) polymetallic copper-lead-zinc-silver; and (4) tin with subordinate tungsten, silver, gold, antimony, bismuth, and molybdenum (Sillitoe, 1976; Clark et al., 1976; Frutos, 1982). The Monterrosas deposit is located at the boundary between the iron and copper metallogenic belts (Figure 5).

Several mineral prospects in the region immediately surround Monterrosas. Most are small deposits of copper in veins (Merwin Bernstein, 1980, personal communication). Centromin Peru is currently conducting an exploration program at two of the copper prospects, the Huanaco Vein and the Azurita deposit, about 6 km northwest of the Monterrosas Mine. Their efforts to date indicate potential reserves

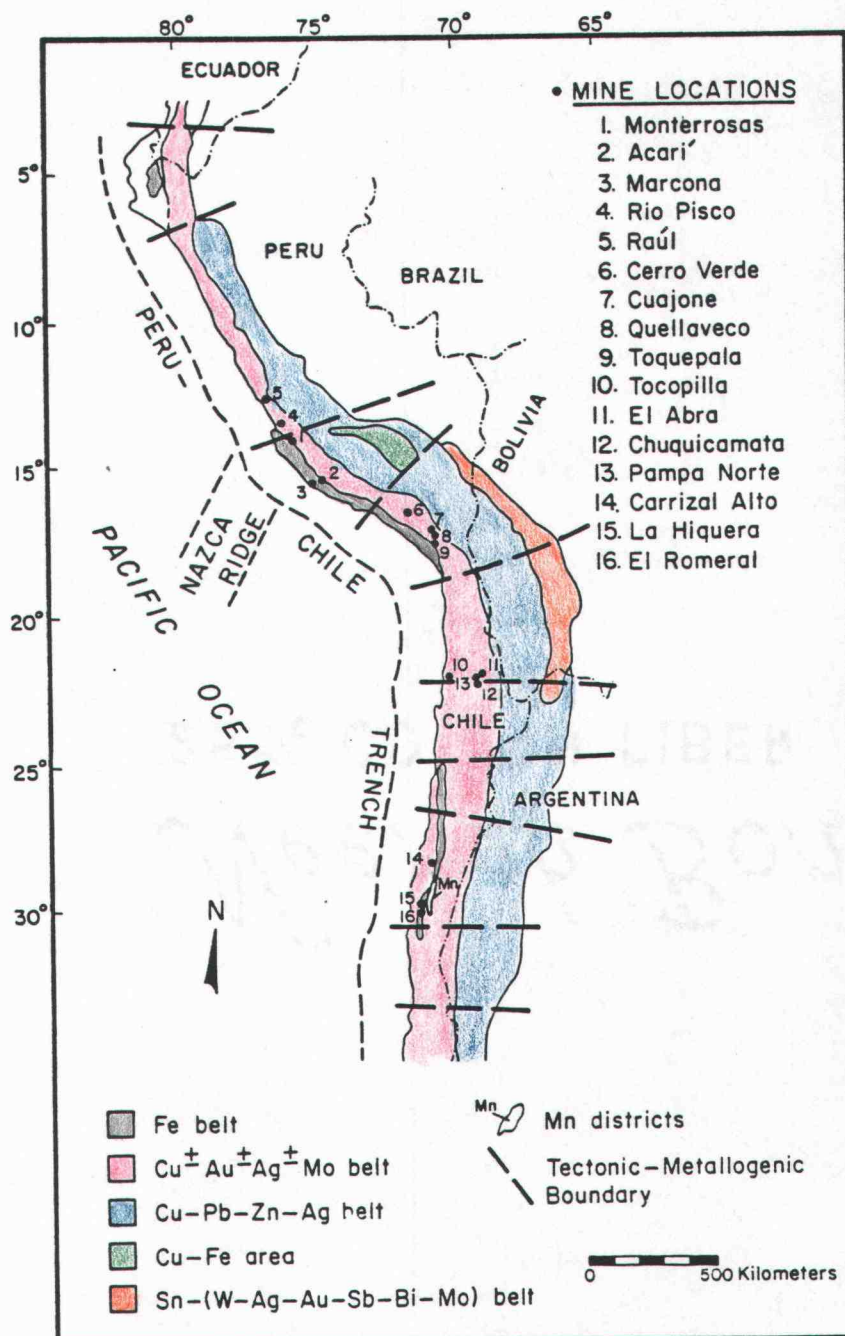


Figure 5. Metallogenic Belts of South America. The locations of some mines mentioned in the text are also shown (after Sillitoe, 1976, Figure 4, p. 73; and Sillitoe, 1974, Figure 1, p. 543).

of at least 3 million tons of ore at these prospects (Todd, 1983). On the basis of an airborne geophysical exploration program, Programmed Neuro Cybernetics Ltd. of Great Britain has identified a belt of copper-cobalt deposits in the Monterrosas area (Hyde, 1984). Acari, Rio Pisco (Eliana), and Raul are among the better known deposits that are found in central and southern Peru near Monterrosas (Figure 5). Each of these deposits, along with Monterrosas, has been classified by Cardozo and Vidal (1981) as part of the amphibole-pyrite-chalcopyrite association that is present commonly along the western flank of the Central Andes. The large porphyry copper deposits of Cerro Verde, Cuajone, Toquepala, and Quellaveco are located about 500 to 625 km farther to the south in southernmost Peru (Bellido et al., 1972).

Acari is an iron-copper deposit hosted by granodiorites of the Linga Superunit (Park, 1972; Cobbing and Pitcher, 1983). It is located approximately 180 km south of Monterrosas near the western edge of the Coastal Batholith. The host rocks contain vein-like (Sillitoe, 1976) or rod-like (Park, 1972) deposits of massive magnetite or chalcopyrite that are related genetically to units of the enclosing Linga Superunit (Cobbing and Pitcher, 1983). Contacts between ore and country rocks are sharp, and there is little evidence of replacement or assimilation by the granodiorite (Park, 1972). The iron deposits at Acari are believed to have formed by magmatic injection (Zevallos, 1966; Bellido, 1974) from an unexposed dioritic magma at depth (Dunin-Borkowski, 1970). Veins of chalcopyrite-actinolite-magnetite which have an appreciable vertical and lateral extent are interpreted to represent hydrothermal deposits localized within fractured granitoid intrusive rocks that possibly are related genetically

to the iron deposits at Acari (Sillitoe, 1976). Marcona, which is a contact metasomatic skarn deposit of iron, is 45 km northwest of Acari (Figure 5). It consists of magnetite-hematite ore localized in thin or lensoid Paleozoic limestone units that have been intruded by dioritic units of the Coastal Batholith (Petersen, 1970).

Orebodies in the Eliana district, about 50 km north of Monterosas, occur as replacement veins and contact lodes within or adjacent to gabbro-diorites of the Patap Superunit (Ponzoni and Vidal, 1982). The primary minerals of these ores consist of massive intergrowths of magnetite, apatite, pyrite, pyrrhotite, and chalcopyrite that are intimately associated with actinolite. Wallrock alteration is pervasive and characterized by uralitized ferromagnesian minerals plus chlorite, sphene, epidote, sodic scapolite after plagioclase feldspar, magnetite, calcite, and minor quartz. Mineralogic and fluid inclusion evidence from the Eliana deposit (Vidal, 1980; Ponzoni and Vidal, 1982) indicates that the ores were deposited from chloride-bearing solutions marked by high Na^+/K^+ ratios. Ponzoni and Vidal (1982) advocated that these mineralizing solutions were evolved from the gabbro-diorite parent intrusions. The genesis of ores in the Eliana area was by bimetasomatic hydrothermal replacement of gabbroic and andesitic host rocks along structural channelways (Vidal, 1980).

In contrast, Agar (1981, 1982) has offered a substantially different explanation for the origin of the copper ore in the Rio Pisco (Eliana) area. Sulfides localized as disseminations in volcanic and gabbroic rocks and as components of veins and mantos in gabbroic rocks have been attributed to porphyry copper-type mineralization. The source of the ore-forming fluids, according to Agar (1981, 1982), was

magmatic hydrothermal brines which emanated from successive intrusions of monzonite that belong to the Linga Superunit.

The Raul Mine, about 170 km north of Monterrosas, is a pyritic copper deposit confined to a eugeosynclinal assemblage of volcanic and sedimentary rocks of Cretaceous age (Ripley and Ohmoto, 1979). The ore is concentrated mainly as mantos, stringers, and disseminations, and also as veins emplaced within the Chilca Formation. Chalcopyrite-pyrite[±]pyrrhotite are present as disseminations and as discontinuous bands and lenses within amphibole-rich altered rocks. Other minerals such as chlorite, scapolite, epidote, quartz, and magnetite are found intergrown with the sulfide-amphibole assemblage of the mantos (Ripley and Ohmoto, 1977, 1979). Ripley and Ohmoto (1977, 1979) and Wauschkuhn and Thum (1982) categorized Raul as a volcanogenic exhalative massive sulfide deposit that formed by submarine hydrothermal activity at or near the interface between the sea floor and sea water. However, Vidal (1980), Cardozo and Vidal (1981), and J. Injoque (personal and written communication, 1981 to 1984) have recognized similarities between Raul, Eliana, and Monterrosas such as: (1) the actinolite-rich alteration assemblage that also includes other amphiboles, magnetite, chlorite, epidote, scapolite, sphene, and apatite; (2) an ore assemblage of chalcopyrite, pyrite, magnetite, and pyrrhotite; (3) gabbro-diorite intrusions as the host rocks (Eliana and Monterrosas) and possible source of the hydrothermal mineralizing fluids; and (4) bimetasomatic reaction with and replacement of mafic and intermediate volcanic or plutonic host rocks along faults, fractures, and contacts. Injoque (personal communication, 1981) has identified skarn-type mineralization adjacent to a gabbroic intrusion of the Patap Superunit

in the Raul-Condestable area. A paragenetic sequence of skarn formation at Raul is recognized in which a deeper, higher temperature garnet-pyroxene assemblage becomes an amphibolitic skarn at stratigraphically shallower levels in the volcanic sequence. Vidal (1980) and Injoque (in preparation) thus interpret mineralization in the Raul-Condestable district to represent hydrothermal replacement, not a volcanogenic massive sulfide deposit, that is possibly associated genetically with a gabbro-diorite intrusion.

Regional Tectonics

The Monterrosas deposit is localized within a regionally complex structural zone. It is located about 50 km south of the Abancay deflection along an inland projection of the Nazca Ridge and just north of a transition zone in the angle of subduction of the Nazca plate (Figure 3). Regional variations of geologic features north and south of the Abancay deflection near 13.5°S indicate that fundamental tectonic elements of Peru may have persisted for long periods of geological time (Cobbing et al., 1981; Dalmayrac et al., 1980). Such regional variations to the north of the Abancay deflection include: (1) a thin, flexible crustal segment with trends inclined to the Brazilian Shield (Audebaud, 1973); (2) a compressional stress pattern denoted by horizontal foreshortening and strike-slip faults (Megard and Philip, 1976); (3) pre-Mesozoic rocks of the Eastern Cordillera that narrow and are deflected westward (Petersen, 1972); (4) a change in the regional strike and paleogeography of Mesozoic sedimentary formations (Gansser, 1973); and (5) a uniform width of the Cenozoic polymetallic belt of Cu-Pb-Zn-Ag in central Peru from 6° to 13°S

(Sillitoe, 1974). To the south of the Abancay deflection, regional variations include: (1) a thick continental crust with an intracrustal character related to the Brazilian Shield (Audebaud, 1973); (2) Precambrian crystalline rocks in the Coastal Cordillera which disappear abruptly north of 13.5°S (Gansser, 1973); (3) extensional tectonics with short-lived compressional phases (Mercier, 1981); (4) Tertiary sediments and silicic tuffs (Noble et al., 1979) and marine Oligocene and younger formations (Jenks, 1956) that were deposited on the Coastal Batholith south of 14°S , but are absent to the north; (5) the polymetallic belt doubled in width, but less intensely mineralized (Cobbing et al., 1981); and (6) most of the important deposits of copper in the Western Cordillera (Sillitoe, 1974).

Some investigators believe that some of the differences in geologic features on either side of the Abancay deflection are related to transverse tectonic segmentation caused by differences in the dip of the underlying subduction zone both at the present and in the past (Sillitoe, 1974; Pitcher, 1978). For example, four major segments of the Nazca plate are presently being subducted beneath South America. Two segments (one beneath southern Peru-northern Chile, and another beneath southern Chile) dip about 30° , and the other two beneath central Peru and central Chile have an average dip of about 10° (Barazangi and Isacks, 1976; Hasegawa and Sacks, 1979). Perhaps the best illustration of this variable dip of the Benioff zone beneath South America is seen in the distribution of Quaternary volcanic activity. The correlation between segments with a shallow dip and the lack of Quaternary volcanism in western South America is universal, as is the correlation between those that dip more steeply and recent

volcanic activity (Hanus and Vanek, 1978). The lack of volcanism associated with low angle subduction underscores the prerequisite of an asthenospheric mantle wedge between the subducted and overriding plates for volcanism to occur (Gill, 1981).

The transition from a shallow to a steeply dipping segment at 15°S between the central Peru and southern Peru-northern Chile segments, respectively (Figure 3), has been identified as a contortion over a lateral section 100 km wide within the continuous slab of the Nazca plate (Hasegawa and Sacks, 1981, see Figures 4, 5, and 6; Sacks, 1983; Boyd et al., 1983). Both segments have been subducted at an angle of about 30° down to at least 100 km depth. However, below 100 km the segment beneath central Peru is bent to a near-horizontal attitude, whereas the more southerly segment continues downward at a 30° angle. The shallow dipping segment extends inland about 700 to 800 km, where it again dips about 30° to depths of about 600 km (Sacks, 1983; Hasegawa and Sacks, 1981). Alternatively, Ocola (1983) has proposed a model that consists of two Benioff zones, which differ in age yet have normal dips of 30° beneath central Peru, that are connected by a detachment zone.

The shallowest depths and lowest angles of subduction of the Nazca plate beneath western South America correlate with topographic features such as the Nazca Ridge and the Juan Fernandez Ridge on the subducted slab (Hanus and Vanek, 1978; Pilger, 1981). Pilger (1981), Cross and Pilger (1982), and Sacks (1983) have concluded that subducted, anomalously buoyant oceanic crust beneath the Nazca Ridge has caused the reduced angle of subduction beneath central Peru. Barazangi and Isacks (1976, 1979) surmised that the Nazca Ridge represents a

zone of weakness in the Nazca plate and thus is a likely site for the plate to tear or deform. However, the Nazca Ridge intersects the Peru-Chile Trench significantly north of the contorted transition zone between the steep and shallow dipping segments. The Nazca Ridge, therefore, may have a rippling effect on the Nazca Plate that transmits the contorted transition zone southward. The fact that Pliocene volcanic activity is recorded farther to the north than is Quaternary volcanism (Pilger, 1981) supports this notion.

Cobbing et al. (1981) have speculated that differences in the location of several discontinuities and deflections, as discussed above, may indicate a slight north-south component in the migration of the South American plate relative to the Nazca Plate. The junction between the Nazca Ridge and the Peru-Chile Trench, according to Pilger (1981), has migrated southward during the late Cenozoic, although this apparent movement might also be in part the result of oblique collision rather than northward motion of South America.

Szatmari (1983) has identified the Pisco-Jurua fault as a major intraplate structure that cuts across Peru and defines the Abancay deflection. Left-lateral movement of more than 100 km along the Pisco-Jurua fault may be responsible for the northward termination of the Coastal Cordillera and the deflection of the Eastern Cordillera associated with the Abancay deflection. According to Szatmari (1983), the separation of North America from Gondwana in early Mesozoic time activated movement on the fault. In addition, reactivation of the fault in Pliocene time may have sheared the subducting slab of the Nazca plate and formed the Quiros fracture zone and the Nazca Ridge as the shear zone propagated through the oceanic plate. Although the

Arequipa segment of the Coastal Batholith may have passed through this structure, it did so without apparent deformation because there was little movement along this fault from late Cretaceous to Pliocene time (Cobbing et al., 1981; Szatmari, 1983).

THE MONTERROSAS MINE

Mine History

The first systematic geologic studies at the Monterrosas Mine were begun in 1967 by the Cerro de Pasco Corporation, headquartered in New York City. Geologists of Cerro discovered the copper-bearing Monterrosas Vein. This spurred subsequent topographic and geologic mapping and exploration, which led to the initiation of mine development work underground in 1970. These efforts included two vertical shafts and several drifts at various subsurface levels, as sketched in Figure 6.

On 1 January 1974, the Peruvian properties of the Cerro de Pasco Corporation were nationalized. The Peruvian government formed Empresa Minera del Centro del Peru (Centromin Peru) specifically to manage and operate the former holdings of Cerro. Centromin Peru has continued exploration and development work at the mine. In 1979, 2 percent ownership of Monterrosas was given to Cia. Minera los Montes S.A., a wholly owned subsidiary of Centromin Peru. Los Montes is now the operator of the Monterrosas Mine.

The Monterrosas deposit was put into production in March, 1982. The mine produced 8,907 tons of concentrate in 1982 that contained about 31 percent copper and 0.43 ounces of gold per ton (Hyde, 1984). About 70 tons of molybdenite concentrate that averaged 53 percent molybdenum was also scheduled for recovery (Hyde, 1983). Pyrite separated from the tailings of copper produced a concentrate with 0.4 percent cobalt (Hyde, 1984). The copper tailings and pyrite concentrate were sent to the Finnish company, Outokumpu Oy, and the copper

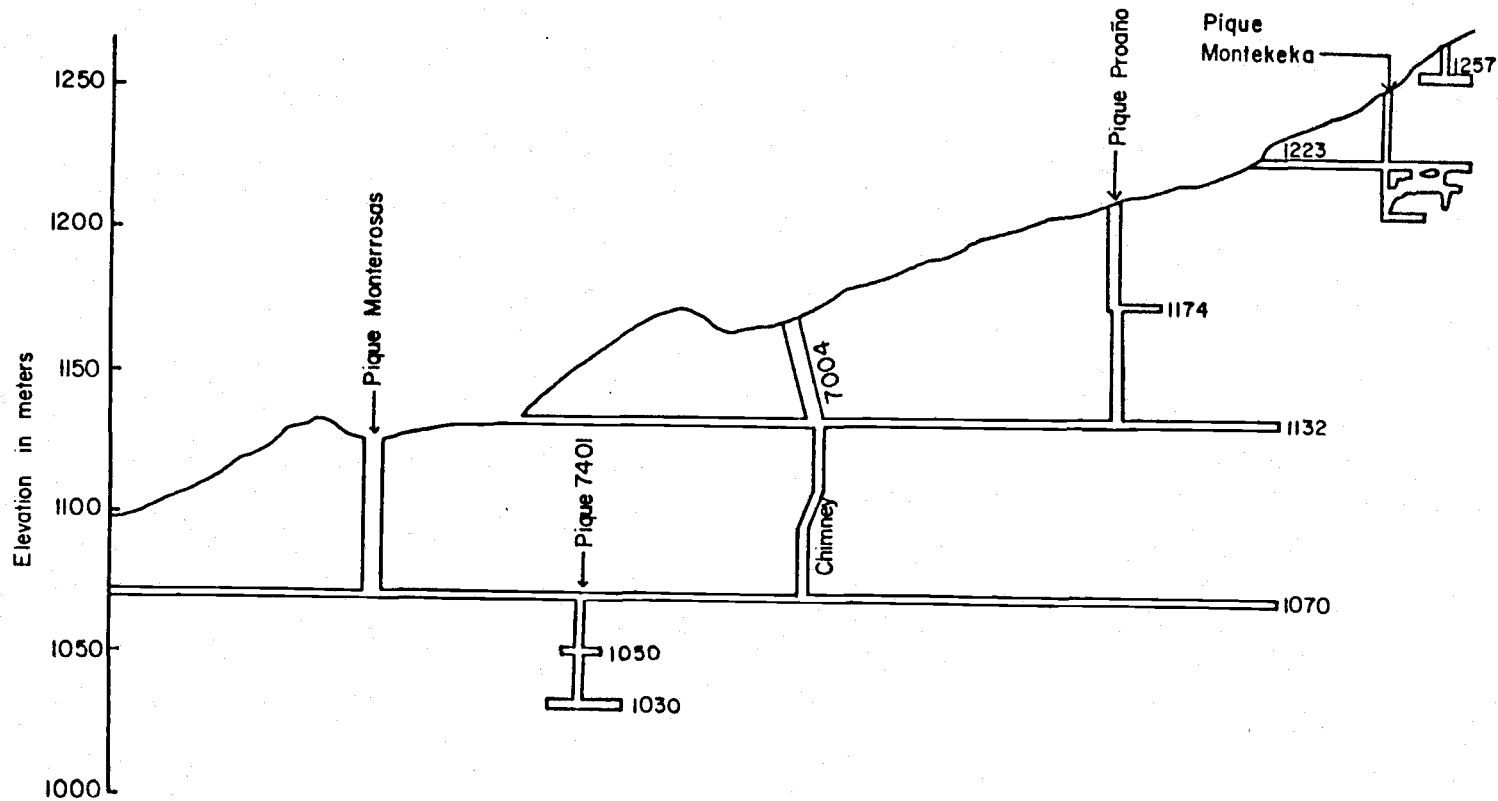


Figure 6. Schematic Cross-Section of the Monterrosas Mine.
View looking northeast, not to scale.

concentrates were shipped to Japan (Todd, 1983; Hyde, 1984). Production is expected to reach 13,000 tons of concentrate annually.

Centromin Peru has calculated ore reserves that total about 1.9 million tons of 2 percent copper-equivalent, or about three years of proven and probable reserves (Todd, 1983).

The cost of the Monterrosas project was about \$14.2 million (Hyde, 1983). The Crocker National Bank provided \$5 million, Corporacion Financiera de Desarrollo (COFIDE) \$3.6 million, the Capital Fund \$1 million, and various local sources accounted for the balance (Hyde, 1983). The mine was expected to be profitable at a 1982 price of copper estimated in 1979 at \$0.90 per pound (Todd, 1983). At present, production covers operating expenses and depreciation, but not financing costs, at the current price of copper (about \$0.70 per pound). The loss for 1982 was about \$500,000. It is estimated that the Monterrosas Mine could cover all its costs at a price of \$0.80 per pound of copper (Todd, 1983).

The Monterrosas Deposit

The Monterrosas orebody is a tabular, fracture-controlled vein-like deposit that is confined to a structurally complex zone characterized by en echelon fractures and splay faults trending approximately east-west and dipping steeply north to vertical. Although this zone is largely defined by a major (unnamed) fault that cuts all plutonic rocks of the area, economic grades of mineralization are located primarily within gabbro-diorites of the Patap Superunit along a splay that trends about N55°W, as shown in Plate 1. The orebody is comprised of nearly massive sulfides that currently measure at least

260 m in length, 3 to 16 m in width, and 150 m in depth. The ore averages 1.9 percent copper, 0.7 ounces silver, and 0.03 ounces gold per ton. It also contains anomalously large concentrations of cobalt (up to 630 ppm) and molybdenum (up to 800 ppm), and minor geochemical anomalies for nickel (up to 200 ppm) and gallium (up to 200 ppm) have been detected in composite rock-chip samples from the ore zone.

An overview of the extent and distribution of copper mineralization, based on the average of assays for channel samples up to two meters in length collected by Centromin Peru, is summarized in Figure 7. The channel samples are of two types. "Back" channel samples were collected across the back, or roof, of the mine tunnel, at right angles to the direction of the tunnel and to the general structural trend of the mineralization, and at 2 m intervals along the length of the tunnel. "Wall" channel samples were collected continuously at 2 m intervals along one of the two walls, or sides, of the tunnel, and thus they parallel the direction of the tunnel and the general structural trend of mineralization. Because locations of the channel samples are controlled by available mine workings, whereas the orebody is defined by these samples as well as those collected from crosscuts and drill core, the mineralization as portrayed in Figure 7 does not define precisely the orebody in terms of location and grade. Although the data for these channel samples imply that rocks outside the ore zone contain as much as 0.5 percent copper, analyses of samples collected in this study from nearly equivalent locations reveal essentially background concentrations for copper of about 0.005 percent (50 ppm).

The primary mineral assemblage consists chiefly of chalcopyrite, magnetite, pyrite, and actinolite in variable proportions, and

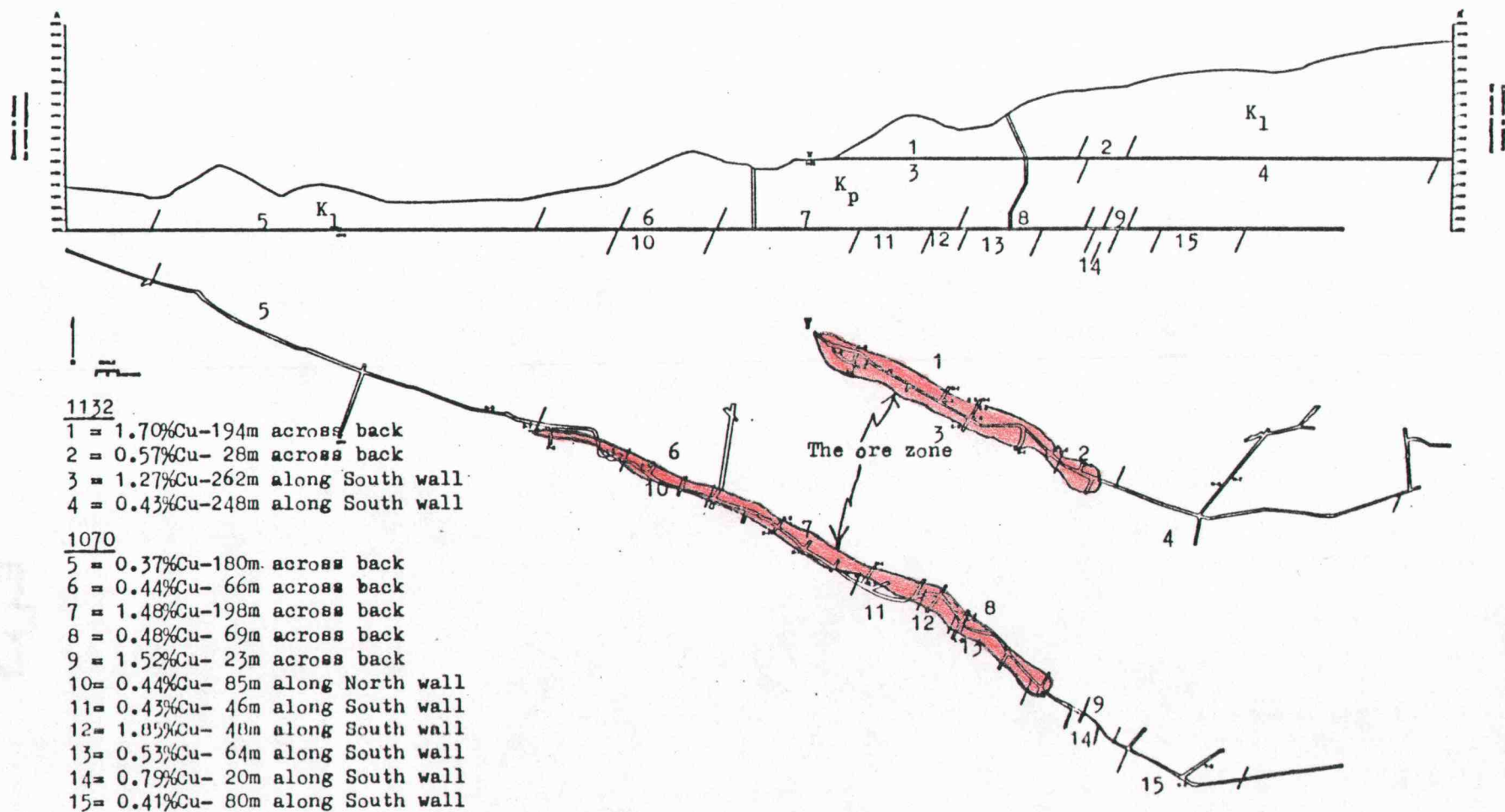


Figure 7. Schematic Diagram of Mineralization in the Subsurface of the Monterrosas Mine.

subordinate amounts of scapolite, quartz, apatite, cubanite, and pyrrhotite. Replacement of the gabbro-diorites was the principal mode of mineral deposition, with lesser filling of fractures, as deduced from petrographic studies of thin and polished sections. The iron and copper minerals in weathered outcrops include hematite, goethite, jarosite, azurite, malachite, chrysocolla, and atacamite as products of oxidation, bornite, covellite, and sooty chalcocite probably formed by supergene enrichment, and minor amounts of residual pyrite, chalcopyrite, and magnetite.

Contacts between the dioritic wall rocks and the orebody are transitional, as deduced from detailed geologic mapping of subsurface exposures and petrographic studies. These contacts are diffuse and indistinct because of locally widespread amphibolization that is accompanied by disseminations and veinlets of ore and gangue minerals to form this transitional zone. The outermost portion of the amphibolized gabbro-diorite passes inward to a zone of finely to coarsely crystalline (to more than 5 cm) actinolite that contains increasingly larger amounts of disseminated and stringer occurrences of oxide and sulfide minerals. The actinolite-rich portion of the ore zone grades inward to a massive zone of magnetite containing stringers and blebs of sulfides and actinolite, which in turn grades into a central zone of massive to nearly massive sulfides with minor gangue. These zones exhibit "pinch and swell" features and may differ significantly in size on either side of the high-grade sulfide zone. In addition, the overall width of the ore zone may also change along strike. Smaller monomineralic lenses of actinolite, magnetite, pyrite, and chalcopyrite

are found both transverse and parallel to the strike of the orebody for distances of several meters or more.

The character of mineralization is markedly different in monzonitic host rocks of the Linga Superunit that are present east-southeast and west of the diorite-hosted Monterrosas orebody. Copper concentrations diminish to negligible amounts (less than about 0.6%), mineralization is dominated by cavity or fracture filling processes, and mineral assemblages of the veins consist of quartz \pm calcite and (or) epidote \pm potassium feldspar. Minor occurrences of copper and iron sulfides within some quartz-rich veins in the monzonitic rocks such as the Monterrosas or Montekeka Veins (Plate 1) might represent minor re-mobilization and redeposition of components from the earlier diorite-hosted ore.

PLUTONIC ROCKS

Gabbro-diorites of the Patap Superunit represent the earliest phase of batholithic magmatism in the Monterrosas area. According to Cobbing (1982), magmas of the Patap Superunit were emplaced about 100 m.y. ago, although an age of 82 ± 3 m.y. was obtained by whole rock K-Ar dating for the least altered sample of gabbro-diorite (6-8-13) exposed in the Monterrosas area. This anomalously young date could be the result of post-crystallization changes in the gabbro-diorites related to mineralization and (or) later intrusions in the mine area. Intrusion of monzonites associated with the Linga Superunit followed emplacement of the Patap Superunit. A K-Ar whole rock age date of 92 ± 3 m.y. for a sample of granodiorite (7-2-13) at Monterrosas agrees with a published age for rocks in the Linga Superunit of about 97 ± 3 m.y. (Cobbing and Pitcher, 1983). Intrusive relationships between the two superunits in the Monterrosas area indicate that rocks of the Linga Superunit are younger than those of the Patap Superunit. For example, xenoliths, although absent in the gabbro-diorite phases, are commonplace in the monzonitic units. These xenoliths are rounded to angular in shape, up to 15 cm in diameter, mafic in composition, and increase in abundance near contacts with the Patap Superunit. They presumably represent fragments of wall rock derived from the gabbro-diorites during emplacement of the more silicic phases in the Linga Superunit.

The Patap Superunit

Gabbros and diorites of the Patap Superunit as shown in Plate 1 are found in the central portion of the Monterrosas area. Surface

exposures of fresh rocks are generally dark greenish-gray to black in color. They are finely to coarsely crystalline equigranular and contain clinopyroxene, plagioclase feldspar, amphibole, sphene, and magnetite that are readily identifiable in hand specimen. As the mineralized zone is approached, the intensity of alteration in the gabbro-diorites increases and new secondary minerals become noticeable. These consist of actinolite, chlorite, epidote, scapolite, tourmaline, and traces of pyrite that are visible along with plagioclase feldspar, sphene, and magnetite.

Petrographic examinations of the Patap rocks indicate that they have fairly consistent textural and mineralogical characteristics. They are generally medium equigranular with crystal sizes ranging from less than 1 to 6 mm. However, a finely crystalline variety of gabbro-diorite with a mean crystal size of less than 2 mm has been recognized in drill core. Sparsely distributed large crystals of plagioclase feldspar impart a porphyritic texture to a few samples. Major primary minerals include plagioclase feldspar, clinopyroxene, and light brownish hornblende, with accessory sphene, magnetite, ilmenite, apatite, and zircon in abundances as indicated in Table 1 and in Appendix 1. Secondary minerals such as uralite or fibrous actinolite, green-brown hornblende, epidote and clinozoisite, scapolite, magnetite, sphene, chlorites, tourmaline, allanite, calcite, apatite, white mica, green and brown biotite, albite, quartz, and pyrite are superimposed as minerals that mainly replace magmatic clinopyroxene, plagioclase feldspar, and ilmenite.

Plagioclase feldspar is the most abundant mineral in Patap gabbro-diorites from the Monterrosas area. Polysynthetic twins that follow

Table 1. Modal Compositions* of the Least Altered Rocks of the Patap and Linga Superunits in the Monterrosas Area (in volume percent)

	<u>Patap Gabbro-Diorites</u>		<u>Linga Monzonites</u>			
	(n=6)		K1a (n=6)		K1b (n=5)	
	mean \pm 1	range	mean \pm 1	range	mean \pm 1	range
Quartz	<1	<1-3	17.8 \pm 4.6	14-26	11.5 \pm 4.1	7-16
Kspar	--	--	19.7 \pm 4.5	12-26	5.8 \pm 2.4	3-9
Plagioclase	59.3 \pm 5.8	49-67	42.9 \pm 2.9	37-46	53.7 \pm 2.5	50-56
Clinopyroxene	13.0 \pm 9.6	<1-26	<1	<1-3	<1	<1-1
Amphibole	15.5 \pm 8.5	2-25	13.0 \pm 2.5	9-16	18.0 \pm 2.2	15-21
Apatite	1.2 \pm 0.9	<1-3	<1	<1	<1	<1
Sphene	1.8 \pm 0.9	<1-3	1.4 \pm 0.8	<1-3	1.8 \pm 1.5	<1-4
Opaque oxide	3.0 \pm 1.7	1-6	2.4 \pm 1.1	<1-3	4.1 \pm 1.7	2-6
Zircon	<1	<1	<1	<1	<1	<1
Allanite	<1	<1	<1	<1	<1	<1
Biotite	--	--	<1	<1	<1	<1
Epidote	2.4 \pm 1.9	<1-6	<1	<1	<1	1-2
Scapolite	2.1 \pm 1.9	<1-5	--	--	--	--
Chlorite	<1	<1	<1	<1	1.0 \pm 1.0	1-3
Sericite	<1	<1-3	<1	<1	2.2 \pm 0.4	2-3
Albite	<1	<1	<1	<1	<1	<1
Calcite	<1	<1	<1	<1	<1	<1

* Modes based on at least 1000 points counted for one or more thin sections per sample.

the albite twin law are widespread in these feldspars, whereas polysynthetic pericline and complex albite-Carlsbad twins are less common. In general, twinning is indistinct and interrupted. Many crystals are fractured, bent, or display offset twins that provide evidence of mild protoclastic or tectonic deformation during or after crystallization of the Patap magma.

It is clear that plagioclase feldspar had a complicated history of crystallization in the Patap magma. Compositions in the gabbro-diorites range from An 33 to An 59, as measured by the Michel-Levy method on albite twins and the combined albite-Carlsbad method (Phillips and Griffen, 1981, pp. 354-358). Analyses of individual crystals by electron microprobe indicate a complex pattern of compositional zoning. For example, normal, discontinuous, and possibly oscillatory and reverse variations are present. Compositions in the cores of fresh crystals are as calcic as An 56 and the rims are as sodic as An 28 (Appendix 2). Differences in composition that are manifest by features such as discontinuous and oscillatory zoning within individual crystals suggest that changes both internal and external to the magma took place during crystallization (Smith and Lofgren, 1983). Deviations in pressure, temperature, water saturation, and (or) the kinetics of crystal growth might account for some of the variations identified in plagioclase feldspar from the Patap gabbro-diorites. Furthermore, resorption and replacement of crystals of andesine-labradorite indicate reaction and decomposition after crystallization from the magma. Secondary minerals such as epidote, scapolite, and clinozoisite are present in the cores of plagioclase feldspar from relatively fresh samples of gabbro-diorite. These

minerals appear to be the products of late magmatic-deuteric alteration. Increased alteration of the plagioclase feldspars associated with mineralization resulted in the formation of other secondary minerals such as chlorite, amphibole, magnetite, calcite, white mica, albite, and quartz. A dark, clouded, dusty appearance in many fresh and altered crystals of plagioclase feldspar may have been caused by the inclusion of minute particles of magnetite, ilmenite, hematite, amphibole, and (or) pyroxene during primary crystallization (Bottinga et al., 1966) and possibly by processes of diffusion and replacement after initial crystallization (Deer et al., 1963, p. 152).

Clinopyroxene, which is present as small, colorless to pale-green, subhedral crystals, is interstitial to plagioclase feldspar in the gabbro-diorites. Simple twins are characteristically observed in some crystals. Petrographic determinations indicate that the composition of the pyroxene is diopsidic augite, and this inference is supported by electron microprobe analyses, shown in Figure 8, which indicate that the average composition of magmatic clinopyroxene in relatively fresh gabbro-diorites is diopside. Analyses of individual crystals plot predominantly as diopside on the pyroxene quadrilateral, with only one or two crystals classified as salite, augite, or endiopside (Figure 8; Appendix 3). Petrographic evidence such as extensions of diopside along the borders of plagioclase feldspar crystals and inclusions of andesine-labradorite in diopside demonstrates that at least some clinopyroxene crystallized after plagioclase feldspar. Diopside became unstable after crystallization, and it was partly to totally replaced by light olive to green-brown actinolitic hornblende

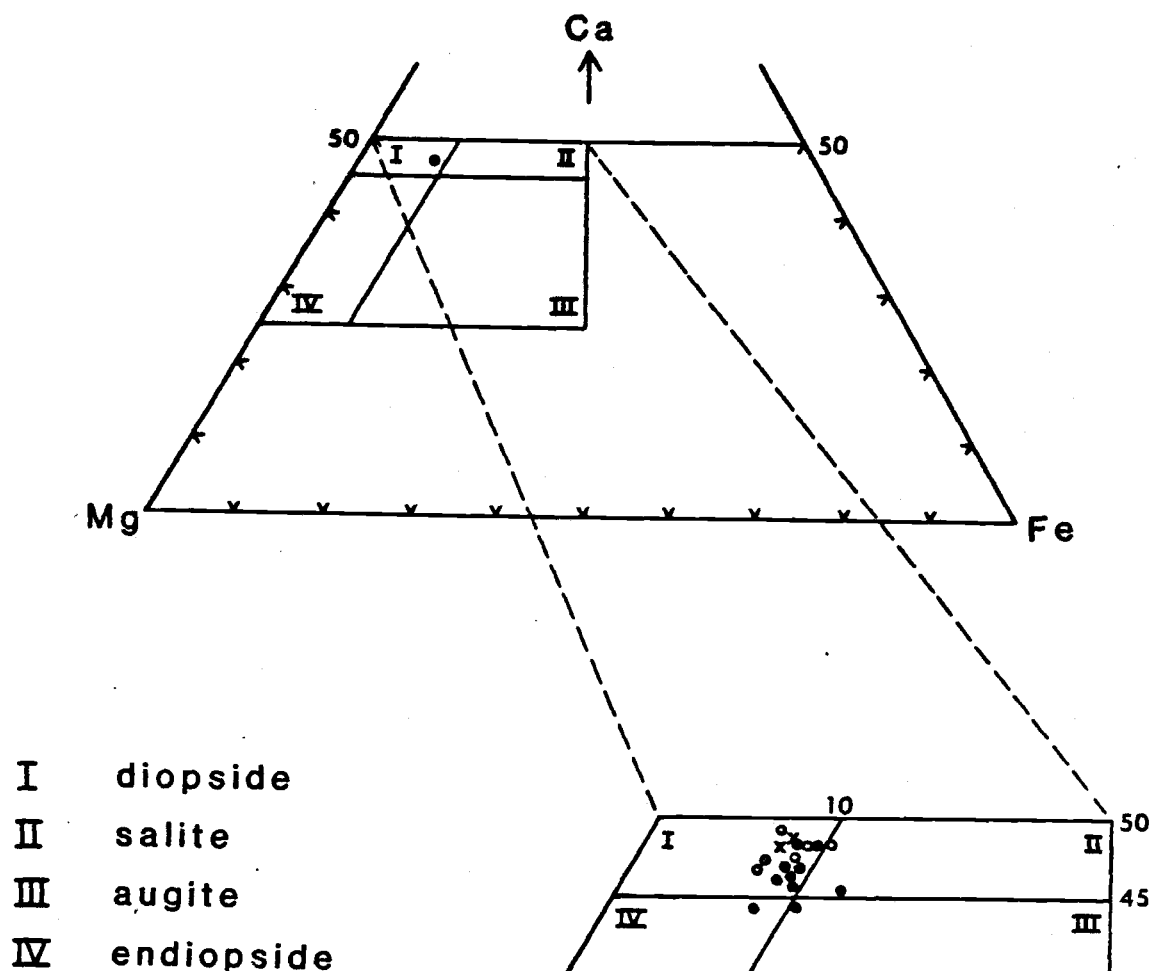


Figure 8. Electron Microprobe Analyses of Clinopyroxenes. Analyses from the Monterrosas deposit are plotted on the pyroxene quadrilateral (in atomic percent), after Deer et al., 1978, Figures 1 and 11, p. 3 and 16, respectively. Upper diagram with plot of the average composition of clinopyroxene in fresh samples of gabbro-diorite (samples 6-8-13 and 10-2-21). Expanded diagram shows plots of individual analyses (closed circles, 6-8-13; open circles, 10-2-21; x, 1-32-15).

and blue-green uraltite or fibrous actinolite. Cores of remnant diopside within amphibole are observed commonly in relatively fresh rocks, and amphibole that is entirely pseudomorphic after pyroxene is widespread in more altered samples of gabbro-diorite. Some crystals of diopside contain inclusions of ilmenite, magnetite, sphene, apatite, and zircon as well as replacement intergrowths of sphene and magnetite or ilmenite.

Some amphiboles in the gabbro-diorites are presumably hornblende and appear to be of primary magmatic origin. They are present as finely crystalline subhedra that occupy interstices between crystals of plagioclase feldspar and diopside. This amphibole exhibits pleochroic colors from brown to greenish brown and is optically negative with a large 2V. Microprobe analyses (Appendix 4) suggest that this amphibole is actinolitic hornblende based on the classification scheme of Leake (1978) and Leake and Hey (1979). Actinolitic hornblende alters to actinolite, chlorites, epidote, sphene, and iron-titanium oxides.

Ilmenite and magnetite have been identified in examinations of polished thin sections and confirmed by electron microprobe analyses (Appendix 5). Minerals such as sphene, apatite, and zircon, in addition to ilmenite and magnetite, are present as subhedral to euhedral crystals that are interstitial to and included within plagioclase feldspar and clinopyroxene. Ilmenite is generally more altered than magnetite in the gabbro-diorites. Complex intergrowths that include hematite, sphene, pseudobrookite, rutile, leucoxene, and (or) magnetite and sulfides replace ilmenite. Leucoxene is a common alteration product of sphene and ilmenite. Magnetite has been altered to hematite

(or martite) and limonite, and may be replaced by pyrite and (or) chalcopyrite.

The Linga Superunit

Monzonitic rocks of the Linga Superunit are distributed widely around gabbro-diorites of the centrally located Patap Superunit (Plate 1). A variety of rock types, as depicted in Figure 9, are contained within this superunit. Quartz monzodiorites and granodiorites are the most prevalent compositions, but quartz diorites, tonalites, and quartz monzonites are also present. Modal variations within the Linga Superunit in the Monterrosas area complicate the identification of individual petrologic units. However, differences in the abundances of minerals characterize the granitoid units of the batholith, and especially the Linga Superunit (W. S. Pitcher, written communication, 1981). For example, Cobbing and Pitcher (1972) have discussed deviations in the content and proportions of mafic minerals and potassium feldspar which result in local modal variations contained within the scale of an individual outcrop. The Linga Superunit in the Monterrosas area has been subdivided tentatively into two units, K_{1a} and K_{1b} , on the basis of the modal percentage of potassium feldspar. Unit K_{1a} includes rocks with more than 10 volume percent potassium feldspar such as granodiorites, quartz monzonites, and quartz monzodiorites, and unit K_{1b} consists of rocks that contain less than 10 volume percent K-feldspar such as quartz diorites, tonalites, and some quartz monzodiorites, as shown in Figure 9, Table 1, and on Plate 1. Both of these units are more leucocratic than the gabbro-diorites, and they range in color from greenish gray to pinkish. This variation in color

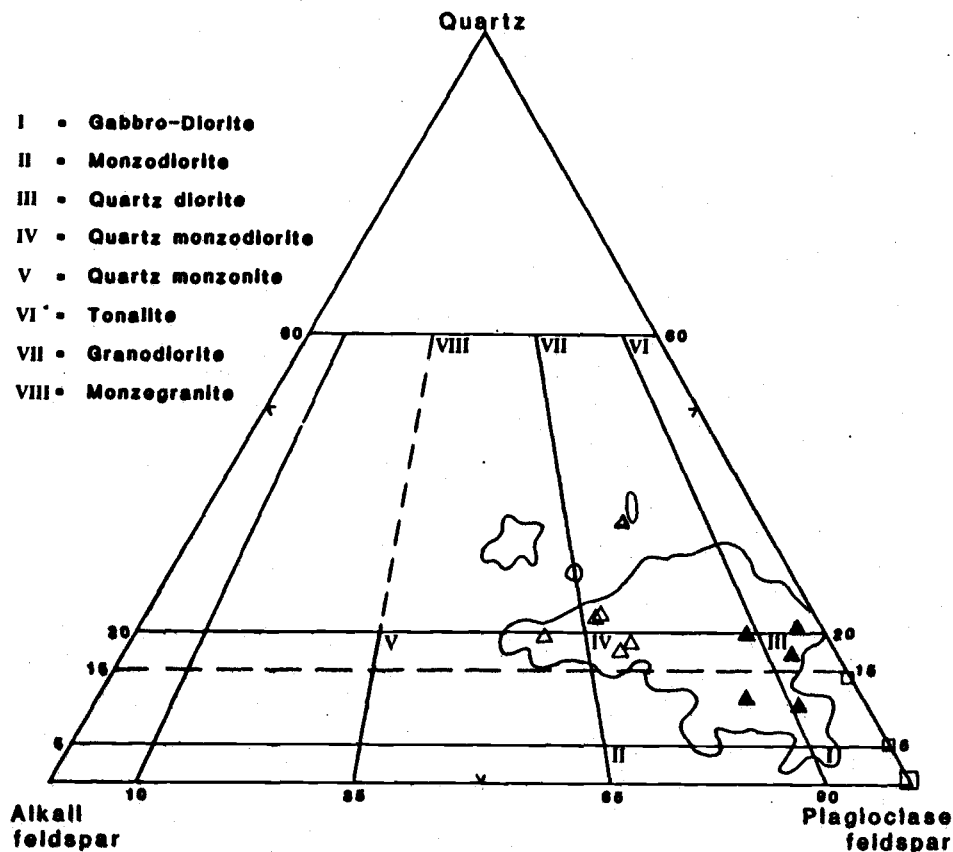


Figure 9. QAP (quartz-alkali feldspar-plagioclase feldspar) Diagram (after Streckeisen, 1973) of Modal Compositions of the Patap and Linga Superunits in the Monterrosas area. Squares, Patap Superunit; closed triangles, Linga Superunit, unit Kl_b; open triangles, Linga Superunit, unit Kl_a. Large square at apex of plagioclase feldspar includes most of the gabbro-diorites. Irregular solid lines enclose fields of granitoids represented in the Arequipa segment of the Coastal Batholith (after Atherton et al., 1979, Figure 9, p. 57). Dashed line at 15 percent quartz indicates boundary used to define the limits of fields for granitoids named by British geologists.

correlates with the amount of pink potassium feldspar and dark ferromagnesian minerals in the rock. The monzonitic rocks in outcrop are fine to medium crystalline equigranular. Rounded to angular and elongated mafic inclusions and clots are characteristic of the Linga units. Minerals such as quartz, potassium feldspar, plagioclase feldspar, hornblende, sphene, and magnetite are visible in hand specimen.

The Linga units have uniform petrographic characteristics. They are fine to medium equigranular, with crystal sizes generally less than 5 mm. A porphyritic texture is imparted to several of the samples by large (> 6 mm) zoned crystals of plagioclase feldspar. Plagioclase is the most abundant primary mineral. Other major primary minerals are quartz, potassium feldspar, and hornblende, with traces of clinopyroxene and biotite. Accessory minerals found in rocks of the Linga Superunit include sphene, magnetite, ilmenite, apatite, and zircon. Secondary minerals such as chlorite, white mica, epidote and clinozoisite, magnetite, sphene, actinolite, quartz, potassium feldspar, albite, calcite, and allanite are present in minor amounts. Traces of tourmaline and scapolite are also present in a few samples.

Plagioclase feldspar is the dominant mineral phase in the Linga Superunit. Abundances range from about 55 percent to about 35 percent (Table 1; Appendix 6). It is present as subhedral to anhedral laths that are generally less than 5 mm in length. Many crystals of plagioclase feldspar exhibit evidence of deformation, as indicated by bent and fractured crystals, discontinuous and indistinct twins, and fractures occupied by veinlets of quartz and (or) calcite. Compositions range from An 24 to An 52, as measured from extinction angles of

albite and combined albite-Carlsbad twins (Phillips and Griffen, 1981, pp. 354-358). Many crystals of plagioclase feldspar are compositionally zoned, with normal, oscillatory, and discontinuous zone types apparently most common. The cores of some zoned crystals are filled with inclusions of opaque minerals, amphibole, and possibly pyroxene. These feldspars may indicate that restitic material was present in the Linga magmas during their ascent and crystallization (Pitcher, 1979). The restitic feldspar was subsequently corroded and overgrown by less calcic plagioclase feldspar. Some mafic clots and xenoliths in the Linga intrusions may also represent restite (White and Chappell, 1977).

Although plagioclase feldspar in rocks of the Linga Superunit is generally unaltered at the Monterrosas Mine, samples from a few localities have been altered thoroughly to intergrowths of coarsely crystalline white mica (essentially muscovite), chlorite, and calcite. Epidote, actinolite, and clinozoisite also replace andesine. In addition, alkali feldspar and quartz may rim and apparently replace crystals of plagioclase. Variable replacement by alkali feldspar may leave merely a remnant core of the original andesine, and discrete veinlets of alkali feldspar in a few samples cut across the albite twins of plagioclase feldspar.

Potassium feldspar is the second most abundant constituent in the more felsic rocks of the Linga Superunit. Its abundance varies from less than 5 percent in the quartz diorites to more than 20 percent in the quartz monzonites. This feldspar is recognized petrographically as microcline perthite and possibly as orthoclase perthite. Much of the potassium feldspar has a dusted and cloudy appearance. It also exhibits unusual overgrowths of anhedral sphene in a few samples.

Crystal sizes range from less than 1 to about 3 mm, and crystal shapes are anhedral to subhedral. Coarsely crystalline perthite exhibits an interstitial relationship to andesine, and it may also replace plagioclase feldspar. Moreover, perthite is commonly intergrown with and adjacent to quartz.

Quartz is usually present in amounts of less than 20 volume percent in rocks of the Linga Superunit in the Monterrosas area. It is commonly associated with perthite in interstices between crystals of plagioclase feldspar. Textural evidence in some samples suggest that quartz also corrodes and replaces plagioclase feldspar. Many of the quartz crystals contain fluid inclusions. Simple vapor + liquid inclusions are most common, but more saline inclusions with halite and other daughter minerals are also present. The fluid inclusions will be discussed in more detail in a later chapter.

Amphibole is the predominant ferromagnesian mineral in plutonic phases of the Linga Superunit. It ranges in abundance from 9 to about 20 volume percent. The pleochroic colors of the amphibole minerals vary from moderate yellowish green to greenish brown and bluish brown. In general, amphiboles in the monzonites are browner than those in the gabbro-diorites. On the basis of petrographic criteria, these amphiboles are classified as hornblendes. Much of the hornblende has been variably altered to blue-green actinolite, chlorite, epidote, biotite, sphene, magnetite, and (or) smectite. Some crystals of hornblende have remnant cores of clinopyroxene, and many contain inclusions of apatite. These minerals provide further evidence that the Linga magmas may have carried restitic material (Hine et al., 1978). White and Chappell (1977) have described the presence of pyroxene cores and inclusions of

apatite in hornblende from I-type granitoids, and these amphiboles are presumed to have been derived from residual pyroxene by equilibration with a hydrous melt as the magma ascended and crystallized.

Clinopyroxene and red-brown biotite are minor ferromagnesian constituents of the Linga Superunit. The clinopyroxene is colorless and is distributed sparsely as remnant cores in crystals of amphibole. The composition of clinopyroxene is probably augite or diopsidic augite based on petrographic data such as optic angle, birefringence, and refractive index (relief). Red-brown biotite is present in trace amounts as subhedral crystals interstitial to andesine and hornblende, or as overgrowths on the margins of amphibole.

Sphene, magnetite, ilmenite, apatite, and zircon are accessory minerals in rocks of the Linga Superunit. They are present as small subhedra and euhedra interstitial to and included within plagioclase feldspar and the ferromagnesian minerals. Sphene and less commonly apatite and the opaque minerals may form larger crystals up to 3 mm in diameter.

Chemistry of the Plutonic Rocks

The Patap Superunit

Gabbro-diorites of the Patap Superunit represent the most mafic rocks in the Monterrosas area. Compositional data for the least altered samples of this superunit, as summarized in Table 2, indicate that the gabbro-diorites are characterized by low average concentrations of FeO as total iron oxide (5.4 wt %) and K₂O (0.2 wt %) and high average concentrations of CaO (11.5 wt %) for an average SiO₂ content of about 55 wt percent. The Na₂O/K₂O ratio is also high

Table 2. Means, Standard Deviations, and Ranges of Major Oxide and Minor and Trace Element Constituents* in the Least Altered Samples of the Patap and Linga Superunits of the Monterrosas Area

	<u>Patap Gabbro-Diorites</u>		<u>Linga Monzonites</u>			
	(n=6)		K1a (n=6)		K1b (n=5)	
	<u>Weight Percent</u>		<u>Weight Percent</u>			
	mean \pm 1	range	mean \pm 1	range	mean \pm 1	range
SiO ₂	54.6 \pm 0.7	54-55	62.9 \pm 1.3	61-65	59.4 \pm 4.0	55-65
TiO ₂	0.91 \pm 0.05	0.9-1.0	0.61 \pm 0.05	0.6-0.7	0.76 \pm 0.10	0.6-0.9
Al ₂ O ₃	17.2 \pm 0.9	16-18	16.2 \pm 0.4	16-17	17.1 \pm 1.1	16-18
FeO _t	5.4 \pm 1.2	4-7	5.3 \pm 0.7	4-6	7.5 \pm 1.6	6-9
MgO	4.9 \pm 1.0	3-6	2.2 \pm 0.1	2	3.1 \pm 0.7	2-4
CaO	11.5 \pm 1.4	10-14	5.3 \pm 1.0	4-7	6.7 \pm 0.9	5-8
Na ₂ O	4.2 \pm 0.3	4-5	4.4 \pm 0.5	4-5	4.6 \pm 0.7	4-5
K ₂ O	0.21 \pm 0.12	0.1-0.4	2.2 \pm 1.0	1-3	0.9 \pm 0.7	1-2
Total	98.9		99.1		99.9	
S.G.	2.85 \pm 0.02		2.71 \pm 0.01		2.76 \pm 0.04	
	<u>ppm (n=6)</u>		<u>ppm (n=11)</u>		<u>ppm (n=14)</u>	
Cu	44 \pm 36	6-85	30 \pm 14	11-55	44 \pm 12	20-65
Mo	1 \pm 1	<1-2	2 \pm 2	<1-7	1 \pm 2	<1-7
Pb	10 \pm 4	5-15	26 \pm 31	5-100	13 \pm 10	4-40
Zn	14 \pm 4	8-19	27 \pm 19	11-70	18 \pm 8	5-30

Table 2--Continued

	<u>Patap Gabbro-Diorites</u>		<u>Linga Monzonites</u>			
			K1a		K1b	
	ppm (n=6)		ppm (n=11)		ppm (n=14)	
Ag	0.3±0.1	<0.3-0.4	≤0.3	<0.3-0.3	0.3±0.2	<0.3-0.7
Co	5±1	4-6	6±2	5-10	8±3	4-12
Ba	326**	300-347		970-1063***		
Ce	26	15-40		47-55		
Cr	24	18-31		7-13		
Ga	19	17-20		17		
La	14	11-17		22-29		
Ni	7	5-11		3-5		
Nb	4	3-5		6		
Rb	6	3-14		36-51		
Sc	28	24-31		22-24		
Sr	471	437-494		291-363		
Th	7	<1-16		12-13		
U	1	<1-2		3-4		
V	120	98-149		124-133		
W	1	<1-3		<1		
Y	17	14-23		27-28		
Zr	96	89-110		155-199		

* Oxide analyses by G. Sidder, Dr. Edward Taylor, and Ms. Ruth Lightfoot, Oregon State University; Cu to Co analyses by Chemical and Mineralogical Services, Salt Lake City, Utah; Ba to Zr analyses by J. Injoque, University of Nottingham, England.

** n=4 for elements Ba to Zr.

*** n=2 for elements Ba to Zr.

(about 20) in these rocks compared to that for similar igneous rocks (2 to 6) in compilations by LeMaitre (1976) and Nockolds (1954).

Minor element and preliminary trace element data in the least altered gabbro-diorites of the Patap Superunit suggest that these rocks have a tholeiitic affinity. High values of Sr (about 470 ppm), low Rb (less than 6 ppm), and low ratios of Rb/Sr in addition to discrimination diagrams (not shown here) of trace elements such as Cr/Y and Ti/Y (Pearce, 1982) are compatible with the proposal that the Patap Superunit was derived from a parental magma of olivine tholeiite composition (Cobbing et al., 1981; Mullan and Bussell, 1977). Other elements such as copper, lead, and molybdenum have normal concentrations for rocks of this composition, whereas zinc, cobalt, and nickel have low abundances (Table 2).

Chemical data for all samples of gabbro-diorite from the Monterrosas area (Appendix 1) show appreciable scatter and poor linearity when plotted by conventional methods in terms of the alkali-lime (Peacock) index or the Harker variation diagram (not illustrated). The cause of this chemical variability is attributed both to the effects of a complex history of emplacement and crystallization for magmas of the Patap Superunit and to subsequent alteration and metalization of these host rocks in the Monterrosas Mine area. Variations imposed by such alteration are best illustrated on the ternary AFM diagram given in Figure 10. The compositional locations of most samples of gabbro-diorite do not occupy the general boundaries for rocks of the Patap Superunit as defined by Cobbing et al. (1981, Fig. 65, p. 104), nor do they follow typical calc-alkaline or tholeiitic trends. A conventional interpretation of these deviations might

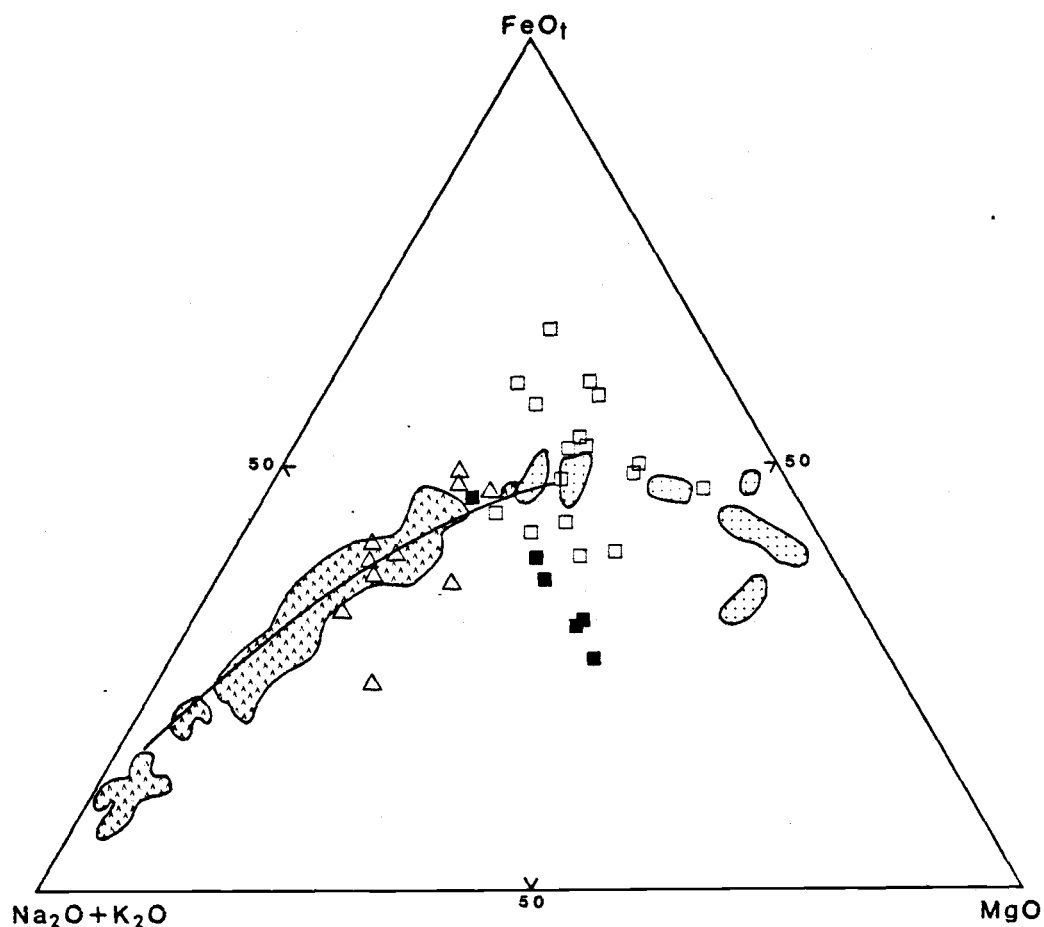


Figure 10. Ternary AFM Diagram. This diagram compares the compositional distribution of samples from the Patap and Linga Superunits at the Monterrosas area to those of the Coastal Batholith (Cobbing et al., 1981) and the calc-alkalic trend line (Nockolds and Allen, 1953). Closed squares, relatively unaltered gabbro-diorites; open squares, altered gabbro-diorites; open triangles, Linga monzonites; dot pattern, gabbros of the Coastal Batholith; check pattern, granitoids of the Coastal Batholith; dark curved line, calc-alkalic trend.

suggest that samples of gabbro-diorite with low values of iron were leached during alteration, or that they were enriched particularly in alkali components. However, these samples are the least altered petrographically. Furthermore, the gabbro-diorites do not have disproportionate amounts of Na_2O or K_2O compared to rocks of the Patap Superunit elsewhere in the batholith, as presented on the ternary NKC diagram in Figure 11 after Cobbing et al. (1981, Fig. 65, p. 104). Thus, variations in total iron oxide appear to be the major factor that is responsible for the scatter of samples plotted in Figure 10. The unusually low concentration of iron in the least altered gabbro-diorites may be related to conditions of crystallization in the gabbro-diorite magma such as the fugacity of oxygen, volatile content, and temperature and pressure. These features will be considered more fully in the following "Discussion" section.

The Linga Superunit

Monzonitic rocks of the Linga Superunit in the Monterrosas area display a calc-alkaline trend on the ternary AFM and NKC diagrams (Figures 10 and 11). This trend is also delineated on variation diagrams such as the Peacock and Harker diagrams. Values of TiO_2 , total iron oxide, MgO , and CaO decrease, and Na_2O and K_2O generally increase with increasing wt percent SiO_2 . The $\text{Na}_2\text{O}/\text{K}_2\text{O}$ ratio is similar to and slightly higher (2 to 5) than average granodiorites, monzonites, and tonalites (< 1 to 3) as recorded by LeMaitre (1976). In particular, rock samples of unit K_{1b} from the Monterrosas area display a higher $\text{Na}_2\text{O}/\text{K}_2\text{O}$ ratio on the NKC diagram (Figure 11) than other similar phases of the Coastal Batholith. However, the sums of the

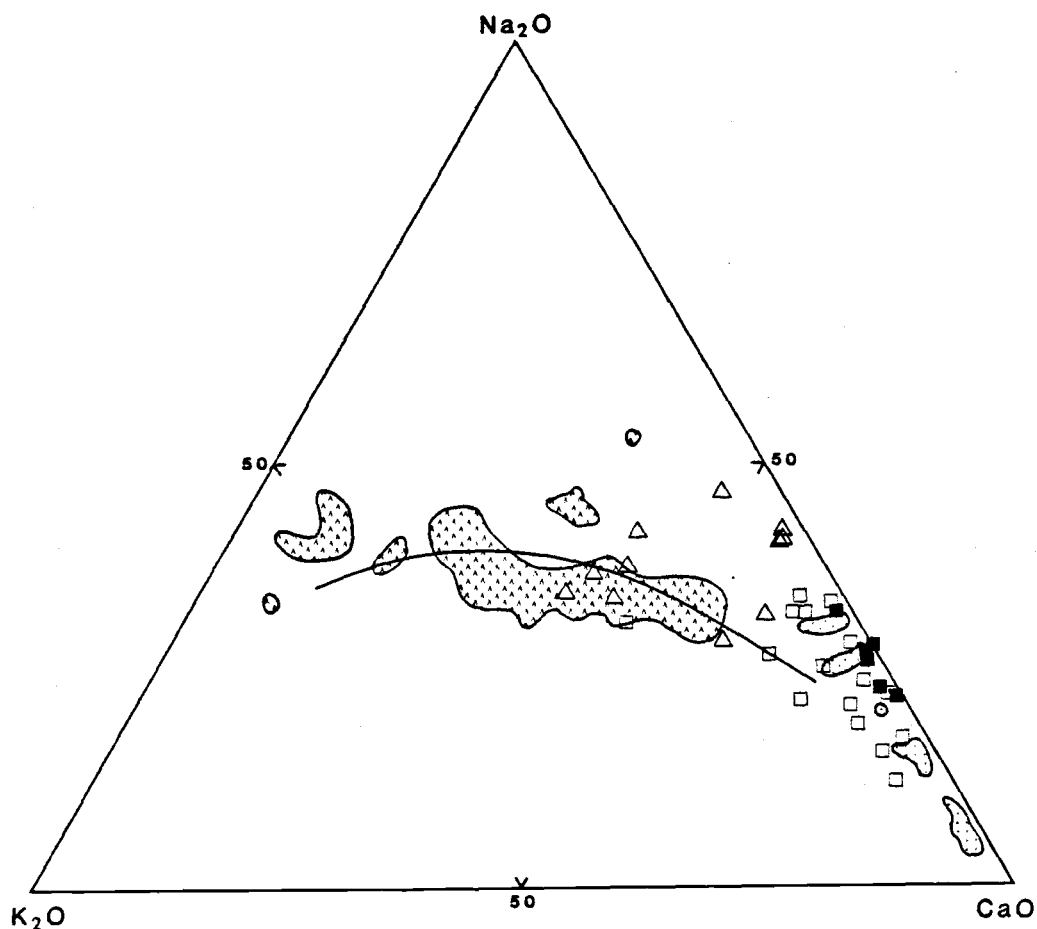


Figure 11. Ternary NKC Diagram. This diagram compares the compositional distribution of samples from the Patap and Linga Superunits at the Monterrosas area to those of the Coastal Batholith (Cobbing et al., 1981) and the calc-alkalic trend line (Nockolds and Allen, 1953). Symbols as in Figure 10.

alkalies ($\text{Na}_2\text{O} + \text{K}_2\text{O}$) remain consistent with those for granitoids elsewhere in the batholith as shown on the AFM diagram (Figure 10).

Concentrations of minor and trace elements in the Linga Superunit at Monterrosas are similar to those recorded for these intrusive phases elsewhere in the batholith as reported by Atherton et al. (1979). For example, the concentrations of La and Ce in two samples of granodiorite are enriched about sixty times relative to those in chondrites, and Sc has a rock/chondrite ratio of about 3. Incompatible elements such as Ba, Rb, and Zr are more abundant in rocks of the Linga Superunit than in those of the Patap Superunit, and lead and zinc also have higher average contents in the more felsic rocks (Table 2), as would be expected according to the distribution of metallic elements in igneous rocks (Rose et al., 1979).

Discussion

The plutonic rocks of the Coastal Batholith of Peru record a complex history of intrusion, crystallization, and deformation. Numerous variations in the form and composition of the intrusions and the complexity of contacts between units and superunits have been documented by Cobbing and Pitcher (1972) and Mullan and Busse11 (1977). Batholithic rocks of the Monterrosas area do not differ in these respects, and interpretations of magma genesis and plutonic sequences are complicated additionally by the effects of alteration associated with formation of the Monterrosas deposit.

The magmatic mineral assemblage of plagioclase feldspar, clinopyroxene, iron-titanium oxides, and minor amphibole in gabbro-diorites of the Monterrosas area is similar to that identified by Mullan and

Busnell (1977) in gabbros and hornblende gabbros elsewhere in the Patap Superunit. Textural evidence indicates that labradorite-andesine and diopside were among the earliest phases to crystallize from the gabbro-diorite magma. Inclusions of orthopyroxene-ilmenite-magnetite and ilmenite-magnetite in crystals of plagioclase feldspar and clinopyroxene, respectively, suggest that iron-titanium oxides and orthopyroxene also formed in minor amounts during the early magmatic stages of crystallization. Additional andesine, diopside, magnetite, and ilmenite as well as actinolitic hornblende, sphene, apatite, and zircon formed during late magmatic crystallization, and secondary minerals such as actinolite, epidote, allanite, scapolite, and others formed subsequently as a result of deuteric and (or) hydrothermal processes.

The crystallization history of the gabbro-diorites must explain several unusual characteristics in the chemistry of whole rocks and certain minerals. For example, in comparison to rocks with similar silica content such as basaltic andesites, as shown in Table 3, samples from Monterrosas contain lower concentrations of total iron oxide, titania, and potash, and higher concentrations of lime. Trace elements such as cobalt and nickel are present at lower abundances than in gabbros elsewhere in the Patap Superunit (Atherton et al., 1979) or basaltic andesites (Table 3). In addition, the composition of clinopyroxenes in the least altered gabbro-diorites is more diopsidic than pyroxenes of similar igneous rocks in which augite is common (Deer et al., 1979). Normal, discontinuous, and possibly oscillatory and (or) reverse compositional zoning in plagioclase

Table 3. Comparison of the Average Concentrations of Major Oxides and Selected Trace Elements in the Least Altered Gabbro-Diorites from the Monterrosas Area and Basaltic Andesites from the Oregon Cascades*

	<u>Gabbro-Diorites</u>	<u>Basaltic Andesites</u>
	(n=6)	(n=8)
	Weight Percent	Weight Percent
SiO ₂	54.6 ±0.7	55.4 ±1.6
TiO ₂	0.91±0.05	1.16±0.13
Al ₂ O ₃	17.2 ±0.9	17.9 ±0.5
FeO _t	5.4 ±1.2	7.5 ±0.7
MgO	4.9 ±1.0	4.8 ±1.0
CaO	11.5 ±1.4	7.7 ±0.6
Na ₂ O	4.2 ±0.3	4.2 ±0.3
K ₂ O	0.21±0.12	1.14±0.18
	<u>ppm</u>	<u>ppm</u>
Co	5± 1	26± 5
Ni	7± 3	58± 39
Ba	326±22	338± 38
Rb	6± 6	18± 9
Sr	471±26	646±111
Zr	96±10	156± 34

* Mount Washington-type basaltic andesites from Hughes (1982). Major oxides by XRF and AAS; trace elements by INAA (basaltic andesites) and AAS and XRF (gabbro-diorites).

feldspar also suggests a complicated history of crystallization from the gabbro-diorite magma.

Crystallization under conditions of variable fluid pressures and (or) partial pressures of oxygen (f_{O_2}) and crystal fractionation might explain some of the chemical-mineralogical characteristics in the gabbro-diorites previously noted. For example, gabbro-diorites in the Monterrosas area could have been derived from magmas that formed the more mafic gabbros of the Coastal Batholith by olivine (\pm plagioclase \pm augite \pm orthopyroxene \pm magnetite) fractionation. Linear trends depicted on diagrams such as wt percent MgO vs. Fe' (molar ratio $FeO/(MgO + FeO)$) and chondrite-normalized La (La_N) vs. Fe', as shown in Figure 12, suggest that the gabbro-diorites were derived from a parental tholeiitic magma by crystal fractionation involving olivine and (or) other ferromagnesian minerals (Hughes, 1982). The low concentrations of cobalt and nickel in the gabbro-diorites might be attributed to extensive olivine fractionation because of the high distribution coefficients for these metals in Mg-Fe silicates.

Complex compositional zonation in plagioclase feldspar as noted above may be explained in part by conditions of variable P_{H_2O} (Smith and Lofgren, 1983). As precipitation of anhydrous minerals such as labradorite-andesine and diopside proceeds, volatile phases would become enriched in the magma. Periodic release of the volatiles during crystallization of the gabbro-diorite magma, as suggested by Mullan and Bussell (1977), could account for changes in fluid pressure within the magma chamber. The formation of amphibole late in the differentiation sequence of the gabbro-diorites indicates that water

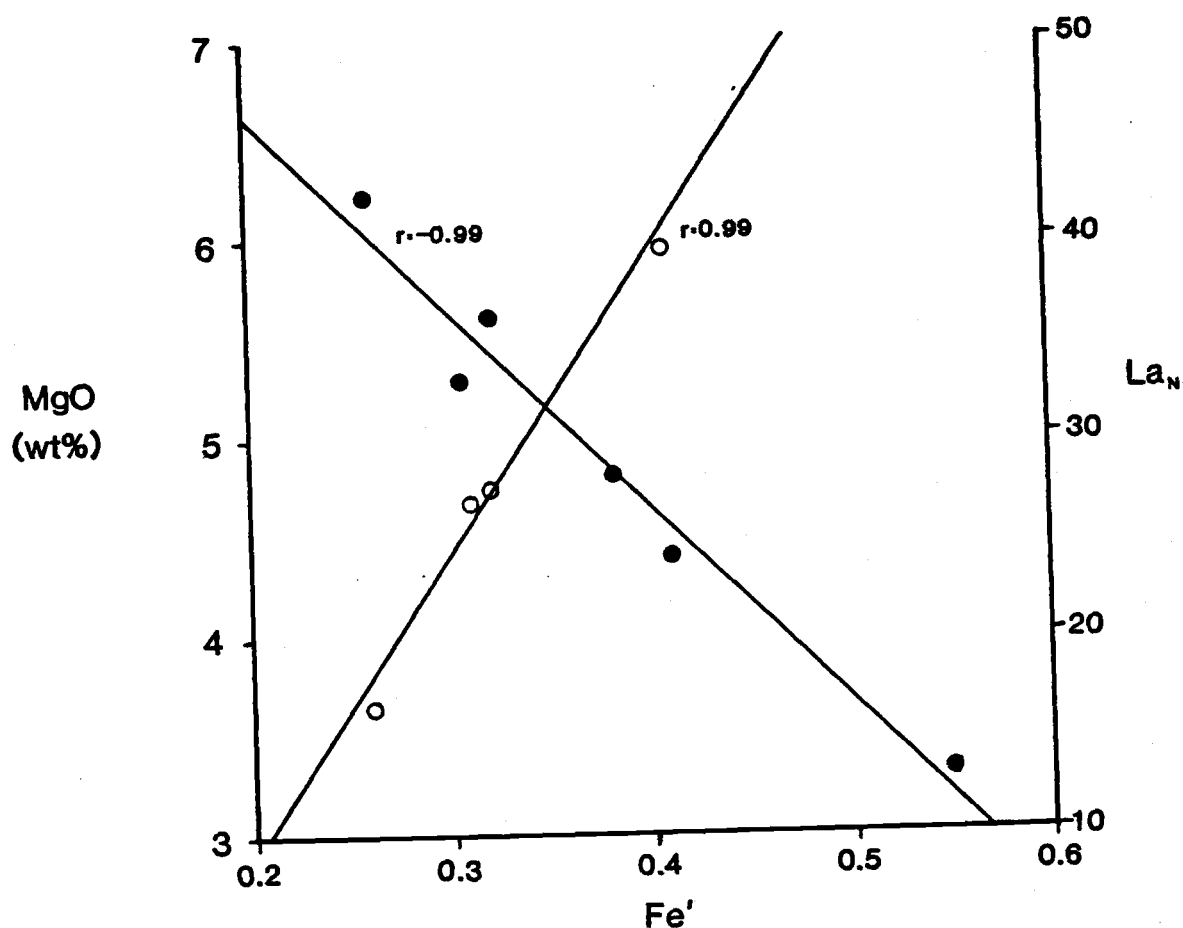


Figure 12. Variation Diagrams of Wt Percent MgO vs. Fe' and La_N vs. Fe' . Closed circles, wt percent MgO ; open circles, La_N . Fe' defined as the molar ratio $FeO/(MgO + FeO)$; La_N defined as La in sample normalized to La in the CI chondrite from Anders and Ebihara (1982).

became concentrated and P_{H_2O} increased in the late and residual magmatic liquids.

Crystallization of ilmenite+magnetite with early-formed plagioclase feldspar and clinopyroxene suggests the f_{O_2} was sufficiently high to oxidize some ferrous iron during the initial crystallization of the gabbroic magma. The formation of iron-titanium oxides might cause the calcic pyroxene to become more diopsidic by preferential removal of the iron-rich hedenbergite component from the magma (Sood, 1981). Partial alteration of ilmenite and magnetite to sphene and the exceptionally low content of ulvospinel molecule in magnetite for most samples precluded the use of the thermobarometric technique of Buddington and Lindsley (1964) and Spencer and Lindsley (1981) to determine the f_{O_2} during crystallization of the gabbro-diorites. However, one oxide pair of magnetite (usp₅ mt₉₅) and ilmenite (ilm₉₀ hem₁₀) indicates that these minerals equilibrated at a temperature of about 650°C and log f_{O_2} of about 10^{-16} between the Ni-NiO (NNO) and Fe₂O₃ - Fe₃O₄ (HM) oxygen buffers. Moreover, magnetite-rich compositions further reflect their formation under unusually high f_{O_2} values and (or) equilibration at low temperatures (Czamanske and Mihalik, 1972).

Fluctuations of P_{H_2O} and high f_{O_2} during crystallization could account for some of the chemical and mineralogical characteristics of the Patap gabbro-diorites in the Monterrosas area. Furthermore, it might be assumed that total pressure was about 1 to 3 kb based on a maximum depth of emplacement to 10 km in the eugeosyncline. The gabbro-diorite magma was initially undersaturated with respect to water and probably contained about 1 to 2 wt percent H₂O on the basis

of the early products of crystallization and the experimentally determined solubility data for andesites (Eggler and Burnham, 1973; McCourt, 1981). According to Burnham (1979), an andesitic magma at a pressure of 2 to 3 kb would approach water saturation at about 6 wt percent H_2O . Thus, it is inferred that the latest residual liquids from the gabbro-diorite magma contained about 6 wt percent H_2O .

Phase relations in the gabbro-diorites from the Monterrosas area may be compared to the melting relations in andesite to infer approximate conditions of crystallization for the primary magmatic minerals in the Patap Superunit. For example, experimental curves for the Mt. Hood andesite investigated by Eggler and Burnham (1973) are applicable to the gabbro-diorites in the Monterrosas area although the two types of rocks are not exact compositional equivalents. The curves, as shown in Figure 13, were determined at total and fluid pressures of 5 kb and at f_{O_2} of the quartz-fayalite-magnetite (QFM) buffer (about 10^{-12} bars at $1000^\circ C$). Plagioclase feldspar is the liquidus phase for all contents of H_2O , and it is precipitated initially at about $1150^\circ C$ and 2 wt percent H_2O . Clinopyroxene and ilmenite crystallize initially at about 1070° , and magnetite precipitates at about $1025^\circ C$. Amphibole is the last phase to form at about $900^\circ C$, and solidification is complete at about $780^\circ C$. It might be noted that "out temperatures" are relatively insensitive to changes in total pressure between 2 and 5 kb according to other diagrams by Eggler and Burnham (1973). Also, if the fugacity of oxygen was nearer the NNO buffer (10^{-10} bars at $1000^\circ C$), as it is in most magmas (Eggler and Burnham, 1973), or higher than the NNO, as indicated possibly by the low titanium composition of magnetite, then the temperatures of initial oxide deposition might

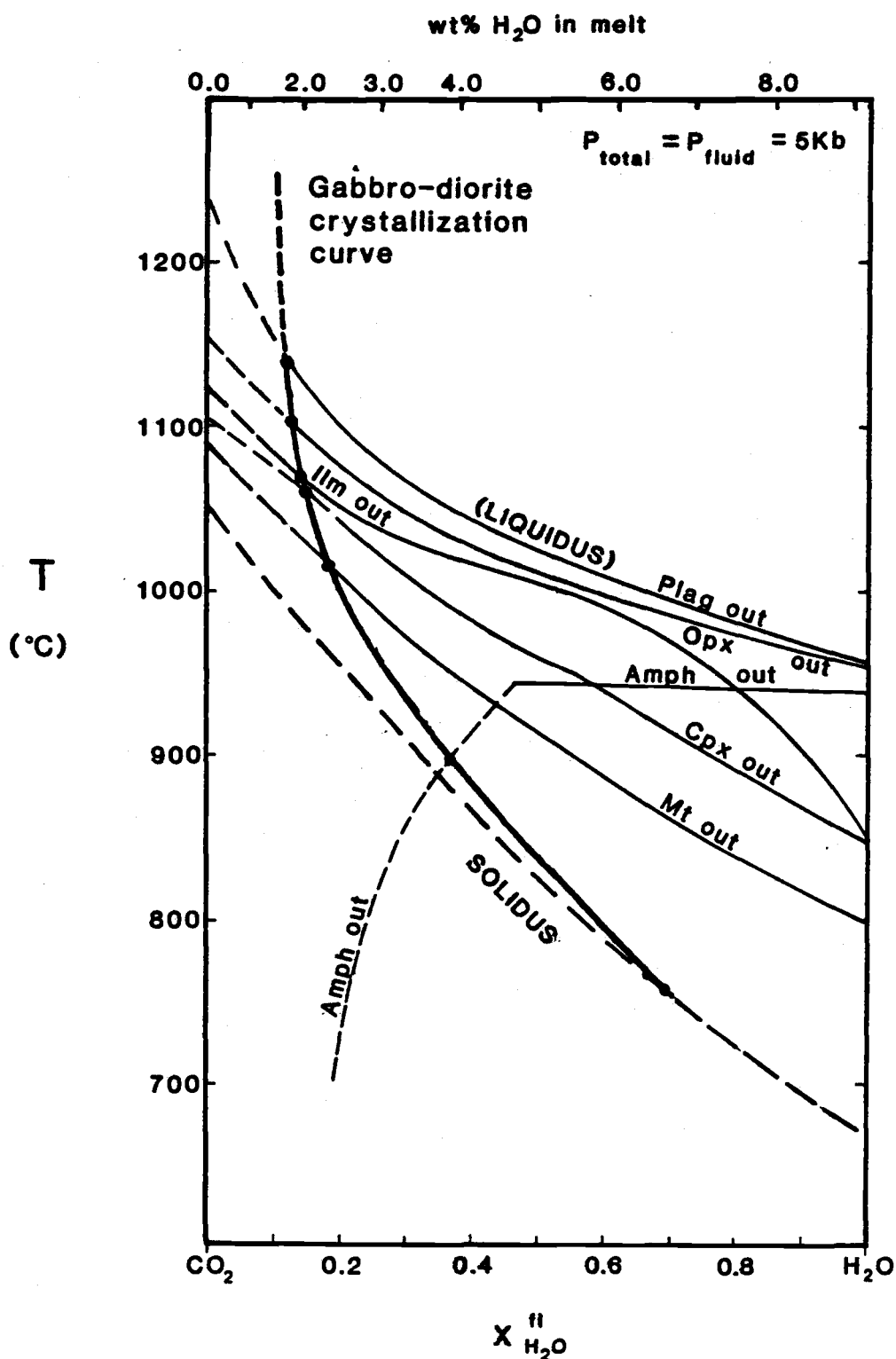


Figure 13. T - $x_{\text{H}_2\text{O}}$ Section at 5 kb for Mt. Hood Andesite (after Eggler and Burnham, 1973, Figure 4, p. 2524). Possible crystallization curve for the Patap gabbro-diorite magma in the Monterrosas area is shown. Liquidi dashed where approximated.

have been slightly higher than depicted in Figure 13. Nonetheless, a high f_{O_2} during crystallization of the gabbro-diorite magma series does not explain the low concentrations of iron in the least altered rocks, which ultimately must be ascribed either to low initial concentrations or to segregation of an iron-rich fluid during the crystallization of these mafic host rocks.

Intrusive phases of the Linga Superunit in the Monterrosas area are similar chemically and mineralogically to those elsewhere in the Coastal Batholith. The granodiorites and quartz monzodiorites are typical I-type (Chappell & White, 1974) and magnetite-series (Ishihara, 1977) granitoids. For example, magnetite and ilmenite are present in all samples, hornblende is a common constituent, and sphene and apatite are accessory phases. In addition, diopside is calculated in the CIPW norms for all samples, normative corundum is less than 1 percent, and the Fe^{3+}/Fe^{2+} ratios average about 1.2.

The Linga Superunit and other granitoids in the Coastal Batholith are believed to be derived from a mantle or lower crustal source (Pitcher, 1979). Bussell (1983) has suggested that a compressive episode of tectonism succeeded a tensile phase during which mafic magmas were emplaced in the upper crust. Compression inhibited ascent of the mafic magmas and promoted crustal underplating. Subsequent fusion of mantle and basaltic material in the underplate with high-level fractionation of plagioclase+pyroxene+hornblende led to the calc-alkaline granitoid suites (Atherton et al., 1979; Bussell, 1983).

The Linga magmas were undersaturated with respect to water, and probably contained initially only 1 to 2 wt percent H_2O (McCourt, 1981). The fugacity of oxygen was probably near the NNO buffer during

crystallization (Ishihara, 1977). Rocks of the Monterrosas area provide petrographic evidence for the early precipitation of plagioclase feldspar, clinopyroxene, and possibly some iron-titanium oxides. However, only traces of pyroxene remain, and hornblende is the dominant ferromagnesian mineral. The browner color of apparently magmatic hornblende in the quartz monzodiorites and granodiorites suggests that the hornblende became a liquidus phase at higher temperatures than in the gabbro-diorites (Hammarstrom, 1981). Quartz and perthitic potassium feldspar were the last mineral phases to form from the Linga magmas. Evidence of deuteric and (or) subsequent hydrothermal alteration is restricted to minor replacements of epidote, actinolite, chlorite, and sericite and to veinlets of quartz+calcite and epidote+potassium feldspar.

METALLIZATION

Petrographic studies of ore samples from the rich, high-grade zone of the Monterrosas deposit show that they consist of a simple assemblage of minerals. Magnetite, chalcopyrite, and pyrite predominate with lesser amounts of cubanite and pyrrhotite, and they are associated with gangue minerals such as actinolite, scapolite, apatite, and quartz. Minor amounts of martite, covellite, bornite, chalcocite, marcasite, and possibly digenite are present as secondary minerals. The orebody contains about 2 million tons of ore that averages 1.9 percent copper, 0.7 ounces silver, and 0.03 ounces gold per ton, as well as anomalously large concentrations of cobalt, molybdenum, and nickel.

Ore Mineralogy

Chalcopyrite is the most abundant copper-bearing mineral at the Monterrosas deposit. It is present in veinlets, as blebs in pyrite and magnetite, as massive monomineralic zones, and as replacements of and intergrowths with other ore and silicate gangue minerals. In zones of massive chalcopyrite, copper grade may average greater than 15 percent for channel samples up to two meters long. Chalcopyrite is recognized in polished sections by its brass-yellow color and anisotropism. Crystal forms vary from subhedral to anhedral, striations are common, and some crystals contain simple twins. The composition of chalcopyrite from the ore zone is close to the stoichiometric formula CuFeS_2 , as given in Table 4 and Appendix 7. However, the Cu:Fe atomic ratio appears to decrease with depth in the Monterrosas orebody. For

Table 4. Electron Microprobe Average Compositions of Chalcopyrite in Ore from the Monterrosas Mine

	<u>1132 (n* = 5)</u>		<u>1070 (n* = 16)</u>		<u>DDH (n* = 3)</u>	
	<u>wt %</u>	<u>at %</u>	<u>wt %</u>	<u>at %</u>	<u>wt %</u>	<u>at %</u>
Fe	29.93	24.7	30.18	25.1	29.88	25.3
Cu	34.63	25.1	33.97	24.8	32.55	24.2
S	<u>34.97</u>	50.2	<u>34.61</u>	50.1	<u>34.29</u>	50.5
Total**	99.94		99.11		96.88	
Cu/Fe	1.157	1.017	1.126	0.989	1.089	0.957
(Fe+Cu)/S		0.992		0.996		0.980

* n is the total number of crystals analyzed.

** Totals include trace amounts of Ag, Ni, Co, Mn, and Mo.

example, sample D-3 from the 1132 level has a Cu:Fe ratio of 1.02, whereas the average ratio of four samples from the 1070 level is 0.99. One sample from drill core about 157 m below the 1070 level has a ratio of 0.96 (Table 4). This decrease in the Cu:Fe atomic ratio may have resulted from differences in temperature, the fugacity of sulfur, and (or) the fugacity of oxygen during the period of ore emplacement. Minor amounts of other metals are also contained in chalcopyrite. Silver averages about 0.19 wt percent and nickel 0.12 percent in microprobe analyses, and cobalt, manganese, and molybdenum are present in amounts less than 0.10 percent. Gold recovered from the Monterrosas deposit may also be contained in chalcopyrite as minute flecks of native gold that are observed in polished sections as unidentified bright yellow metallic inclusions.

Pyrite is the most abundant iron-bearing sulfide mineral at Monterrosas. It occurs as large (to about 20 mm) euhedral to subhedral crystals in monomineralic zones, associated with gangue and other ore minerals, in altered host rocks, and as anhedral blebs in magnetite and chalcopyrite, and in veinlets. Most pyrite has a pale brass-yellow color and is isotropic. However, some has been altered to marcasite which has a distinct whitish-yellow color and is anisotropic. Electron microprobe analyses, given in Table 5 and Appendix 8, indicate that pyrites from the ore zone have nearly an ideal stoichiometric composition. Furthermore, pyrite appears to be the source of geochemical anomalies for cobalt and molybdenum at the Monterrosas Mine. An average concentration of 0.43 wt percent cobalt is present in pyrite, and some crystals contain up to 1.14 percent. Molybdenum averages about 0.56 percent and ranges up to 0.76 percent in pyrite. Other

Table 5. Electron Microprobe Average Compositions of Pyrite in Ore from the Monterrosas Mine

	<u>1132 (n* = 6)</u>		<u>1070 (n* = 17)</u>		<u>DDH (n* = 7)</u>	
	<u>wt %</u>	<u>at %</u>	<u>wt %</u>	<u>at %</u>	<u>wt %</u>	<u>at %</u>
Fe	45.28	32.7	45.92	33.0	45.40	32.9
S	53.59	67.3	53.48	67.0	53.17	67.1
Mo	0.59		0.53		0.59	
Co	<u>0.52</u>		<u>0.39</u>		<u>0.45</u>	
Total	99.99		100.30**		99.61***	
Fe/S	0.845	0.485	0.859	0.493	0.854	0.490
Metals/S		0.494		0.500		0.499

* n is the total number of crystals analyzed.

** Total includes trace amounts of Cu, Ni, and Mn.

*** Total includes trace amount of As.

metals such as nickel, copper, manganese, and arsenic are present at trace concentrations (< 0.10 percent) in some pyrite. Neither the Fe:S atomic ratio nor the concentration of trace elements in pyrite varies significantly in the orebody.

Magnetite is the predominant iron oxide mineral. It occurs in massive monomineralic zones as coarse euhedral to subhedral crystals, as disseminated crystals and veinlets in gangue minerals, especially actinolite, and in altered gabbro-diorites, and as blebs in pyrite and chalcopyrite. Magnetite is pinkish gray in color and isotropic, which indicates that it contains little titanium in solid solution. Microprobe analyses, given in Table 6 and Appendix 5, confirm this inference and establish the magnetite to be nearly pure Fe_3O_4 with only trace amounts of titanium, aluminum, vanadium, silicon, cobalt, manganese, and magnesium. Some of the magnetite contains tiny (< 0.5 mm) blebs of quartz, and martite (pseudomorphous hematite) replaces some crystals of magnetite.

Cubanite and pyrrhotite are present in small amounts as blebs in pyrite and as intergrowths with chalcopyrite in pyrite, as shown in the photomicrograph given by Figure 14. Pronounced pleochroism from light to dark cream or pinkish brown and moderately strong anisotropism distinguish cubanite from the other ore minerals. It has an ideal stoichiometric composition of CuFe_2S_3 , as may be observed from the microprobe data listed in Table 7 and Appendix 9. Minor amounts (up to 0.45 wt percent) of trace elements such as silver, cobalt, molybdenum, nickel, and manganese are contained in cubanite. Pyrrhotite at Monterrosas is recognized by its weak pleochroism from light to moderate brown and weak anisotropism. It has a composition of about

Table 6. Electron Microprobe Average Compositions of Magnetite in Ore from the Monterrosas Mine

	(n* = 3)	(n* = 4)
	<u>X-7</u>	<u>F-3</u>
	Wt Percent	
TiO ₂	0.08	0.09
Al ₂ O ₃	0.38	0.11
Cr ₂ O ₃	<0.01	<0.01
V ₂ O ₃	0.08	0.14
Fe ₂ O ₃ **	68.81	69.54
FeO*	30.97	31.55
FeO _t ***	92.88	94.13
MnO	<0.01	0.02
MgO	<u>0.39</u>	<u><0.01</u>
Total***	92.20	94.50
Total**	98.99	101.47
Number of Ions per 4 O		
Ti	0.0023	0.0025
Al	0.0174	0.0047
Cr	-	-
V	0.0026	0.0043
Fe ³⁺ ***	1.9838	1.9859
Fe ²⁺ ***	0.9923	1.0013
Mn	0.0002	0.0007
Mg	0.0229	-

* n is the total number of crystals analyzed.

** Calculated

*** Analyzed

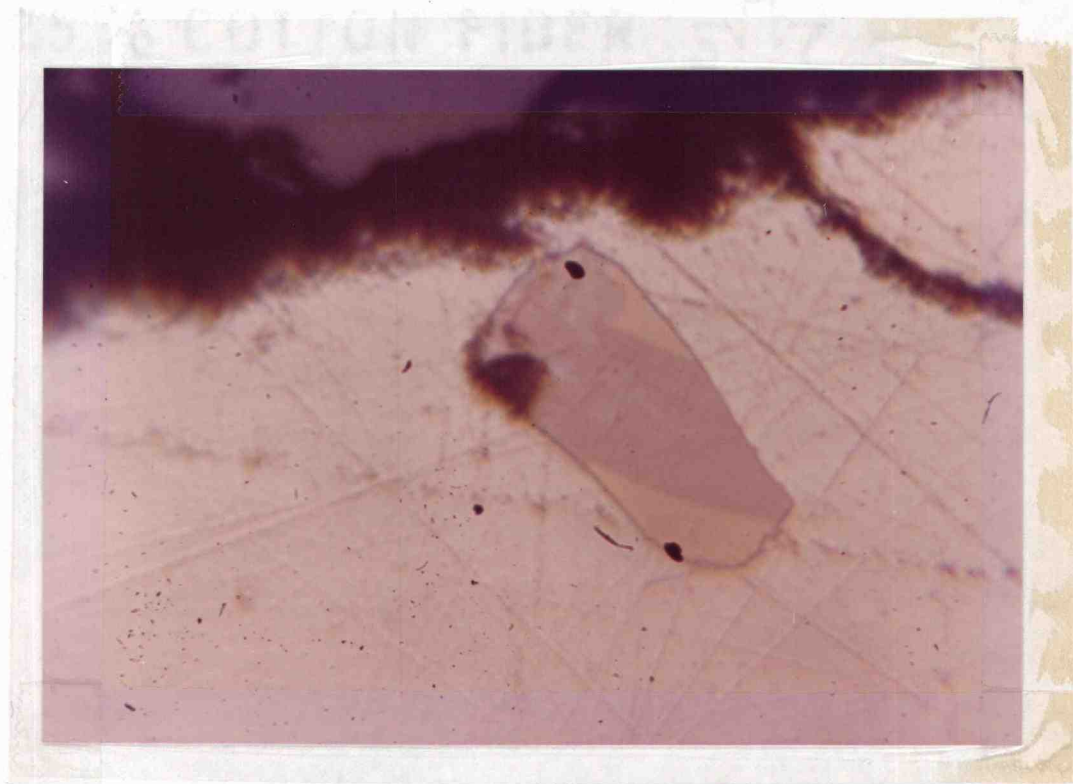


Figure 14. Photomicrograph of Chalcopyrite-Cubanite-Pyrrhotite Bleb in Pyrite. Whitish, pyrite; yellow, chalcopyrite; brown, pyrrhotite; lavender, cubanite (note pleochroism); gray at top, magnetite. Sample X-3, 800X magnification, in oil, plane polarized light.

Table 7. Electron Microprobe Average Compositions of Cubanite and Pyrrhotite in Ore from the Monterrosas Mine

Cubanite (n* = 7)			Pyrrhotite (n* = 4)		
	<u>wt %</u>	<u>at %</u>		<u>wt %</u>	<u>at %</u>
Fe	40.00	33.2	Fe	59.85	47.5
Cu	22.29	16.3	S	<u>38.07</u>	52.5
S	<u>34.97</u>	50.5	Total***	98.62	
Total**	97.40		Fe/S	1.572	0.903
Cu/Fe	0.557	0.490	Metals/S		0.911
(Fe+Cu)/S		0.980			

* n is the total number of crystals analyzed.

** Total includes trace amounts of Mo, Ag, Co, Ni, and Mn.

*** Total includes trace amounts of Cu, Ni, Co, Mo, and Mn.

$\text{Fe}_{0.9}\text{S}_{1.0}$, as determined from microprobe data shown in Table 7 and Appendix 10. Up to 0.52 wt percent copper is contained in the pyrrhotite, whereas molybdenum, cobalt, nickel, and manganese are detected in trace amounts.

Molybdenite is sparsely distributed in the ore zone. Where present, it is intergrown with actinolite and isolated from direct contact with other sulfide minerals by distances of a millimeter or more.

Covellite (CuS), chalcocite (Cu_2S), bornite (Cu_5FeS_4), and possibly digenite (Cu_9S_5) along with hematite and other iron and (or) copper carbonates, silicates, and oxyhydroxides are products of supergene oxidation and enrichment of the primary hypogene ore. The effects of this oxidation are pronounced in surface outcrops, but are minimal in underground exposures. Ore reserves at Monterrosas include these oxidation products from only the upper 30 m of the deposit.

The paragenesis of minerals within the ore zone is difficult to ascertain because of conflicting spatial and temporal relationships between the sulfide, oxide, and silicate phases. In general, magnetite is the earliest ore mineral. It is commonly fractured and brecciated, and silicate and (or) sulfide minerals may occupy these secondary openings. Pyrite appears to be the earliest sulfide, although intergrowths with chalcopyrite in a few samples imply contemporaneity. Nonetheless, chalcopyrite is the first copper-bearing mineral to have formed, and it commonly replaces pyrite and forms veinlets that cut both pyrite and magnetite. Textural features exhibited by the silicate gangue minerals such as scapolite and actinolite provide evidence of contemporaneous deposition (intergrowths) and late paragenesis (crosscutting veinlets) with respect to associated sulfide and oxide

phases. Thus, these silicates were apparently precipitated throughout much of the period of ore deposition. Apatite is a minor gangue mineral in the ore zone. It is most abundant (up to 3 volume percent) in the magnetite-rich parts of the orebody. Quartz is present as disseminations and veinlets in the ore. Highly saline fluid inclusions characterized by halide, opaque, and unknown birefringent daughter minerals are particularly abundant in the disseminated crystals of quartz. Innumerable simple (vapor + liquid) and complex (vapor + liquid + daughter minerals) fluid inclusions are present in the late vein quartz. These fluid inclusions suggest that a saline fluid circulated within the Monterrosas deposit throughout much of the period of ore deposition. The characteristics of fluid inclusions and their significance with respect to ore genesis will be discussed more fully in subsequent chapters.

Distribution of Metals

Concentrations of copper, molybdenum, lead, zinc, silver, and cobalt were determined in 108 samples from the Monterrosas deposit. These samples are comprised of 13 from the ore zone, 55 from the Patap gabbro-diorites, and 40 from the Linga monzonites, with 60 collected from the subsurface and 48 from the surface (Appendix 12). In addition, Centromin Peru has provided geochemical data for numerous channel and drill hole samples collected from subsurface locations on the 1132 and 1070 levels, other sublevels, and shafts.

The grade of copper in the ore zone ranges from 0.2 to 15 wt percent, as listed in Table 8. Other metals which are contained in recoverable quantities include gold (0.03 oz/ton), silver (0.7 oz/ton),

Table 8. Range and Threshold Values of Trace Elements in Samples of Ore and Country Rocks at Monterrosas (in ppm)

Ore	<u>Gabbro-diorites</u>		<u>Linga Monzonites</u>	
	Range	Threshold*	Range	Threshold*
Cu 2000-150,000 (15%)	6-5200	70	11-440	70
Mo 7-800	1-90	6	1-30	7
Pb 4-50	4-60	9	4-100	30
Zn 12-80	5-60	17	5-290	55
Ag 0.3-10.7 (0.34 oz/ton)	0.3-1.5	0.8	0.3-0.8	0.5
Co 5-630	4-250	52	4-50	14
Au 0.6-1.0 (0.03 oz/ton)	tr-0.6			
Ni 100-200	100			
Ga 100-200	50-100			

* Threshold values determined from diagrams of concentration versus cumulative frequency

cobalt (to 0.5 wt percent), and molybdenum (to 800 ppm). Nickel (up to 200 ppm) and gallium (up to about 200 ppm) are present in anomalous concentrations, whereas neither lead nor zinc occurs in significant abundance. None of the metals vary markedly along the length of the ore zone, and only copper and cobalt appear to vary with depth.

According to Centromin Peru, concentrations of copper decrease and those of cobalt increase with increasing depth in the ore zone below the 1070 level (Alberto Caballero, 1981, personal communication).

Decreasing amounts of chalcopyrite (to less than 2 modal percent) and diminishing Cu/Fe ratios in chalcopyrite with depth, as previously noted from microprobe data in Table 4, support the trend for copper. Furthermore, the tenfold increase in cobalt content from about 600 ppm to about 5000 ppm is consistent with an increase in the abundance of pyrite (to greater than 70 modal percent) in ore at depth.

The geochemical effects of mineralization on gabbro-dioritic host rocks at the Monterrosas are limited to a narrow zone that borders the orebody. The concentrations of metals were plotted versus cumulative frequency to determine their distribution. The fitting of more than one distinct linear segment on the cumulative probability plot indicates that more than one subpopulation of concentrations is present (Sinclair, 1976). The lower population represents normal background values in the least altered rocks, and the upper population reflects anomalous quantities of a metal possibly introduced by ore-bearing fluids. Concentrations of metals above the threshold value, defined as the upper limit to the range of background values, are considered anomalous. For example, Figure 15 shows that background concentrations of copper in gabbro-diorites from Monterrosas range from 6 ppm to a

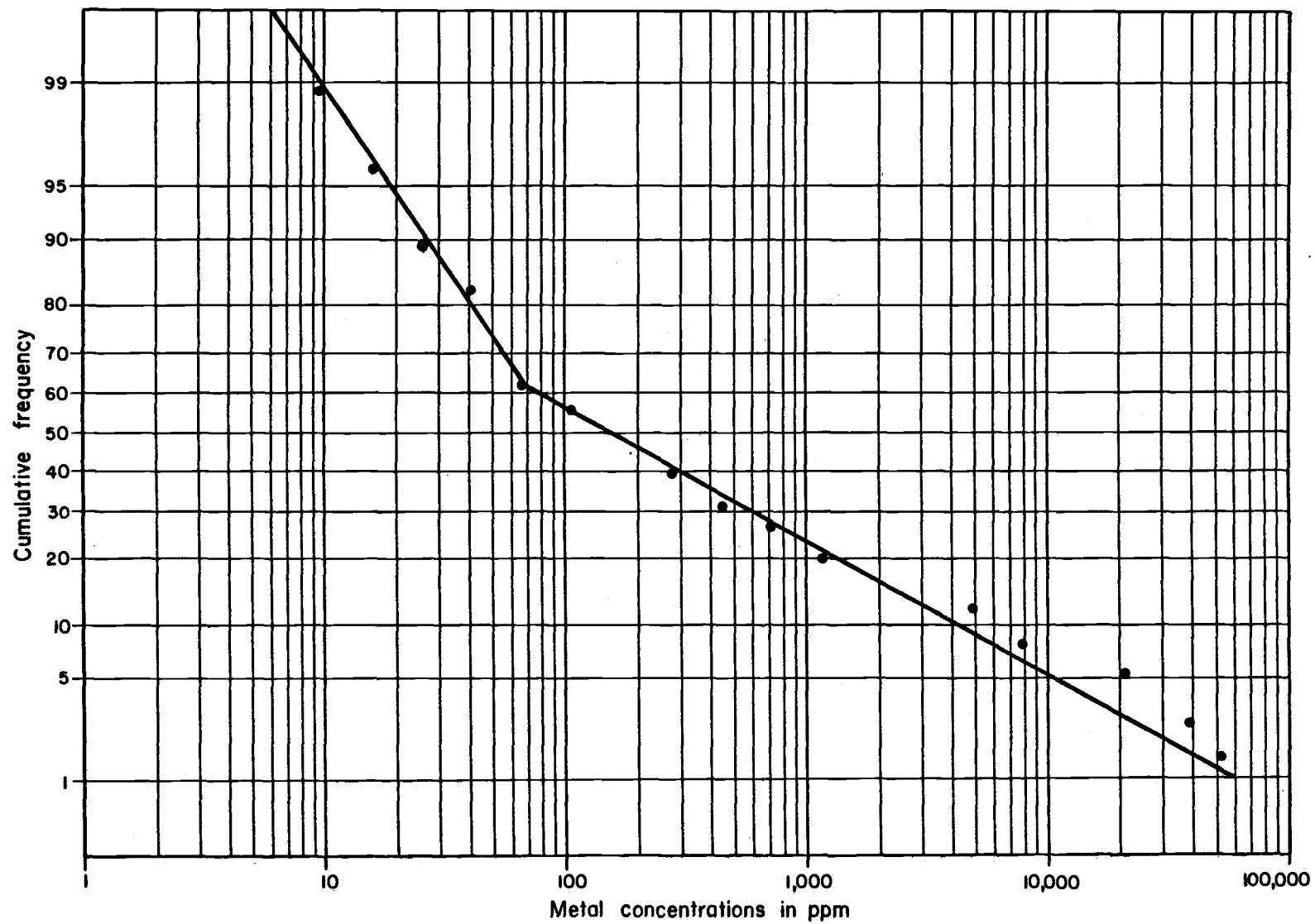


Figure 15. Cumulative Frequency Diagram for Copper.

threshold of about 70 ppm, and samples with concentrations above 70 ppm are anomalous. Concentrations of the trace elements are below their respective threshold values in most samples of gabbro-diorite beyond about 30 m or more from the ore zone. This distribution of metals is most likely related to the structural control of the Monterrosas orebody where fluids migrated into the gabbro-diorites through fractures and along faults. Moreover, those samples greater than 30 m beyond the ore zone which contain anomalous concentrations of metals are commonly located near small fractures.

Trace metals in samples of the Linga monzonites at Monterrosas have background concentrations similar to the gabbro-diorites, as listed in Table 8. For example, concentrations of copper range from 11 to a threshold of about 70 ppm. Minor anomalies of up to 650 ppm copper are present in granodiorites and quartz monzodiorites near the ore zone and adjacent to the quartz-rich Monterrosas and Montekeka veins. Some rocks from the Linga Superunit contain anomalous concentrations of zinc (up to 290 ppm), whereas in contrast the copper ore in gabbro-diorites has much lower concentrations (less than 50 ppm). Centromin Peru has also identified anomalous values of lead in some samples of granodiorite and quartz monzodiorite collected underground from the easternmost part of the mine (Luis Sassarini, 1981, personal communication). Thus, it is possible that the Linga magmas introduced zinc and lead into the Monterrosas area.

ALTERATION

Alteration of the Patap and Linga Superunits in the Monterrosas area is widespread. Petrographic studies indicate that much of the alteration is late magmatic or deuteritic in origin. For example, epidote, clinozoisite, and chlorite replace the cores of plagioclase feldspar crystals in plutonic phases of both superunits. Moreover, amphibole ubiquitously rims and replaces clinopyroxene, which according to Atherton et al. (1979) is an alteration effect that is extensive throughout and characteristic of intrusions in the Arequipa segment of the Coastal Batholith.

Specific patterns of alteration in the Monterrosas area are evident only in the Patap gabbro-diorites where the intensity of these effects increases with proximity to the mineralized zone. For example, the abundance and variety of hydrous minerals such as amphiboles, epidotes, chlorites, and biotite are greatest (up to about 55 modal %) in wall rocks adjacent to the ore zone. Scapolite also has a systematic distribution with respect to mineralization in that samples of altered gabbro-diorite within 20 m of the ore zone contain up to 50 modal percent scapolite. Other secondary minerals such as magnetite, sphene, tourmaline, and allanite are more abundant in gabbro-dioritic wall rocks than in samples of gabbro-diorite farther from ore.

Profound chemical changes took place within the gabbro-diorites during alteration and metallization. A summary equation of several alteration reactions and the difference in whole-rock chemistry between relatively unaltered and altered samples of gabbro-diorite indicate that iron, magnesium, and potassium were gained, and calcium,

sodium, titanium, silicon, and possibly aluminum were lost during alteration. The ratio of oxides lost versus oxides gained, normalized to the least altered sample of gabbro-diorite, defines an alteration index that correlates with the intensity of mineralization and distance to the ore zone.

Mineralogy of the Alteration Assemblage

Replacement of diopside by amphiboles in the gabbro-diorites is the most prevalent alteration at the Monterrosas deposit. Variations in color and pleochroism from light brown to greens, blue-greens, and indigo, and diffuse patches of different colors and textures within a single crystal indicate that the amphiboles have had a complex history of crystallization. Microprobe analyses of these amphiboles provide further evidence that they are heterogeneous in composition. The amphibole formulae are calculated on the basis of 23 oxygen (anhydrous), and iron is considered to be entirely Fe^{2+} . The tetrahedral, M1 to M3, M4, and A sites are filled according to the rules of Hawthorne (1983) and Robinson et al. (1982) for the formula $\text{A}_{0-1}(\text{M4})_2(\text{M1},2,3)_5(\text{T1})_4(\text{T2})_4\text{O}_{22}(\text{OH},\text{F},\text{Cl})_2$. On the basis of the compositional scheme given by Leake (1978), the amphiboles range from actinolitic hornblende ($\text{Na}_{.13}\text{K}_{.05}\text{Ca}_{1.86}\text{Mg}_{3.34}\text{Fe}_{1.37}^{2+}\text{Mn}_{.01}\text{Ti}_{.02}\text{Al}_{1.40}^{\text{VI}}\text{Si}_{7.38}\text{Al}_{1.62}^{\text{IV}}(\text{OH},\text{Cl})_2$) to actinolite ($\text{Na}_{.06}\text{K}_{.02}\text{Ca}_{1.83}\text{Na}_{.02}\text{Mg}_{3.74}\text{Fe}_{1.22}^{2+}\text{Mn}_{.01}\text{Ti}_{.01}\text{Al}_{1.17}^{\text{VI}}\text{Si}_{7.75}\text{Al}_{1.25}^{\text{IV}}\text{O}_{22}(\text{OH},\text{Cl})_2$). Some analyses with unacceptable totals (less than 96 wt % or greater than 102 wt %) could not be categorized, but these deep blue-green to indigo crystals appear to be iron-rich (to 20 wt % FeO_t) and chlorine-rich (to 1.09 wt % Cl) amphiboles. Actinolitic hornblende was the earliest amphibole to crystallize.

It may be in part primary, or magmatic, but this amphibole also replaces diopside. Some crystals that have remnant cores of diopside are zoned from actinolitic hornblende to actinolite on the margins. Such zonations are readily observed in thin section where green-brown actinolitic hornblende grades into pale green or blue-green actinolite and were tentatively identified from microprobe analyses. Actinolite is the dominant secondary amphibole in the Monterrosas deposit. It replaces diopside, actinolitic hornblende, and labradorite-andesine, is an abundant gangue mineral in the sulfide-oxide ore, and forms veins and veinlets in altered wall rocks and in ore. Actinolitization is pervasive in the wall rocks adjacent to ore, where it forms replacement patches, seams, and veinlets throughout the host rock. Some actinolite is so pale in color that it appears to be tremolitic in composition. However, tremolite was not identified by microprobe analyses.

Scapolite replaces plagioclase feldspar in gabbro-diorites at the Monterrosas deposit. It is most abundant (to 50 modal %) in samples of gabbro-diorite within about 20 m of the ore zone where scapolitization of labradorite-andesine is nearly complete. Moreover, veinlets of scapolite and corrosion at the margins of ferromagnesian minerals are common in areas of intense scapolitization. Scapolite is distinguished from plagioclase feldspar by its uniaxial negative character, parallel extinction, lack of twinning, and birefringence up to first-order yellow. Low relief and low birefringence suggest that marialitic compositions dominate (Phillips and Griffen, 1981). Microprobe analyses confirm that scapolite in the Monterrosas deposit has a composition of marialite-dipyre, or $\text{Me } 27 \pm 3$, and an equivalent

anorthite content (EqAn) of 29 ± 4 . The formula of scapolite may be written as $\text{Na}_{2.75}\text{K}_{.14}\text{Ca}_{1.06}\text{Fe}_{.01}\text{Al}_{3.84}\text{Si}_{8.16}\text{O}_{24}(\text{O}_{.77}\text{Cl}_{.0.22}\text{CO}_3)$. This marialitic composition indicates that abundant Cl^- was added to plagioclase feldspar in the gabbro-diorites during alteration.

At least four minerals of the epidote group are present in the alteration assemblage at the Monterrosas deposit. Epidote is the most abundant (up to 14 modal %), clinozoisite and allanite occur in trace to minor amounts (< 2 modal %), and piemontite is present in trace amounts (< 1 modal %). Crystals of epidote and clinozoisite which replace the cores of plagioclase feldspar in relatively unaltered gabbro-diorites are interpreted to be deuteric in origin. Some of these secondary crystals are zoned from a core of colorless clinozoisite to a margin of yellow epidote. Epidote, allanite, and piemontite are abundant in more altered gabbro-diorites as replacements of plagioclase feldspar and the mafic minerals and as veinlets. Some crystals of allanite are zoned to rims of epidote, which is evident petrographically from changes in color, pleochroism, and birefringence. The compositions of the epidote group minerals were not determined chemically.

Two or more minerals of the chlorite group are present in altered gabbro-diorites from the Monterrosas deposit. One variety is distinguished by strong pleochroism from dark green to yellow, anomalous berlin-blue birefringence, and negative sign. It replaces amphibole, plagioclase feldspar, and biotite, and also is present in veinlets. This chlorite is associated commonly with epidote, actinolite, sphene, magnetite, and white mica. A semi-quantitative microprobe analysis (analyzed with a hornblende reference standard) suggests an Fe/Mg

ratio of about 2.5. On the basis of its petrographic characteristics and microprobe analysis, the composition of this iron-rich chlorite is probably prochlorite (Phillips and Griffen, 1981) or ripidolite (Deer et al., 1962). A second member of the chlorite group, which shows much weaker pleochroic colors from light green to light greenish brown and has low first-order gray birefringence, is a less common alteration product of actinolitic hornblende. This chlorite is probably Mg-rich (Phillips and Griffen, 1981).

Sphene, magnetite, hematite, and other iron- and titanium-bearing oxide phases are common in the assemblages of alteration and gangue minerals at the Monterrosas deposit. However, the distribution and crystallization history of sphene and the oxide minerals are complex. For example, sphene has several varieties of texture and association. Some forms subhedral crystals interstitial to feldspar and pyroxene. Elsewhere, the sphene may be present as anhedral intergrowths with hematite and (or) magnetite that replace ilmenite and mafic minerals, as coarse subhedral to euhedral crystals intergrown with coarse-grained actinolite, as veinlets with epidote and chlorite, and as microveinlets that extend outward from interstitial sphene along and through crystals of plagioclase feldspar, clinopyroxene, and amphibole. The interstitial variety of sphene is probably a product of late magmatic crystallization. Others may have formed as reaction products of ilmenite and diopside or labradorite-andesine in the presence of the hydrothermal fluids, or as a primary hydrothermal phase deposited directly from the fluids. The composition of sphene was not determined quantitatively. However, it is believed to contain minor amounts of iron and possibly rare earth elements because of variations

in birefringence and pleochroic colors from brownish yellow to darker brown and orange-brown. Two qualitative microprobe analyses (analyzed with an ilmenite reference standard) yielded approximate compositions of $\text{Ca}_{1.00}\text{Fe}_{1.04}^{2+}\text{Ti}_{1.90}\text{Al}_{1.04}\text{Si}_{1.05}\text{O}_5$.

Other secondary iron and titanium oxide minerals such as hematite, magnetite, mangano-ilmenite, ferropseudobrookite_{ss}, leucoxene, and rutile predominantly replace the magmatic oxide and mafic minerals. In general, primary ilmenite is more altered than magnetite. Hematite, sphene, leucoxene, and possibly magnetite commonly replace ilmenite in both relatively unaltered and altered gabbro-diorites, whereas mangano-ilmenite, ferropseudobrookite_{ss}, and rutile increase in abundance (to about 2 modal %) with proximity to the ore zone. The compositions of secondary magnetite ($\text{Fe}_{0.09}\text{Co}_{0.01}\text{Fe}_{1.79}\text{Al}_{0.01}\text{Si}_{0.01}\text{Ti}_{0.09}\text{O}_4$), hematite ($\text{Fe}_{0.02}\text{Co}_{0.01}\text{Fe}_{3.93}\text{Al}_{0.01}\text{Ti}_{0.01}\text{Si}_{0.02}\text{O}_6$), ferropseudobrookite_{ss} ($\text{Fe}_{0.83}\text{Mn}_{0.03}\text{Fe}_{2.7}\text{Al}_{0.01}\text{Si}_{0.05}\text{Ti}_{1.81}\text{O}_5$), and mangano-ilmenite ($\text{Fe}_{1.16}\text{Mn}_{0.71}\text{Fe}_{0.25}\text{Al}_{0.01}\text{Si}_{0.01}\text{Ti}_{1.86}\text{O}_6$) were determined quantitatively by microprobe analyses, whereas leucoxene and rutile were identified tentatively by microprobe analyses in addition to petrographic examinations. The oxide assemblage may actually be more complicated than inferred because the microprobe data were reduced according to the rules of Stormer (1983) and Spencer and Lindsley (1981). These procedures assume that the composition of the oxide minerals lies along the ulvospinel-magnetite or ilmenite-hematite joins. Thus, some of the secondary Ti-bearing magnetite may actually be maghemite or titanomaghemite which are intermediate in composition between the Fe_2TiO_4 - Fe_3O_4 join and the FeTiO_3 - Fe_2O_3 join (Lindsley, 1976). Although X-ray diffraction analyses were not undertaken to determine the unit

cell dimensions of the various oxide minerals, complexities of replacement and alteration may have allowed other secondary minerals such as maghemite and pseudobrookite to be unrecognized.

White mica, or sericite, is moderately abundant (to 27 modal %) as an alteration product of plagioclase feldspar. The intensity of sericitization varies from complete in some plagioclase crystals to incipient in others within the same sample of gabbro-diorite. In general, samples close to the ore zone are more sericitized, and where some is sufficiently coarse-grained to be called muscovite. Sericite is commonly associated with chlorite and (or) calcite.

Other secondary minerals such as tourmaline, biotite, apatite, and possibly diopside and zircon are present in trace to minor amounts (< 2 modal %). Tourmaline is present as a replacement of amphibole in gabbro-dioritic wall rocks, as veinlets, and as a minor gangue mineral in the ore zone. Strong pleochroism from dark violet-brown to light blue-brown suggests that its composition is that of iron-rich schorl (Phillips and Griffen, 1981). Parallel extinction, uniaxial negative character, and moderately high birefringence distinguish tourmaline from iron-chlorine-rich amphibole. Secondary biotite is recognized by its shredded habit and bluish green color. It forms rims that replace the outer margins of amphibole crystals. This blue-green biotite is present at trace amounts in some samples of gabbro-diorite. Some anhedral of Cl-bearing apatite (to 0.75 wt percent Cl) are associated with scapolite and magnetite in both altered gabbro-dioritic wall rocks and ore. Numerous minute (< 5 μm) fluid inclusions are present in some crystals. Some relicts of clinopyroxene are present within pegmatitic growths of actinolite adjacent to the ore zone. Two microprobe

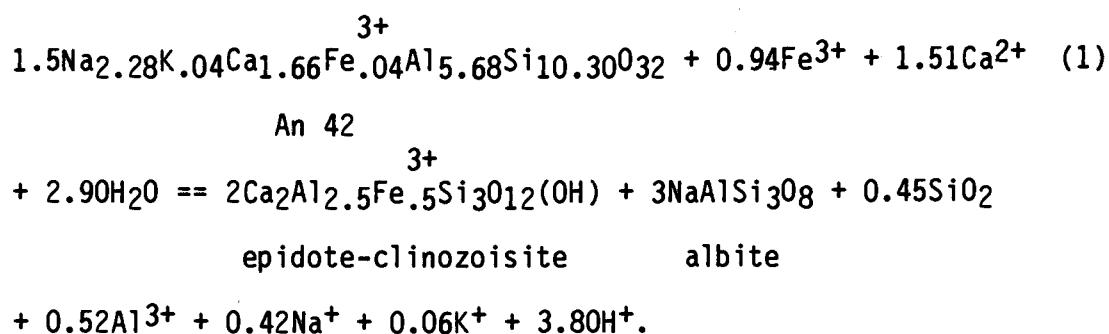
analyses (sample 1-32-15 in Figure 8) indicate that this clinopyroxene has the same composition as magmatic diopside in relatively unaltered gabbro-diorites. It is possible that these crystals are remnants of the wall rocks. Alternatively, this diopside may represent an early period of anhydrous alteration in the gabbro-diorites. The former interpretation is favored, whereas Injoque (1984, written communication) favors the latter. Small anhedral and subhedral of zircon (< 0.2 mm) are particularly abundant (to 1 modal %) in heavily altered gabbro-dioritic wall rocks. They are disseminated in both plagioclase feldspar and the ferromagnesian minerals. The unusual form of these zircons suggests that they may be either late magmatic to hydrothermal in origin or crystals corroded by metasomatic alteration (Deer et al., 1966).

Geochemistry of Alteration

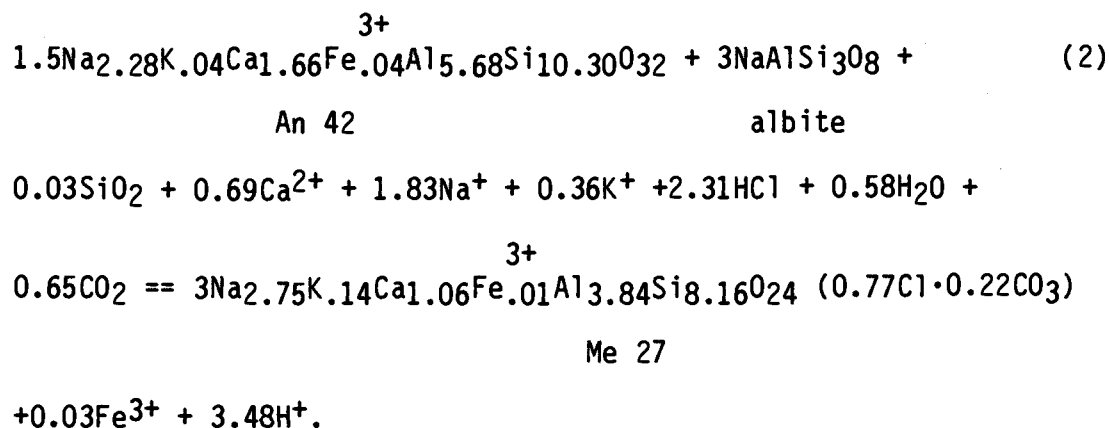
Several reactions may be written to generalize the exchange of elements during alteration of the gabbro-diorites in the Monterrosas area. In the equations that follow, certain assumptions have been made for computational purposes. For example, average compositions are used for minerals such as plagioclase feldspar, clinopyroxene, amphiboles, scapolite, iron-titanium oxides, sphene, and chlorite that were analyzed by electron microprobe. Because the valence state of iron cannot be determined by this method, all iron is treated as ferric in plagioclase feldspar (Ribbe, 1975), scapolite, and epidote (Deer et al., 1962) and as ferrous in amphiboles (Hawthorne, 1983; Robinson et al., 1982) and pyroxene (Robinson, 1980; Deer et al., 1978). The compositions of epidote and chlorite used in the following

equations are derived from petrographic determinations and published chemical analyses of minerals with similar optical characteristics.

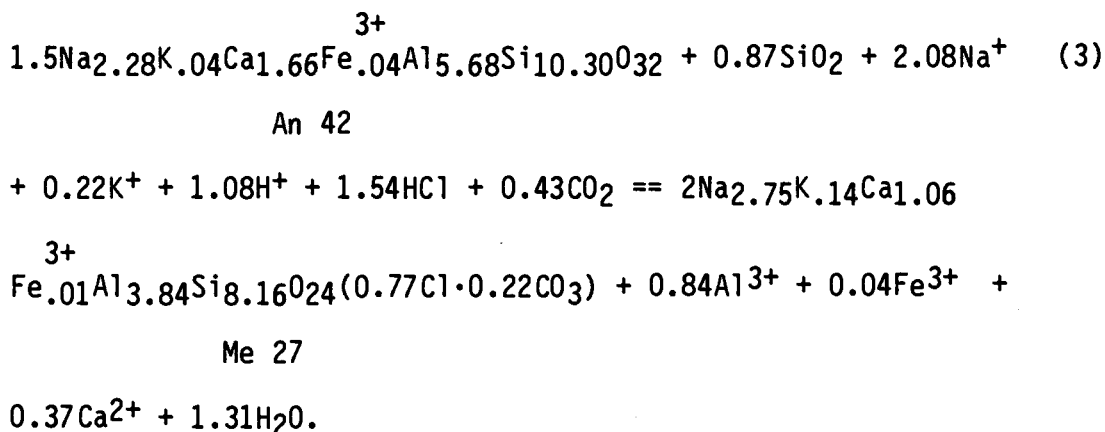
Plagioclase feldspar in the gabbro-diorites alters predominantly to epidote, clinozoisite, and scapolite. The formula for plagioclase feldspar is taken as An 42, which is both its normative and average microprobe composition. This is considered to be representative of plagioclase feldspar in unaltered gabbro-diorites. A composition intermediate between the epidote and clinozoisite end members has been assumed based on petrographic evidence that some epidote is zoned to a core of clinozoisite. Scapolite has an average composition of Me 27 (marialite/dipyre). The following equations exemplify the alteration of andesine to epidote-clinozoisite and scapolite:



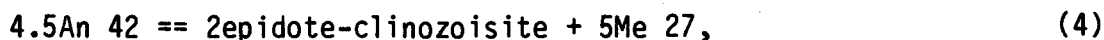
Because albite is not a common constituent of the alteration assemblage in the Monterrosas deposit, it may have reacted with andesine and hydrothermal fluids to form scapolite in the following manner:



Scapolite may also form directly from plagioclase feldspar, as illustrated by the following reaction:

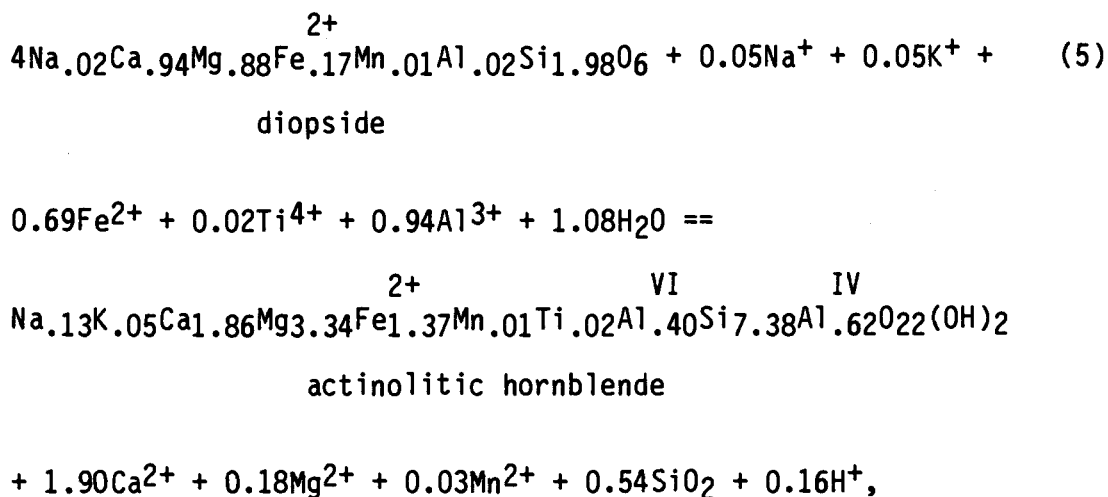


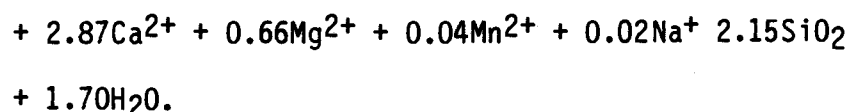
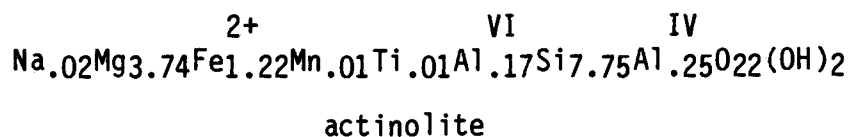
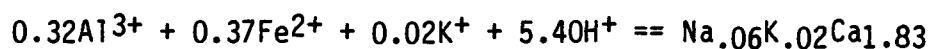
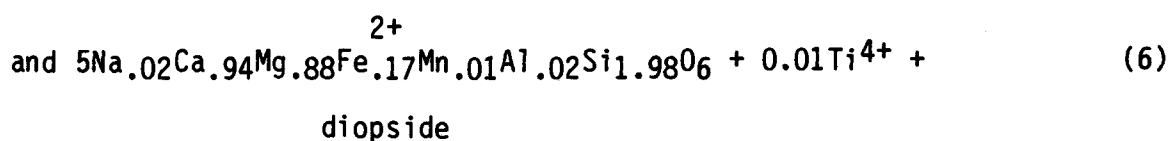
A summary of reactions 1 to 3 for the alteration of andesine to epidote-clinozoisite and scapolite,



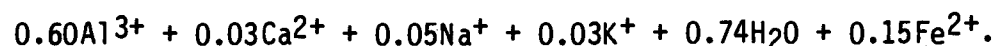
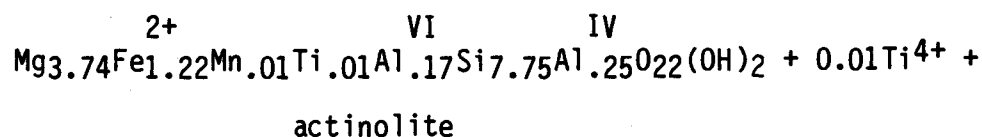
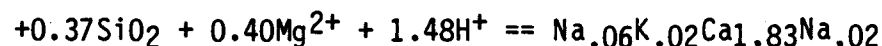
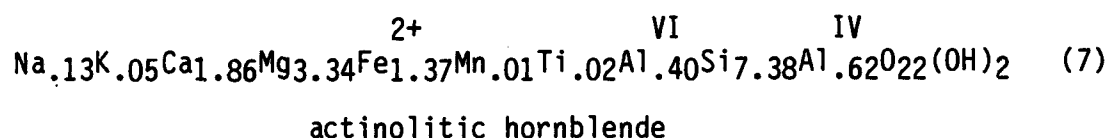
indicates that SiO_2 , Fe^{3+} , Ca^{2+} , Na^+ , K^+ , HCl , H_2O , and CO_2 are consumed and Al^{3+} and H^+ are liberated.

Actinolitic hornblende and actinolite replace diopside extensively in the gabbro-diorites at Monterrosas. Possible reactions that describe the alterations include:



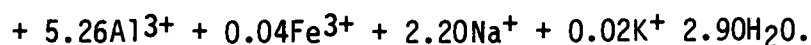
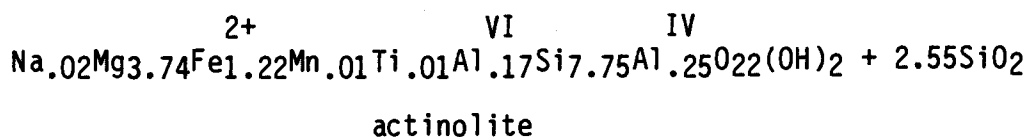
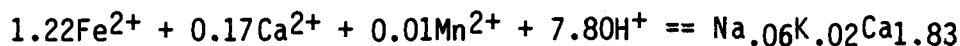
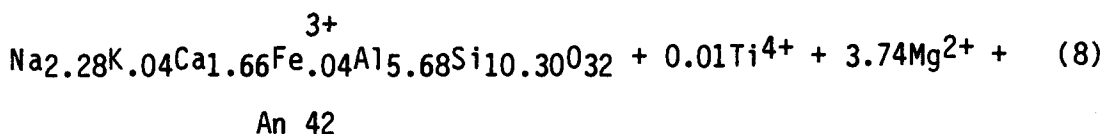


Actinolite also replaces actinolitic hornblende, and this reaction may be written as follows:

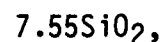
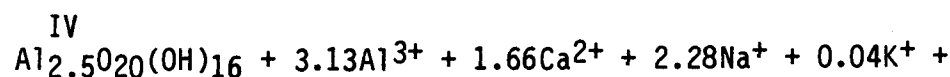
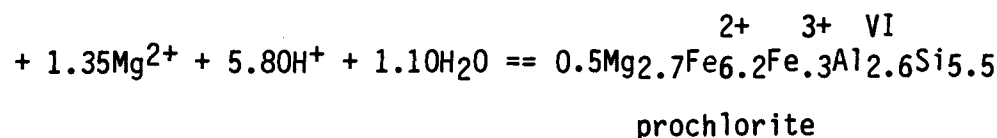
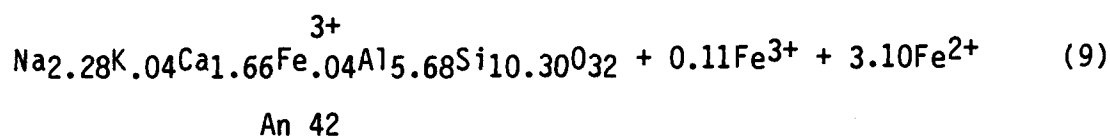


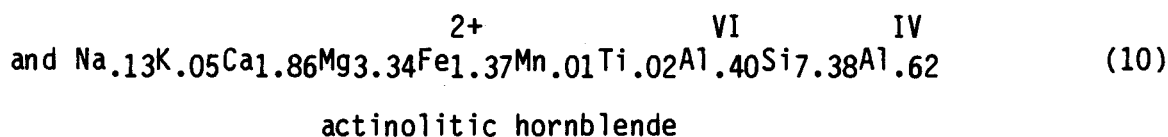
The sum of equations 5, 6, and 7 (9 diopside = 2 actinolite) consumes Ti^{4+} , Al^{3+} , Fe^{2+} , K^+ , and H^+ , and releases SiO_2 , Ca^{2+} , Mg^{2+} , Mn^{2+} , Na^+ , and H_2O .

Actinolite also replaces andesine in the more intensely altered samples of gabbro-diorite near the ore zone. The alteration of andesine to actinolite may be represented as follows:

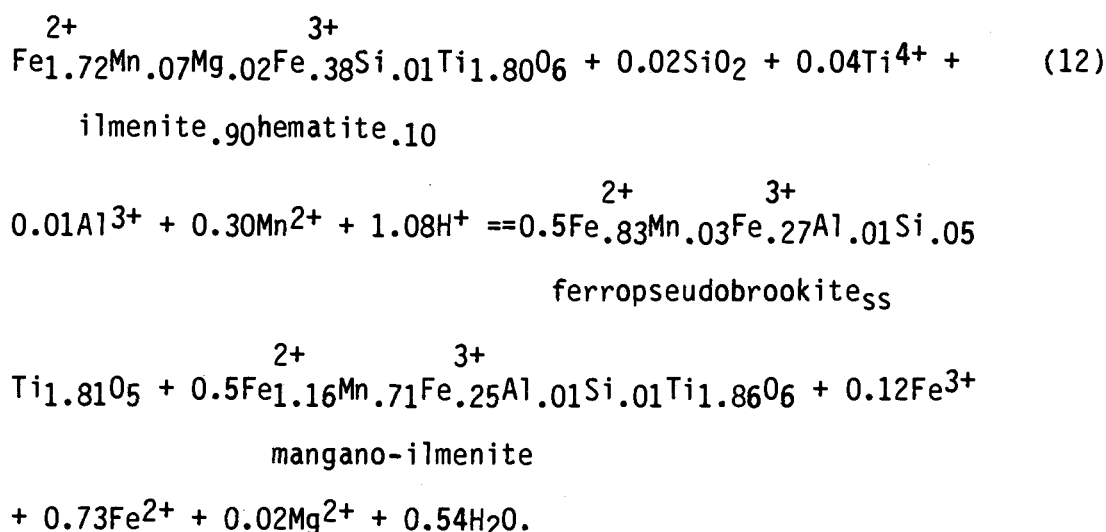


Other secondary minerals contained in altered gabbro-diorites include sphene, magnetite, chlorites, sulfides, apatite, tourmaline, piemontite, hematite, mangano-ilmenite, ferropseudobrookite, and others. Because the compositions for some of these minerals were determined chemically, equations may also be written to generalize the exchange of elements during the formation of these secondary minerals. For example, prochlorite replaces amphibole, plagioclase feldspar, and biotite in altered gabbro-diorites. Balanced equations for the alteration of plagioclase feldspar and actinolitic hornblende to prochlorite might include:

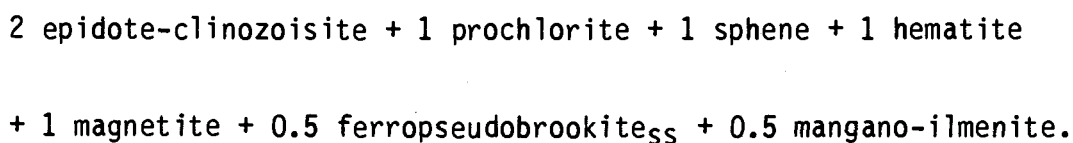
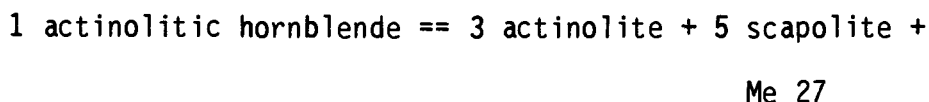
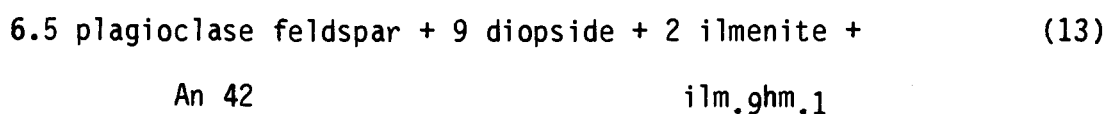




The formation of some of the other secondary oxide minerals such as ferropseudobrookite_{ss} and mangano-ilmenite may be represented by equation 12:



The destruction of primary magmatic minerals and concomitant formation of secondary alteration minerals in gabbro-dioritic host rocks of the Monterrosas deposit may be summarized by the following reaction:



Equation 13 is a summation of all the reactions (Eqs. 1-12) previously described. Although this summary reaction cannot define in detail all

of the chemical and mineralogical effects that accompanied alteration, it does provide a good approximation of the major changes that resulted from exchange and interaction between gabbro-diorites and the late magmatic to hydrothermal fluids. The substitution of chemical formulae for the mineral reactants and products of equation 13 provides a means to quantify the exchange of elements, or mass transfer, between host rocks and fluids. The exchange of elements, given as gains or losses in moles, is listed in Table 9.

These tabulated data document substantial additions of H_2O , Fe^{3+} , Fe^{2+} , HCl , Mg^{2+} , and CO_2 and depletions of SiO_2 , Al^{3+} , Ca^{2+} , and Na^+ to accommodate the mineralogical changes imposed by alteration. However, this list of constituents gained and lost is necessarily incomplete, because the formation of other secondary minerals such as apatite, tourmaline, and sulfides dictate the addition of P, B, and S to these host rocks from the fluids. Moreover, the exchange of some components listed in Table 9 may be mistaken in consideration of the overall mineralization process. For example, gains of Fe^{2+} and Fe^{3+} must be appreciably larger than noted in Table 9 because of the deposition of massive amounts of pyrite, chalcopyrite, and magnetite in the orebody, whereas losses of SiO_2 , Al^{3+} , and Ca^{2+} are probably less than indicated on account of the deposition of other secondary minerals such as quartz, carbonate, and clay group minerals in altered wall rocks and as gangue in the ore.

Concentrations of the major oxides in samples of gabbro-diorites from the Monterrosas area reflect the mineralogical changes imposed by alteration and metallization. For example, a comparison between the six least altered samples of gabbro-diorite identified petrographically

Table 9. Exchanges of Elements in the Gabbro-Diorites from
a Summary Reaction of Alteration (in moles)

Gains	Losses
6.31 Fe^{3+}	0.75 Ti^{4+}
5.66 Fe^{2+}	7.49 Al^{3+}
2.62 Mg^{2+}	5.32 Ca^{2+}
0.16 Mn^{2+}	1.14 Na^{+}
0.02 Co^{2+}	15.51 SiO_2
0.45 K^{+}	
0.96 H^{+}	
3.85 HCl	
8.59 H_2O	
1.08 CO_2	

and sixteen more altered samples reveals geochemically significant variations for most of the elements, as listed in Table 10. The oxides of iron, magnesium, and potassium are present at greater concentrations in the more altered samples, whereas the oxides of silicon, titanium, calcium, and sodium are depleted. Because alteration in the gabbro-diorites is dominantly through replacement processes, the metasomatic exchange of oxides is better interpreted on the basis of mass-per-volume units ($\text{g}/100 \text{ cm}^3$) by accounting for the specific gravity of samples. This conversion is made by multiplying the wt percent of oxide in a sample and its specific gravity. The difference between the means of the individual oxides in the six relatively unaltered and the sixteen altered samples of gabbro-diorite was evaluated statistically for the reliability of apparent gains and losses (Koch and Link, 1971). For example, the differences in silica and total iron oxide between fresh and altered rocks, as listed in Table 10, are significant at the 99 percent confidence level. This indicates that there is only a 1 percent possibility that the differences are not real, but rather result from random chance or error. Changes in TiO_2 , CaO , Na_2O , and K_2O are significant at the 95 percent confidence interval, and changes in MgO are significant at the 80 percent confidence level (Table 10). The difference in Al_2O_3 between unaltered and altered rocks is not significant. Although the means of most of the major oxides show overall variations between relatively fresh and altered samples of gabbro-diorite, they have only fair correlations ($r = \pm 0.16$ to ± 0.90) with distance to the ore zone, intensity of alteration (measured as the percentage of secondary minerals), or intensity of metallization (measured as the concentration of copper).

Table 10. Chemical Changes Between Relatively Unaltered and Altered Patap Gabbro-Diorites (in wt % and g/100 cm³)

Oxide	(n = 6) Unaltered	(n = 16) Altered	Difference
SiO ₂	54.6 wt %	51.0 wt %	
TiO ₂	0.91	0.67	
Al ₂ O ₃	17.2	17.0	
FeO _t	5.4	10.7	
MgO	4.9	6.1	
CaO	11.5	9.1	
Na ₂ O	4.2	3.2	
K ₂ O	0.21	0.75	
S. G.	2.81	2.80	
A. I.	9.68	49.61	
SiO ₂	155.53 g/100 cm ³	144.87 g/100 cm ³	-10.66***
TiO ₂	2.59	1.90	- 0.69**
Al ₂ O ₃	48.72	48.22	- 0.50
FeO _t	14.59	30.49	+15.90***
MgO	14.05	17.33	+ 3.28*
CaO	32.84	25.80	- 7.04**
Na ₂ O	11.86	9.05	- 2.81**
K ₂ O	0.61	2.14	+ 1.53**

* Significant at the 80% confidence interval

** Significant at the 95% confidence interval

*** Significant at the 99% confidence interval

$$A. I. = \text{Alteration Index} = \frac{(R_S - R_X) \times 100}{R_S}$$

$$\text{where } R = \frac{(Na_2O + CaO + TiO_2 + SiO_2)}{(K_2O + MgO + FeO_t)}$$

R_S = R of least altered sample, 6-8-13

R_X = R of any sample

These distributions apparently result from the lack of specific assemblages of alteration minerals. In an effort to quantify the chemical effects of alteration, a ratio for each sample was established as the sum of oxides lost ($\text{Na}_2\text{O} + \text{CaO} + \text{TiO}_2 + \text{SiO}_2$) versus the sum of oxides gained ($\text{K}_2\text{O} + \text{MgO} + \text{FeO}_t$). Each ratio (R_x) was then normalized against the ratio for the least altered sample of gabbro-diorite (R_s). This recast equation, $\frac{R_s - R_x}{R_s} \times 100$, defines the alteration index (A.I.). The A.I. varies from 0.00 for the least altered sample of gabbro-diorite (6-8-13) to 69.36 for the most heavily altered sample of gabbro-diorite (B-4) analyzed. The alteration index has good correlations with both distance from ore ($r = -0.82$) and intensity of mineralization ($r = 0.75$), as illustrated in Figure 16. These correlations emphasize that mass transfer of elements in the gabbro-diorites was a major result of the mineralization process at the Monterrosas deposit.

Variations of the major oxides within samples of altered and unaltered gabbro-diorites document the interaction between these host rocks and the late magmatic to hydrothermal fluids that circulated in the Monterrosas deposit. Moreover, these data confirm that large amounts of FeO_t as well as K_2O and MgO were gained, whereas SiO_2 , CaO , Na_2O , and TiO_2 were lost during alteration. In addition, significant amounts of H_2O , Cl, other volatiles, and metals must have been added by fluids to account for secondary minerals such as scapolite, amphiboles, apatite, tourmaline, and the ore minerals in the alteration assemblage.

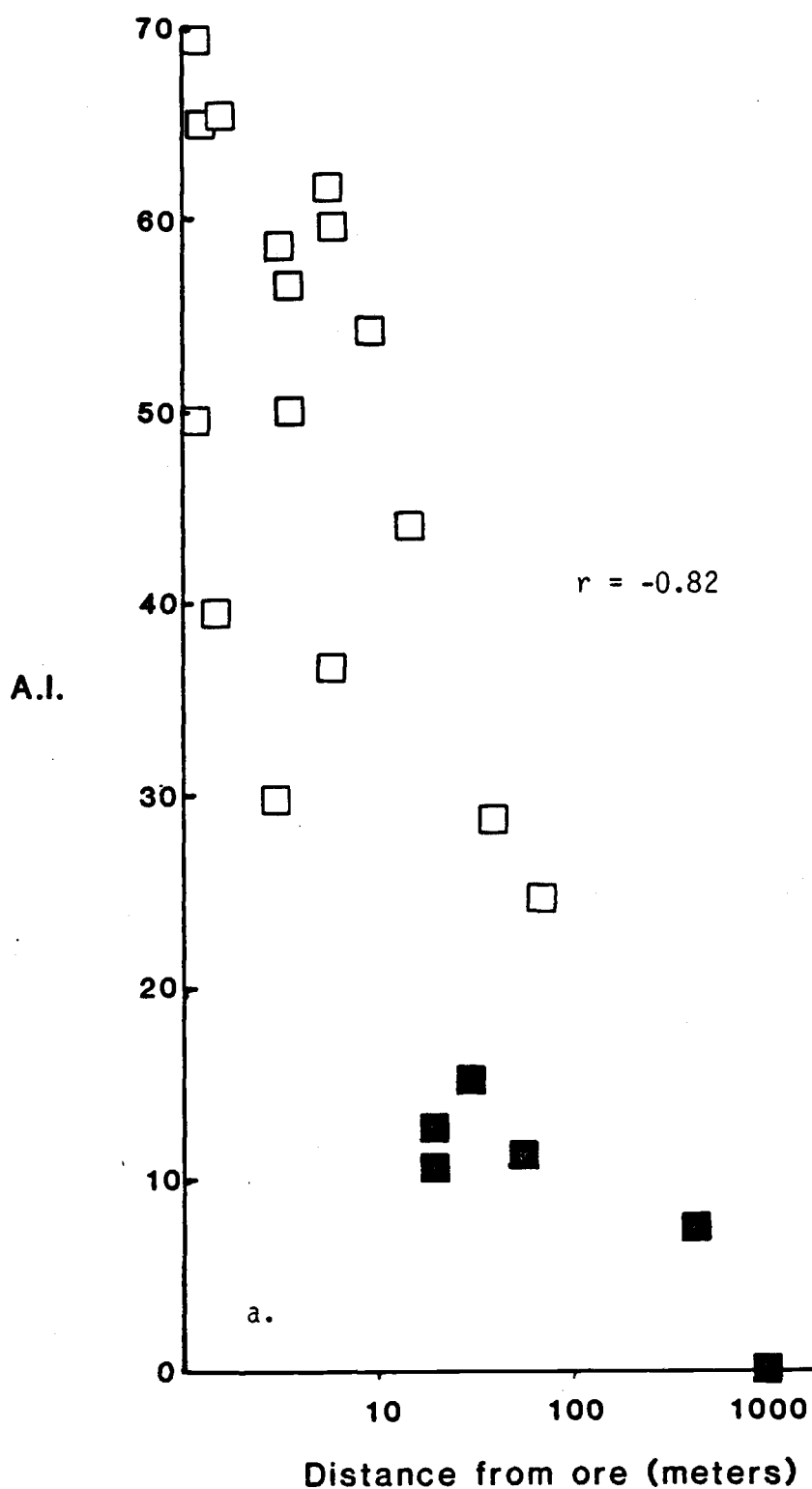


Figure 16. Alteration Index Versus Distance from the Ore Zone (a) and Versus Concentration of Copper (b). Closed squares, relatively unaltered gabbro-diorites; open squares, altered gabbro-diorites.

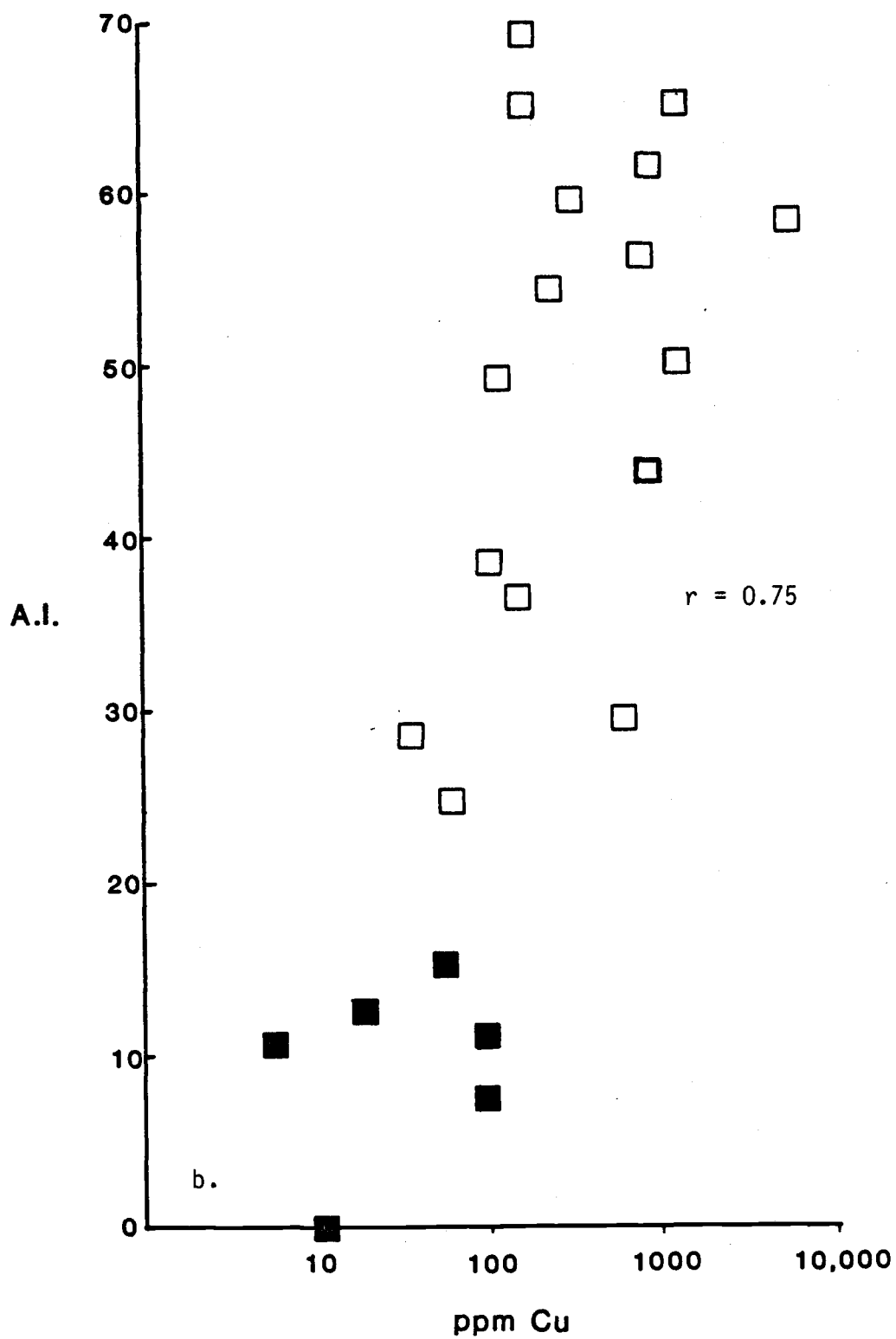


Figure 16 (continued)

FLUID INCLUSIONS

The study of fluid inclusions has provided a wealth of chemical and physical data relevant to the ore-forming fluids of hydrothermal mineral deposits. These contributions have particularly enhanced existing knowledge of ore genesis in systems of the porphyry copper (Roedder, 1971; Nash, 1976) and strata-bound Mississippi Valley (Roedder, 1976) types of deposits. The investigation of fluid inclusions in samples of altered wall rocks and ore at the Monterrosas Mine has contributed to a better understanding of the genesis of this deposit.

Type III halite-bearing inclusions in gangue quartz at Monterrosas document the high temperature and high salinity of the mineralizing fluids. All halite-bearing inclusions homogenize by halite dissolution at temperatures up to 500°C. These inclusions have an average salinity of about 52 wt percent NaCl. Inclusions with daughter crystals of halite and sylvite have salinities of about 62 wt percent NaCl + KCl and delineate a halite trend on a phase diagram of the NaCl-KCl-H₂O system. The halite trend and the high salinities and temperatures suggest that the fluids exsolved directly from a magma.

Methodology

All types of rock in the Monterrosas area were examined in standard and polished thin sections for the presence of fluid inclusions. Quartz was found to host the only inclusions suitable for analysis. Other minerals, such as apatite, scapolite, and actinolite,

contain inclusions that are too small ($<1\text{ }\mu\text{m}$) for optical examination. Quartz-bearing samples selected for thermometric analyses included magnetite-sulfide ore, altered diorite, granodiorite, and quartz veins in ore, altered diorite, and granodiorites. Doubly polished plates approximately $200\text{ }\mu\text{m}$ (0.2 mm) in thickness were prepared from those samples selected for analysis. Locations of samples are shown on Plates 2 and 3.

Microthermometric measurements were made on a Chaixmeca heating and freezing stage. The heating stage was calibrated by measuring the final melting point of a series of crystalline standards. Calibration of the freezing stage was accomplished by freezing a series of liquids and a liquid CO_2 inclusion with known melting points and measuring the final melting point of the ice upon reheating. The approximate error for these heating and freezing measurements is about $\pm 7^\circ\text{C}$ and $\pm 1.0^\circ\text{C}$, respectively, which are consistent with those reported by Jehl (1975) and Poty et al. (1976) for the Chaixmeca microthermometry apparatus. The heating and freezing data for fluid inclusions at Monterrosas provide estimates of the temperatures and salinities for the mineralizing fluids.

Fluid inclusions are samples of the fluid that was present at the time of growth or recrystallization of the host mineral (Roedder, 1979; 1972). Crystal irregularities formed and sealed during growth of the mineral host may contain primary fluid inclusions; those sealed by recrystallization along fractures at some later time may enclose secondary or pseudosecondary fluid inclusions (Roedder, 1981). As has been the case in most studies of porphyry copper deposits (Roedder, 1971; Ahmad and Rose, 1980), it has been difficult to document the

primary origin of most inclusions in samples from the Monterrosas Mine. Inclusions located along fracture planes are obviously secondary in origin (based on criteria in Roedder, 1981, Table 5.1). Aligned inclusions without trace of a fracture plane were considered to be secondary because the linear arrangement may represent an older healed fracture (Ahmad and Rose, 1980). Primary inclusions were identified by their isolated occurrence (Roedder, 1981, Table 5.1) and the absence of evidence for a secondary origin (Bloom, 1981; Ahmad and Rose, 1980).

Fluid inclusions from Monterrosas are classified according to the scheme suggested by Nash (1976), which is based on the phase relations observable at room temperature. Three types of fluid inclusions recognized are noted simply as types I, II, and III. Type I inclusions consist of a water-rich liquid plus a small vapor bubble without any daughter minerals. The vapor bubble occupies less than 20 volume percent of the inclusion, and commonly less than 10 volume percent. Type I inclusions are all less than 35 μm in diameter and most are less than 10 μm . Some exhibit negative crystal shapes, but most are round or irregular. All Type I inclusions homogenize into the liquid phase by disappearance of the vapor.

Fluid inclusions of the type II variety are gas-rich and contain liquid plus a large water vapor bubble that occupies more than 60 percent of the inclusion. Daughter minerals are not present in type II inclusions. These inclusions are rare at Monterrosas, and where present are usually associated with types I or III. Type II inclusions homogenize into the vapor phase by disappearance of the liquid.

Type III fluid inclusions contain 1 or more daughter minerals such as halite, sylvite, and others, small vapor bubbles (< 15 volume percent), and liquid, as illustrated by the photomicrographs of Figure 17. These inclusions are generally larger than those of type I, and their shapes are irregular. Sizes range from less than 10 μm to more than 25 μm , with the largest observed measuring 27 μm by 15 μm . Nearly all type III inclusions homogenize into the liquid phase by dissolution of halite.

Types I and III inclusions dominate in samples from the Monterrosas deposit, and type II inclusions are rare. Of the two main kinds observed, type III are present as probable primary as well as secondary and (or) pseudosecondary varieties, whereas type I are in most cases demonstrably secondary. Ambiguities in the distinction between primary and secondary inclusions are commonplace, and especially in porphyry-type hydrothermal systems that are characterized by repeated episodes of fracturing, fluid movement, and rehealing of fractured host rocks and ore minerals (Roedder, 1971; 1976). Several linear trends of innumerable type I and some type III inclusions within single crystals of quartz demonstrate that similar events accompanied ore formation at Monterrosas. Most of the type II inclusions appear to have resulted from necking down of other inclusions (see Roedder, 1979, for a schematic representation of necking down).

Halite is the most abundant daughter mineral in type III inclusions at Monterrosas. This mineral is identified by its cubic outline and colorless, isotropic character (Figure 17). Halite generally exhibits euhedral cubic form, although some corners may be rounded. Crystals of halite in type III inclusions are up to two or more times

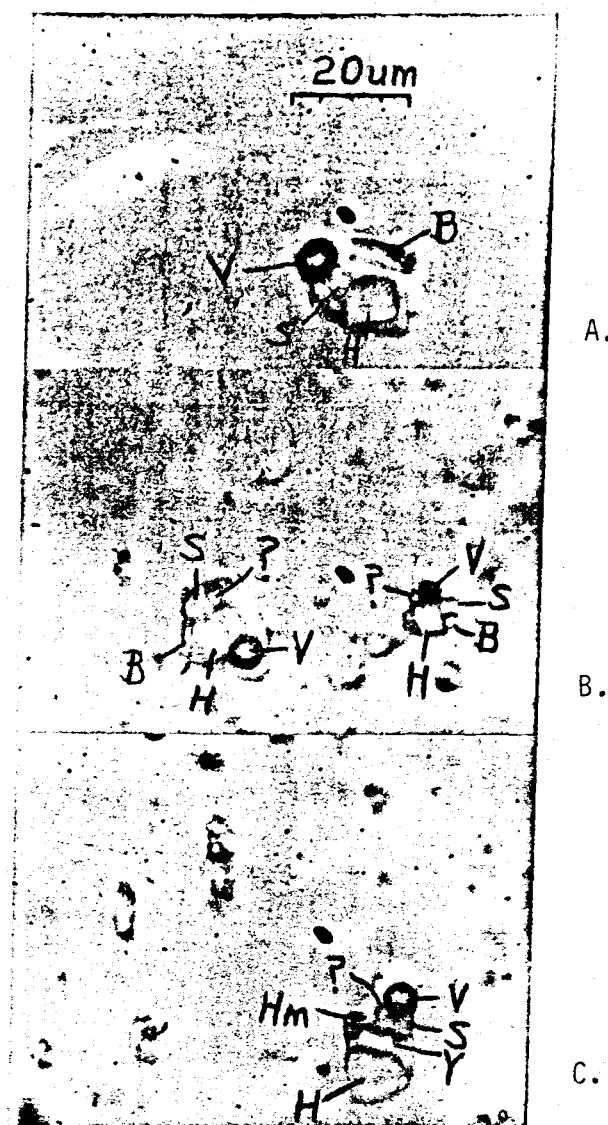


Figure 17. Type III Inclusions in Samples of Ore from the Monterrosas Mine. A. Sample 3-18-70A-B1 with halite (H), sylvite (S), vapor bubble (V), and unidentified birefringent rod (B) that is possibly anhydrite or molysite. B. Samples 5-18-70B-B1A and 5-18-70B-B2A with halite (H), sylvite (S), and unidentified daughter minerals (B,?), with vapor bubble (V). C. Sample 5-18-70BA-C2 with halite (H), sylvite (S), unidentified birefringent yellow crystal (Y), hematite (Hm), a second unidentified daughter mineral (?), and a vapor bubble (V). Note rounded corners of halite.

larger than the vapor bubble, and they may occupy 10 to 25 volume percent of the inclusion.

At least five other daughter minerals are seen in type III inclusions. Sylvite is present in about 15 percent of the type III inclusions at the Monterrosas Mine. It is recognized by its cubic form and colorless, isotropic appearance (Figure 17). Sylvite, in contrast to halite, has a lower refractive index and is smaller and more anhedral in shape. Tentative identifications of sylvite were confirmed by subsequent heating experiments. Sylvite undergoes dissolution prior to halite because of its higher temperature coefficient of solubility (Roedder, 1971).

Hematite is a less common phase in type III inclusions. It displays a characteristic yellowish orange to red color, and most crystals also show a subhedral hexagonal platy form. Another opaque mineral, possibly pyrite, chalcopyrite, or magnetite, has rounded to square outlines. Efforts to determine its magnetic properties were unsuccessful because of the presence of magnetite as solid inclusions in or surrounding the fluid inclusion-bearing quartz.

The halite-bearing type III inclusions contain at least three other unidentified daughter minerals. One or more unidentified daughter crystal is present in nearly 50 percent of these inclusions. Elongate crystals of a prismatic, rectangular, and colorless mineral (Figure 17) that have low to moderate birefringence, moderate positive relief in liquid, and parallel to slightly inclined extinction may be anhydrite (CaSO_4), molysite ($\text{FeCl}_2 \cdot 4\text{H}_2\text{O}$), or unnamed $\text{CaCl}_2(\cdot 6\text{H}_2\text{O})$ (Kwak and Tan, 1981a; Ted Theodore, 1983, personal communication). This mineral generally persists beyond the temperature of final halite

dissolution in type III inclusions, and in some inclusions it did not dissolve totally even at temperatures greater than 500°C. Another unidentified mineral that forms pleochroic yellow tabular crystals with moderate birefringence and parallel extinction could be amaranthite ($\text{FeSO}_4(\text{OH}) \cdot 4\text{H}_2\text{O}$) according to the data of Eadington (1983) and Kwak and Tan (1981a). These yellow crystals also dissolve at temperatures above those for the disappearance of halite. Several type III inclusions have small, rounded to cubic (rhombohedral?) colorless crystals with moderate to high birefringence and relief. The sizes of these crystals are generally too small ($<1 \text{ } \mu\text{m}$) for effective identification by optical methods. They could be any of the above-mentioned anisotropic minerals, or possibly calcite.

Homogenization Temperatures

Most fluid inclusions at room temperature consist of both a liquid and vapor phase, and sometimes these may be accompanied by a solid crystalline phase. The homogenization temperature is defined as the lowest temperature at which only a single liquid or vapor phase is present (Roedder and Bodnar, 1980). Ideally, it provides a thermal minimum for the formation of the host mineral, and of the associated rock or mineral deposit by extrapolation. At Monterrosas, for example, the homogenization of simple, liquid-rich type I inclusions is marked by the disappearance of the less abundant vapor phase. Homogenization of type II inclusions takes place with the disappearance of liquid into the gas phase. The homogenization temperature of most type III inclusions is that characterized by the dissolution of halite, and not the lower temperature of vapor disappearance. Only two type III

inclusions homogenized by vapor disappearance at temperatures greater than that of the halite dissolution. As will be discussed more fully in a later section, homogenization by halite dissolution indicates that the solutions were trapped under relatively unusual conditions of pressure and temperature (Erwood et al., 1979; Wilson et al., 1980). In most type III inclusions with more than one daughter mineral, hematite, magnetite, a sulfide mineral, anhydrite, or another unidentified daughter mineral usually persisted beyond the temperature of halite dissolution. This is ascribed to necking down, disequilibrium, kinetic effects on dissolution, or postentrapment oxidation of the fluid because of hydrogen diffusion through the walls of the host quartz crystal (Roedder, 1972; 1971). Hence, the temperature of homogenization is not based on dissolution of these refractory minerals.

Temperatures of homogenization were obtained from a total of 136 inclusions from twelve samples of the Monterrosas area. Although inclusions in many additional samples were also observed during this study, problems relating to poor visibility, decrepitation, and leakage rendered the data of limited value. Of those for which reliable data were obtained, about 65 percent were type I and 35 percent were type III inclusions. Results of the heating runs are given in Table 11. Homogenization for type I inclusions took place between 62° and 243°C, as shown in Figure 18. Most type I inclusions homogenized at about 170°C as recorded by the peak on the histogram (Figure 18). Similar homogenization temperatures were observed in samples of all the different rocks analyzed. Temperatures of vapor disappearance (NOT homogenization) in type III inclusions range from

Table 11. Fluid Inclusion Data for the Monterrosas Deposit

Sample	Rock Type	Inclusion	Type	Daughter Minerals	V out	H out	Other	First Melt	Last Melt	Salinity
2-32-3A1	Quartz vein in diorite	B1	I		<144					
		B2	III	H+B	198	448	B>500		- 7.0	10.5
		D1	III	H+B	147	480	B>500			50.7
		D2	I		<147					54.1
		E1	I		161				-10.3	14.3
		E2	III	H+B	196	382	B=388		-10.4	14.4
		F1	I		163					44.4
		F2	III	H+B	198	401	B=482		-10.7	14.7
		F3	III	H	184	262				46.2
		F4	III	H+B	198	369	B>500			35.4
		G1	I		163			-47.4	- 9.7	43.3
		G2	I		163				- 9.7	13.7
		H2	III	H+B	196	436	B>500			13.7
F-3C	Massive ore	1A	I		180					49.5
		2B	I		168			-53.3	-15.6	19.3
		1F	I		183				-17.5	20.8
									-13.5	17.5
E-1B	Quartz vein in ore	1B	I		174					
		1D	I		<174			-41.5	-15.2	19.0
		1F	I		<174				-16.8	20.3
3-18-70A	Massive ore						S=177			
		B1	III	H+B+S	290	461	B=462			52.1
		B2	III	H+B	294	418	B=505			47.7
		C1	III	H+B	326	398	B=452			45.9
		D1	III	H+B	<300	462	B>505			52.2
5-18-70BA	Massive ore	B1	III	H+Y	117	459	Y=462			51.9
		B2	III	H+Y+S	168	465	S=196			52.5
							Y=468			
		C1	III	H+Y	123	465	Y=480			52.5

Table 11 (continued)

Sample	Rock Type	Inclusion	Type	Daughter Minerals	V out	H out	Other	First Melt	Last Melt	Salinity
5-18-70BA (continued)	Massive ore	C2	III	H+Y+S+hm+?	123	364	Y=486 S<364 hm>500			42.9
		F1	III	H+Y	117	444	Y=486			50.3
5-18-70BB	Massive ore	1A	III	H+S+B+?	291	491	S=163			55.3
		2A	III	H+S+B+?	282	426	B=225 S=130 B=257			48.5
		2B	III	H	292	>489				>55.1
		3B	III	H+B	292	>473	B>473			>53.3
		1D	III	H+S+B	305	442	S=134 B>512			50.1
		2D		H+B+?	292	474	B>507			53.4
		3D	III	H+B	311	445	B=490			50.4
5-18-70AA	Massive ore	1A	III	H+S+B	168	444	S=129 B>445			50.3
		1B	III	H+B	178	482	B>490			54.3
		2B	III	H+B	225	360	B>380			42.5
		3B	III	H+B	172	488	B>488			55.0
5-18-70AB	Massive ore	1A	I		127				-15.7	19.4
		1D	I		125				-11.1	15.1
		1E	I		161			-50.5	-13.5	17.5
		2E	I		154				-13.1	17.1
		1F	I		162				-12.8	16.8
		2F	I		154				-12.8	16.8
5-18-70AC1	Massive ore	1A	I		104				-11.7	15.7
		1E	I		187			-44.3	-12.2	16.2
		2E	I		177			-60.0	-7.2	10.2
		3E	I		172				-17.9	21.1
		2F	I		171				-17.5	20.8
		9F	I		184				-13.1	17.1

Table 11 (continued)

Sample	Rock Type	Inclusion	Type	Daughter Minerals	V out	H out	Other	First Melt	Last Melt	Salinity
K-5A1	Massive ore	1A	III	H+O	221	477	O>540			53.8
DDH-13-10A	Massive mt-py	1A	III	H+B+?	177	416	B>535			47.6
		1B	III	H+hm	175	437	hm>535			49.6
		1C	III	H+B	100	459	B>535			51.9
		1D	III	H+hm	148	469	hm>535			52.9
		1E	III	H+hm	158	424	hm>535			48.3
		1G	III	H+O	148	476	O>535			53.7
		1H	III	H+B	177	463	B>535			52.3
12-2-22A	Gabbro-diorite	2A	III	H	183	225				33.2
12-2-22B2	Gabbro-diorite	3A	I		181					
		1C	III	H	256	253				34.8
		2C	III	H	256	317				39.2
12-8-13B	Granodiorite	1A	III	H+Y+O	<219	359	Y=305			42.5
		2A	III	H+O	<229	351	O>375			41.8
12-8-13E	Granodiorite	1A	III	H	219	207				31.0
		1C	I		233					
12-8-13F	Granodiorite	2B	III	H+S+B+O	238	461	S=201 B>480 O>480			52.1
		3B	III	H+hm	234	383	hm>400			44.5
8-2-13F	Granodiorite	1A	III	H+S+O	172	373	S=130 O>380			43.7
8-2-14A	Quartz vein in granodiorite	1A	I		62				-16.5	20.0
		2A	I		139				-20.2	22.8
		2C	I		60			-46.0	-17.3	20.7

Table 11 (continued)

Sample	Rock Type	Inclusion	Type	Daughter Minerals	V out	H out	Other	First Melt	Last Melt	Salinity
10-2-13B2	Quartz vein in granodiorite	B1	I		178			-40.5	-17.3	23.7
		C1	I		127				-14.5	18.4
		C2	I		138				-20.1	22.7
		E1	I		183				-13.8	17.7
10-2-13A2	Quartz vein in granodiorite	A3	I		168				-10.5	14.5
		D2	I		170				-12.9	16.9

Type I = V+L

Type III = V+L+H ± other daughter minerals

V out = Temperature of disappearance of vapor bubble

H out = Temperature of dissolution of halite

Other = Temperature of dissolution of other daughter minerals

First Melt = Temperature of first melt of ice formed by freezing the inclusion

Last Melt = Temperature of last melt of ice formed by freezing the inclusion

All temperatures in °C and corrected for machine calibration

Salinity = equivalent wt percent NaCl

V = vapor

H = halite

B = birefringent rod

S = sylvite

Y = yellow birefringent rod

O = opaque

hm = hematite

? = unknown small birefringent crystal

All analyses by G. B. Sidder on a Chaixmeca heating and freezing stage at Oregon State University.

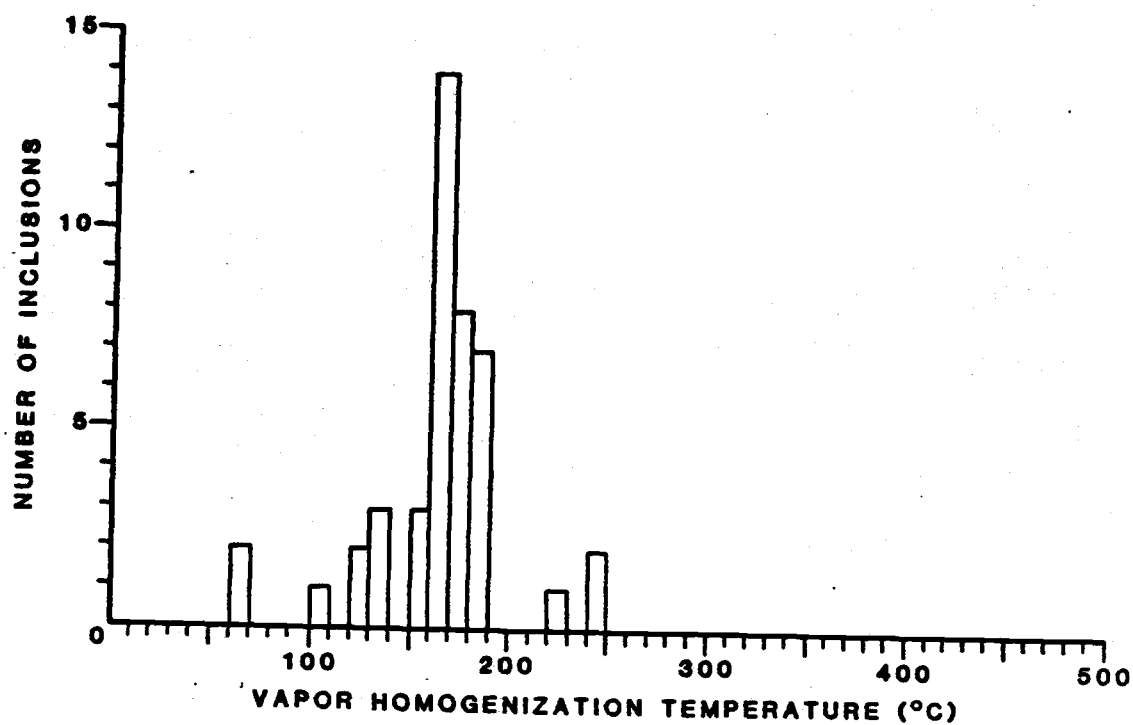


Figure 18. Histogram of the Temperatures of Vapor Homogenization in Type I Inclusions

114° to 326°C as illustrated in Figure 19. However, one type III inclusion in gabbro-diorite homogenized by vapor disappearance at 256° and another in granodiorite at 219°C. In general, there are not any well-defined peaks of vapor disappearance on the histogram. Temperatures of halite dissolution in type III inclusions range between 211° and 490°C, as depicted in Figure 20. A few samples decrepitated near 500°, but with their halite cube remaining visible although diminished in size. Inclusions composed of liquid, vapor bubble, and halite as the only daughter mineral homogenized by halite dissolution at temperatures between 211° and 359°C. However, those with one or more daughter minerals in addition to halite homogenized at higher temperatures ranging from 351° to 488°C. The homogenization temperatures for these inclusions exhibit a frequency maximum at about 465°C (Figure 20). Inclusions hosted by disseminated and vein quartz in massive ore recorded the highest homogenization temperatures (to 488°C), whereas those in gabbro-dioritic wall rocks and in granodiorites homogenized commonly at lower temperatures (about 225° to 380°C).

Among the other daughter minerals in type III inclusions, some of the colorless, rod-shaped crystals (anhydrite?, molysite?) and the yellow crystals (amarantite?) dissolved at temperatures between 452° and 490°C (Table 11). Although some unidentified daughter minerals disappeared at temperatures less than 300°C, the majority of these did not totally dissolve at the maximum temperatures of heating (to 550°C), and all remained at temperatures above that of halite dissolution in their respective inclusions. Sylvite always dissolved before halite

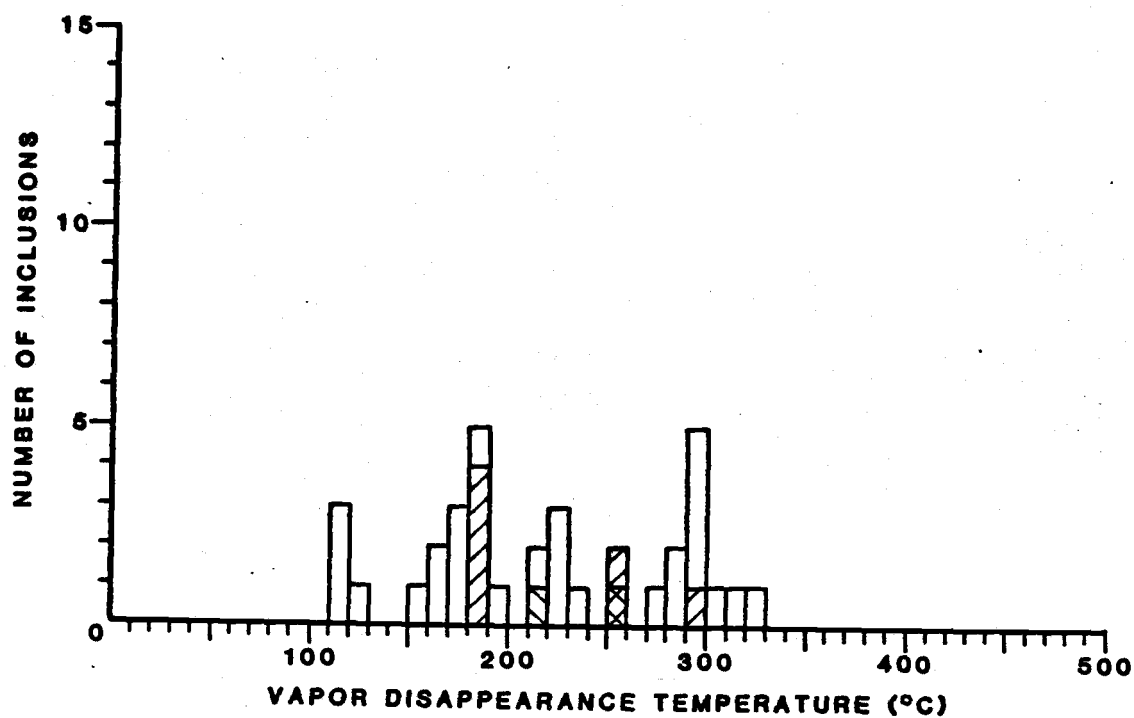


Figure 19. Histogram of the Temperatures of Vapor Disappearance in Type III Inclusions. Hachured left, vapor disappearance in V + L + H inclusions; open, vapor disappearance in V + L + H + other daughter inclusions; hachured right, vapor homogenization.

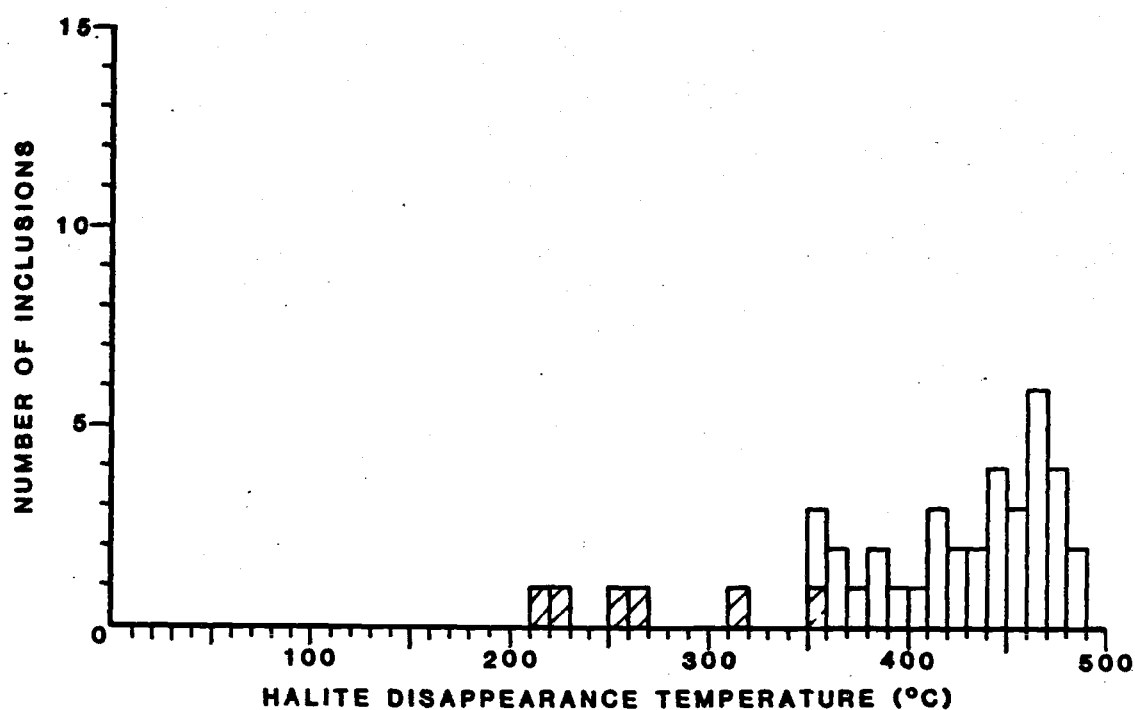


Figure 20. Histogram of the Temperatures of Halite Disappearance in Type III Inclusions. Hachured left, V + L + H; open, V + L + H + other daughter crystals.

in the type III inclusions, and its temperature of disappearance ranged from about 129° to 196°C (Table 11).

Salinities

The salinities of fluid inclusions at the Monterrosas Mine were determined from the freezing point depression for type I inclusions (Roedder, 1963; Potter et al., 1978) and by the temperatures of halite dissolution for type III inclusions (using the data of Keevil, 1942; Sourirajan and Kennedy, 1962; and Potter et al., 1977). The freezing point depression of an inclusion is defined as the final melting temperature of ice that was formed by freezing of the liquid phase in the inclusion (Roedder, 1962). The temperature of initial melting was also recorded when observed. This latter temperature approximates the eutectic point for water-salt systems and indicates what salts other than NaCl may be present in the fluid (Roedder, 1971). All salinities reported in this section are represented as the wt percent NaCl equivalent.

Freezing point depression data listed in Table 11 were obtained from a total of 49 type I inclusions in seven samples from Monterrosas. Salinities of these inclusions range from about 10 to 24 wt percent NaCl equivalent. A histogram of the salinities measured is given in Figure 21 and shows a frequency maximum at about 18 wt percent NaCl for type I inclusions. In addition, the salinities of 41 type III inclusions from nine samples were calculated from the temperature of final halite dissolution (Table 11). They are appreciably more saline than the type I inclusions, and concentrations range from about 30 to 56 wt percent NaCl equivalent (Figure 21). Type III inclusions exhibit

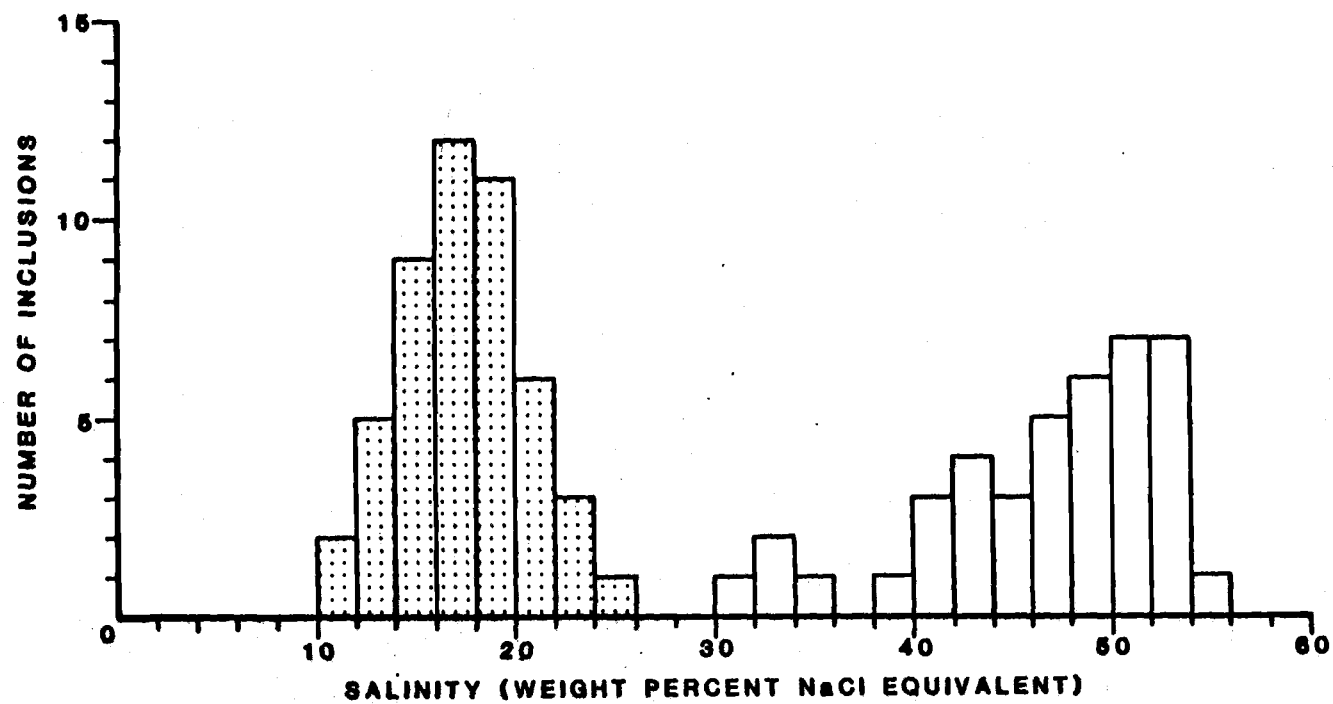


Figure 21. Histogram of the Salinity for Types I (stippled) and III (open) Inclusions.

a broad frequency maximum at about 52 wt percent NaCl. Samples of massive ore host the most saline inclusions (to 56 wt percent), and inclusions in gabbro-dioritic wall rocks and granodiorites are moderately saline (30 to 45 wt percent).

The two dominant types of fluid inclusions from the Monterrosas Mine occupy distinct fields on a diagram of salinity versus temperature, as illustrated in Figure 22. The saturation curve for the NaCl-H₂O system defines one field of high temperatures and high salinities for type III inclusions, and a field of lower temperatures and moderate salinities circumscribes type I inclusions. Nearly all of the type III inclusions plot on the saturation curve because of their homogenization by halite dissolution. Data for six inclusions from samples of massive ore are plotted above the saturation curve in Figure 22 and represent salinities determined on the NaCl-KCl-H₂O ternary diagram, as shown in Figure 23, from the solution temperatures of halite and sylvite. Total salinities (wt % NaCl + KCl) for these six inclusions range from 57 to 67 wt percent with a mean of 61 wt percent, and their Na/K atomic ratios range from 1.36 to 1.98 and average 1.58. The absence of sylvite at room temperature in other type III inclusions limits the concentration of KCl in the solutions to a maximum of about 12 percent (Erwood et al., 1979). The minimum Na/K atomic ratio in these type III inclusions is about 2.5.

Total salinities of the type III inclusions were determined by the saturation temperature method from the solution temperatures of halite or halite and sylvite. However, this method assumes that the major salts present in the liquid are exclusively NaCl and KCl. As noted

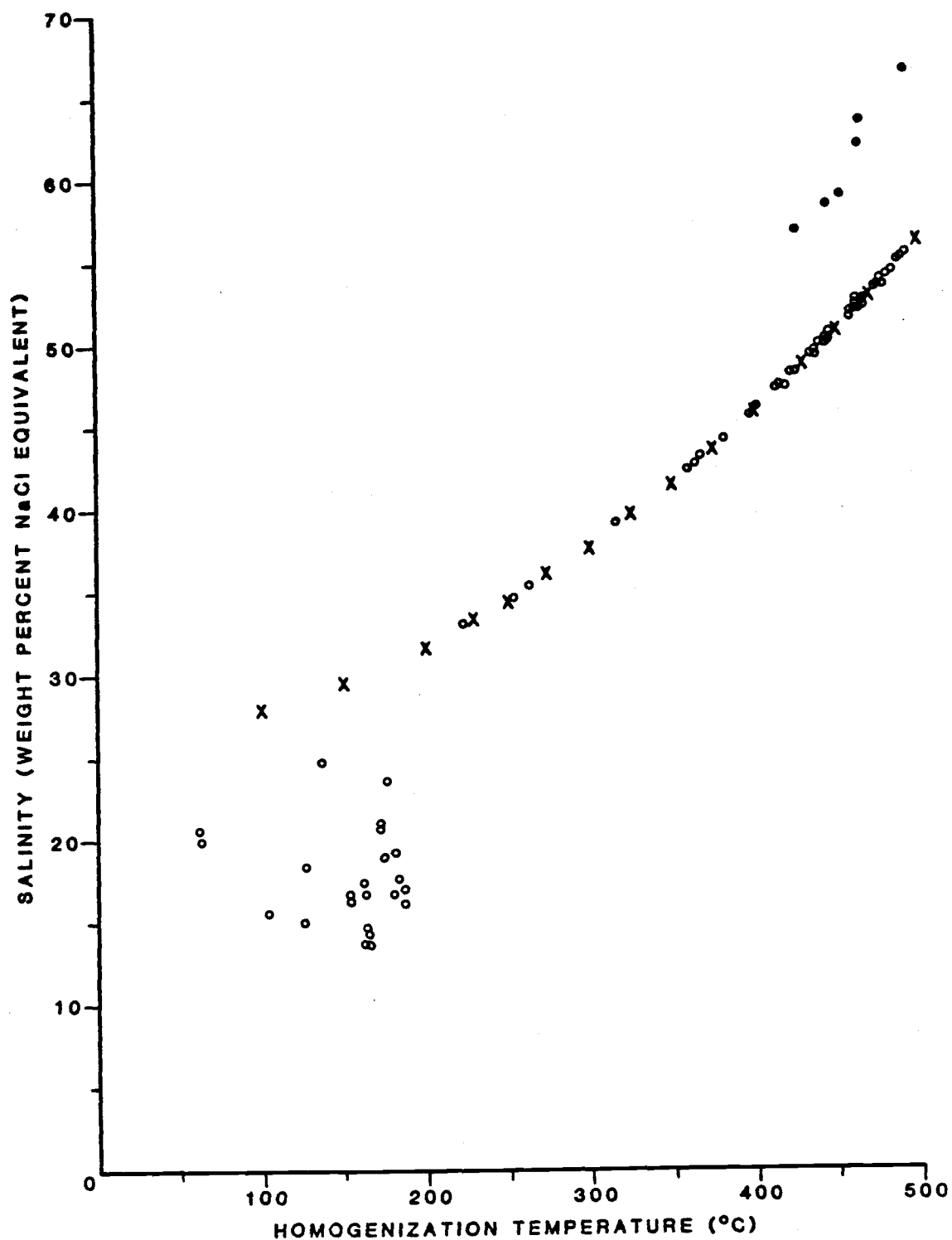


Figure 22. Salinity vs. Temperature of Homogenization for Type I and Type III Inclusions. Open circles, weight percent NaCl equivalent; closed circles, NaCl + KCl total salinity; x, trace of NaCl saturation curve (from Sourirajan and Kennedy, 1962). All type I inclusions plot at $T < 200^\circ$; type III, $T > 200^\circ$.

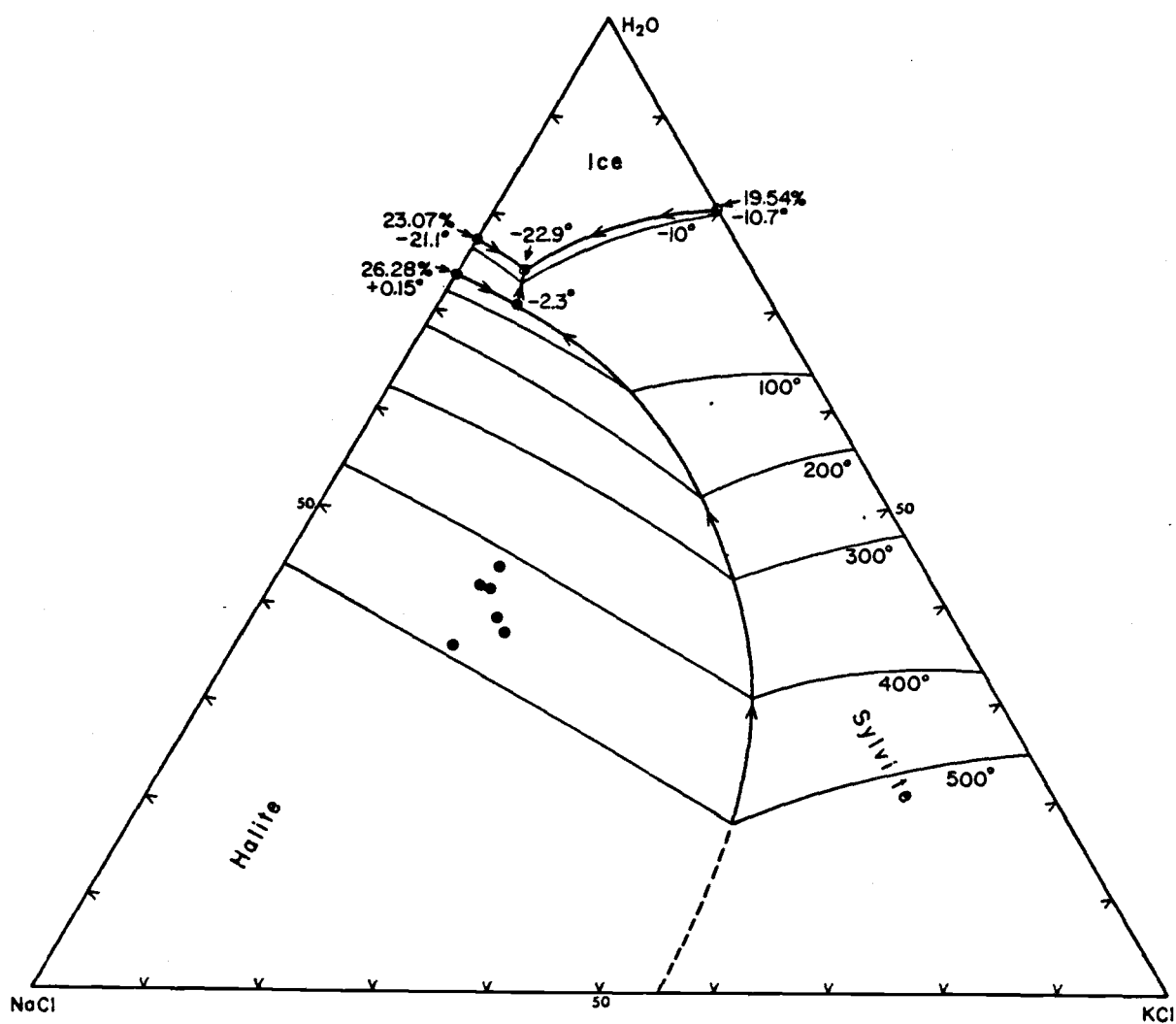


Figure 23. Phase Relations in the System NaCl-KCl-H₂O (from Ravich and Borovaya, 1977, Figure 4, p. 337). Closed circles, data points from the Monterrosas Mine.

previously, daughter minerals other than halite and sylvite are present in type III inclusions, and at least two of these (anhydrite?/molysite? and amarantite?) probably contain Ca^{2+} and Fe^{2+} . To include these elements in the calculation of total salinity by the solution temperature method, phase relations at high temperatures for the $\text{NaCl-KCl-CaCl}_2\text{-FeCl}_2\text{-H}_2\text{O}$ system are needed (Kwak and Tan, 1981b). These data are not available. Therefore, inferred total salinities reported here are probably low because CaCl_2 is more soluble than NaCl or KCl and affects the dissolution behavior of halite and sylvite (Kwak and Tan, 1981b).

Two other methods besides the saturation temperature method may be used to determine total fluid compositions. One utilizes the temperature of first melting in frozen inclusions, and the other is the phase volume method (Kwak and Tan, 1981b). The latter method requires accurate volumetric measurements of the different phases in an inclusion. These measurements can be taken, for example, with a scaled ocular, from photographs on a scanning electron microscope, and (or) by modelling the individual phases of a fluid inclusion in plasticine and weighing the various parts (Kwak and Tan, 1981a). The phase volume method was utilized in part during the present study by measuring most inclusions and phases with a scaled ocular. However, the method could not be applied fully because only two dimensions could be measured. Attempts to freeze type III inclusions were also unsuccessful, and this failure precludes the determination of first melting temperatures. Some inclusions were cooled to -157°C for more than five minutes and still would not freeze. Thus, inferences cannot be made in regard to some of the more soluble chloride salts such as

those of Ca, Fe, Mg, and Zn. Roedder (1976) has reported that gross supercooling of 40° or more below the equilibrium freezing temperature was required to freeze fluid inclusions in samples from Mississippi Valley-type deposits. Furthermore, daughter crystals of halite and other phases did not act as nuclei for the formation of ice (Roedder, 1976). Such problems of metastability and the small amount of liquid in multiphase type III inclusions from Monterrosas apparently inhibited freezing.

The salinities of type I inclusions from the Monterrosas Mine are reported as wt percent NaCl equivalent. However, the temperatures of initial melt formation in these inclusions indicate that salts other than NaCl and KCl are present in the liquids. The temperatures of first melting (recognized by the appearance of liquid between crystals of ice and (or) an increase in translucency of the inclusion) range from about -56° to -20°C. The initial melting, or eutectic, temperature in the NaCl-H₂O system for fluid compositions up to 61.9 wt percent NaCl is -20.8°C (Crawford, 1981). Other water-salt systems have different, but characteristic, eutectic temperatures. For example, the temperatures of initial melting in the NaCl-KCl-H₂O and NaCl-CaCl₂-H₂O systems are -22.9° and -52.0°, respectively (Crawford et al., 1979). Thus, it appears that some of the type I inclusions from the Monterrosas Mine are also mixtures of chloride salts.

Interpretation of the Fluid Inclusion Data

Nearly all type III fluid inclusions from the Monterrosas Mine homogenize by disappearance of the halite daughter crystal after disappearance of the vapor bubble. The data for six sylvite-bearing

inclusions from samples of massive ore are plotted on the ternary NaCl-KCl-H₂O diagram in Figure 23. These points are located at the temperature of halite disappearance on a straight line between the NaCl apex and a point on the halite-sylvite cotectic at the dissolution temperature of sylvite. The data points form linear arrays which project to the NaCl-KCl join, as depicted in Figure 24.

Erwood et al. (1979) have recognized that sylvite-bearing inclusions from the Naica deposit which homogenized by halite dissolution delineated a so-called "halite trend" on a phase diagram for the NaCl-KCl-H₂O system (Figure 24). They have concluded that the halite trend formed by removal of halite from a highly saline and saturated parent solution under pressure-temperature conditions exceeding those of the solubility curve in the NaCl-H₂O system (Wilson et al., 1980; Erwood et al., 1979). Evidence presented in the discussion that follows suggests that type III inclusions at Monterrozas may have formed in a similar manner.

The solubility curve and phase relations for the NaCl-H₂O system at 52 wt percent NaCl are shown on a pressure-temperature diagram in Figure 25. The boundary curves of interest in the following discussion are the three-phase (L + V + H) solubility curve, the halite liquidus (L + H/L), and the liquid plus vapor (L/L + V) boundary curve (Figure 25). Cloke and Kesler (1979) have projected the phase relations in the NaCl-KCl-H₂O system onto the pressure-temperature plane as shown in Figure 26. Contours for L + H/L and L/L + V equilibria at 50 and 60 wt percent combined NaCl and KCl and the solubility curves for the NaCl-KCl-H₂O (solid line) and NaCl-H₂O (dashed line) systems are also represented. Note that substitution of KCl for NaCl causes

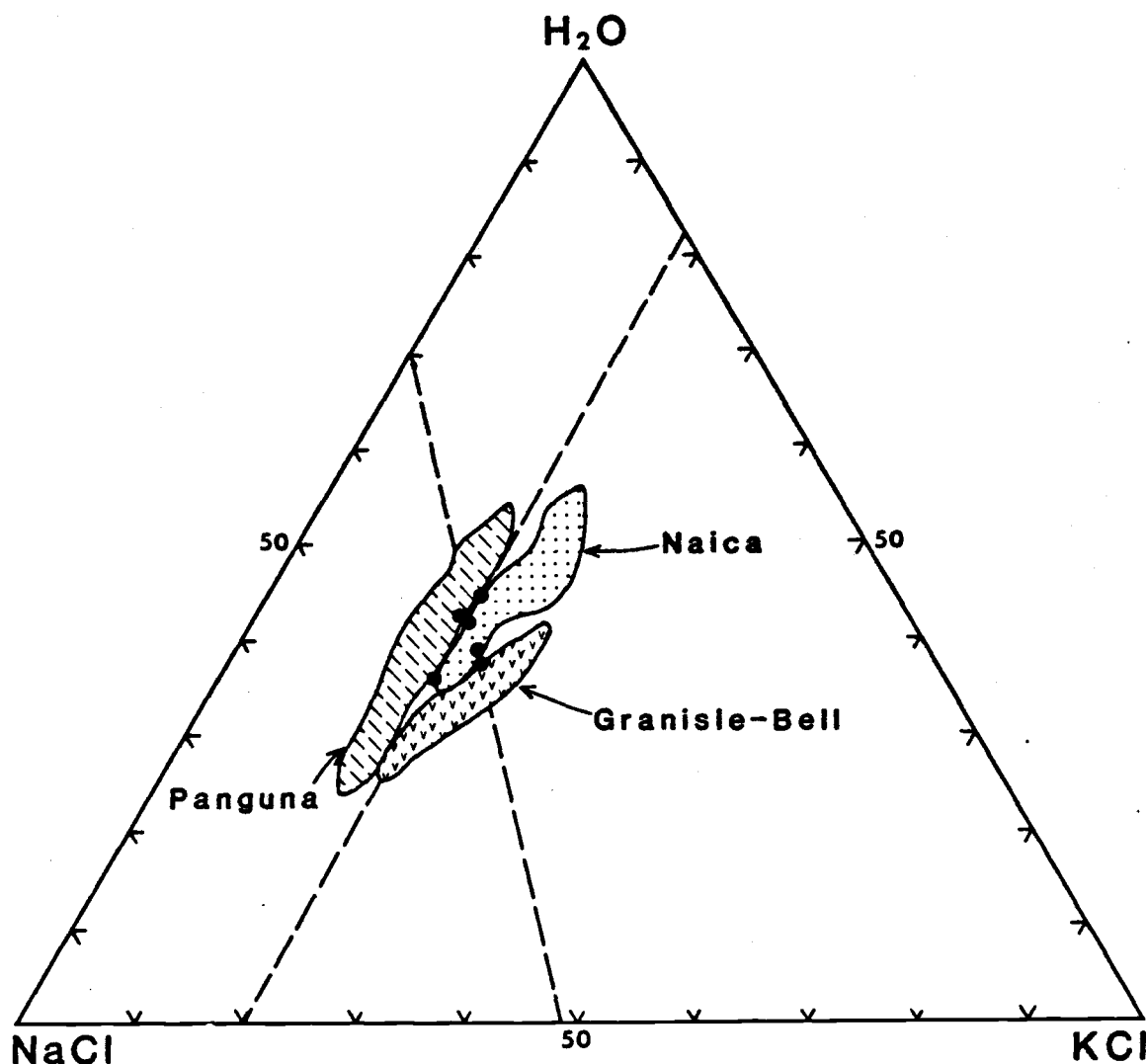


Figure 24. Location of the Halite Trends Observed at the Naica Pb-Zn-Ag, Limestone Replacement Deposit (Erwood et al., 1979), and at the Panguna (Eastoe, 1978, 1982), and Granisle and Bell (Wilson et al., 1980) Porphyry Copper Deposits. Closed circles, data for the Monterrosas Mine (this study). The dashed lines show two possible projections through the data from Monterrosas to the edges of the NaCl-KCl-H₂O system (after Cloke and Kesler, 1979, Figure 1, p. 1824).

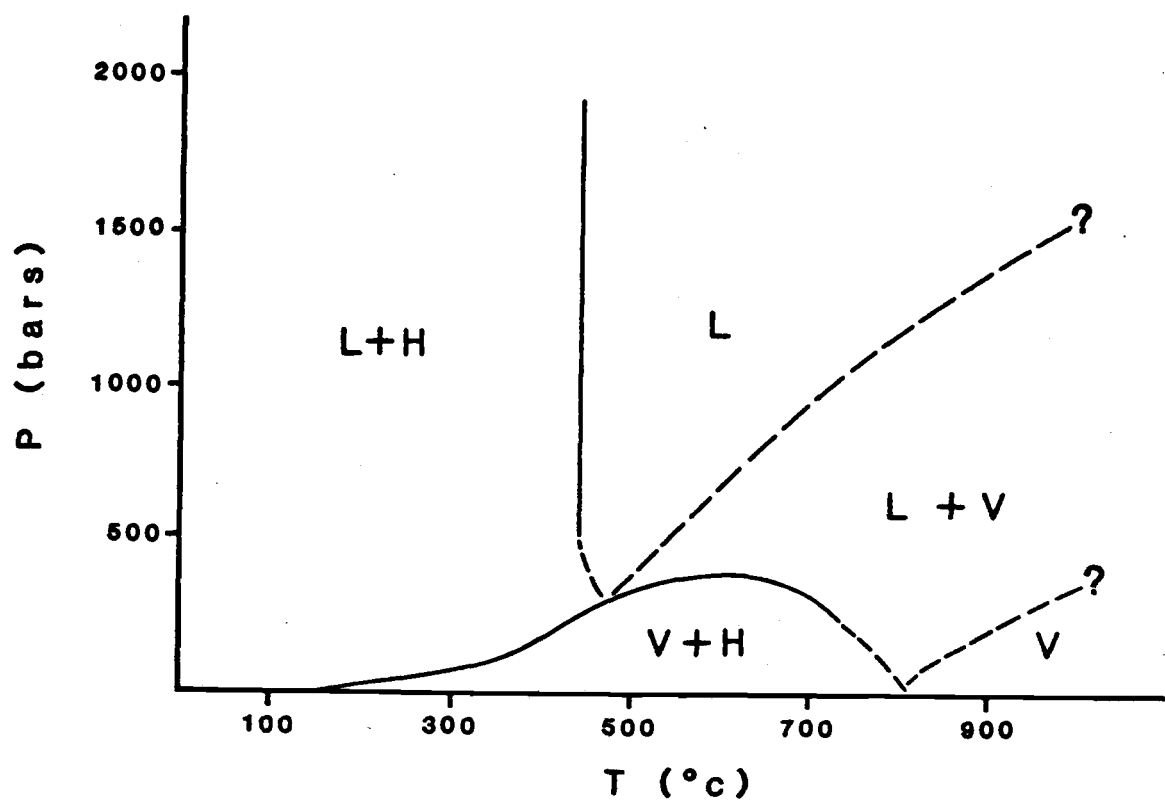


Figure 25. Plane of Constant Composition (isopleth) at 52 Wt Percent NaCl in the NaCl-H₂O System. L, liquid; V, vapor; H, halite (after Gunter et al., 1983, Figure 6a, p. 869).

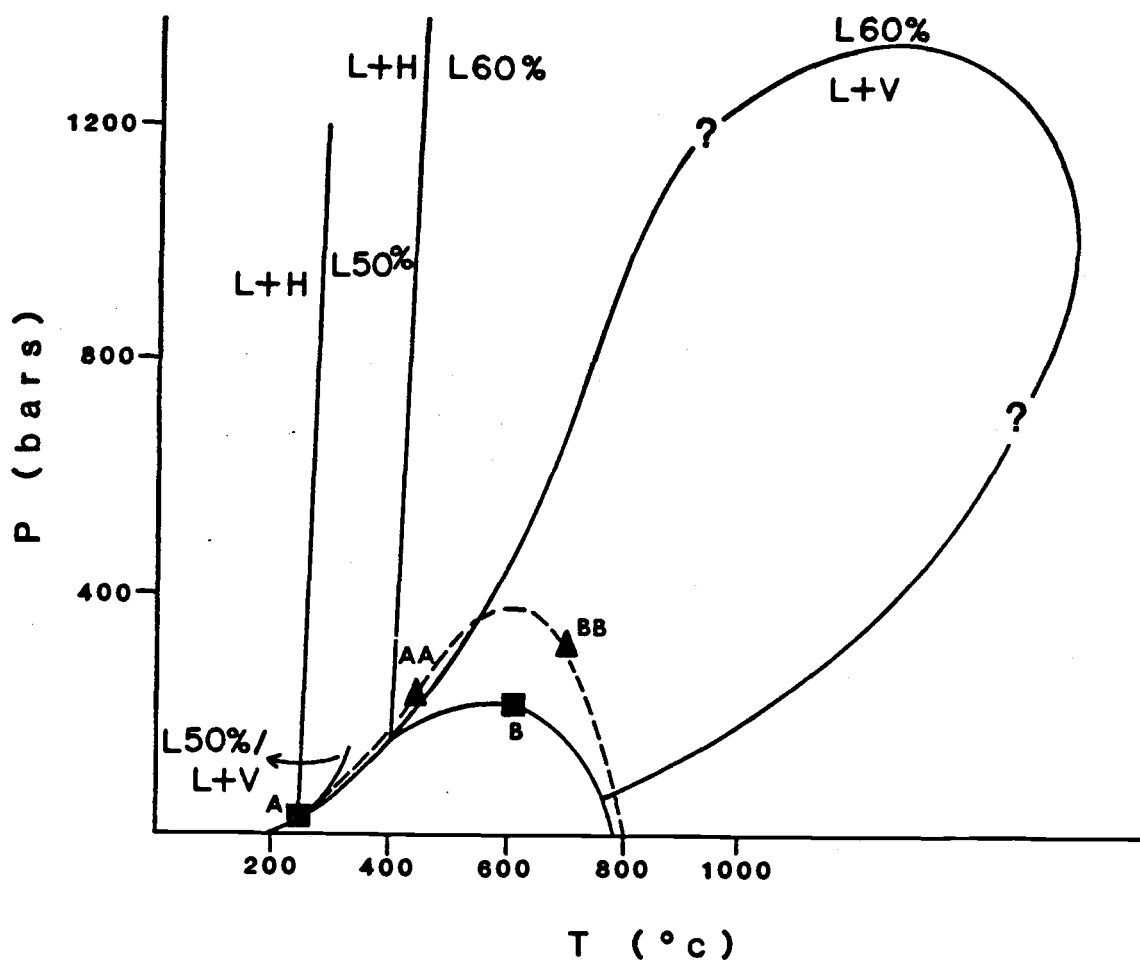


Figure 26. Phase Relations in the NaCl-KCl-H₂O System at 50 and 60 Percent Combined NaCl + KCl (after Cloke and Kesler, 1979, Figure 4, p. 1286). See text for a discussion of points A, AA, B, and BB. Dashed curve, solubility curve in the NaCl-H₂O system.

an appreciable change in the position of the solubility curve. Points A and AA represent total salinities of 50 wt percent in the NaCl-KCl-H₂O and NaCl-H₂O systems, respectively. However, point AA is located at a temperature of about 200° higher than that of A. At higher temperatures and salinities, the temperature difference between the two systems decreases. For example, points B and BB are both plotted at total salinities of 80 wt percent. Cloke and Kesler (1979) have suggested that the addition of CaCl₂ or FeCl₂ would have an undetermined, but possibly similar, effect on the boundaries of the liquid field and points of equal salinity.

Cloke and Kesler (1979) have described four reaction paths that could lead to the halite trend in the NaCl-KCl-H₂O system. The most likely path that might account for homogenization by halite disappearance in the sylvite-bearing type III inclusions at Monterrosas is that of the equilibrium liquid, (EL), which is caused by the equilibrium separation of halite from liquid (Cloke and Kesler, 1979). This path may originate by the crystallization of KCl-bearing halite in the parental hydrothermal fluid prior to entrapment in the inclusions.

The EL reaction path that could lead to the halite trend observed in samples from the Monterrosas Mine is illustrated in Figure 27. A solution of 65 wt percent total salinity (NaCl + KCl) lies at the pressure and temperature of point 1. As this fluid cools isobarically to point 2, or with a simultaneous drop in pressure and temperature to point 4, the solution becomes saturated in NaCl. Further cooling along either path causes the precipitation of halite, and the liquid itself becomes less saline, e.g., 60 percent at points 3 and 5. This

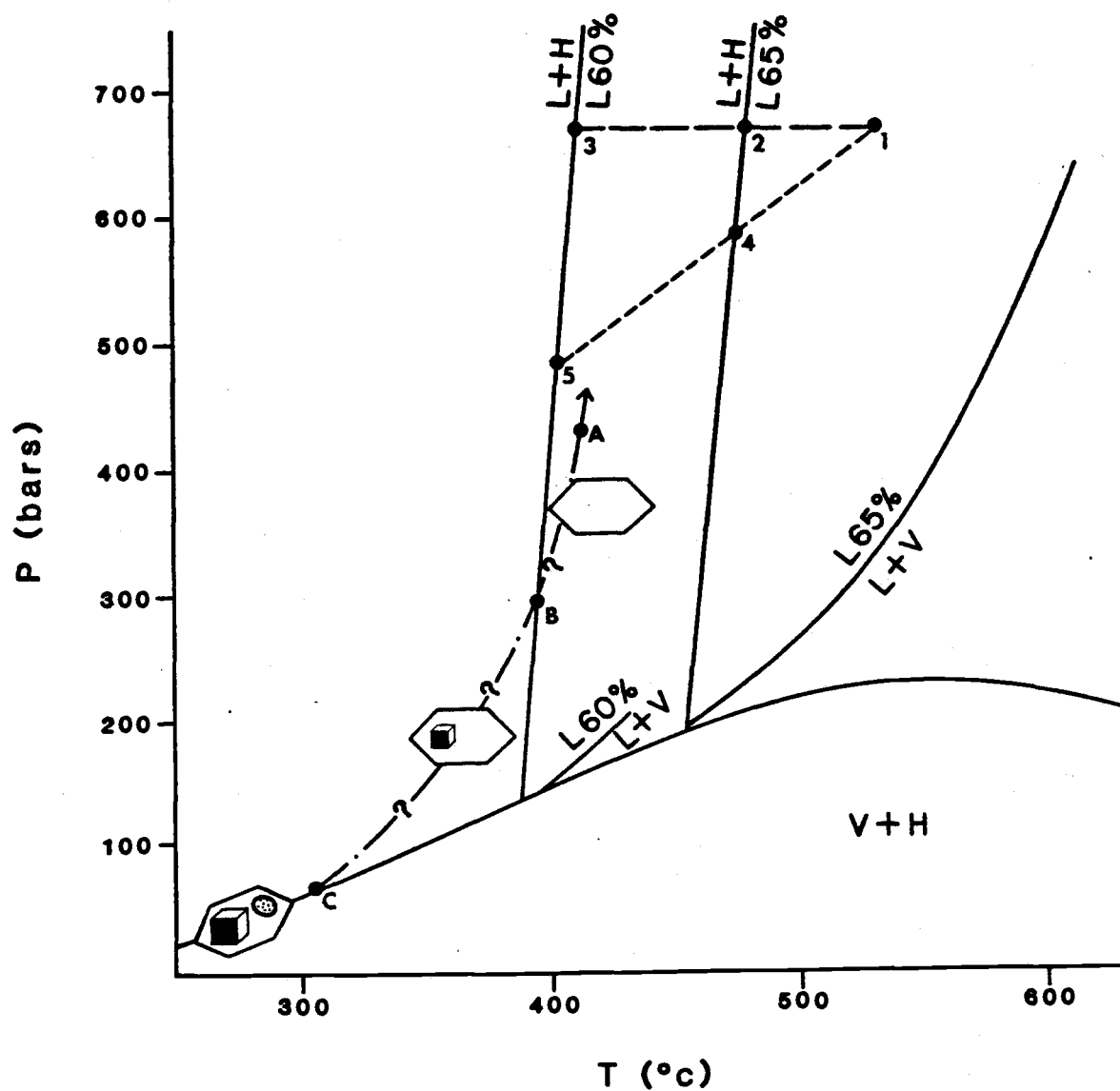


Figure 27. Possible Path Followed by Saline Fluids in Type III Inclusions at the Monterrosas Mine. Phase relations at 60 and 65 percent combined NaCl + KCl are shown. Points 1 to 5 and A to C discussed in text. (Modified after Wilson et al., 1980, Figure 11, p. 56; Cloke and Kesler, 1979, Figure 5, p. 1827; and Weisbrod et al., 1976, Figure 1, p. 143.)

decrease in fluid salinity results entirely from the precipitation of halite containing some KCl in solid solution, but without precipitation of sylvite. If some of this liquid migrates upward adiabatically with a concomitant decrease in pressure and then is trapped as a fluid inclusion, it would cool along a line of constant density, or molar volume, known as an isochore (Hollister, 1981). Liquids follow isochores as they cool in a closed system because contraction of the host quartz mineral is small as compared to that of the liquid (Erwood et al., 1979). Isochores in the liquid region of the NaCl-H₂O and NaCl-KCl-H₂O systems have a shallower slope than the L + H/L halite liquidus (Cloke and Kesler, 1979). For example, a solution with a salinity of about 60 percent NaCl + KCl that is trapped at point A (Figure 27) follows an isochore as it cools to point B. At point B, halite begins to precipitate from the liquid. Eventually, the liquid reaches the solubility curve at the conditions of pressure and temperature represented by point C. Vapor begins to separate from the liquid at point C, and the liquid follows the solubility curve to lower temperatures (Erwood et al., 1979). Sylvite precipitates from the liquid upon reaching the sylvite liquidus at temperatures less than about 200°C. The reaction path for type III inclusions at Monterrozas that do not contain sylvite is similar to that outlined above, because phase relations in the NaCl-H₂O system are very similar to those in the system NaCl-KCl-H₂O (e.g., Figure 25).

Erwood et al. (1979) have noted that homogenization by the dissolution of halite is rare because only those solutions trapped on or close to the halite liquidus can give rise to inclusions that intersect the L + H/L curve before intersecting the liquid plus vapor boundary

curve or the solubility curve as they cool. Liquids that reach the L/L + V curve or the solubility curve instead of the halite liquidus, would homogenize by vapor disappearance or by simultaneous disappearance of vapor and halite, respectively, according to Cloke and Kesler (1979). They concluded that systems in which a halite trend consists entirely of liquid-rich inclusions that homogenize by halite dissolution must result from an EL reaction path such as 1-2-3 or 1-4-5 shown in Figure 27.

Direct geologic evidence that solutions were saturated with NaCl prior to entrapment in inclusions which homogenize by the dissolution of halite is scant. Wilson et al. (1980) have suggested that halite xenocrysts in the inclusions, minute, solitary halite xenocrysts in the host mineral, or halite crystals or casts in the ore assemblage would constitute direct evidence. However, none of these features have been observed at Granisle-Bell, Panguna, or King Island (Wilson et al., 1980; Eastoe, 1978; Kwak and Tan, 1981b). Neither the inclusions, the host quartz crystals, nor the ore assemblage at the Monterrosas Mine provide direct evidence that the solutions were saturated before entrapment. Wilson et al. (1980) have concluded that the linear halite trend at Granisle-Bell shown on the NaCl-KCl-H₂O ternary diagram (Figure 24) was strong indirect evidence that the solutions were saturated with NaCl before the inclusions were formed.

Kwak and Tan (1981b) have reported that CaCl₂ has an important effect on compositional trends in fluids from the King Island (Dolphin) skarn deposit of scheelite in Tasmania, Australia. They determined total fluid compositions by using the phase volume and first melting methods in addition to the saturation temperature

method. Inclusions at King Island that contain halite, sylvite, and $\text{CaCl}_2 \cdot 6\text{H}_2\text{O}$ at 25°C have a $\text{NaCl}:\text{KCl}:\text{CaCl}_2$ wt percent ratio of 0.6:3.2:44.8 (Kwak and Tan, 1981a; 1981b). Nearly all CaCl_2 is present in the liquid phase whereas most NaCl and KCl is present in the daughter minerals. Liquid compositions (assuming that CaCl_2 is not present) plotted on the $\text{NaCl}-\text{KCl}-\text{H}_2\text{O}$ ternary diagram define a linear trend similar to those from the Naica, Granisle-Bell, Panguna, and Monterrosas deposits (Figure 24). However, if CaCl_2 is accounted for in the liquid phase, then the entire field of data points is shifted dramatically towards the H_2O apex. A best fit line through the data intersects the $\text{KCl}-\text{H}_2\text{O}$ join at 3 wt percent, versus 14 wt percent KCl when CaCl_2 is not considered. Inasmuch as a linear trend is still evident, the range of $\text{NaCl}:\text{KCl}$ ratios in halite daughter crystals is not shifted significantly. Kwak and Tan (1981b) have interpreted the apparent "halite trend" of the King Island deposit to result from dilution of saline magmatic fluids by meteoric waters, perhaps with some boiling, and reactions that formed iron calc-silicate minerals such as hedenbergite and andradite and caused the solution of CaCO_3 to produce CaCl_2 . This conclusion is contrary to the observation by Cloke and Kesler (1979) that inclusions which fall on the halite trend are not diluted. Because the halite trends at Naica, Granisle-Bell, Panguna, and Monterrosas do not converge on the H_2O apex (Figure 24), they do not provide direct evidence of mixing between magmatic and meteoric waters or boiling of a hydrothermal solution (Cloke and Kesler, 1979). Although the presence of Ca^{2+} may be inferred from tentative identifications of daughter minerals, the actual effect of CaCl_2 on the "halite trend" at Monterrosas cannot be

evaluated directly. Nonetheless, the lack of boiling and the contribution of magmatic fluids may be evaluated from the fluid inclusion data.

The best evidence that boiling may have occurred in a fluid is the presence of vapor-rich inclusions among liquid-rich fluid inclusions (Roedder, 1981). Inclusions that trap a boiling fluid represent conditions of pressure and temperature along the liquid plus vapor boundary curve. Vapor-rich inclusions contain a large bubble (generally > 60 volume percent) with proportionately less liquid at room temperature, and they homogenize in the vapor phase by disappearance of the liquid. Liquid-rich inclusions consist of liquid with a small vapor bubble that occupies 10 to 40 percent of the volume (Nash, 1976). Characteristic of a system that has boiled, the liquid-rich inclusions homogenize into the liquid phase at the same temperature as that at which the gaseous inclusions homogenize (Roedder and Bodnar, 1980).

Gas-rich type II inclusions at the Monterrosas Mine are rare. Although the homogenization temperatures of type II inclusions were not measured, it was observed that they homogenized at temperatures both much higher and lower than those of either type I or type III inclusions. Roedder (1979) has noted that variable gas/liquid ratios may be caused by mechanisms other than boiling such as necking down, leakage, or entrapment of fluids at different times under different conditions of temperature and pressure. Most of the type II inclusions at Monterrosas appear to have resulted from necking and therefore the evidence suggests that boiling did not occur extensively.

All inclusions, except those trapped from boiling fluids, require a

temperature (also known as the pressure) correction to obtain the true temperature of entrapment (Roedder and Bodnar, 1980; Theodore and Blake, 1978). The pressure correction for nonboiling fluids is necessary because the total pressure at the time and temperature of entrapment exceeded the vapor pressure of the solution. The magnitude of this pressure correction cannot be estimated directly because the inclusion may have been trapped along its isochore at any pressure and temperature greater than that of homogenization (Erwood et al., 1979). Nonetheless, Lemmlein and Klevtsov (1961) and Potter (1977) have demonstrated experimentally that the pressure correction diminishes from about 20° at temperatures of homogenization near 350° to less than 5° at 400°C and higher, and at a total pressure of about 300 bars. Therefore, homogenization data for type III inclusions at the Monterrosas Mine have not been corrected for pressure. Corrections for a pressure of 250 bars and the range of salinities measured in type I inclusions at Monterrosas are about $35^{\circ} \pm 10^{\circ}\text{C}$ (from Potter, 1977). Estimated pressures for type I inclusions (discussed below) are lower than 250 bars, and the pressure correction is probably even less than 35° based on the investigations of Potter (1977) and Lemmlein and Klevtsov (1961). Thus, the temperatures of homogenization for type I inclusions have not been corrected in Table 11.

Inclusions that homogenize by the simultaneous disappearance of vapor and halite provide the closest approximation of the actual pressure at the time of entrapment (Wilson et al., 1980). Because the precision of heating runs during this study was $\pm 7^{\circ}$, inclusions are considered to have homogenized by simultaneous disappearance of vapor and halite if their disappearance temperatures differ by less than 14°.

Only two inclusions from the Monterrosas Mine fall into this category, and both are type III inclusions in which the vapor bubble disappeared after total halite dissolution (12-2-22B2-1C and 12-8-13E1A, Table 11). Estimates of pressure for these two inclusions are 28 and 12 bars, respectively.

Halite-bearing inclusions provide only a minimum estimate of pressure at the temperature of vapor disappearance along the three-phase solubility curve (Wilson et al., 1980). Minimum pressures that may be estimated from the temperature of vapor disappearance for type III inclusions at the Monterrosas Mine range from about 10 to 80 bars. These pressures are lower than those that may be estimated from the temperature of halite dissolution. For example, temperatures of halite dissolution projected onto the solubility curve in the systems NaCl-KCl-H₂O and NaCl-H₂O indicate that pressure approached 200 and 350 bars, respectively (Figure 26). However, slopes of isochores in the liquid plus halite field are not known (Wilson et al., 1980), and estimates of pressure above the solubility curve may only be approximated from an assumed isochore.

Roedder and Bodnar (1980) have determined the pressures for some inclusions that homogenize by halite dissolution. Their calculation utilizes data for the host quartz crystal, and data from the NaCl-H₂O system for the vapor bubble, halite daughter mineral, and density of the fluid, and includes measurements of temperature, volume, composition, and solubilities. They have computed a pressure of about 650 bars for inclusions in which the vapor bubble disappeared at 310° and halite dissolved at 400°C (Roedder and Bodnar, 1980). Additional ions in solution such as K⁺ and Ca²⁺ might significantly lower this

minimum pressure. Although the accuracy of their calculations awaits experimental volumetric data along the halite liquidus in the NaCl-H₂O system at high temperatures and pressures, it remains the best method to estimate pressure above the solubility curve. The conditions of formation for several inclusions from the Monterrosas Mine may be inferred by this same calculation (e.g., samples 3-18-70A and 5-18-70BB, Table 11). Although pressures of 650 bars are considerably above other estimates of minimum pressure from inclusions at the Monterrosas Mine, if K⁺ and Ca²⁺ are considered in the calculations, then resultant pressures would be lower. Nonetheless, if entrapment of type III inclusions at Monterrosas followed a path such as that outlined in Figure 27, then it must be realized that the isothermal change of pressure did not cause boiling. Hence, this change in pressure probably did not take place at shallow depths because a condensed fluid is much more likely to boil as a consequence of decreasing pressure at shallow depths (Cunningham, 1978). The minimum load in a lithostatic system that could generate 600 bars pressure would be about 1.8 km. In an entirely hydrostatic system, a pressure of 600 bars corresponds to a depth of about 6 km. The type III inclusions at Monterrosas were most likely trapped at intermediate depths and pressures that were associated with both hydrostatic and lithostatic conditions (see Roedder and Bodnar, 1980, Figure 1 for the range of possible pressure conditions).

Kelly and Rye (1979) have noted that fluid pressures in areas of active faults and fractures may fluctuate widely between hydrostatic and lithostatic values at a constant depth. Therefore, the minimum estimate of the maximum total pressure, and its corresponding depth in

a hydrostatic system, is the most reliable estimate of depth for fluid inclusions. However, the maximum pressure in type III inclusions that homogenize by the dissolution of halite cannot be constrained along an isochore above the solubility curve. In such cases, the only depth that may be approximated is the maximum (or hydrostatic) equivalent at the lowest estimate of minimum pressure (Kelly and Rye, 1979). Type III inclusions in samples from the Monterrosas Mine that homogenize by the disappearance of halite formed at a minimum pressure of about 200 bars (in the system $\text{NaCl-KCl-H}_2\text{O}$) and a depth of about 2 km.

Minimum pressures for type I inclusions in samples from Monterrosas may be estimated from the phase diagram of the unsaturated system $\text{NaCl-H}_2\text{O}$ (see Roedder and Bodnar, 1980, Figure 4, or Crawford, 1981, Figure 4.12) or from the data of Haas (1971; 1976). The minima are present along the two-phase, liquid-plus-vapor curve. The range of pressures estimated for type I inclusions at Monterrosas varies from about 20 to less than 2 bars. However, because these inclusions do not provide evidence of boiling, and they appear to have trapped a homogeneous, one-phase fluid, it might be presumed that the pressure at the time and temperature of entrapment was greater than the vapor pressure of the solution (Roedder and Bodnar, 1980). The amount above the vapor pressure is not constrained by these inclusions. Entrapment may have taken place at higher pressures and temperatures along an isochore of appropriate salinity (Bodnar and Bethke, 1984). The maximum depth at which type I inclusions may have formed corresponds to an average pressure of 7 bars, which represents a hydrostatic pressure equivalent to about 60 m below the local water table at the time of formation (Haas, 1971; 1976).

ORE GENESIS

Fluid inclusions and the assemblages of ore and alteration minerals in the Monterrosas deposit indicate that mineralization formed at relatively high temperatures from saline fluids exsolved directly from a magma. Progressive crystallization of plagioclase feldspar and clinopyroxene from gabbro-diorite magma resulted in the concentration of iron, volatiles, and other ore-forming constituents in residual liquids. Saline fluids probably separated from this interstitial magma at temperatures greater than 800°C before the gabbro-diorites were solidified completely. The chloride content of the fluids was a critical factor in the concentration, transportation, and precipitation of iron, copper, and other metals. These fluids migrated upward along faults and fractures and reacted with gabbro-dioritic wall rocks. Decreases in the temperature and (or) acidity of the fluids led to deposition of ore and alteration minerals. This model for mineralization at Monterrosas is similar to that for some skarn-type deposits of iron.

Conditions and Processes of Mineralization

The presence of abundant sodic scapolite and the salinities and temperatures of homogenization recorded for type III fluid inclusions in altered wall rocks and ore from the Monterrosas deposit document the presence and circulation of a high temperature saline fluid within the gabbro-diorites. Investigators such as Vanko and Bishop (1980, 1982), Kotel'nikov (1978), and Newton and Goldsmith (1976) have confirmed that marialitic scapolite is stable in saline fluids at high

temperatures. For example, Vanko and Bishop (1980, 1982) have synthesized marialite of about Me 20 at temperatures of 700° to 750°C and pressures of about 1.5 to 3.0 kb from fluids that have a salinity of about 75 wt percent NaCl and only traces of CaCO₃. Although temperatures and salinities of this magnitude have not been measured in fluid inclusions from the Monterrosas deposit, the presence of the halite trend (as discussed previously) suggests that KCl-bearing halite was precipitated from a highly saline fluid prior to entrapment of the liquid in the inclusions. Instead, the incorporation of NaCl and some KCl into marialite-dipyre by reaction between labradorite-andesine of the gabbro-dioritic wall rocks and saline fluids might have decreased the salinity of the fluids prior to entrapment. Thus, the formation of sodic scapolite may account for the EL path (paths 1-2-3 or 1-4-5 in Figure 27) of the halite trend as identified from homogenization by halite dissolution in type III inclusions. Furthermore, similarities in composition between vein and replacement scapolite (Me 25 to 27, and Me 22 to 32, respectively) might imply that the fluids maintained their high temperatures and salinities over a prolonged period of time, and (or) that scapolitization resulted from a single episode of alteration.

The highly saline fluids at Monterrosas may have been produced throughout, and especially during the later stages of, crystallization in the gabbro-diorite magma. For example, Kilinc and Burnham (1972) have demonstrated that the amount of chlorine partitioned into the aqueous phase of a magma with a low initial content of water and crystallizing at low pressures (as postulated for the gabbro-diorite magma) increases as solidification proceeds. Moreover, the fluids

derived from such magmas separate over a longer period of time and are more saline during the final stages of consolidation than those exsolved from melts that have higher concentrations of water (Cloke and Kesler, 1979).

Burnham (1979) has suggested that copper and other chalcophile metals are concentrated in aqueous chloride solutions in preference to coexisting silicate melts. Transport of copper in these saline brines may be accomplished by complexes of one or more chloride species. For example, CuCl and its polymers, NaCuCl_2 or NaCu_2Cl_3 , are stable complexes at temperatures greater than 700°C (Eastoe, 1982).

Iron, as well as sodium, potassium, and volatile components, is also partitioned into the aqueous phase at magmatic temperatures and low pressures (Burnham, 1979; Holland, 1972). The partition coefficient for iron (the ratio of iron in the aqueous phase vs. that in the magma) increases as temperature or pressure decreases (Burnham, 1979). Chloride complexes such as FeCl^+ , FeCl_2 , FeCl_3 , their dimers NaFeCl_3 and NaFeCl_4 , or hydroxide complexes such as $\text{Fe}_2(\text{OH})_5^+$ and $\text{Fe}_2(\text{OH})_6^0$ are species that might transport iron at temperatures greater than 350°C (Eastoe, 1982; Wang et al., 1984; Helz, 1972). Inter-growths of chlorine-bearing apatite with magnetite in the Monterrozas ore and with scapolite in altered gabbro-dioritic host rocks suggest that phosphorous, probably as phosphate (PO_4^{-3}) complexes, might also have been important in the transport of iron. Chou and Eugster (1977) have measured the solubility of magnetite in chloride solutions at pressures of 2 kb and temperatures between 500° and 650°C . The major solute species under these conditions is FeCl_2 , and the dissolution of magnetite may be represented by the equation:



and

$$K_{14} = (a_{\text{FeCl}_2})^3 \cdot (a_{\text{H}_2\text{O}})^4 / (a_{\text{HCl}})^6 \cdot a_{\text{H}_2}. \quad (15)$$

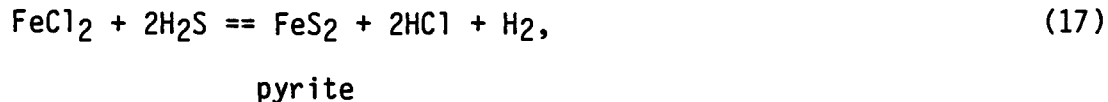
If it is assumed that the activity of H_2O is near unity and that the activity coefficient ratio $\gamma_{\text{FeCl}_2}/(\gamma_{\text{HCl}})^2$ is also near unity, and using the standard states of pure gas at 1 bar and T for hydrogen and of a one molal solution at P and T for FeCl_2 and HCl , then K_{14} simplifies to $K_{14} = (m_{\text{FeCl}_2})^3 / (m_{\text{HCl}})^6 \cdot f_{\text{H}_2}$. Chou and Eugster (1977) have determined that K_{14} may be expressed by the equation:

$$(\log K_{14})_{2 \text{ kb}}, T \text{ } ^\circ\text{K} = 29410.6/T - 25.90. \quad (16)$$

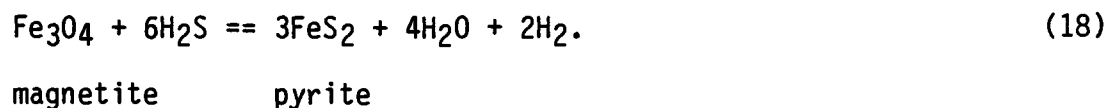
The solution to equation 16 indicates that the solubility of magnetite increases as the temperature decreases from 650° to 500°C . However, assumptions that the activity coefficient quotient is near unity and that undissociated chloride molecules are dominant in the fluids are not valid below temperatures of about 550°C , and species other than FeCl_2 may become important at lower temperatures (Eugster and Chou, 1979; Chou and Eugster, 1977).

Different generations of magnetite deposition at the Monterosas Mine may possibly reflect decreases in the stability of chloride complexes and the increased stability of other iron complexes such as hydroxy species at temperatures less than 500°C . For example, Seward (1977) has suggested that hydroxy complexes are important for the transport of iron in solutions with low concentrations of chloride, and Helz (1972) has proposed that $\text{Fe}_2(\text{OH})_5^+$ is the dominant species in acidic solutions and that $\text{Fe}_2(\text{OH})_6^0$ predominates in basic to neutral solutions at temperatures over about 350°C .

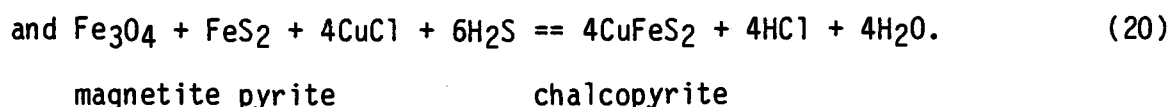
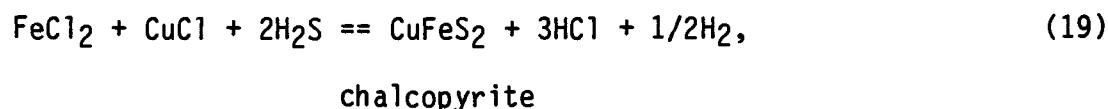
Deposition of ore and alteration minerals may have resulted from decreases of temperature and (or) acidity in the fluids as they migrated upwards and reacted with gabbro-dioritic wall rocks. Reactions such as the replacement of andesine by marialite-dipyre (reaction 3) and the formation of actinolite from diopside (reaction 6) and andesine (reaction 8) consume H^+ from the fluids and therefore increase pH. Moreover, deposition of marialite-dipyre consumes Cl^- , and formation of actinolite requires iron. Thus, decreases in temperature, a_{FeCl_2} , and possibly a_{H^+} may have initially promoted the deposition of magnetite at Monterrosas. Subsequent precipitation of sulfides may have ensued because of a relative increase of a_{H_2S} and continued decrease of a_{FeCl_2} in the fluids as iron oxide was deposited. Pyrite may have formed directly from the fluids by the reaction:



or by reaction with magnetite:



The deposition of some chalcopyrite presumably took place by analagous reactions such as:



The amount of HCl produced as a consequence of sulfide deposition may have exceeded that originally present in the aqueous phase (Burnham, 1979). Subsequent hydrogen metasomatism that accompanied dissociation of HCl with decreasing temperature may account for the extensive sericitization of gabbro-dioritic wall rocks.

Phase relations in the Cu-Fe-S system may be used to characterize the conditions of formation for the assemblage of chalcopyrite, pyrite, cubanite, and pyrrhotite. For example, three principal solid solution series dominate this system at temperatures greater than 600°C (Barton and Skinner, 1979). They are: (1) intermediate solid solution (iss); (2) pyrrhotite; and (3) chalcocite-digenite-bornite, as shown in Figure 28 after Cabri (1973, Figure 3, p. 446). Some chalcopyrite±cubanite±pyrrhotite blebs in pyrite most likely formed as decomposition products of iss+pyrite deposited from saline fluids at temperatures near 600°C. Chalcopyrite solid solution becomes a stable phase in the iss+pyrite field (Figure 28) and coexists with cubic iss of CuFe_2S_3 composition upon cooling below 557°C (Barton, 1973). The field of chalcopyrite solid solution is reduced to stoichiometric CuFeS_2 at lower temperatures, and the iss undergoes a complex series of inversions, ordering of Cu-Fe, and exsolution between 500° and 200°C (Craig and Scott, 1974). The cubic iss transforms to orthorhombic cubanite between 210° and 200°C, and the species talnakhite ($\text{Cu}_9\text{Fe}_8\text{S}_{16}$), mooihoekite ($\text{Cu}_9\text{Fe}_9\text{S}_{16}$), and haycockite ($\text{Cu}_4\text{Fe}_5\text{S}_8$) become stable at lower temperatures (Cabri, 1973). Although none of the latter three phases have been identified in samples of Monterrozas ore, a few microprobe analyses of the Cu-Fe sulfides exhibit low totals (about 96 wt percent) and may be indicative of one or more of these minerals.

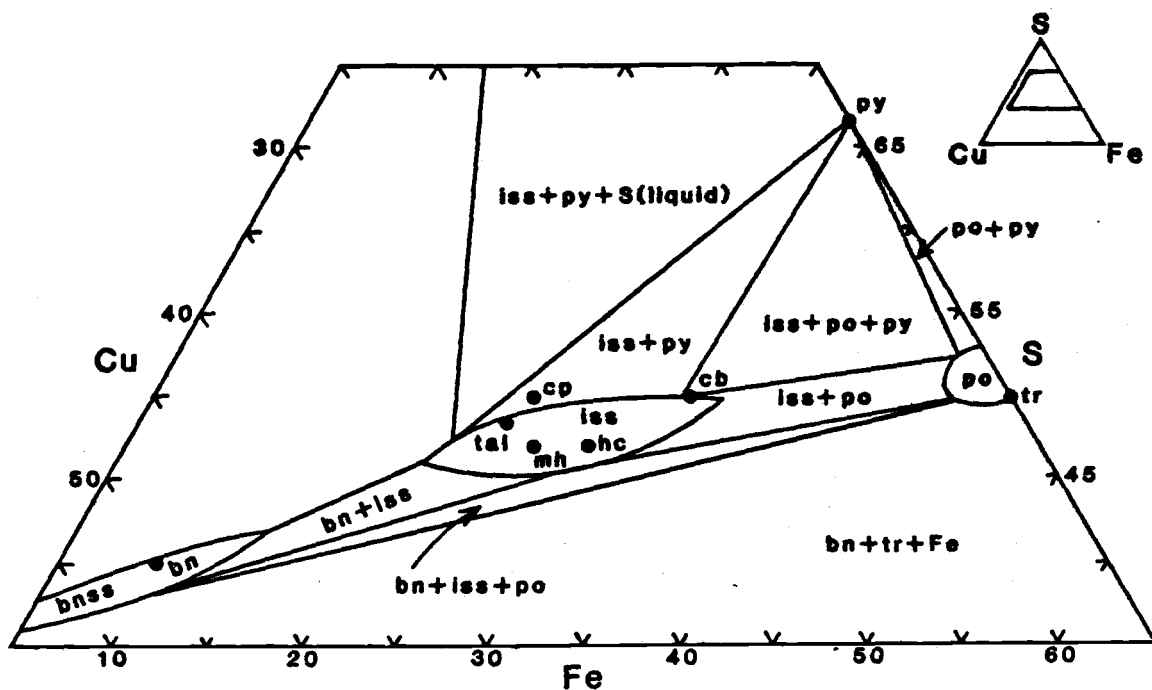


Figure 28. Some Phase Relations in the Central Portion of the Cu-Fe-S System at 600°C (after Cabri, 1973, Figure 3, p. 446). Closed circles represent the stoichiometric compositions for the minerals pyrite (py), troilite (tr), cubanite (cb), chalcocite (cp), talnakhite (tal), mooihoekite (mh); haycockite (hc), and bornite (bn). Copper, iron, and sulfur in atomic percent. Field of chalcocite-digenite-bornite represented as bn ss.

Most pyrrhotite in ore from the Monterrosas Mine area probably formed by reequilibration within the Cu-Fe-S system at temperatures of less than 350°C. Microprobe analyses indicate that the pyrrhotite contains less than about 0.5 wt percent copper (Appendix 10). Yund and Kullerud (1966) have determined that the field of pyrrhotite solid solution in the system Cu-Fe-S contains a maximum of 4.5 wt percent copper at 700°C and retreats to the binary Fe-S join at lower temperatures. Pyrrhotite solid solution extends along the Fe-S join with less than 0.6 wt percent copper at temperatures less than 350°C (Sugaki et al., 1975). Thus, the compositions of pyrrhotite determined from microprobe analyses of ore samples probably do not reflect the initial composition or conditions of formation, such as f_{S_2} and temperature, of this mineral.

The isotopic composition of sulfur in pyrite and chalcopyrite from the ore zone at the Monterrosas deposit confirms that these minerals formed at temperatures of about 500°C and supports a magmatic source of the fluids. Ohmoto and Rye (1979) have summarized equations for the temperature dependency of sulfur isotope fractionation between various pairs of coexisting sulfide minerals, and these provide a potentially useful isotopic geothermometer. For example, the temperature for a pyrite-chalcopyrite pair formed in equilibrium may be calculated from the equation provided by Ohmoto and Rye (1979, Table 10-2, p. 518):

$$T_{OK} = 0.67 \pm 0.04 \times 10^3 / \Delta^{1/2}, \text{ where } \Delta = \delta^{34}S_{py} - \delta^{34}S_{cp}. \quad (21)$$

One such pyrite-chalcopyrite pair, sample 5-18-70 listed in Table 12, yields a delta (Δ) value of 0.7, which gives a depositional temperature of about $525^\circ \pm 48^\circ\text{C}$ as determined from equation 21. According

Table 12. Sulfur Isotope Data for Sulfides of the
Monterrosas Deposit (in permil)

Sample	Mineral	Rock Type	$\delta^{34}\text{S}$
5-18-70P	Py*	Massive ore	2.5
K-3P	Py	Massive pyrite	2.9
DDH-13-20	Py	Massive ore	2.7
Shaft	Py	Massive pyrite	2.4
6-32-3P	Py	Coarse pyrite in gabbro-diorite wall rocks	1.6
5-18-70***	Py	Massive ore	2.9
5-18-70***	Cp**	Massive ore	2.2
5-18-70C	Cp	Massive ore	2.5
X-7C	Cp	Massive ore	3.3

* Py = Pyrite

** Cp = Chalcopyrite

*** $\Delta_{\text{py-cp}5-18-70} = 2.9 - 2.2 = 0.7$

Samples separated by G. B. Sidder. Analyses by C. W. Field and R. Fifarek at USGS, Branch of Isotope Geochemistry, Denver, Colorado.

to Ohmoto and Rye (1979), average $\delta^{34}\text{S}$ compositions of about 2.7 permil in both pyrite and chalcopyrite and the range of values from 1.6 to 3.3 permil are consistent with a magmatic source of the fluids. Moreover, the isotopic compositions of sulfur for pyrite and chalcopyrite at Monterrosas are similar to those recorded for sulfide deposits in magnetite-series plutonic suites of the Japanese island arc (Czamanske et al., 1981) and for gabbroids in magnetite-series granitic terranes (Sasaki and Ishihara, 1979).

The expulsion of volatiles in an aqueous phase accompanied with diffusive loss of hydrogen (as H_2 gas from a crystallizing magma) leads to more highly oxidizing conditions in both the magma and the later magmatic fluids. The fugacity of oxygen increases because of a decrease in f_{H_2} in response to the equilibrium relation: $\text{H}_2\text{O} == \text{H}_2 + 1/2\text{O}_2$. The secondary oxide assemblage of magnetite, sphene, and other minerals in gabbro-dioritic wall rocks provides evidence of a high f_{O_2} during the alteration stage. For example, ferropseudobrookite solid solution enriched in FeTi_2O_5 component, as noted previously in the alteration section, may signify rapid oxidation of ilmenite in the gabbro-diorites at high temperatures (Haggerty, 1976a, 1976b). Manganese enrichment in ilmenite (up to 24 wt % MnO) also suggests that oxidizing conditions prevailed in the gabbro-diorites during reaction with fluids (Czamanske and Mihalik, 1972). The formation of mangano-ilmenite results from the oxidation of Fe^{2+} more readily than Mn^{2+} in ilmenite. Abundant sphene and an increased proportion of magnetite in the late magmatic and secondary oxide assemblage are further indications of increased oxygen fugacities during late magmatic crystallization and deuteric alteration (Czamanske and Mihalik, 1972).

The compositional variability of ilmenites and amphiboles may reflect conditions of progressively increasing oxidation during late magmatic crystallization and deuteric alteration. For example, the average concentration of MnO in ilmenite of the least altered sample of gabbro-diorite (6-8-13, A. I. = 0.00) is 1.67 ± 0.28 wt percent. In contrast, concentrations of MnO average 3.04 ± 0.33 wt percent and 16.89 ± 4.69 wt percent in lightly altered (12-2-22, A. I. = 15.63) and intensely altered (D-1, A. I. = 59.78) samples of gabbro-diorite, respectively. This trend of increasing MnO concentrations with progressive alteration of ilmenite may correlate with increasing oxidation which results in higher residual $\text{Mn}^{2+}/\text{Fe}^{2+}$ ratios as a consequence of reactions with the fluids. Alternatively, manganese may have been added to the wall rocks by reaction with the fluids. However, the sum of alteration reactions (equation 13 and Table 9) and microprobe analyses of sulfides indicate that only traces of Mn were added by the fluids. The atomic Fe/Mg ratio for amphiboles decreases from greater than 0.40 in actinolitic hornblende to about 0.30 in actinolite. This decrease suggests that actinolite formed under higher f_{O_2} which lowers a_{FeO} in the fluids and thus the ferrous iron content in amphibole (Czamanske and Wones, 1973). The lower Fe/Mg ratio in actinolite may also result from the simultaneous formation of other iron-bearing phases such as magnetite, epidote, or sulfides.

Consistent with the high f_{O_2} postulated on the basis of the secondary oxide assemblage is the predominance of epidote over clinozoisite in the alteration suite from the Monterrosas deposit. The presence of epidote and clinozoisite in slightly altered gabbro-diorites and of epidote \pm allanite in the more intensely altered gabbro-diorites indicates

that alteration took place under relatively oxidizing conditions (Holdaway, 1972). Liou (1973) and Holdaway (1972) have demonstrated experimentally that epidote is stable at temperatures up to about 650°C and pressures of 2 kb and at f_{O_2} above the NNO buffer. As f_{O_2} decreases, epidote becomes more aluminous in composition and approaches clinozoisite, and other minerals such as garnet, anorthite, and corundum become stable. The compositions and distributions of epidote and clinozoisite at Monterrosas suggest that f_{O_2} remained relatively high during alteration as temperatures decreased.

Similarities to Other Deposits

Host rock alteration and ore assemblages at the Monterrosas deposit resemble some skarn-type deposits of iron. For example, Einaudi et al. (1981) and Einaudi and Burt (1982) have recognized that calcic iron skarns form typically in oceanic island-arc environments, contain copper, cobalt, and gold as minor metals, are associated with primitive intrusive rocks predominantly dioritic in composition, and are hosted commonly by andesitic volcanic rocks in addition to carbonate and other sedimentary rocks. Textures of the intrusions are medium to finely equigranular, and the formation of extensive endoskarns (alteration of the intrusive rocks) is characteristic of these iron deposits. Magnetite and sulfide deposition, including pyrite and chalcopyrite, was in part contemporaneous with the skarn minerals. Although the concentrations of total alkalies in plutonic rocks associated with calcic iron skarns are similar to that of intrusions in other types of skarns, Meinert (1984) has noted that the Na_2O/K_2O ratios in these plutons are generally greater than 5 and as much as 20 or more. These

ratios are much higher than those (< 1 to about 6) common to intrusive rocks and plutons of other metallic skarns, but they are similar to those of the gabbro-diorites from Monterrosas. Moreover, the low iron content of plutons (1 to 7 wt % FeO_t) associated with calcic iron skarns is inversely proportional to the high concentrations in alteration assemblages of the associated skarns (Meinert, 1984).

Skarn-type deposits which are mined for iron \pm copper are present in numerous countries, including Chile, the United States, China, the Soviet Union, Peru, Japan, and Canada. Although not all of these deposits have been classified as skarns by their respective investigators, most have been interpreted to be late magmatic to hydrothermal replacement deposits. For example, Bookstrom (1975, 1977) has described the magnetite deposits at El Romeral, Chile (Figure 5), which are hosted by andesitic and metasedimentary rocks adjacent to a diorite pluton. Unaltered and altered samples of Romeral diorite are strikingly similar to equivalent gabbro-diorites at Monterrosas. Relatively fresh diorites consist of magmatic plagioclase feldspar (An 26 to An 51), augite, ilmenite, and magnetite, with deuteric actinolitic hornblende, actinolite, and sphene. They contain about 55 wt percent SiO_2 , 4.3 wt percent FeO_t , and 10.5 wt percent CaO , and have $\text{Na}_2\text{O}/\text{K}_2\text{O}$ ratios of about 11 (Bookstrom, 1975). Alteration of these diorites resulted in the formation of secondary minerals such as actinolite, magnetite, sphene, clinozoisite, chlorapatite, tourmaline, pyrite, chalcopryrite, chlorite, and biotite. Bookstrom (1975, 1977) concluded that residual concentration of iron, water, volatiles, and other metals during crystallization of the Romeral dioritic magma led to the separation of saline, metal-enriched aqueous fluids. Reactions

between these fluids and wall rocks along faults and fractures resulted in the deposition of magnetite, actinolite, apatite, and other minerals at temperatures of about 550° to 475°C.

Reeves and Kral (1955) have examined iron ore deposits in the Buena Vista Hills, Nevada, where dioritic and metavolcanic rocks host tabular replacement bodies of magnetite. Fluids within a dioritic stock became enriched in volatiles and metals by residual concentration as crystallization proceeded, and magnetite deposition and intense scapolitization took place in the outer shell of the stock and adjacent country rocks as these fluids escaped along faults and tension fractures (Reeves and Kral, 1955).

Zharikov (1970) and Sokolov and Pavlov (1970) have discussed metasomatic deposits of magnetite and sodic scapolite (Me 8 to 37). Zharikov (1970) has described certain iron deposits in gabbroic rocks that are the products of intense calcium metasomatism. Actinolite, scapolite, epidote, magnetite, apatite, and chlorite are common secondary minerals in the gabbroic host rocks. These magnetite deposits are classified as autoreactional skarns which formed from fluids that evolved within the gabbroic magma and infiltrated and replaced its fractured outer parts. Sokolov and Pavlov (1970) have concluded that chlorine was "an exceedingly active agent" during iron segregation from magmas and its subsequent concentration into postmagmatic solutions.

Chaochun (1981) has reported that the Na-Cl type of iron skarn deposits are the most important in China. Marialitic scapolite is well developed in these deposits, and the intensity of scapolitization is directly proportional to that of iron mineralization. These deposits are interpreted to be magmatic-hydrothermal in origin on the basis of

the isotopic compositions of sulfur (-1.36 to +2.90 ‰) as well as the high concentrations of associated elements such as cobalt (to 0.5 wt %) and nickel (to 1 wt %).

Ruiz and Ericksen (1962) and Ruiz et al. (1965) have described deposits of chalcopyrite-magnetite-actinolite in Chile such as Carrizal Alto (Figure 5) that bear a genetic similarity to contact metasomatic deposits of iron such as El Romeral. These copper-iron deposits are mostly tabular replacements along fractures within gabbros and diorites, and they contain both massive and finely disseminated chalcopyrite, pyrite, and magnetite. Ore tonnages are commonly small (about 3 million tons), but high grade (to 5% copper), and minor amounts of cobaltiferous pyrite and (or) arsenopyrite (known as loellingite), molybdenite, and uraninite may also be associated. Ruiz and Ericksen (1962) considered these deposits to be epigenetic hydrothermal in origin. Mineralizing fluids were derived from the host plutonic rocks and were released soon after emplacement of the intrusion, and possibly during its crystallization (Ruiz et al., 1965). As discussed previously, Cardozo and Vidal (1981) have classified the deposits at Monterrosas, Eliana, Acari, and possibly Raul as part of this amphibole-chalcopyrite-magnetite-pyrite association.

Gabbroic to granodioritic magmas are considered to be the source of metals and volatiles in these deposits of iron \pm copper. However, the plutonic rocks are not enriched in iron. Rather, their low concentrations of iron are inversely proportional to the high concentrations in the alteration assemblages. Bookstrom (1975) has suggested that the parent materials of these magmas were therefore not iron-rich, and that little iron was assimilated during rise of the magmas.

Residual concentration and separation of an iron-rich fluid during crystallization of the magmas appear to offer the best explanation for distribution of iron in these deposits. However, the sources of chlorine are ambiguous and possibly include: (1) primary magmatic chlorine; (2) evaporites of Cl-rich brines in sedimentary rocks intruded and assimilated by the magma; and (3) deeply circulated seawater. Whereas chlorine in deposits such as the Raul Mine, Peru, and those in the Buena Vista Hills, Nevada, was most likely derived externally to the intrusions from seawater and evaporitic sediments, respectively (Vidal, 1980; Vanko and Bishop, 1982), these potential sources probably were not present and available for assimilation by the magmas at other deposits such as Monterrosas and El Romeral. Therefore, the primary source magmas of these deposits must have had a high initial concentration of chlorine such that the separated aqueous phase, upon removal of chlorine from the magma, could attain the high salinities at high temperatures necessary to stabilize sodic scapolite. Furthermore, the system must have been sufficiently closed (or impermeable) to prevent dilution of these saline fluids. At Monterrosas, moderately saline type I inclusions (10 to 26 wt % NaCl) and saline type III inclusions (30 to 56 wt % NaCl) indicate that dilute meteoric fluids probably did not enter into the hydrothermal system that circulated during the formation of the ore deposit.

SUMMARY AND CONCLUSIONS

The hydrothermal copper-iron deposit at Monterrosas is hosted by gabbro-diorites of the Upper Cretaceous Patap Superunit within the Coastal Batholith of central Peru. Ore and alteration minerals were deposited at high temperatures from saline fluids by replacement of wall rocks adjacent to faults and fractures. Least altered gabbro-diorites consist of magmatic diopside, labradorite-andesine, ilmenite, magnetite, and minor actinolitic hornblende and possibly orthopyroxene. Deuteric epidote, clinozoisite, and fibrous actinolite are also common. Products of hydrothermal mineralization include major quantities of actinolite, sodic scapolite, magnetite, and sulfides, as well as minor amounts of epidotes, sphene, chlorites, apatite, tourmaline, allanite, hematite, and quartz. The alteration minerals become more abundant with increasing proximity to the ore zone and obscure contacts between gabbro-diorite wall rocks and the chalcopryite-magnetite-pyrite ores where metasomatic replacement has been most intense. Variations in concentrations of the major oxides in samples of gabbro-diorite are correlative with mineralogical changes imposed by alteration and metallization. These include additions of FeO_t , K_2O , and MgO , and coincident depletions of SiO_2 , CaO , Na_2O , and TiO_2 . Moreover, volatiles such as H_2O , Cl , S , P , and B and the ore-forming metals (Cu , Co , Au , Ag , and Mo) must also have been added to account for the assemblages of ore and alteration minerals. An alteration index, based on the ratio of losses to gains of major oxide components in samples of gabbro-diorite, exhibits excellent correlations with both proximity to ore and the intensity of metallization-alteration.

These chemical and mineralogical trends are supported by a summary equation of several reactions that define the destruction of primary magmatic minerals and concomitant formation of alteration minerals in the gabbro-diorite host rocks. The overall summary equation shows substantial additions of H_2O , Fe^{3+} , Fe^{2+} , HCl , Mg^{2+} , and CO_2 and depletions of SiO_2 , Ca^{2+} , Al^{3+} , and Na^+ .

Ore was deposited at high temperatures from saline fluids that were enriched in metals and volatiles. Primary fluid inclusions in gangue quartz document the high temperatures and salinities of the mineralizing fluids. All halite-bearing inclusions homogenized by halite dissolution at temperatures as high as 500°C . These inclusions have average salinities of about 52 wt percent NaCl . Inclusions with daughter crystals of both halite and sylvite have salinities of about 62 wt percent $\text{NaCl}+\text{KCl}$, and they delineate the halite trend on a phase diagram of the $\text{NaCl}-\text{KCl}-\text{H}_2\text{O}$ system. The halite trend and homogenization by the disappearance of halite at high temperatures and salinities suggest that the fluids exsolved directly from a magma. The fluid inclusion data are supported by those of sulfur isotopes in which average concentrations of 2.7 permil in both pyrite and chalcopyrite approximate magmatic values and a pyrite-chalcopyrite pair provides an isotopic temperature estimate of 525°C .

Mineralization took place after progressive crystallization of labradorite-andesine, diopside, and ilmenite from gabbro-diorite magma resulted in the residual concentration of iron, water, chlorine, and other metals and volatiles. The chloride content of the fluids was a critical factor in the concentration, and subsequent transportation and precipitation of iron, copper, and other elements. These

metal-enriched, saline fluids separated from the magma at temperatures possibly exceeding 800°C and before crystallization of the gabbro-diorites was complete. The fluids migrated upward along faults and fractures and reacted with early-formed gabbro-diorite wall rocks. Decreases in temperature and (or) acidity of the fluids resulted in the deposition of ore and alteration minerals. This model is similar to that proposed for the genesis of some skarn-type replacement deposits of iron. For example, Bookstrom (1977, 1975) has concluded that residual concentration of iron, water, volatiles, and other metals during crystallization of a dioritic magma led to the separation of saline, metal-enriched fluids and ultimately to deposition of the magnetite deposits at El Romeral, Chile.

This study of the Monterrosas Mine has documented most clearly the composition of the mineralizing fluids, their effects on the host gabbro-diorites, and the conditions of ore formation. The proposed model for ore genesis incorporates the bulk chemistry of the gabbro-diorites and the ore in addition to more selective compositional data for the fluids and the primary magmatic, secondary alteration, and ore minerals. Future investigations might consider in more detail the composition of hydrothermal fluids associated with the gabbro-diorite and the monzonitic intrusions in order to identify and (or) distinguish the effect of fluids possibly derived from the latter on remobilization and reconcentration of metals (Sidder, 1981). Studies might include the identification of daughter minerals by SEM and microprobe techniques and analyses of leachates from fluid inclusions in both intrusive rock types and ore; more detailed electron microprobe analyses of the hydrous minerals such as amphiboles, chlorites, biotites, and

others; and Ar-Ar age determinations of gabbro-diorites, monzonites, and secondary minerals. These analyses might establish the concentrations of iron, calcium, potassium, magnesium, chlorine, fluorine, bromine, boron, and other volatile and trace elements in the hydrothermal fluids and identify similarities and (or) differences between halide contents of alteration minerals and the fluids as well as determine the precise chronologic sequence of events that formed the Monterrosas deposit.

REFERENCES

- Agar, R. A., 1981, Copper mineralization and magmatic hydrothermal brines in the Rio Pisco section of the Peruvian Coastal Batholith: *Economic Geology*, v. 76, p. 677-693.
- Agar, R. A., 1982, Copper mineralization and magmatic hydrothermal brines in the Rio Pisco section of the Peruvian Coastal Batholith --a reply: *Economic Geology*, v. 77, p. 1954-1955.
- Ahmad, S. N., and Rose, A. W., 1980, Fluid inclusions in porphyry and skarn ore at Santa Rita, New Mexico: *Economic Geology*, v. 75, p. 229-250.
- Anders, E., and Ebihara, M., 1982, Solar-system abundances of the elements: *Geochimica et Cosmochimica Acta*, v. 46, p. 2362-2380.
- Atherton, M. P., McCourt, W. J., Sanderson, L. M., and Taylor, W. P., 1979, The geochemical character of the segmented Peruvian Coastal Batholith and associated volcanics, in Atherton, M. P., and Tarney, J., eds., *Origin of granite batholiths*: Kent, U.K., Shiva Publishing Ltd., p. 45-64.
- Audebaud, M. E., 1973, Apropos d'une zone de haute conductivite electrique: Differences geologiques et geophysiques entre le Nord et le Sud des Andes Peruvienes: *Comptes Rendus Hebdomadaires des Seances de l'Academie des Sciences*, v. 277, p. 1729-1732.
- Barazangi, M., and Isacks, B. L., 1976, Spatial distribution of earthquakes and subduction of the Nazca Plate beneath South America: *Geology*, v. 8, p. 686-692.
- Barazangi, M., and Isacks, B. L., 1979, Subduction of the Nazca Plate beneath Peru: Evidence from spatial distribution of earthquakes: *Geophysical Journal of the Royal Astronomical Society*, v. 57, p. 537-555.
- Barnes, H. L., 1979, Solubilities of ore minerals, in Barnes, H. L., ed., *Geochemistry of hydrothermal ore deposits* (second edition): New York, John Wiley and Sons, p. 404-460.
- Barton, P. B. Jr., 1973, Solid solutions in the system Cu-Fe-S, Part I: The Cu-S and CuFe-S joins: *Economic Geology*, v. 68, p. 455-465.
- Barton, P. B., Jr., and Skinner, B. J., 1979, Sulfide-mineral stabilities, in Barnes, H. L., ed., *Geochemistry of hydrothermal ore deposits* (second edition): New York, John Wiley and Sons, p. 278-403.
- Bellido Bravo, E., 1974, Depositos de hierro en el Peru: *Servicio de Geologia y Minería, Geologia Economica*, no. 3, 43 pages.

- Bellido Bravo, E., Girard, D., and Paredes, J., 1972, Mapa metalogénico del Perú: Servicio de Geología y Minería, Lima, Perú.
- Bloom, M. S., 1981, Chemistry of inclusion fluids: Stockwork molybdenum deposits from Questa, New Mexico, and Hudson Bay Mountain and Endako, British Columbia: *Economic Geology*, v. 76, p. 1906-1920.
- Bodnar, R. J., and Bethke, P. M., 1984, Systematics of stretching of fluid inclusions I: Fluorite and sphalerite at 1 atmosphere confining pressure: *Economic Geology*, v. 79, p. 141-161.
- Bookstrom, A. A., 1975, Magnetite deposits of El Romeral, Chile: Physical geology, sequence of events, and processes of formation: unpublished Ph.D. Dissertation, Stanford University, 417 pages.
- Bookstrom, A. A., 1977, The magnetite deposits of El Romeral, Chile: *Economic Geology*, v. 72, p. 1101-1130.
- Bottinga, Y., Kudo, A., and Weill, D., 1966, Some observations on oscillatory zoning and crystallization of magmatic plagioclase: *American Mineralogist*, v. 51, p. 792-806.
- Boyd, T. M., Snoke, J. A., Sacks, I. S., and Rodriguez B., A., 1983, High-resolution study of the Benioff zone beneath southern Peru (abst.): *EOS*, v. 64, p. 311.
- Buddington, A. F., and Lindsley, D. H., 1964, Iron-titanium oxide minerals and synthetic equivalents: *Journal of Petrology*, V. 5, p. 310-357.
- Burnham, C. W., 1979, Magmas and hydrothermal fluids, in Barnes, H. L., ed., *Geochemistry of hydrothermal ore deposits* (second edition): New York, John Wiley and Sons, p. 71-136.
- Bussell, M. A., 1983, Timing of tectonic and magmatic events in the Central Andes of Peru: *Journal of the Geological Society of London*, V. 140, p. 279-286.
- Cabri, L. J., 1973, New data on phase relations in the Cu-Fe-S system: *Economic Geology*, V. 68, p. 443-454.
- Cardozo, M., and Vidal, C., 1981, Metalogenesis y magmatismo en el flanco occidental de Los Andes Centrales: Revision: *Boletín de la Sociedad Geológica del Perú*, no. 68, p. 13-24.
- Carmichael, I. S. E., Turner, F. J., and Verhoogen, J., 1974, *Igneous Petrology*: New York, McGraw-Hill Book Co., 739 pages.
- Chappell, B. W., and White, A. J. R., 1974, Two contrasting granite types: *Pacific Geology*, v. 8, p. 173-174.

- Chaochun, Y., 1981, The geological-geochemical characteristics of the Na-Cl type skarn iron ore deposit and its genetic mechanism: Bulletin of the Yichang Institute of Geology and Mineral Resources, Chinese Academy of Geological Sciences, No. 3, p. 1-19.
- Chou, I-Ming, and Eugster, H. P., 1977, Solubility of magnetite in supercritical chloride solutions: *American Journal of Science*, V. 277, p. 1296-1314.
- Clark, A. H., Farrar, E., Cuelles, J. C., Haynes, S. J., Lortie, R. B., McBride, S. L., Quirt, G. S., Robertson, R. C. R., and Zentilli, M., 1976, Longitudinal variations in the metallogenetic evolution of the central Andes: A progress report: Geological Association of Canada, Special Paper No. 14, p. 23-58.
- Cloke, P. L., and Kesler, S. E., 1979, The halite trend in hydrothermal solutions: *Economic Geology*, v. 74, p. 1823-1831.
- Cobbing, E. J., 1978, The Andean geosynclines in Peru, and its distinction from Alpine geosynclines: *Journal of the Geological Society of London*, v. 135, p. 207-218.
- Cobbing, E. J., 1982, The segmented Coastal Batholith of Peru: Its relationship to volcanicity and metallogenesis: *Earth-Science Reviews*, V. 18, p. 241-251.
- Cobbing, E. J., Ozard, J. M., and Snelling, N. J., 1977, Reconnaissance geochronology of the crystalline basement of southern Peru: *Geological Society of America Bulletin*, v. 88, p. 241-246.
- Cobbing, E. J., and Pitcher, W. S., 1972, The Coastal Batholith of central Peru: *Journal of the Geological Society of London*, v. 128, p. 421-460.
- Cobbing, E. J., and Pitcher, W. S., 1983, Andean plutonism in Peru and its relationship to volcanism and metallogenesis at a segmented plate edge, in Roddick, J. A., ed., *Circum-Pacific plutonic terranes: Geological Society of America Memoir 159*, p. 277-291.
- Cobbing, E. J., Pitcher, W. S., and Taylor, W. P., 1977, Segments and super-units in the Coastal Batholith of Peru: *Journal of Geology*, v. 85, p. 625-631.
- Cobbing, E. J., Pitcher, W. S., Wilson, J. J., Baldock, J. W., Taylor, W. P., McCourt, W., and Snelling, N. J., 1981, The geology of the Western Cordillera of northern Peru: *Institute of Geological Sciences, London, Overseas Memoir 5*, 143 pages.
- Couch, R., and Whitsett, R. M., 1981, Structures of the Nazca Ridge and the continental shelf and slope of southern Peru, in Kulm, L. D., and others, eds., *Nazca plate: Crustal formation and Andean convergence: Geological Society of America Memoir 154*, p. 569-586.

- Craig, J. R., and Scott, S. D., 1974, Sulfide phase equilibria, in Ribbe, P. H., ed., Sulfide mineralogy: Mineralogical Society of America Short Course Notes, V. 1, p. CS-1-CS-110.
- Crawford, M. L., 1981, Phase equilibria in aqueous fluid inclusions, in Hollister, L. S., and Crawford, M. L. eds., Short course in fluid inclusions: Applications to petrology: Calgary, Mineralogical Association of Canada, v. 6, p. 75-100.
- Crawford, M. L., Kraus, D. W., and Hollister, L. S., 1979, Petrologic and fluid inclusion study of calc-silicate rocks, Prince Rupert, British Columbia: American Journal of Science, v. 279, p. 1135-1159.
- Cross, T. A., and Pilger, R. H., Jr., 1982, Controls of subduction geometry, location of magmatic arcs, and tectonics of arc and back-arc regions: Geological Society of America Bulletin, v. 93, p. 545-562.
- Cunningham, C. G., 1978, Pressure gradients and boiling as mechanisms for localizing ore in porphyry systems: Journal of Research, U.S. Geological Survey, v. 6, p. 745-754.
- Czamanske, G. K., Ishihara, S., and Atkin, S. A., 1981, Chemistry of rock-forming minerals of the Cretaceous-Paleocene batholith in southwestern Japan and implications for magma genesis: Journal of Geophysical Research, v. 86, p. 1043-10469.
- Czamanske, G. K., and Mihalik, P., 1972. Oxidation during magmatic differentiation, Finnmarka Complex, Oslo area, Norway: Part 1, the opaque oxides: Journal of Petrology, v. 13, p. 493-509.
- Czamanske, G. K., and Wones, D. R., 1973, Oxidation during magmatic differentiation, Finnmarka Complex, Oslo area, Norway: Part 2, the mafic silicates: Journal of Petrology, v. 18, p. 349-380.
- Dalmayrac, B., Lancelot, J. R., and Leyreloup, A., 1977, Two-billion-year granulites in the Late Precambrian metamorphic basement along the southern Peruvian coast: Science, v. 198, p. 49-51.
- Dalmayrac, B., Laubacher, G., and Marocco, R., 1980, Geologie des Andes peruvienes: Caracteres generaux de l'evolution geologique des Andes peruvienes: Paris, Travaux et Documents de l'O.R.S.T.O.M., #122, 501 pages.
- Deer, W. A., Howie, R. A., and Zussman, J., 1962, Rock-forming minerals, Volume 3, sheet silicates: London, Longmans, Green, and Co., Ltd., 270 pages.
- Deer, W. A., Howie, R. A., and Zussman, J., 1963, Rock-forming minerals, Volume 4, framework silicates: London, Longmans, Green, and Co., Ltd., 435 pages.

- Deer, W. A., Howie, R. A., and Zussman, J., 1966, An introduction to the rock-forming minerals: London, Longman Group Limited, 528 pages.
- Deer, W. A., Howie, R. A., and Zussman, J., 1978, Rock-forming minerals, Volume 2A, second edition, single-chain silicates: New York, John Wiley and Sons, 668 pages.
- Dunin-Borkowski, E., 1970, Der Acari-Pluton (Peru) als Beispiel der Differentiation des tonalitischen Magmas [The Acari Pluton (Peru) as an example of the differentiation of tonalitic magma]: *Geologische Rundschau*, v. 59, p. 1141-1180.
- Eadington, P. J., 1983, A fluid inclusion investigation of ore formation in a tin-mineralized granite, New England, New South Wales: *Economic Geology*, v. 78, p. 1204-1221.
- Eastoe, C. J., 1978, A fluid inclusion study of the Panguna porphyry copper deposit, Bougainville, Papua New Guinea: *Economic Geology*, v. 73, p. 721-748.
- Eastoe, C. J., 1982, Physics and chemistry of the hydrothermal system at the Panguna porphyry copper deposit, Bougainville, Papua New Guinea: *Economic Geology*, v. 77, p. 127-153.
- Eggler, D. H., and Burnham, C. W., 1973, Crystallization and fractionation trends in the system andesite - H_2O - CO_2 - O_2 at pressures to 10 kb: *Geological Society of America Bulletin*, V. 84, p. 2517-2532.
- Einaudi, M. T., and Burt, D. M., 1982, Introduction-terminology, classification, and composition of skarn deposits: *Economic Geology*, V. 77, p. 745-754.
- Einaudi, M. T., Meinert, L. S., and Newberry, R. J., 1981, Skarn deposits: *Economic Geology*, 75th Anniversary Volume, p. 317-391.
- Ellis, D. E., 1978, Stability and phase equilibria of chloride and carbonate bearing scapolite at 750°C and 4000 bar: *Geochimica et Cosmochimica Acta*, V. 42, p. 1271-1281.
- Erwood, R. J., Kesler, S. E., and Cloke, P. L., 1979, Compositionally distinct, saline hydrothermal solutions, Naica Mine, Chihuahua, Mexico: *Economic Geology*, v. 74, p. 95-108.
- Eugster, H. P., and Chou, I-Ming, 1979, A model for the deposition of Cornwall-type magnetite deposits: *Economic Geology*, v. 74, p. 763-774.
- Frutos, J., 1982, Andean metallogeny related to the tectonic and petrologic evolution of the Cordillera. Some remarkable points, in Amstutz, G. C., and others, eds., *Ore Genesis--the state of the art*: Berlin, Springer-Verlag, p. 493-507.

- Gansser, A., 1973, Facts and theories on the Andes: Journal of the Geological Society of London, v. 129, p. 93-131.
- Gill, J. B., 1981, Orogenic andesites and plate tectonics: New York, Springer-Verlag, 390 pages.
- Griffin, T. J., White, A. J. R., and Chappell, B. W., 1978, The Moruya Batholith and geochemical contrasts between the Moruya and Jindabyne suites: Journal of the Geological Society of Australia, v. 25, p. 235-247.
- Gunter, W. D., Chou, I-Ming, and Girsperger, S., 1983, Phase relations in the system NaCl-KCl-H₂O binary above 450°C: Geochimica et Cosmochimica Acta, v. 47, p. 863-873.
- Haas, J. L., Jr., 1971, The effect of salinity on the maximum thermal gradient of a hydrothermal system at hydrostatic pressure: Economic Geology, v. 66, p. 940-946.
- Haas, J. L., Jr., 1976, Thermodynamic properties of the coexisting phases and thermochemical properties of the NaCl component in boiling NaCl solutions: U.S. Geological Survey Bulletin 1421-B, 71 pages.
- Haggerty, S. E., 1976a, Oxidation of opaque mineral oxides in basalts, in Rumble, D., III, ed., Oxide minerals: Mineralogical Society of America Short Course Notes, v. 3, p. Hg1-Hg100.
- Haggerty, S. E., 1976b, Opaque mineral oxides in terrestrial igneous rocks, in Rumble, S., III, ed., Oxide Minerals: Mineralogical Society of America Short Course Notes, v. 3, p. Hg101-Hg300.
- Hammarstrom, J. M., 1981, Chemical and mineralogical variation in the Pioneer Batholith, southwest Montana: unpublished M.S. thesis, Virginia Polytechnic Institute and State University, 220 pages.
- Hanus, V., and Vanek, J., 1978, Morphology of the Andean Wadati-Benioff zone, andesitic volcanism, and tectonic features of the Nazca Plate: Tectonophysics, v. 44, p. 65-77.
- Hasegawa, A., and Sacks, I. S., 1979, Subduction of the Nazca Plate beneath Peru as determined from seismic observations: Carnegie Institution of Washington Year Book 78, p. 276-284.
- Hasegawa, A., and Sacks, I. S., 1981, Subduction of the Nazca Plate beneath Peru as determined from seismic observations: Journal of Geophysical Research, v. 86, p. 4971-4980.
- Hawthorne, F. C., 1983, The crystal chemistry of the amphiboles: A review: Canadian Mineralogist, v. 21, p. 173-480.
- Helz, G. R., 1972, Hydrothermal solubility of magnetite: Dissertation Abstracts International, V. 32, No. 9, p. 5352-B.

- Hine, R., Williams, I. S., Chappell, B. W., and White, A. J. R., 1978, Contrasts between I- and S- type granitoids of the Kosciusko Batholith: *Journal of the Geological Society of Australia*, v. 25, p. 219-234.
- Holdaway, M. J., 1972, Thermal stability of Al-Fe epidote as a function of f_{O_2} and Fe content: *Contributions to Mineralogy and Petrology*, V. 37, p. 307-340.
- Holland, H. D., 1972, Granites, solutions, and base metal deposits: *Economic Geology*, V. 67, p. 281-301.
- Hollister, L. S., 1981, Information intrinsically available from fluid inclusions, in Hollister, L. S., and Crawford, M. L., eds., *Short course in fluid inclusions: Applications to petrology*: Calgary, Mineralogical Association of Canada, p. 1-12.
- Hughes, S. S., 1982, Petrochemical evolution of High Cascade volcanic rocks in the Three Sisters region, Oregon: unpublished Ph.D. thesis, Oregon State University, 199 pages.
- Hyde, D. M., 1983, The mineral industry of Peru: U. S. Bureau of Mines, *Minerals Yearbook*, 1981, V. III, Area reports: International, p. 773-787.
- Hyde, D. M., 1984, The mineral industry of Peru: U.S. Bureau of Mines, *Minerals Yearbook*, 1982, V. III, Area reports: International (preprint), 12 pages.
- Isacks, B. L., and Barazangi, M., 1977, Geometry of Benioff zones: Lateral segmentation and downwards bending of the subducted lithosphere, in Talwani, M., and Pitman, W. C., III, *Island arcs, deep sea trenches, and back-arc basins*: American Geophysical Union Maurice Ewing Series 1, p. 99-114.
- Ishihara, S., 1977, The magnetite-series and ilmenite-series granitic rocks: *Mining Geology*, V. 27, p. 293-305.
- Jehl, V., 1975, Le metamorphisme et les fluides associes des roches oceaniques de l'Atlantique Nord: These Docteur-Ingenieur, University of Nancy I, 242 pages (as translated by Barabas, A., and Poty, B., 197, *Chaixmeca Microthermometry Apparatus* (-180°/+600°C range): Nancy, France, Chaixmeca Ltd., p. 21-27.
- Jenks, W. F., 1956, Peru, in Jenks, W. F., ed., *Handbook of South American Geology*: Geological Society of America, Memoir 65, p. 219-247.
- Jenks, W. F., and Harris, E. G., 1953, Plutonics near Arequipa as a petrologic sample of the Coastal Batholith in Peru: *Boletin de la Sociedad Geologica del Peru*, v. 26, p. 79-94.

- Keevil, N. B., 1941, Vapor pressures of aqueous solutions at high temperatures: *Journal of the American Chemical Society*, v. 64, p. 841-850.
- Kelly, W. C., and Rye, R. O., 1979, Geologic, fluid inclusion, and stable isotope studies of the tin-tungsten deposits of Panasqueira, Portugal: *Economic Geology*, v. 74, p. 1721-1822.
- Kilinc, J. A., and Burnham, C. W., 1972, Partitioning of chloride between a silicate melt and coexisting aqueous phase from 2 to 8 kb: *Economic Geology*, v. 67, p. 231-235.
- Koch, G. S., Jr., and Link, R. F., 1971, Statistical analysis of geological data: New York, Dover Publications, Inc., V. I, 375 pages.
- Kotel'nikov, A. R., 1978, Hydrothermal stability of scapolite: *Geochemistry International*, V. 15, #3, p. 83-85.
- Kwak, T. A. P., and Tan, T. H., 1981a, The geochemistry of zoning in skarn minerals at the King Island (Dolphin) Mine: *Economic Geology*, v. 76, p. 468-497.
- Kwak, T. A. P., and Tan, T. H., 1981b, The importance of CaCl_2 in fluid composition trends--evidence from the King Island (Dolphin) skarn deposit: *Economic Geology*, v. 76, p. 955-960.
- Lapham, D. M., and Gray, C., 1973, Geology and origin of the Triassic magnetite deposit and diabase at Cornwall, Pennsylvania: *Pennsylvania Geological Survey Mineral Resources Report, Bulletin M56*, 343 pages.
- Leake, B. E., 1978, Nomenclature of amphiboles: *American Mineralogist*, v. 63, p. 1023-1052.
- Leake, B. E., and Hey, M. H., 1979, Addendum to the nomenclature of amphiboles: *Mineralogical Magazine*, v. 42, p. 561-563.
- LeMaitre, R. W., 1976, The chemical variability of some common igneous rocks: *Journal of Petrology*, V. 17, p. 589-637.
- Lemmlin, G. G., and Klevtsov, P. V., 1961, Relations among the principal thermodynamic parameters in a part of the system $\text{H}_2\text{O}-\text{NaCl}$: *Geochemistry*, v. 2, p. 148-158.
- Lindsley, D. H., 1976, The crystal chemistry and structure of oxide minerals as exemplified by the Fe-Ti oxides, in Rumble, D., III, ed., *Oxide minerals: Mineralogical Society of America Short Course Notes*, v. 3, p. L1-L60.
- Liou, J. G., 1973, Synthesis and stability relations of epidote $\text{Ca}_2\text{Al}_2\text{FeSi}_3\text{O}_{12}(\text{OH})$: *Journal of Petrology*, V. 14, p. 381-413.

- McCourt, W. J., 1981, The geochemistry and petrography of the Coastal Batholith of Peru, Lima segment: *Journal of the Geological Society of London*, v. 138, p. 407-420.
- Megard, F., and Philip, H., 1976, Plio-Quaternary tectono-magmatic zonation and plate tectonics in the central Andes: *Earth and Planetary Science Letters*, v. 33, p. 231-238.
- Meinert, L. S., 1984, Mineralogy and petrology of iron skarns in western British Columbia, Canada: *Economic Geology*, V. 79, p. 869-882.
- Mercier, J. L., 1981, Extensional-compressional tectonics associated with the Aegean Arc: Comparison with the Andean Cordillera of south Peru-north Bolivia: *Philosophical Transactions of the Royal Society of London*, v. A300, p. 337-355.
- Mullan, H. S., and Bussell, M. A., 1977, The basic rock series in batholithic associations: *Geological Magazine*, v. 114, p. 265-280.
- Nash, J. T., 1976, Fluid inclusion petrology--data from porphyry copper deposits and applications to exploration: U.S. Geological Survey Professional Paper, 907-D, 16 pages.
- Newton, R. C., and Goldsmith, J. R., 1976, Stability of the end-member scapolites: $3\text{NaAlSi}_3\text{O}_8 \cdot \text{NaCl} - 3\text{CaAl}_2\text{Si}_2\text{O}_8 \cdot \text{CaCO}_3 - 3\text{CaAl}_2\text{Si}_2\text{O}_8 \cdot \text{CaSO}_4$: *Zeitschrift fur Kristallographie*, v. 143, p. 333-353.
- Noble, D. C., Farrar, E., and Cobbing, E. J., 1979, The Nazca Group of south-central Peru: Age, source, and regional volcanic and tectonic significance: *Earth and Planetary Science Letters*, v. 45, p. 80-86.
- Nockolds, S. R., 1954, Average chemical composition of some igneous rocks: *Geological Society of America Bulletin*, V. 65, p. 1007-1032.
- Nockolds, S. R., and Allen, R., 1953, The geochemistry of some igneous rock series: *Geochimica et Cosmochimica Acta*, V. 4, p. 105-142.
- Ocola, L., 1983, Geophysical data and the Nazca-South American subduction zone kinematics: Peru-north Chile segment, in Cabre, R., ed., *Geodynamics of the eastern Pacific region, Caribbean and Scotia arcs*: Washington, D.C., American Geophysical Union, *Geodynamics Series*, v. 9, p. 95-112.
- Ohmoto, H., and Rye, R. O., 1979, Isotopes of sulfur and carbon, in Barnes, H. L., ed., *Geochemistry of hydrothermal ore deposits* (second edition): New York, John Wiley and Sons, p. 509-567.
- Park, C. F., Jr., 1972, The iron ore deposits of the Pacific basin: *Economic Geology*, v. 67, p. 339-349.

- Pearce, J. A., 1982, Trace element characteristics of lavas from destructive plate boundaries, in Thorpe, R. S., ed., *Andesites-orogenic andesites and related rocks*: New York, John Wiley and Sons, p. 525-548.
- Petersen, U., 1970, Metallogenic provinces in South America: *Geologische Rundschau*, v. 59, p. 834-897.
- Petersen, U., 1972, Geochemical and tectonic implications of South American metallogenic provinces: *Annals of the New York Academy of Sciences*, v. 196, p. 1-38.
- Phillips, W. R., and Griffen, D. T., 1981, *Optical mineralogy--the nonopaque minerals*: San Francisco, W. H. Freeman and Company, 677 pages.
- Pilger, R. H., Jr., 1981, Plate reconstructions, aseismic ridges, and low-angle subduction beneath the Andes: *Geological Society of America Bulletin*, v. 92, p. 448-456.
- Pitcher, W. S., 1978, The anatomy of a batholith: *Journal of the Geological Society of London*, v. 135, p. 157-181.
- Pitcher, W. S., 1979, The nature, ascent and emplacement of granitic magmas: *Journal of the Geological Society of London*, v. 136, p. 627-662.
- Ponzoni, E., and Vidal, C., 1982, Copper mineralization and magmatic hydrothermal brines in the Rio Pisco section of the Peruvian Coastal Batholith--a discussion: *Economic Geology*, v. 77, p. 1951-1954.
- Potter, W., II, 1977, Pressure corrections for fluid-inclusion homogenization temperatures based on the volumetric properties of the system NaCl-H₂O: *Journal of Research, U.S. Geological Survey*, v. 5, p. 603-607.
- Potter, R. W., II, Babcock, R. S., and Brown, D. L., 1977, A new method for determining the solubility of salts in aqueous solutions at elevated temperatures: *Journal of Research, U.S. Geological Survey*, v. 5, p. 389-395.
- Potter, R. W., II, Clynne, M. A., and Brown, D. L., 1978, Freezing point depression of aqueous sodium chloride solutions: *Economic Geology*, v. 73, p. 284-285.
- Poty, B., Leroy, J., and Jachimowicz, L., 1976, Un nouvel appareil pour la mesure des temperatures sous le microscope: l'installation de microthermometrie chaixmeca: *Bulletin de la Societe Francaise de Mineralogie et de Cristallographie*, v. 99, p. 182-186 (translated in Roedder, E., ed., 1976, *Fluid inclusion research--Proceedings of COFFI*: Ann Arbor, The University of Michigan Press, v. 9, p. 173-178).

- Presnall, D. C., and Bateman, P. C., 1973, Fusion relations in the system $\text{NaAlSi}_3\text{O}_8\text{-CaAl}_2\text{Si}_2\text{O}_8\text{-KAlSi}_3\text{O}_8\text{-SiO}_2\text{-H}_2\text{O}$ and generation of granite magmas in the Sierra Nevada Batholith: Geological Society of America Bulletin, v. 84, p. 3181-3202.
- Ravich, M. I., and Borovaya, F. E., 1949, Phase equilibria in ternary water-salt systems at high temperatures: Akad. Nauk SSSR, Izv. Sek. Fiziko-Khimi Anal., V. 19, p. 69-81 (translated in Roedder, E., ed., 1977, Fluid inclusion research: Proceedings of COFFI, V. 10, p. 330-340).
- Reeves, R. G., and Kral, V. E., 1955, Iron ore deposits of Nevada: Part A. Geology and iron ore deposits of the Buena Vista Hills, Churchill and Pershing Counties, Nevada: Nevada Bureau of Mines, Bulletin 53, 34 pages.
- Ribbe, P. H., 1975, The chemistry, structure, and nomenclature of feldspars, in Ribbe, P. H., ed., Feldspar mineralogy: Mineralogical Society of America Short Course Notes, v. 2, p. R1-R52.
- Ripley, E. M., and Ohmoto, H., 1977, Mineralogic, sulfur isotope, and fluid inclusion studies of the stratabound copper deposits at the Raul Mine, Peru: Economic Geology, v. 72, p. 1017-1041.
- Ripley, E. M., and Ohmoto, H., 1979, Oxygen and hydrogen isotopic studies of ore deposition and metamorphism at the Raul mine, Peru: Geochimica et Cosmochimica Acta, v. 43, p. 1633-1643.
- Robinson, P., 1980, The composition space of terrestrial pyroxenes--internal and external limits, in Prewitt, C. T., ed., Pyroxenes: Mineralogical Society of America Reviews in Mineralogy, v. 7, p. 419-494.
- Robinson, P., Spear, F. S., Schumacher, J. C., Laird, J., Klein, C., Evans, B. W., and Doolan, B. L., 1982, Phase relations of metamorphic amphiboles: Natural occurrence and theory, in Veblen, D. R., and Ribbe, P. H., eds., Amphiboles: Petrology and experimental phase relations: Mineralogical Society of America Reviews in Mineralogy, v. 9B, p. 1-227.
- Roedder, E., 1962, Studies of fluid inclusions I: Low temperature application of a dual-purpose freezing and heating stage: Economic Geology, v. 57, p. 1045-1061.
- Roedder, E., 1963, Studies of fluid inclusions II: Freezing data and their interpretation: Economic Geology, v. 58, p. 167-211.
- Roedder, E., 1971, Fluid inclusion studies on the porphyry-type ore deposits at Bingham, Utah, Butte, Montana, and Climax, Colorado: Economic Geology, v. 66, p. 98-120.
- Roedder, E., 1972, The composition of fluid inclusions: U.S. Geological Survey Professional Paper 440 JJ, 164 pages.

- Roedder, E., 1976, Fluid-inclusion evidence on the genesis of ores in sedimentary and volcanic rocks, in Wolf, K. H., ed., Handbook of strata-bound and stratiform ore deposits: Amsterdam, Elsevier, v. 2, p. 67-110.
- Roedder, E., 1979, Fluid inclusions as samples of ore fluids, in Barnes, H. L., ed., Geochemistry of hydrothermal ore deposits (second edition): New York, John Wiley and Sons, p. 684-737.
- Roedder, E., 1981, Origin of fluid inclusions and changes that occur after trapping, in Hollister, L. S., and Crawford, M. L., eds., Short course in fluid inclusions: Applications to petrology: Calgary, Mineralogical Association of Canada, p. 101-137.
- Roedder, E., and Bodnar, R. J., 1980, Geologic pressure determinations from fluid inclusion studies: Annual Review of Earth and Planetary Sciences, v. 8, p. 263-301.
- Rose, A. W., Hawkes, H. E., and Webb, J. S., 1979, Geochemistry in mineral exploration, second edition: London, Academic Press, 657 pages.
- Ruiz, F. C., Aguirre, L., Corvalan, J., Klohn, C., Klohn, E., and Levi, G., 1965, Geologia y yacimientos metaliferos de Chile: Instituto de Investigaciones Geologicas, Chile, 386 pages.
- Ruiz, F. C., and Erickson, G. E., 1962, Metallogenic provinces of Chile, South America: Economic Geology, v. 57, p. 91-106.
- Sacks, I. S., 1983, The subduction of young lithosphere: Journal of Geophysical Research, v. 88, p. 3355-3566.
- Sasaki, A., and Ishihara, S., 1979, Sulfur isotopic composition of the magnetite-series and ilmenite-series granitoids in Japan: Contributions to Mineralogy and Petrology, v. 68, p. 107-115.
- Seward, T. M., 1977, Solubility of coexisting pyrite and pyrrhotite in the system $\text{NaHS-H}_2\text{S-NaCl-H}_2\text{O}$ at elevated temperature and pressure: in A. P. W. Hodder (ed.), Geochemistry 1977: New Zealand Department of Science and Industry Research, Bulletin 218.
- Shackleton, R. M., Ries, A. C., Coward, M. P., and Cobbold, P. B., 1979, Structure, metamorphism, and geochronology of the Arequipa Massif of coastal Peru: Journal of the Geological Society of London, v. 136, p. 195-214.
- Shaw, D. M., 1960, The geochemistry of scapolite, Part 1. Previous work and general mineralogy, Part II. Trace elements, petrology, and general geochemistry: Journal of Petrology, V. 1, p. 218-260, p. 261-285.

- Shelton, K. L., 1983, Composition and origin of ore-forming fluids in a carbonate-hosted porphyry copper and skarn deposit: A fluid inclusion and stable isotope study of Mines Gaspe, Quebec: *Economic Geology*, v. 78, p. 387-421.
- Sidder, G. B., 1981, Metallization and alteration at the Monterrosas Mine, Ica, Peru: unpublished M.S. thesis, University of Oregon, 109 pages.
- Sillitoe, R. H., 1974, Tectonic segmentation of the Andes: Implication for magmatism and metallogeny: *Nature*, v. 250, p. 542-545.
- Sillitoe, R. H., 1976, Andean mineralization: A model for the metallogeny of convergent plate margins: *Geological Association of Canada, Special Paper No. 14*, p. 59-100.
- Sinclair, A. J., 1976, Applications of probability graphs in mineral exploration: *The Association of Exploration Geochemists, Special Volume No. 4*, 95 pages.
- Smith, R. K., and Lofgren, G. E., 1983, An analytical and experimental study of zoning in plagioclase: *Lithos*, v. 16, p. 153-168.
- Sokolov, G. A., and Pavlov, D. I., 1970, Scapolite from magnetite deposits as a criterion for ore matter sources: *International Union of Geological Sciences A, No. 2: Problems of hydrothermal ore deposition, Schweizerbart, Stuttgart*, p. 29-32.
- Sood, M. K., 1981, *Modern igneous petrology*: New York, John Wiley and Sons, 244 pages.
- Sourirajan, S., and Kennedy, G. C., 1962, The system $H_2O-NaCl$ at elevated temperatures and pressures: *American Journal of Science*, v. 260, p. 115-144.
- Spencer, K. J., and Lindsley, D. H., 1981, A solution model for co-existing iron-titanium oxides: *American Mineralogist*, v. 66, p. 1189-1201.
- Stewart, J. S., Evernden, J. F., and Snelling, N. J., 1974, Age determinations from Andean Peru: A reconnaissance survey: *Geological Society of America Bulletin*, v. 85, p. 1107-1116.
- Stormer, J. C., 1983, The effects of recalculation on estimates of temperature and oxygen fugacity from analyses of multicomponent iron-titanium oxides: *American Mineralogist*, v. 68, p. 586-594.
- Streckeisen, A. L., 1973, Plutonic rocks--classification and nomenclature recommended by the IUGS Subcommittee on the Systematics of Igneous Rocks: *Geotimes*, v. 18, p. 26-30.
- Sugaki, A., Shima, H., Kitakaze, A., and Harada, H., 1975, Isothermal phase relations in the system $Cu-Fe-S$ under hydrothermal conditions at 350°C and 300°C: *Economic Geology*, V. 70, p. 806-823.

- Szatmari, P., 1983, Amazon rift and Pisco-Jurua fault: Their relation to the separation of North America from Gondwana: *Geology*, v. 11, p. 300-304.
- Theodore, T. G., and Blake, W., 1978, Geology and geochemistry of the West ore body and associated skarns, Copper Canyon porphyry copper deposits, Lander County, Nevada: U.S. Geological Survey Professional Paper, 798-C, 85 pages.
- Todd, J. C., 1983, Vertical crater retreat at Peru's new copper mine proves successful: *Engineering and Mining Journal*, v. 184, p. 28-29.
- Vanko, D. A., and Bishop, F. C., 1980, Experimental determination of NaCl-rich scapolite stability (abstract): *Geological Society of American Abstracts with Programs*, V. 12, p. 540.
- Vanko, D. A., and Bishop, F. C., 1982, Occurrence and origin of marialitic scapolite in the Humboldt Lopolith, N.W. Nevada: *Contributions to Mineralogy and Petrology*, v. 81, p. 277-289.
- Vidal, C., 1980, Mineral deposits associated with the Peruvian Coastal Batholith and its volcanic cover rocks: unpublished Ph.D. thesis, University of Liverpool, England, 270 pages.
- Wang, S., Eugster, H. P., and Wilson, G. A., 1984, Solubility of magnetite in supercritical HCl and NaCl solutions (abst.): *The Geological Society of America, Abstracts with Programs*, v. 16, no. 6, p. 686.
- Wauschkuhn, A., and Thum, R., 1982, The Condestable Mine, a volcano-exhalative deposit in the Mesozoic Coastal Belt of central Peru, in Amstutz, G. C., and others, eds., *Ore genesis--the state of the art*: Berlin, Springer-Verlag, p. 174-188.
- Weisbrod, A., Poty, B., and Touret, J., 1976, Les inclusions fluides en geochimie-petrologie: Tendances actuelles: *Bulletin de la Societe Francaise de Mineralogie et de Cristallographie*, v. 99, p. 140-152.
- White, A. J. R., and Chappell, B. W., 1977, Ultrametamorphism and granitoid genesis: *Tectonophysics*, v. 43, p. 7-22.
- Wilson, J. W. J., Kesler, S. E., Cloke, P. L., and Kelly, W. C., 1980, Fluid inclusion geochemistry of the Granisle and Bell porphyry copper deposits, British Columbia: *Economic Geology*, v. 75, p. 45-61.
- Yund, R. A., and Kullerud, G., 1966, Thermal stability of assemblages in the Cu-Fe-S system: *Journal of Petrology*, V. 7, p. 454-488.
- Zevallos, R. A., 1966, Geology of the Acari iron mining district Arequipa, Peru: unpublished M.S. thesis, University of Missouri at Rolla, 170 pages.

Zharikov, V. A., 1970, Skarns--Parts I, II, III: International Geology Review, V. 12, p. 541-559, 619-647, 760-775.

APPENDICES

APPENDIX 1

CHEMICAL ABUNDANCES, MODAL ABUNDANCES, AND NORMATIVE
MINERAL ABUNDANCES OF THE PATAP GABBRO-DIORITES

Table 1-A. Chemical abundances^a of the Patap Gabbro-diorites.

	6-8-13	13-9-10	10-2-21	2-2-22	13-2-22	12-2-22
Major Oxides (wt %)						
SiO ₂	55.4	55.4	54.3	53.7	54.7	54.3
TiO ₂	0.98	0.95	0.85	0.91	0.92	0.85
Al ₂ O ₃	15.9	16.3	17.9	18.2	16.8	17.6
Fe ₂ O ₃ ^b	n.a.	n.a.	1.6	3.3	1.7	4.2
FeO	n.a.	n.a.	2.9	2.5	3.3	3.4
FeO _t	4.22	5.25	3.9	5.5	4.7	7.2
MgO	5.3	4.8	6.2	4.4	5.6	3.3
CaO	13.51	11.36	13.0	10.4	10.8	10.1
Na ₂ O	4.0	4.3	3.9	4.0	4.0	4.8
K ₂ O	<u>0.09</u>	<u>0.11</u>	<u>0.4</u>	<u>0.19</u>	<u>0.2</u>	<u>0.3</u>
Total	99.40	98.47	100.45	97.31	97.72	98.45
S. G.	2.87	2.85	2.87	2.82	2.83	2.84
A. I.	0.00	7.81	10.75	11.13	12.77	15.63
Trace Elements (ppm)						
Cu	13	85	6	85	17	55
Mo	<1	2	<1	<1	<1	1
Pb	5	14	5	8	15	12
Zn	15	8	10	15	16	19
Ag	0.4	0.3	<0.3	<0.3	<0.3	<0.3
Co	4	5	<5	6	<5	5
Ba	316	n.a.	300	340	347	n.a.
Ce	23		15	40	26	
Co	8		10	10	14	
Cr	31		27	18	20	
Cu	6		9	48	11	
Ga	18		17	20	19	
La	13		11	17	15	
Ni	7		5	5	11	
Nb	5		3	4	4	
Pb	9		13	10	13	
Rb	3		14	4	2	
S	n.d.		n.d.	70	327	
Sc	28		24	31	27	
Sr	494		465	489	437	
Th	7		n.d.	5	16	
U	n.d.		n.d.	2	2	
V	121		98	149	111	
W	n.d.		n.d.	3	2	
Y	23		14	15	14	
Zn	14		18	16	17	
Zr	95		110	89	91	

Table 1-A. (cont.)

	8-9-9	1-21-70	9-9-9	10-2-22	C-8	A-1	10-9-9	C-2	A-5
Major Oxides (wt %)									
SiO ₂	53.5	55.7	52.8	50.7	54.4	52.7	57.0	48.6	52.0
TiO ₂	0.80	0.97	0.74	0.75	0.86	0.84	0.40	0.25	0.90
Al ₂ O ₃	19.3	17.4	16.9	21.9	17.3	18.0	13.2	20.3	15.8
Fe ₂ O ₃ ^b	2.6	n.a.	n.a.	4.2	n.a.	n.a.	2.7	4.4	5.4
FeO	4.0	n.a.	n.a.	3.4	n.a.	n.a.	5.3	5.1	5.8
FeO _t	6.1	5.43	7.69	7.2	7.53	7.33	8.1	9.12	11.0
MgO	5.5	6.3	4.6	4.1	5.6	5.1	7.9	6.8	5.8
CaO	10.8	9.02	11.42	8.8	9.38	8.12	8.2	11.65	9.08
Na ₂ O	3.6	4.2	3.5	4.5	3.5	3.5	4.2	2.5	3.7
K ₂ O	<u>0.3</u>	<u>0.39</u>	<u>0.2</u>	<u>0.7</u>	<u>0.86</u>	<u>1.46</u>	<u>0.25</u>	<u>0.36</u>	<u>0.3</u>
Total	99.90	99.50	97.85	98.55	99.43	97.05	99.25	99.58	98.58
S. G.	2.82	2.81	2.81	2.83	2.81	2.85	2.78	2.88	2.81
A. I.	24.91	24.99	28.71	29.82	36.65	38.98	44.13	49.67	50.04
Trace Elements (ppm)									
Cu	60	30	35	550	140	100	790	115	1230
Mo	1	<1	3	<1	3	3	2	1	5
Pb	<4	7	6	9	14	25	4	35	20
Zn	12	19	11	14	12	18	15	15	10
Ag	0.7	<0.3	0.5	0.3	1.5	0.8	0.3	1.0	0.5
Co	5	14	25	17	4	11	12	11	20

Table 1-A. (cont.)

	L-1	C-1	C-5	D-1	22-9-10	B-1	B-2	B-4
Major Oxides (wt %)								
SiO ₂	48.0	49.2	49.8	52.7	49.1	51.1	47.6	46.2
TiO ₂	0.45	0.38	0.65	0.93	0.90	0.93	0.21	0.72
Al ₂ O ₃	20.7	18.2	13.1	16.3	14.3	6.4	17.8	11.4
Fe ₂ O ₃ ^b	4.9	n.a.	n.a.	n.a.	n.a.	n.a.	n.a.	n.a.
FeO	6.0	n.a.	n.a.	n.a.	n.a.	n.a.	n.a.	n.a.
FeO _t	10.8	10.45	13.84	13.33	13.78	12.11	14.15	18.53
MgO	5.8	7.5	5.4	4.2	6.6	11.2	6.1	5.2
CaO	10.0	11.01	8.19	4.17	9.67	10.72	6.90	6.98
Na ₂ O	2.8	2.1	4.5	2.8	2.4	1.6	2.2	3.6
K ₂ O	<u>0.85</u>	<u>0.78</u>	<u>0.60</u>	<u>2.07</u>	<u>0.81</u>	<u>0.73</u>	<u>1.07</u>	<u>0.68</u>
Total	99.40	99.62	96.08	96.50	97.56	94.79	96.03	93.31
S. G.	2.83	2.89	2.87	2.78	2.87	2.87	2.89	2.92
A. I.	54.34	56.46	58.61	59.78	61.90	65.18	65.28	69.36
Trace Elements (ppm)								
Cu	240	720	5200	295	810	160	1180	160
Mo	2	1	17	2	8	1	6	2
Pb	14	60	11	14	25	12	20	7
Zn	30	25	17	60	30	14	45	30
Ag	0.5	1.0	1.3	0.7	0.3	0.3	1.0	0.3
Co	11	20	17	25	25	4	16	14

^aMajor oxides by XRF and AAS by Gary B. Sidder, E. Taylor, and R. Lightfoot at Oregon State University. Trace elements (Cu to Co) by Chemical and Mineralogical Services, Salt Lake City, Utah, and Ba to Zr by J. Injoque at University of Nottingham, by AAS and XRF, respectively.

^bFe₂O₃ and FeO by Skyline Laboratories, Denver, Colorado.

Table 1-B. Modal abundances of the Patap Gabbro-diorites. Modes based on 1000 or more points counted.

	6-8-13	13-9-10	10-2-21	2-2-22	13-2-22	12-2-22	8-9-9	1-21-70	9-9-9
	Modal Percent								
Plagioclase	67.3	60.5	49.4	60.5	58.4	59.4	50.0	14.4	42.2
Clinopyroxene	26.3	<1	22.9	11.8	7.7	9.2	<1	-	1.1
Amphibole	2.1	25.2	14.0	17.8	23.1	10.6	26.7	31.9	35.3
Apatite	1.4	<1	tr	2.0	tr	2.7	<1	tr	tr
Sphene	1.2	<1	2.2	1.7	1.9	3.2	4.6	2.9	2.1
Zircon	tr	tr	tr	tr	tr	tr	tr	tr	tr
Opaques	2.2	6.0	1.2	2.1	2.8	3.8	1.2	2.8	<1
Epidote	<1	2.4	5.9	1.7	2.9	1.3	3.8	1.5	5.3
Scapolite	<1	3.0	tr	1.7	2.0	5.4	5.6	42.0	6.6
Allanite	tr	tr	tr	-	tr	tr	-	-	-
Chlorite	tr	<1	tr	tr	tr	tr	1.5	1.2	tr
Sericite	tr	<1	3.2	<1	1.0	<1	tr	3.0	4.3
Tourmaline	-	-	-	-	-	-	-	-	-
Biotite	-	-	-	-	-	-	-	-	-
Quartz	-	-	-	-	-	3.3	-	-	-
Albite	-	-	-	-	-	-	-	<1	-
Kspar	-	-	-	-	-	-	-	-	-
Calcite	-	+	tr	-	tr	-	5.2	-	2.4

Table 1-B. (cont.)

	10-2-22	C-8	A-1	10-9-9	C-2	A-5	L-1	C-1	C-5
	Modal Percent								
Plagioclase	59.5	46.4	16.0	42.3	57.3	60.0	49.5	45.7	4.7
Clinopyroxene	-	-	-	-	3.8	-	<1	1.1	-
Amphibole	24.3	35.7	29.7	44.0	25.1	29.9	29.8	26.1	29.6
Apatite	<1	tr	tr	tr	<1	<1	tr	tr	-
Sphene	1.0	2.8	2.5	1.2	<1	1.4	1.1	<1	2.6
Zircon	tr	tr	<1	tr	tr	tr	tr	tr	tr
Opakes	3.1	2.3	3.5	<1	4.6	3.6	6.6	4.6	10.1
Epidote	1.6	1.2	14.2	tr	<1	1.1	2.9	7.4	<1
Scapolite	<1	<1	-	tr	tr	<1	4.8	-	48.5
Allanite	<1	tr	tr	-	-	-	tr	-	-
Chlorite	2.4	2.0	6.7	5.7	4.8	2.6	4.2	13.6	1.0
Sericite	9.1	9.2	26.9	1.5	tr	<1	<1	<1	tr
Tourmaline	-	-	-	-	-	-	<1	-	1.9
Biotite	<1	-	-	-	1.6	-	<1	-	-
Quartz	<1	-	-	2.0	-	<1	<1	-	-
Albite	-	<1	<1	-	-	<1	-	-	<1
Kspar	-	-	-	-	-	<1	-	-	-
Calcite	-	tr	<1	2.6	<1	-	<1	<1	-

Table 1-B. (cont.)

	D-1	22-9-10	B-1	E-2	B-4
	Modal Percent				
Plagioclase	38.5	29.3	53.2	56.4	46.3
Clinopyroxene	-	-	-	-	-
Amphibole	19.1	38.4	28.6	28.7	29.8
Apatite	<1	tr	tr	tr	1.2
Sphene	tr	2.3	1.3	tr	1.7
Zircon	tr	tr	1.0	tr	<1
Opagues	5.9	3.6	6.8	5.1	10.3
Epidote	<1	6.1	3.2	<1	3.8
Scapolite	tr	<1	<1	<1	3.9
Allanite	-	tr	<1	<1	1.6
Chlorite	11.3	5.8	5.7	5.8	1.8
Sericite	15.7	13.6	<1	1.4	tr
Tourmaline	-	-	-	tr	tr
Biotite	-	-	-	1.5	<1
Quartz	6.7	1	-	-	-
Albite	<1	<1	-	-	-
Kspar	tr	-	-	-	-
Calcite	1.1	<1	<1	-	-

Table 1-C. Normative mineral abundances in the Patap Gabbro-diorites.

	6-8-13	13-9-10	10-2-21	2-2-22	13-2-22	12-2-22	8-9-9	1-21-70	9-9-9
Volume Percent									
quartz	3.2	5.1	-	5.4	3.6	3.4	2.3	2.7	3.6
orthoclase	0.5	0.7	2.4	1.1	1.2	1.8	1.8	2.3	1.2
albite	33.6	36.4	33.0	33.8	33.8	40.6	30.5	35.5	29.6
anorthite	25.2	24.8	30.2	31.1	27.3	25.6	35.6	27.4	29.8
diopside	32.1	24.4	26.2	15.0	20.1	18.9	13.8	13.3	21.2
hypersthene	0.4	1.2	3.9	4.4	7.6	0.8	11.1	14.3	7.0
olivine	-	-	1.3	-	-	-	-	-	-
magnetite	2.3	4.3	2.3	4.8	2.5	6.1	3.8	2.0	4.1
ilmenite	1.9	1.8	1.6	1.7	1.7	1.6	1.5	1.8	1.4
Total	99.9	98.8	100.9	97.3	97.8	98.8	100.4	99.3	97.9
normative An	42.6	40.6	47.7	47.9	44.6	38.7	53.9	43.6	50.2
	10-2-22	C-8	A-1	10-9-9	C-2	A-5	L-1	C-1	C-5
Volume Percent									
quartz	-	2.8	1.4	4.4	-	3.3	-	-	-
orthoclase	4.1	5.1	8.6	1.5	2.1	1.8	5.0	4.6	3.5
albite	38.1	29.6	29.6	35.5	21.2	31.3	30.5	17.8	38.1
anorthite	37.5	29.0	29.1	16.4	43.1	25.6	41.4	37.9	13.8
diopside	4.4	13.7	8.5	18.9	11.2	15.1	6.1	13.0	21.5
hypersthene	1.4	14.9	14.9	17.6	11.3	12.1	8.5	17.6	1.2
olivine	6.0	-	-	-	4.1	-	6.8	2.5	9.4
magnetite	6.1	2.9	3.5	3.9	6.4	7.8	7.1	5.9	7.0
ilmenite	1.4	1.6	1.6	0.8	0.5	1.7	0.9	0.7	1.2
Total	99.0	99.8	97.5	99.0	99.9	98.7	99.5	100.3	96.8
normative An	49.6	49.4	49.6	31.6	67.1	45.0	63.6	68.1	26.6

Table 1-C. (cont.)

	D-1	22-9-10	B-1	E-2	B-4
	Volume Percent				
quartz	8.9	1.8	3.9	2.7	0.2
orthoclase	12.2	4.8	4.3	6.3	4.0
albite	23.7	20.3	13.5	18.6	30.5
anorthite	20.0	25.9	19.0	33.6	12.9
diopside	-	17.5	26.6	-	17.3
hypersthene	20.8	18.0	21.8	24.9	14.5
olivine	-	-	-	-	-
magnetite	7.5	8.1	8.4	9.4	13.5
ilmenite	<u>1.8</u>	<u>1.7</u>	<u>1.8</u>	<u>0.4</u>	<u>1.4</u>
Total	97.27*	98.3	99.6	96.9**	94.5
normative An	45.8	56.0	58.4	64.3	29.8

*Total includes corundum 2.1

**Total includes corundum 0.7

APPENDIX 2

ELECTRON MICROPROBE COMPOSITIONS OF PLAGIOCLASE
FELDSPAR IN THE PATAP GABBRO-DIORITES

Appendix 2. Electron microprobe compositions of plagioclase feldspar in the Patap gabbro-diorites.

	6-8-13-1	6-8-13-2	6-8-13-3a (rim)	6-8-13-3b	6-8-13-3c	6-8-13-3d	6-8-13-3f	6-8-13-3g (core)	6-8-13-4	6-8-13-5c (rim)
Weight Percent										
SiO ₂	55.90	61.37	61.23	61.16	59.81	58.58	55.31	55.73	61.87	55.17
Al ₂ O ₃	26.82	24.57	24.46	24.79	25.17	25.33	26.96	28.31	25.12	27.56
Fe ₂ O _{3t}	0.23	0.27	0.52	0.13	0.26	0.22	0.32	0.36	0.29	0.34
CaO	8.88	5.89	6.39	6.24	6.70	6.91	9.23	9.73	6.15	9.20
Na ₂ O	6.30	8.22	8.06	8.16	7.68	7.87	5.90	5.78	7.80	5.82
K ₂ O	<u>0.10</u>	<u>0.20</u>	<u>0.22</u>	<u>0.41</u>	<u>0.21</u>	<u>0.10</u>	<u>0.17</u>	<u>0.13</u>	<u>0.18</u>	<u>0.12</u>
Total	98.23	100.52	100.88	100.89	99.83	99.01	97.89	100.04	101.41	98.21
Number of ions on the basis of 32 oxygen										
Si	10.216	10.860	10.828	10.804	10.684	10.576	10.156	10.024	10.840	10.092
Al ₃₊	5.776	5.124	5.096	5.160	5.300	5.388	5.832	6.000	5.184	5.940
Fe ³⁺	0.032	0.032	0.068	0.016	0.032	0.028	0.040	0.044	0.036	0.044
Ca	1.736	1.116	1.208	1.180	1.280	1.336	1.816	1.876	1.152	1.800
Na	2.228	2.820	2.764	2.792	2.660	2.752	2.100	2.012	2.648	2.064
K	0.020	0.044	0.048	0.092	0.048	0.024	0.036	0.028	0.036	0.024
<u>Ca</u>	<u>43.6</u>	<u>28.0</u>	<u>30.0</u>	<u>29.0</u>	<u>32.1</u>	<u>32.5</u>	<u>46.0</u>	<u>47.9</u>	<u>30.0</u>	<u>46.3</u>
<u>Na+K+Ca</u>										

Wavelength dispersive analyses on the Applied Research Laboratory (ARL) electron microprobe at the University of Oregon by Gary B. Sidder. Acceleration potential, 15kV; sample current, 0.012uA; beam diameter, 10um; count time, 20 seconds. Measured X-ray intensities were corrected for detector dead-time, background, and matrix effects using a Bence-Albee correction technique with alpha factors by Albee and Ray (1970).

Albee, A. L., and Ray, L, 1970, Correction factors for electron probe microanalysis of silicates, oxides, carbonates, phosphates, and sulfates: Analytical Chemistry, V. 42, p. 1409-1414.

Appendix 2. (cont.)

	6-8-13-5a	6-8-13-5 (core)	6-8-13-6	6-8-13-7	6-8-13-8b (rim)	6-8-13-8a (core)	6-8-13-9a (rim)	6-8-13-9b	6-8-13-9c	6-8-13-9d
Weight Percent										
SiO ₂	54.87	55.19	55.82	58.31	58.29	56.32	55.52	57.02	54.93	55.51
Al ₂ O ₃	27.69	26.49	27.88	27.51	27.34	26.24	26.91	27.13	28.87	29.05
Fe ₂ O _{3t}	0.51	0.40	0.39	0.32	0.28	0.31	0.44	0.36	0.28	0.47
CaO	10.27	8.99	9.93	9.16	9.24	8.70	8.92	8.88	10.21	10.72
Na ₂ O	5.41	5.86	6.49	6.34	6.58	5.64	6.35	6.26	5.48	5.52
K ₂ O	<u>0.16</u>	<u>0.13</u>	<u>0.12</u>	<u>0.16</u>	<u>0.17</u>	<u>0.11</u>	<u>0.13</u>	<u>0.11</u>	<u>0.14</u>	<u>0.13</u>
Total	98.91	97.06	100.63	101.80	101.90	97.32	98.27	99.76	99.91	101.40
Number of ions on the basis of 32 oxygen										
Si	10.008	10.212	10.020	10.276	10.276	10.348	10.164	10.252	9.904	9.888
Al	5.948	5.776	5.896	5.712	5.680	5.680	5.804	5.748	6.136	6.096
Fe ³⁺	0.068	0.052	0.052	0.040	0.036	0.040	0.060	0.048	0.036	0.060
Ca	2.004	1.780	1.908	1.728	1.744	1.712	1.748	1.708	1.972	2.044
Na	1.912	2.100	2.260	2.164	2.244	2.008	2.252	2.180	1.912	1.904
K	0.036	0.028	0.024	0.036	0.036	0.024	0.028	0.024	0.028	0.028
<u>Ca</u> <u>Na+K+Ca</u>	50.7	45.5	45.5	44.0	43.3	45.7	43.4	43.7	50.4	51.4

Appendix 2. (cont.)

	6-8-13-9e (core)	12-2-22-1	12-2-22-2	12-2-22-3c (outer to inner core)	12-2-22-3a (inner core)	12-2-22-4a (film)	12-2-22-4b (core)	D-1-1	D-1-2
Weight Percent									
SiO ₂	55.91	56.85	55.29	54.17	54.02	58.92	54.00	57.08	56.35
Al ₂ O ₃	28.81	26.68	27.90	26.98	29.09	25.39	28.85	27.45	27.85
Fe ₂ O _{3t}	0.43	0.51	0.32	0.44	0.48	0.71	0.40	0.40	0.58
CaO	10.95	8.87	10.01	9.94	11.24	6.75	11.20	9.58	9.94
Na ₂ O	5.84	6.27	5.07	5.36	5.25	6.38	4.85	6.30	5.75
K ₂ O	<u>0.15</u>	<u>0.27</u>	<u>0.18</u>	<u>0.14</u>	<u>0.09</u>	<u>1.05</u>	<u>0.09</u>	<u>0.33</u>	<u>0.40</u>
Total	102.09	99.45	98.77	97.03	100.17	99.20	99.39	101.14	100.87
Number of ions on the basis of 32 oxygen									
Si	9.908	10.276	10.056	10.060	9.764	10.268	9.812	10.172	10.080
Al	6.016	5.684	5.980	5.904	6.196	5.396	6.176	5.764	5.872
Fe ₃₊	0.056	0.068	0.044	0.060	0.064	0.096	0.052	0.052	0.076
Ca	2.076	1.716	1.948	1.976	2.176	1.304	2.180	1.828	1.904
Na	2.004	2.196	1.788	1.928	1.836	2.228	1.708	2.176	1.992
K	0.032	0.060	0.040	0.032	0.020	0.240	0.020	0.088	0.088
<u>Ca</u> <u>Na+K+Ca</u>	50.5	43.2	51.6	54.0	50.2	34.6	55.8	44.7	47.8

Appendix 2. (cont.)

	D-1-3	D-1-5	D-1-6a (rim)	D-1-6b (core)	K-10-2	K-10-10
Weight Percent						
SiO ₂	55.26	55.27	56.82	55.92	53.54	55.71
Al ₂ O ₃	28.94	27.91	27.98	28.18	28.23	27.88
Fe ₂ O _{3t}	0.46	0.39	0.43	0.37	0.27	0.31
CaO	11.02	10.23	9.78	10.15	10.98	10.28
Na ₂ O	5.00	5.86	6.17	5.49	5.29	5.74
K ₂ O	<u>0.33</u>	<u>0.32</u>	<u>0.13</u>	<u>0.44</u>	<u>0.11</u>	<u>0.10</u>
Total	101.01	99.98	101.31	100.55	98.42	100.02
Number of ions on the basis of 32 oxygen						
Si	9.884	9.988	10.100	10.028	9.828	10.027
Al ₃₊	6.100	5.944	5.860	5.956	6.104	5.914
Fe ³⁺	0.060	0.052	0.056	0.048	0.037	0.043
Ca	2.108	1.980	1.860	1.948	2.160	1.982
Na	1.732	2.052	2.124	1.904	1.884	2.004
K	0.072	0.072	0.028	0.100	0.026	0.023
<u>Ca</u> <u>Na+K+Ca</u>	53.9	48.2	46.4	49.3	53.1	49.4

APPENDIX 3

ELECTRON MICROPROBE COMPOSITIONS OF CLINOPYROXENE
IN THE PATAP GABBRO-DIORITES

Appendix 3. Electron microprobe compositions of clinopyroxene in the Patap gabbro-diorites.

	6-8-13-1	6-8-13-3	6-8-13-4	6-8-13-6	6-8-13-7	6-8-13-8	6-8-13-9	6-8-13-10	6-8-13-12	6-8-13-12a
Weight Percent										
SiO ₂	53.53	54.11	54.53	52.31	51.73	53.12	53.47	54.66	54.43	55.10
TiO ₂	≤0.04	0.07	≤0.04	0.09	0.06	0.04	≤0.04	≤0.04	≤0.04	≤0.04
Al ₂ O ₃	0.36	0.38	0.67	0.30	0.25	0.29	0.25	0.37	0.34	0.23
FeO _t	5.87	6.22	7.78	6.05	6.19	5.43	5.17	5.39	5.83	5.71
MnO	0.21	0.11	0.26	0.23	0.14	0.24	0.16	0.20	0.14	0.21
MgO	16.09	15.91	15.60	15.07	15.45	16.81	16.55	16.59	15.86	16.26
CaO	22.76	21.89	23.46	24.06	23.30	23.71	21.53	24.30	22.99	25.31
Na ₂ O	<u>0.41</u>	<u>0.30</u>	<u>0.33</u>	<u>0.32</u>	<u>0.21</u>	<u>0.30</u>	<u>0.26</u>	<u>0.36</u>	<u>0.24</u>	<u>0.19</u>
Total	99.23	98.99	102.72*	98.43	97.33	99.94	97.39	101.87	99.92**	103.01
Number of ions on the basis of 6 oxygen										
Si	1.986	2.005	1.972	1.971	1.969	1.962	2.005	1.976	2.001	1.976
Al ^{IV}	<u>0.014</u>	-	<u>0.028</u>	<u>0.013</u>	<u>0.011</u>	<u>0.012</u>	-	<u>0.016</u>	-	<u>0.010</u>
T=	<u>2.00</u>	<u>2.01</u>	<u>2.00</u>	<u>1.98</u>	<u>1.98</u>	<u>1.97</u>	<u>2.00</u>	<u>1.99</u>	<u>2.00</u>	<u>1.99</u>
Al ^{VI}	0.001	0.016	-	-	-	-	0.011	-	0.015	-
Ti	-	0.002	-	0.002	0.002	0.001	-	-	-	-
Fe ²⁺	0.182	0.193	0.235	0.191	0.197	0.168	0.162	0.163	0.179	0.171
Mn	0.007	0.003	0.008	0.007	0.004	0.007	0.005	0.006	0.004	0.006
Mg	0.890	0.879	0.841	0.846	0.877	0.925	0.925	0.894	0.869	0.869
Ca	0.904	0.869	0.909	0.971	0.950	0.938	0.865	0.941	0.906	0.972
Na	<u>0.029</u>	<u>0.022</u>	<u>0.023</u>	<u>0.024</u>	<u>0.015</u>	<u>0.022</u>	<u>0.019</u>	<u>0.025</u>	<u>0.017</u>	<u>0.013</u>
M1+M2=	<u>2.02</u>	<u>1.98</u>	<u>2.02</u>	<u>2.04</u>	<u>2.06</u>	<u>2.06</u>	<u>1.99</u>	<u>2.03</u>	<u>1.99</u>	<u>2.03</u>
Mg	44.9	45.2	42.2	42.0	43.2	45.4	47.3	44.6	44.5	43.1
Fe+Mn	9.5	10.1	12.2	9.8	9.9	8.6	8.5	8.5	9.2	8.8
Ca	45.6	44.7	45.6	48.2	46.8	46.0	44.2	46.9	46.3	48.2

*Total includes CoO 0.09

**Total includes K₂O 0.09

Appendix 3. (cont.)

	10-2-21-3	10-2-21-4	10-2-21-5	10-2-21-6	10-2-21-8	10-2-21-10b	1-32-15-7	1-32-15-8
Weight Percent								
SiO ₂	52.78	53.91	54.69	54.47	53.65	54.59	55.53	53.99
TiO ₂	< 0.04	< 0.04	< 0.04	< 0.04	0.08	< 0.04	< 0.04	< 0.04
Al ₂ O ₃	0.35	0.24	0.27	1.00	0.45	0.16	0.42	0.30
FeO _t	4.50	6.27	5.81	5.26	4.81	4.56	5.16	5.26
MnO	0.19	0.20	0.15	0.18	0.11	0.12	0.23	0.05
MgO	16.12	14.88	15.96	15.53	16.52	16.93	16.19	15.71
CaO	25.05	24.18	25.20	23.47	23.86	24.07	24.58	24.56
Na ₂ O	<u>0.19</u>	<u>0.16</u>	<u>0.13</u>	<u>0.16</u>	<u>0.21</u>	<u>0.10</u>	<u>0.14</u>	<u>0.14</u>
Total	99.18	99.84	102.21	100.07	99.78*	100.53	102.25	99.96
Number of ions on the basis of 6 oxygen								
Si	1.963	1.996	1.977	1.994	1.977	1.989	1.992	1.986
Al ^{IV}	<u>0.015</u>	<u>0.004</u>	<u>0.012</u>	<u>0.006</u>	<u>0.020</u>	<u>0.007</u>	<u>0.008</u>	<u>0.013</u>
T _Σ	1.98	2.00	1.99	2.00	2.00	2.00	2.00	2.00
Al ^{VI}	-	0.006	-	0.037	-	-	0.010	-
Ti	-	-	-	-	0.002	-	-	-
Fe ²⁺	0.140	0.194	0.176	0.161	0.148	0.139	0.155	0.162
Mn	0.006	0.006	0.005	0.005	0.003	0.004	0.007	-
Mg	0.893	0.821	0.860	0.847	0.907	0.920	0.866	0.861
Ca	0.998	0.959	0.976	0.921	0.942	0.939	0.945	0.968
Na	<u>0.014</u>	<u>0.012</u>	<u>0.009</u>	<u>0.011</u>	<u>0.015</u>	<u>0.007</u>	<u>0.010</u>	<u>0.010</u>
M1+M2 _Σ	2.05	2.00	2.03	1.98	2.02	2.01	1.99	2.00
Mg	43.8	41.5	42.7	43.8	45.4	46.0	44.1	43.2
Fe+Mn	7.2	10.1	8.9	8.6	7.5	7.1	7.9	8.1
Ca	49.0	48.4	48.4	47.6	47.1	46.9	48.1	48.6

*Total includes CoO 0.09

Wavelength dispersive analyses on the ARL probe at the University of Oregon by G. B. Sidders. Conditions of operation as cited in Appendix 2, except beam diameter, 2- μ m, and sample current, 0.015 μ A.

APPENDIX 4

ELECTRON MICROPROBE COMPOSITIONS OF AMPHIBOLES IN THE PATAP GABBRO-DIORITES AND IN ORE

Appendix 4. Electron microprobe compositions of amphiboles in the
Patap gabbro-diorites and in ore.

	6-8-13-2 act-hbl*	6-8-13-15 act-hbl	10-2-21-2a act-hbl	10-2-21-10 act-hbl	X-7-1 act*	X-7-2 act	X-7-3 act
Weight Percent							
SiO ₂	55.33	52.68	50.76	52.37	55.15	54.99	57.28
TiO ₂	≤0.04	0.37	0.04	0.05	0.02	0.13	0.02
Al ₂ O ₃	10.77	4.51	5.07	4.85	1.84	1.84	2.85
FeO _t	7.19	11.14	14.81	13.30	8.96	9.47	11.80
MnO	0.08	0.10	0.13	0.12	0.07	0.06	0.08
MgO	15.82	16.98	14.87	16.31	18.44	17.83	17.53
CaO	12.68	12.00	12.54	12.29	13.06	13.03	12.50
Na ₂ O	0.27	0.66	0.48	0.44	0.30	0.35	0.27
K ₂ O	0.42	0.13	0.42	0.17	0.03	0.12	0.10
Cl	0.07	0.16	0.41	0.05	n. a.	n. a.	n. a.
Total	102.63	98.87**	99.53***	99.95	97.86	97.83	102.41
Number of ions on the basis of 23 oxygen							
Si	7.328	7.465	7.319	7.407	7.786	7.789	7.778
Al ^{IV}	0.672	0.535	0.681	0.593	0.214	0.211	0.222
T=	8.000	8.000	8.000	8.000	8.000	8.000	8.000
Al ^{VI}	1.010	0.218	0.181	0.215	0.091	0.096	0.233
Ti	-	0.039	0.005	0.005	0.001	0.014	-
Fe ²⁺	0.797	1.151	1.617	1.342	1.028	1.121	1.220
Mn	0.009	-	-	-	-	0.004	-
Mg	3.125	3.586	3.197	3.438	3.880	3.765	3.547
M1-M3=	4.941	5.000	5.000	5.000	5.000	5.000	5.000
Fe ²⁺	-	0.170	0.169	0.232	0.030	-	0.120
Mn	-	0.012	0.015	0.014	0.007	0.003	0.009
Ca	1.799	1.822	1.938	1.862	1.975	1.977	1.818
Na	0.068	-	-	-	-	0.020	0.053
M4=	1.867	2.014	2.132	2.108	2.012	2.000	2.000
Na	-	0.181	0.134	0.121	0.082	0.075	0.018
K	0.070	0.024	0.077	0.031	0.005	0.021	0.017
A=	0.070	0.205	0.211	0.151	0.087	0.096	0.035
Mg							
Fe+Mg	0.797	0.731	0.642	0.686	0.786	0.771	0.726

*act-hbl = actinolitic hornblende; act = actinolite

**Total includes Cr₂O₃ 0.05, CoO 0.09.

***Total includes CoO 0.10

Appendix 4. (cont.)

	X-7-4 act	K-10-1 act	K-10-2 act	K-10-3 act	K-10-4 act	K-10-5 act	K-10-6 act	K-10-7 act
Weight Percent								
SiO ₂	55.37	53.54	53.87	54.09	55.36	56.98	54.18	54.50
TiO ₂	0.20	0.21	0.23	0.16	0.20	0.04	0.38	0.13
Al ₂ O ₃	2.46	3.07	2.23	2.09	2.00	2.94	2.89	2.54
FeO _t	10.35	12.45	11.60	11.17	11.90	10.68	11.37	11.99
MnO	0.12	0.14	0.09	0.13	0.08	0.10	0.11	0.15
MgO	17.91	16.58	17.89	17.51	17.88	18.63	17.47	17.06
CaO	12.80	12.36	12.25	12.35	12.47	12.26	12.17	12.19
Na ₂ O	0.40	0.38	0.31	0.36	0.29	0.13	0.44	0.28
K ₂ O	0.15	0.08	0.10	0.19	0.14	0.12	0.19	0.18
Cl	<u>n. a.</u>	<u>0.13</u>	<u>0.09</u>	<u>0.11</u>	<u>0.07</u>	<u>0.12</u>	<u>0.12</u>	<u>0.15</u>
Total	99.77	98.94	98.66	98.16	100.39	102.00	99.32	99.17

Number of ions on the basis of 23 oxygen								
Si	7.716	7.602	7.637	7.698	7.707	7.728	7.620	7.692
Al ^{IV}	<u>0.284</u>	<u>0.398</u>	<u>0.363</u>	<u>0.302</u>	<u>0.293</u>	<u>0.272</u>	<u>0.380</u>	<u>0.308</u>
T=	8.000	8.000	8.000	8.000	8.000	8.000	8.000	8.000
Al ^{VI}	0.120	0.116	0.010	0.049	0.035	0.198	0.099	0.114
Ti	0.020	0.022	0.025	0.017	0.021	0.004	0.040	0.013
Fe ²⁺	1.139	1.353	1.183	1.220	1.232	1.032	1.198	1.283
Mn	-	-	-	-	-	-	-	-
Mg	<u>3.721</u>	<u>3.509</u>	<u>3.782</u>	<u>3.714</u>	<u>3.712</u>	<u>3.766</u>	<u>3.663</u>	<u>3.590</u>
M1-M3=	5.000	5.000	5.000	5.000	5.000	5.000	5.000	5.000
Fe ²⁺	0.067	0.126	0.192	0.109	0.153	0.179	0.139	0.132
Mn	0.013	0.016	0.011	0.015	0.010	0.011	0.013	0.018
Ca	1.911	1.880	1.860	1.883	1.859	1.781	1.834	1.843
Na	<u>0.009</u>	-	-	-	-	<u>0.029</u>	<u>0.014</u>	<u>0.007</u>
M4=	2.000	2.022	2.063	2.007	2.022	2.000	2.000	2.000
Na	0.098	0.104	0.085	0.099	0.079	0.005	0.107	0.069
K	<u>0.027</u>	<u>0.015</u>	<u>0.018</u>	<u>0.035</u>	<u>0.025</u>	<u>0.005</u>	<u>0.034</u>	<u>0.032</u>
A=	0.125	0.119	0.103	0.134	0.104	0.010	0.141	0.101
<u>Mg</u>								
<u>Fe+Mg</u>	0.755	0.703	0.733	0.736	0.728	0.757	0.733	0.717

Appendix 4. (cont.)

	1-32-15-1 act	15-32-30-1 act	15-32-30-2 act	15-32-30-3 act	10-2-21-2 act	D-1-4 act	D-1-6 act
Weight Percent							
SiO ₂	55.73	53.93	56.74	55.68	53.31	54.30	54.99
TiO ₂	0.04	0.06	0.09	0.08	0.04	0.13	0.09
Al ₂ O ₃	3.69	2.78	0.52	4.02	3.83	1.46	0.89
FeO _t	12.46	9.69	11.14	8.53	12.36	9.43	13.66
MnO	0.07	0.09	0.08	0.12	0.14	0.36	0.51
MgO	16.37	17.93	17.94	18.32	16.96	20.05	17.67
CaO	12.03	12.67	13.00	12.83	12.72	11.44	12.34
Na ₂ O	0.10	0.34	0.11	0.21	0.33	0.18	0.18
K ₂ O	0.28	0.05	0.04	0.13	0.16	0.05	0.05
Cl	<u>0.22</u>	<u>0.07</u>	<u>0.05</u>	<u>0.12</u>	<u>0.06</u>	<u>0.08</u>	<u>0.23</u>
Total	100.99	97.61	99.67	100.04	99.87	97.43	100.61
Number of ions on the basis of 23 oxygen							
Si	7.706	7.658	7.924	7.649	7.514	7.707	7.738
Al ^{IV}	<u>0.294</u>	<u>0.342</u>	<u>0.076</u>	<u>0.351</u>	<u>0.486</u>	<u>0.245</u>	<u>0.147</u>
T=	8.000	8.000	8.000	8.000	8.000	7.952	7.885
Al ^{VI}	0.307	0.124	0.010	0.299	0.150	-	-
Ti	0.004	0.006	0.009	0.009	-	0.014	0.010
Fe ²⁺	1.315	1.074	1.247	0.939	1.287	0.742	1.282
Mn	-	-	-	-	-	-	-
Mg	<u>3.374</u>	<u>3.796</u>	<u>3.734</u>	<u>3.753</u>	<u>3.563</u>	<u>4.243</u>	<u>3.708</u>
M1-M3=	5.000	5.000	5.000	5.000	5.000	5.000	5.000
Fe ²⁺	0.126	0.076	0.054	0.041	0.171	0.376	0.325
Mn	0.009	0.011	0.010	0.014	0.017	0.043	0.061
Ca	1.781	1.927	1.945	1.888	1.921	1.740	1.861
Na	<u>0.027</u>	-	-	<u>0.056</u>	-	-	-
M4=	1.943	2.014	2.009	1.999	2.108	2.159	2.247
Na	-	0.095	0.030	-	0.090	0.049	0.049
K	<u>0.049</u>	<u>0.009</u>	-	<u>0.023</u>	<u>0.029</u>	-	<u>0.009</u>
A=	0.049	0.104	0.030	0.023	0.119	0.049	0.058
<u>Mg</u>							
Fe+Mg	0.701	0.767	0.742	0.793	0.710	0.791	0.698

Appendix 4. (cont.)

	10-2-21-9 ?mg-hbl?*	10-2-21-10A ?mg-hbl?	10-2-21-11 ?mg-hbl?	D-1-2 ?mg-hbl?	1-32-15-3 ?mg-hbl?	1-32-15-4 ?ed-hbl?*
Weight Percent						
SiO ₂	53.06	51.36.	44.54	43.86	48.98	46.00
TiO ₂	0.07	0.75	0.15	0.06	0.90	1.15
Al ₂ O ₃	6.29	6.29	5.59	8.88	6.80	9.27
FeO _t	15.36	11.88	13.22	20.06	8.38	11.09
MnO	0.16	0.10	0.13	0.59	0.06	0.13
MgO	16.90	17.50	16.66	15.09	17.66	15.85
CaO	12.00	12.47	12.06	8.26	12.42	12.25
Na ₂ O	0.34	0.91	0.64	0.10	1.14	1.97
K ₂ O	0.79	0.24	0.29	0.12	0.26	0.57
Cl	<u>1.09</u>	<u>0.21</u>	<u>0.36</u>	<u><0.03</u>	<u>0.08</u>	<u>0.34</u>
Total	106.06	101.71	97.02	93.64	96.82	98.62

Number of ions on the basis of 23 oxygen						
Si	7.212	7.134	6.874	6.619	7.060	6.674
Al ^{IV}	<u>0.788</u>	<u>0.866</u>	<u>1.017</u>	<u>1.381</u>	<u>0.940</u>	<u>1.326</u>
T=	8.000	8.000	7.891	8.000	8.000	8.000
Al ^{VI}	0.220	0.164	-	0.198	0.216	0.255
Ti	0.007	0.079	0.018	0.007	0.097	0.125
Fe ²⁺	1.349	1.134	1.148	1.400	0.891	1.192
Mn	-	-	-	-	-	-
Mg	<u>3.424</u>	<u>3.623</u>	<u>3.834</u>	<u>3.395</u>	<u>3.796</u>	<u>3.428</u>
M1-M3=	5.000	5.000	5.000	5.000	5.000	5.000
Fe ²⁺	0.397	0.246	0.558	1.132	0.119	0.153
Mn	0.018	0.012	0.017	0.075	0.008	0.016
Ca	1.748	1.856	1.994	1.335	1.917	1.904
Na	-	-	-	-	-	-
M4=	<u>2.163</u>	<u>2.114</u>	<u>2.569</u>	<u>2.542</u>	<u>2.044</u>	<u>2.074</u>
Na	0.090	0.244	0.192	0.029	0.318	0.554
K	<u>0.137</u>	<u>0.043</u>	<u>0.058</u>	<u>0.023</u>	<u>0.048</u>	<u>0.106</u>
A=	0.227	0.288	0.250	0.052	0.366	0.660
Mg						
Fe+Mg	0.662	0.724	0.692	0.573	0.790	0.718

*?mg-hbl? = possibly magnesio-hornblende; ?ed-hbl? = possibly edenitic hornblende.

Wavelength dispersive analyses on the ARL probe at the University of Oregon by G. B. Sidder. Conditions of operation as cited in Appendix 3.

APPENDIX 5

ELECTRON MICROPROBE COMPOSITIONS OF IRON-TITANIUM OXIDES
IN THE PATAP GABBRO-DIORITES AND IN ORE

Appendix 5. Electron microprobe compositions of iron-titanium oxides in the Patap gabbro-diorites and in ore.

	6-8-13-1 mt*	6-8-13-7 mt	6-8-13-7A mt	6-8-13-8A mt	12-2-22-1 mt	12-2-22-3 mt
Weight Percent						
SiO ₂	0.21	0.42	0.19	0.12	0.17	0.13
TiO ₂	0.05	0.08	0.06	1.66	0.04	0.04
Al ₂ O ₃	0.19	0.23	0.20	0.19	0.15	0.17
Cr ₂ O ₃	0.05	0.56	0.50	0.27	-	0.04
Fe ₂ O ₃ **	68.43	66.46	66.76	64.12	68.56	67.56
FeO**	31.23	31.20	30.72	32.24	31.34	30.84
FeO _t ***	92.80	91.00	90.79	89.94	93.03	91.63
MnO	0.10	0.10	0.10	0.05	-	-
MgO	0.07	0.06	0.04	-	-	-
CoO	0.09	0.07	0.09	0.09	0.09	0.08
Total***	93.56	92.52	91.97	92.32	93.48	92.09
Total**	100.42	99.18	98.66	98.74	100.35	98.86

Number of ions on the basis of 4 oxygen

Si	0.0081	0.0163	0.0074	0.0047	0.0065	0.0051
Ti	0.0014	0.0023	0.0018	0.0486	0.0012	0.0012
Al	0.0086	0.0105	0.0092	0.0087	0.0068	0.0078
Cr	0.0015	0.0171	0.0154	0.0083	-	0.0012
Fe ³⁺ ***	1.9709	1.9352	1.9571	1.8766	1.9779	1.9785
Fe ²⁺ ***	0.9995	1.0097	1.0007	1.0487	1.0049	1.0037
Mn	0.0032	0.0033	0.0033	0.0016	-	-
Mg	0.0040	0.0035	0.0023	-	-	-
Co	0.0028	0.0022	0.0028	0.0028	0.0028	0.0025
X _{usp} ^a	0.001	0.002	0.002	0.052	0.001	0.001

*mt = magnetite

**Fe₂O₃ and FeO calculated according to Stormer (1983)

***Total iron analyzed

$$X_{usp}^a = \frac{(n_{Ti,F})(X_{Fe^{2+},S^{2+}})}{(0.5n_{Fe^{3+},F})(X_{Fe^{3+},S^{3+}}) + (n_{Ti,F})(X_{Fe^{2+},S^{2+}})},$$

where n = total cations of element per formula unit(F)

X = mole fraction of an element vs. all other cations of equal charge (S)

after Stormer (1983)

Appendix 5. (cont.)

	12-2-22-5 mt	12-2-22-7 mt	12-2-22-7A mt	12-2-22-8 mt	12-2-22-8A mt	D-1-4 mt
Weight Percent						
SiO ₂	0.27	0.15	0.23	0.15	0.28	0.20
TiO ₂	-	-	-	-	0.05	5.16
Al ₂ O ₃	0.16	0.16	0.17	0.14	0.12	0.21
Cr ₂ O ₃	0.06	-	0.05	-	0.06	0.05
Fe ₂ O ₃ *	67.58	68.59	67.42	67.00	67.78	57.35
FeO*	31.10	31.26	30.88	30.60	31.29	35.31
FeO _t **	91.91	92.98	91.54	90.89	92.28	86.91
MnO	-	-	0.07	-	-	0.22
MgO	-	-	-	-	-	-
CoO	0.09	0.07	0.08	-	0.08	0.21
Total**	92.49	93.36	92.14	91.18	92.87	92.96
Total*	99.26	100.23	98.90	97.89	99.66	98.71
Number of ions on the basis of 4 oxygen						
Si	0.0105	0.0058	0.0089	0.0059	0.0108	0.0078
Ti	-	-	-	-	0.0015	0.1504
Al	0.0073	0.0072	0.0078	0.0065	0.0055	0.0096
Cr	0.0018	-	0.0015	-	0.0018	0.0015
Fe ³⁺ *	1.9699	1.9812	1.9728	1.9817	1.9682	1.6725
Fe ²⁺ *	1.0077	1.0036	1.0041	1.0059	1.0098	1.1445
Mn	-	-	0.0023	-	-	0.0072
Mg	-	-	-	-	-	-
Co	0.0028	0.0022	0.0025	-	0.0025	0.0065
X' _{usp}	0.000	0.000	0.000	0.000	0.002	0.152

*Fe₂O₃ and FeO calculated

**Total iron analyzed

Appendix 5. (cont.)

	D-1-5B mt	D-1-7 mt	X-7-1 mt	X-7-2 mt	^{Flm} X-7-3A mt	X-7-3B mt	X-7-3C mt
Weight Percent							
SiO ₂	0.18	0.20	n.a.	n.a.	n.a.	n.a.	n.a.
TiO ₂	1.84	2.07	0.05	0.13	0.05	0.06	0.05
Al ₂ O ₃	0.26	0.25	0.18	0.65	0.32	0.48	0.14
Cr ₂ O ₃	0.06	0.10	-	-	0.01	0.01	-
V ₂ O ₃	n.a.	n.a.	0.12	0.08	0.06	0.02	0.10
Fe ₂ O ₃ *	63.18	62.45	68.87	65.80	70.00	67.73	68.99
FeO*	32.18	32.23	31.09	28.80	31.78	30.06	30.93
FeO _t **	89.03	88.42	93.06	88.01	94.76	91.01	93.00
MnO	-	0.11	-	0.01	0.03	0.02	0.01
MgO	-	-	0.09	0.87	0.02	0.47	0.19
CoO	<u>0.21</u>	<u>0.19</u>	<u>n.a.</u>	<u>n.a.</u>	<u>n.a.</u>	<u>n.a.</u>	<u>n.a.</u>
Total**	91.58	91.34	93.50	89.75	95.26	92.07	93.49
Total*	97.91	97.60	100.40	96.34	102.27	98.85	100.41
Number of ions on the basis of 4 oxygen							
Si	0.0071	0.0079	-	-	-	-	-
Ti	0.0542	0.0612	0.0013	0.0040	0.0015	0.0017	0.0014
Al	0.0120	0.0116	0.0083	0.0305	0.0141	0.0218	0.0063
Cr	0.0019	0.0031	-	-	0.0002	0.0001	-
V	-	-	0.0035	0.0027	0.0019	0.0007	0.0032
Fe ³⁺ *	1.8636	1.8472	1.9855	1.9589	1.9807	1.9740	1.9877
Fe ²⁺ *	1.0547	1.0594	0.9660	0.9527	0.9993	0.9737	0.9902
Mn	-	0.0037	-	0.0002	0.0010	0.0006	0.0002
Mg	-	-	0.0054	0.0510	0.0012	0.0273	0.0110
Co	0.0066	0.0060	-	-	-	-	-
X' usp	0.055	0.062	0.001	0.004	0.002	0.002	0.001

*Fe₂O₃ and FeO calculated

**Total iron analyzed

Appendix 5. (cont.)

	X-7-3D core mt	F-3-1 mt	F-3-2 mt	F-3-3 mt	F-3-4 mt
Weight Percent					
SiO ₂	n.a.	n.a.	n.a.	n.a.	n.a.
TiO ₂	0.04	0.03	0.27	0.03	0.02
Al ₂ O ₃	0.25	0.11	0.09	0.06	0.16
Cr ₂ O ₃	0.01	0.03	-	-	-
V ₂ O ₃	0.01	0.11	0.14	0.19	0.12
Fe ₂ O ₃ *	68.22	69.68	69.44	69.25	69.80
FeO*	30.64	31.54	31.84	31.32	31.51
FeO _t **	92.03	94.25	94.32	93.62	94.31
MnO	0.01	0.01	0.02	0.03	0.03
MgO	0.17	-	-	-	0.04
CoO	<u>n.a.</u>	<u>n.a.</u>	<u>n.a.</u>	<u>n.a.</u>	<u>n.a.</u>
Total*	92.52	94.54	94.83	93.94	94.68
Total**	99.35	101.52	101.79	100.88	101.67

Number of ions on the basis of 4 oxygen

Si	-	-	-	-	-
Ti	0.0013	0.0009	0.0077	0.0009	0.0005
Al	0.0113	0.0050	0.0038	0.0029	0.0070
Cr	0.0004	0.0008	-	-	-
V	0.0002	0.0033	0.0043	0.0058	0.0036
Fe ³⁺	1.9857	1.9890	1.9766	1.9895	1.9883
Fe ²⁺	0.9911	1.0006	1.0072	0.9999	0.9974
Mn	0.0001	0.0003	0.0005	0.0010	0.0010
Mg	0.0100	-	-	-	0.0021
Co	-	-	-	-	-
X' usp	0.001	0.001	0.008	0.001	0.001

*Fe₂O₃ and FeO calculated

**Total iron analyzed

Wavelength dispersive analyses on the ARL probe at the University of Oregon by G. B. Sidder. Conditions of operation as cited in Appendix 3, except count time, 40 seconds for Si, Cr, V, Mn, Co

Appendix 5. (cont.)

	6-8-13-3 ilm*	6-8-13-4 ilm	6-8-13-4A ilm	6-8-13-8 ilm	12-2-22-6 ilm	12-2-22-6A ilm
Weight Percent						
SiO ₂	0.18	0.12	0.16	0.11	0.12	0.30
TiO ₂	47.25	47.77	47.16	46.98	47.68	49.02
Al ₂ O ₃	0.07	0.09	0.05	0.09	0.05	-
Fe ₂ O ₃ **	9.87	3.02	9.34	10.51	7.15	3.30
FeO**	40.35	41.27	40.67	40.34	39.97	40.70
FeO _t ***	49.23	43.99	49.08	49.80	46.40	43.67
MnO	1.88	1.38	1.33	1.78	2.80	3.27
MgO	0.25	0.24	0.33	0.13	0.12	0.24
CoO	-	-	-	-	-	-
Total***	98.86	93.59	98.11	98.89	97.17	96.50
Total**	99.85	93.89	99.04	99.94	97.89	96.83
Number of ions on the basis of 3 oxygen						
Si	0.0046	0.0032	0.0041	0.0028	0.0031	0.0078
Ti	0.9003	0.9648	0.9053	0.8956	0.9266	0.9598
Al	0.0021	0.0028	0.0015	0.0027	0.0015	-
Fe ³⁺ ***	0.1881	0.0610	0.1795	0.2005	0.1390	0.0647
Fe ²⁺ ***	0.8551	0.9271	0.8683	0.8553	0.8638	0.8862
Mn	0.0403	0.0314	0.0288	0.0382	0.0613	0.0721
Mg	0.0094	0.0096	0.0126	0.0049	0.0046	0.0093
Co	-	-	-	-	-	-
X _{ilm} ^a	0.903	0.969	0.908	0.897	0.928	0.966

*ilm = ilmenite

**Fe₂O₃ and FeO calculated according to Stormer (1983)

***Total iron analyzed

$$a_{X_{ilm}} = \frac{((n_{Fe^{2+},F})(n_{Ti,F}))^{1/2}}{(0.5n_{Fe^{3+},F}) + ((n_{Fe^{2+},F})(n_{Ti,F}))^{1/2}}$$

where n = total cations of element per formula unit (F)
after Stormer (1983).

Appendix 5. (cont.)

	D-1-2 ilm	D-1-6 ilm	D-1-6B ilm	D-1-6E ilm	6-8-13-6 hm*	6-8-13-6A hm
Weight Percent						
SiO ₂	0.19	0.14	0.11	0.18	0.13	0.21
TiO ₂	47.55	48.87	47.67	48.89	0.05	0.46
Al ₂ O ₃	0.05	0.13	0.12	0.10	0.32	0.33
Cr ₂ O ₃	-	-	-	-	0.14	0.12
Fe ₂ O ₃ **	8.46	5.36	7.61	5.08	98.61	98.61
FeO**	32.19	29.10	18.75	27.68	0.13	0.67
FeO _t ***	39.80	33.92	25.60	32.25	88.86	89.40
MnO	10.66	14.63	23.71	16.08	0.07	-
MgO	-	0.06	0.06	0.06	-	-
CoO	-	0.09	0.13	0.11	-	-
Total***	98.25	97.84	97.40	97.67	89.57	90.52
Total**	99.10	98.39	98.16	98.18	99.45	100.40
Number of ions on the basis of 3 oxygen						
Si	0.0049	0.0036	0.0028	0.0046	0.0035	0.0055
Ti	0.9131	0.9428	0.9217	0.9448	0.0010	0.0091
Al	0.0015	0.0039	0.0036	0.0030	0.0101	0.0103
Cr	-	-	-	-	0.0030	0.0025
Fe ³⁺ ***	0.1626	0.1034	0.1473	0.0982	1.9781	1.9579
Fe ²⁺ ***	0.6874	0.6243	0.4032	0.5948	0.0028	0.0147
Mn	0.2306	0.3179	0.5164	0.3500	0.0016	-
Mg	-	0.0023	0.0023	0.0023	-	-
Co	-	0.0019	0.0027	0.0023	-	-
X' _{ilm}	0.907	0.937	0.892	0.939	0.002	0.012

*hm = hematite

**Fe₂O₃ and FeO calculated

***Total iron analyzed

Appendix 5. (cont.)

	6-8-13-9 hm	12-2-22-2 hm	12-2-22-2A hm	12-2-22-6B hm	D-1-4A hm	D-1-5A hm
Weight Percent						
SiO ₂	0.35	0.14.	0.17	0.17	0.30	0.47
TiO ₂	0.08	-	0.05	0.13	0.52	0.25
Al ₂ O ₃	0.21	0.13	0.13	0.15	0.27	0.41
Cr ₂ O ₃	0.08	-	0.08	0.06	-	-
Fe ₂ O ₃ *	98.80	98.03	100.30	99.53	96.40	94.24
FeO*	0.31	0.17	0.18	0.32	0.56	0.50
FeO _t **	89.21	88.38	90.43	89.88	87.31	85.30
MnO	0.07	-	0.07	-	0.06	-
MgO	-	-	-	-	-	-
CoO	0.12	-	-	-	0.21	0.30
Total**	90.12	88.65	90.93	90.39	88.67	86.73
Total*	100.02	98.47	100.98	100.36	98.32	96.17
Number of ions on the basis of 3 oxygen						
Si	0.0093	0.0038	0.0045	0.0045	0.0081	0.0129
Ti	0.0016	-	0.0010	0.0026	0.0105	0.0052
Al	0.0066	0.0041	0.0040	0.0047	0.0086	0.0133
Cr	0.0017	-	0.0017	0.0013	-	-
Fe ³⁺	1.9700	1.9883	1.9834	1.9799	1.9542	1.9505
Fe ²⁺	0.0068	0.0038	0.0039	0.0071	0.0127	0.0115
Mn	0.0016	-	0.0016	-	0.0014	-
Mg	-	-	-	-	-	-
Co	0.0025	-	-	-	0.0045	0.0066
X' _{ilm}	0.003	0.000	0.002	0.004	0.012	0.008

*Fe₂O₃ and FeO calculated

**Total iron analyzed

Appendix 5. (cont.)

	D-1-3 fpsb*	D-1-6D fpsb	6-8-13-5 sphene	12-2-22-4 sphene
Weight Percent				
SiO ₂	1.04	1.33	29.83	29.54
TiO ₂	54.59	59.43	33.67	34.42
Al ₂ O ₃	1.00	0.29	1.02	1.06
Cr ₂ O ₃	-	-	-	-
Fe ₂ O ₃ **	7.37	8.65		
FeO**	21.66	24.45		
FeO _t ***	28.29	32.23	1.22	1.40
MnO	1.32	0.90	-	-
MgO	0.09	0.06	0.03	-
CoO	-	-	-	-
CaO	-	-	26.5 ^a	26.5 ^a
Total**	86.62	94.24		
Total***	87.07	95.11	92.3	92.9
Number of ions on the basis of 5 oxygen				
Si	0.0458	0.0538	1.0536	1.0381
Ti	1.8063	1.8077	0.8943	0.9096
Al	0.0519	0.0138	0.0425	0.0439
Cr	-	-	-	-
Fe ³⁺	0.2440	0.2632		
Fe ²⁺	0.7970	0.8270	0.0360	0.0411
Mn	0.0492	0.0308	-	-
Mg	0.0059	0.0036	0.0016	-
Co	-	-	-	-
Ca	-	-	1.0028	0.9977

*fpsb = ferropseudobrookite solid solution

**Fe₂O₃ and FeO calculated

***Total iron analyzed

^aCaO estimated from stoichiometry and Deer et al. (1966)

APPENDIX 6

CHEMICAL ABUNDANCES, MODAL ABUNDANCES, AND NORMATIVE
MINERAL ABUNDANCES OF THE LINGA SUPERUNIT

Appendix 6. Chemical abundances, modal abundances, and normative mineral abundances of the Linga Superunit.

Table 6-A. Chemical abundances* of the Linga Superunit, Unit K_{1a}.

	7-2-13 q.md.**	12-8-13 q.md.	8-2-13 q.m.**	9-2-13 grd**	7-2-22 grd	17-9-10 grd
Weight Percent						
SiO ₂	61.3	61.6	63.1	63.0	64.1	64.5
TiO ₂	0.65	0.67	0.55	0.65	0.60	0.55
Al ₂ O ₃	16.3	16.6	15.7	16.2	15.8	16.5
Fe ₂ O ₃ ***	2.7	n.a.	2.9	n.a.	4.3	1.1
FeO***	3.7	n.a.	2.4	n.a.	2.3	1.5
FeO _t	6.0	5.84	4.7	5.6	5.3	4.1
MgO	2.3	2.4	2.1	2.3	2.1	2.2
CaO	5.1	5.99	4.3	4.9	4.6	6.9
Na ₂ O	4.0	3.9	4.1	4.5	4.7	5.1
K ₂ O	<u>2.8</u>	<u>2.57</u>	<u>3.3</u>	<u>2.3</u>	<u>1.9</u>	<u>0.25</u>
Total	98.45	99.62	97.85	99.45	99.10	100.10
S. G.	2.71	2.70	2.69	2.72	2.71	2.71
ppm						
Cu	11	25	19	19	45	200
Mo	30	<1	7	6	2	2
Pb	70	6	100	50	20	17
Zn	50	25	70	50	20	11
Ag	<0.3	0.3	<0.3	<0.3	<0.3	<0.3
Co	5	6	5	6	5	5
Ba	970	1063	n.a.	n.a.	n.a.	n.a.
Ce	47	55				
Co	18	17				
Cr	13	7				
Cu	10	10				
Ga	17	17				
La	22	29				
Ni	3	5				
Nb	6	6				
Pb	10	11				
Rb	51	36				
Sc	24	22				
Sr	291	363				
Th	12	13				
U	4	3				
V	133	124				
W	n.d.	n.d.				
Y	27	28				
Zn	20	22				
Zr	199	155				
Mo	2	n.d.				

Appendix 6. (cont.)

Table 6-B. Chemical abundances* of the Linga Superunit, Unit K_{1b}.

	11-2-14 q.d.**	6-2-19 q.md.	7-2-19 q.md.	4-9-13 q.d.	P-8 ton**
Weight Percent					
SiO ₂	54.8	56.4	65.0	61.0	59.9
TiO ₂	0.85	0.85	0.60	0.75	0.75
Al ₂ O ₃	18.4	17.4	16.2	17.6	15.7
Fe ₂ O ₃ ***	5.3	4.4	3.4	3.4	5.6
FeO***	3.6	4.5	2.2	1.9	2.8
FeO _t	8.5	8.4	5.7	5.8	8.9
MgO	4.0	3.2	2.2	3.3	2.9
CaO	7.6	6.9	5.1	7.0	6.7
Na ₂ O	4.1	3.6	5.2	5.1	4.9
K ₂ O	<u>1.2</u>	<u>1.9</u>	<u>0.7</u>	<u>0.3</u>	<u>0.3</u>
Total	99.45	98.65	100.70	100.85	100.05
S. G.	2.82	2.75	2.73	2.76	2.72
ppm					
Cu	50	45	40	115	355
Mo	<1	2	3	<1	4
Pb	40	25	12	10	4
Zn	25	30	18	5	10
Ag	0.3	0.3	<0.3	0.5	0.5
Co	11	9	17	8	18

*Major oxides by XRF and AAS by G. B. Sidder, E. Taylor, and R. Lightfoot at Oregon State University. Trace elements Cu to Co by Chemical and Mineralogical Services, Salt Lake City, Utah, and Ba to Mo by J. Injoque at University of Nottingham, England, by AAS and XRF, respectively.

**q.md. = quartz monzodiorite; q.m. = quartz monzonite; grd = granodiorite; q.d. = quartz diorite; ton = tonalite.

***Fe₂O₃ and FeO by Skyline Laboratories, Denver, Colorado, with ferric iron determined by titration and total iron by plasma spectrometry. Ferrous iron determined by difference. FeO_t by XRF at Oregon State University.

Appendix 6. (cont.)

Table 6-C. Modal abundances of Units K_{1a} and K_{1b} in the Linga Superunit. Modes based on 1000 or more points counted.

	7-2-13	12-8-13	8-2-13 ^{K1a}	9-2-13	7-2-22	17-9-10///	11-2-14	6-2-19 ^{K1b}	7-2-19	4-9-13	P-8
	q.md.	q.md.	q.m.	grd	grd	grd	q.d.	q.md.	q.md.	q.d.	ton
	Modal Percent										
Quartz	14.1	14.4	15.5	17.8	18.9	26.3	6.9	7.4	15.5	12.5	15.1
Kspar	19.9	18.0	26.1	20.2	21.5	12.3	5.8	9.1	7.2	3.7	3.3
Plagioclase	45.7	44.4	37.4	42.0	44.3	43.3	55.8	49.6	54.7	55.1	53.2
Clinopyroxene	tr	-	-	-	-	3.0	-	1.0	-	1.0	-
Amphibole	14.6	16.5	13.4	12.4	9.3	12.0	20.6	20.0	17.2	17.1	15.2
Apatite	<1	<1	<1	<1	<1	tr	<1	1.1	<1	<1	tr
Sphene	<1	2.7	1.5	1.3	<1	1.7	<1	tr	1.5	2.7	3.8
Opaque oxides	2.7	1.9	3.1	3.3	3.0	<1	5.7	6.0	3.0	3.7	2.2
Zircon	tr	tr	tr	tr	tr	tr	tr	tr	tr	tr	tr
Epidote	<1	<1	<1	<1	tr	<1	1.3	1.8	<1	<1	<1
Allanite	-	tr	-	-	-	-	tr	tr	-	-	-
Biotite	-	-	-	-	<1	-	-	-	tr	-	-
Scapolite	-	-	-	-	-	-	-	tr	-	2.3	1.8
Chlorite	<1	<1	<1	<1	<1	<1	<1	1.0	<1	<1	2.8
Sericite	1.4	<1	1.3	1.5	<1	tr	1.9	2.8	2.2	1.7	2.4
Tourmaline	-	-	-	-	-	-	-	tr	-	-	-
Albite	tr	-	-	-	-	-	-	-	-	-	-
Calcite	tr	-	tr	-	-	-	-	-	-	-	-

Appendix 6. (cont.)

Table 6-D. CIPW normative mineral abundances in Units K_{1a} and K_{1b} of the Linga Superunit.

	7-2-13	12-8-13	8-2-13	9-2-13	7-2-22	17-9-10	11-2-14	6-2-19	7-2-19	4-9-13	P-8
	Volume Percent										
quartz	13.0	13.4	15.3	14.7	18.0	18.2	5.9	9.1	19.3	12.5	14.4
orthoclase	16.5	15.2	19.5	13.6	11.2	1.5	7.1	11.2	4.1	2.0	2.0
albite	33.8	33.0	34.7	38.1	39.8	43.2	34.7	30.6	44.0	43.2	41.5
anorthite	18.2	20.2	14.7	17.2	16.4	21.4	28.3	25.7	18.8	24.1	19.8
diopside	5.2	7.2	4.8	5.2	4.5	9.7	6.9	6.3	4.6	7.7	9.9
hypersthene	6.8	5.8	4.2	5.6	3.2	2.0	7.6	8.2	3.7	4.6	2.6
magnetite	3.9	4.1	4.2	4.1	5.8	1.6	7.7	6.4	4.9	4.3	7.2
hematite	-	-	-	-	0.3	-	-	-	-	0.5	0.7
ilmenite	<u>1.2</u>	<u>1.3</u>	<u>1.0</u>	<u>1.2</u>	<u>1.1</u>	<u>1.0</u>	<u>1.6</u>	<u>1.6</u>	<u>1.1</u>	<u>1.4</u>	<u>1.4</u>
Total	98.6	100.2	98.4	99.7	100.3	98.8	99.8	99.0	100.5	100.6	99.8
normative An	35.0	38.0	29.7	31.1	29.2	33.1	44.9	45.8	29.9	35.9	32.4

APPENDIX 7

ELECTRON MICROPROBE COMPOSITIONS OF CHALCOPYRITE IN ORE

Appendix 7. Electron microprobe compositions of chalcopyrite in ore.

	D-3-1	D-3-2	D-3-3	D-3-4	D-3-5	5-18-70-1	5-18-70-2	5-18-70-4	5-18-70-5	X-7-1	X-7-2
Weight Percent											
Fe	29.84	30.08	29.95	29.85	29.95	30.31	30.25	30.67	30.45	30.96	29.57
Cu	35.09	34.27	34.52	34.80	34.46	34.04	34.07	34.51	34.14	33.52	34.75
S	35.25	35.37	35.23	34.17	34.81	34.22	34.48	35.06	34.20	34.59	34.16
Ag	0.16	-	-	0.21	0.18	0.16	0.25	0.25	0.22	0.17	0.21
Ni	0.11	0.12	0.10	-	-	0.14	0.14	0.11	0.13	0.10	0.14
Co	0.08	0.08	0.07	0.09	0.09	0.07	0.06	0.06	0.05	0.05	-
Mn	0.03	0.05	-	0.04	0.03	0.03	0.05	0.04	0.04	0.04	0.04
Mo	-	0.26	-	-	-	-	-	-	-	-	0.19
Total	100.56	100.23	99.87	99.16	99.52	98.97	99.30	100.70	99.23	99.43	99.06
Atomic Percent											
Fe	24.4	24.7	24.6	24.9	24.8	25.3	25.2	25.1	25.4	25.7	24.7
Cu	25.3	24.7	24.9	25.5	25.1	25.0	24.9	24.8	25.0	24.4	25.5
S	50.3	50.6	50.4	49.6	50.2	49.7	49.9	50.0	49.6	49.9	49.7
Cu/Fe	1.034	1.001	1.013	1.025	1.011	0.987	0.990	0.989	0.985	0.952	1.033
$\frac{\text{Fe}+\text{Cu}}{\text{S}}$	0.988	0.977	0.983	1.015	0.994	1.011	1.002	0.999	1.015	1.003	1.010

Appendix 7. (cont.)

	X-7-4	X-7-5	X-7-6	X-7-7	X-7-8	L-5-1	L-5-7	L-5-8	1-10-70B-1	1-10-70B-2	DDH-13-20-1
Weight Percent											
Fe	30.48	30.19	30.94	29.86	29.63	30.07	29.11	29.35	30.38	30.60	29.64
Cu	33.74	33.52	32.35	33.68	34.39	33.88	33.89	34.54	34.03	34.43	33.87
S	34.94	34.77	34.78	34.53	34.40	34.40	34.84	34.82	34.56	34.91	33.77
Ag	0.18	0.16	0.16	0.30	-	-	0.17	0.25	0.16	0.21	-
Ni	0.15	0.18	0.20	0.10	0.14	0.11	0.09	-	0.10	0.13	-
Co	0.04	0.08	0.10	0.06	-	0.12	0.09	0.07	0.07	0.10	0.08
Mn	0.03	0.03	0.04	0.03	-	0.03	0.03	-	0.05	-	-
Mo	-	-	-	-	-	-	-	-	-	-	-
Total	99.56	98.93	98.57	98.56	98.56	98.61	98.22	99.03	99.35	100.38	97.36
Atomic Percent											
Fe	25.2	25.1	25.8	25.0	24.7	25.1	24.3	24.4	25.2	25.1	25.1
Cu	24.5	24.5	23.7	24.8	25.2	24.9	24.9	25.2	24.8	24.9	25.2
S	50.3	50.4	50.5	50.3	50.0	50.0	50.7	50.4	50.0	50.0	49.7
Cu/Fe	0.973	0.976	0.919	0.991	1.020	0.990	1.023	1.034	0.985	0.989	1.005
$\frac{\text{Fe}+\text{Cu}}{\text{S}}$	0.988	0.985	0.980	0.989	0.999	0.999	0.971	0.984	1.002	1.001	1.010

Appendix 7. (cont.)

DDH-13-20-2 DDH-13-20-3		
Weight Percent		
Fe	29.91	30.09
Cu	31.21	32.56
S	34.59	34.52
Ag	0.15	-
Ni	0.09	0.08
Co	0.05	0.10
Mn	0.04	-
Mo	-	-
Total	96.04	97.35
Atomic Percent		
Fe	25.4	25.3
Cu	23.3	24.1
S	51.2	50.6
Cu/Fe	0.917	0.951
$\frac{\text{Fe}+\text{Cu}}{\text{S}}$	0.952	0.976

Wavelength dispersive analyses on the ARL probe at the University of Oregon by G. B. Sidder. Conditions of operation as cited in Appendix 3.

APPENDIX 8

ELECTRON MICROPROBE COMPOSITIONS OF PYRITE IN ORE

Appendix 8. Electron microprobe compositions of pyrite in ore.

	D-3-1	D-3-2	D-3-3	D-3-4	D-3-5	D-3-6	5-18-70-1	5-18-70-2	5-18-70-3	X-7-1	X-7-2	X-7-3
Weight Percent												
Fe	44.52	45.21	46.41	44.87	45.07	45.61	47.00	46.44	46.28	46.21	45.88	46.63
S	53.57	53.70	53.42	53.54	53.78	53.55	53.62	52.52	52.94	52.54	52.92	53.15
Co	0.84	0.16	0.07	1.14	0.18	0.74	0.06	-	0.54	0.58	0.17	0.17
Mo	0.69	0.69	0.50	0.55	0.63	0.48	0.54	0.54	0.36	0.55	0.60	0.64
Ni	-	-	-	-	-	-	0.11	-	0.11	-	0.09	-
Mn	-	-	-	-	-	-	-	-	-	-	-	-
Cu	-	-	-	-	-	-	-	-	-	-	-	-
Ag	-	-	-	-	-	-	-	-	-	-	-	-
Total	99.67*	99.76	100.40	100.10	99.66	100.38	101.33	99.50	100.23	99.88	99.66	100.59
Atomic Percent												
Fe	32.3	32.6	33.3	32.5	32.5	32.8	33.5	33.7	33.4	33.6	33.2	33.5
S	67.7	67.4	66.7	67.5	67.5	67.2	66.5	66.3	66.6	66.4	66.8	66.5
Fe/S	0.477	0.483	0.499	0.481	0.481	0.489	0.503	0.508	0.502	0.505	0.498	0.504
<u>metals</u> S	0.490	0.489	0.503	0.496	0.487	0.500	0.513	0.511	0.513	0.514	0.504	0.510

*Total includes As 0.05

Appendix 8. (cont.)

	X-7-4	X-7-5	X-7-6	X-7-7	L-5-1	L-5-2	L-5-3	L-5-4	L-5-5	1-10-70B-1	1-10-70B-2
Weight Percent											
Fe	44.78	45.83	46.86	46.59	44.53	44.78	46.04	46.32	45.04	44.28	47.21
S	53.48	53.44	53.70	53.37	54.26	53.78	54.26	54.43	54.06	53.19	53.54
Co	0.95	0.15	0.07	0.73	0.67	0.75	0.20	0.28	0.58	0.38	0.43
Mo	0.51	0.54	0.43	0.40	0.56	0.66	0.59	0.48	0.56	0.48	0.58
Ni	-	0.14	0.15	-	-	-	-	-	-	-	-
Mn	-	-	-	-	-	-	-	-	-	-	0.03
Cu	-	-	-	-	-	-	-	-	-	0.13	-
Ag	-	-	-	-	-	-	-	-	-	-	-
Total	99.72	100.10	101.21	101.09	100.02	99.97	101.09	101.51	100.24	98.46	101.79
Atomic Percent											
Fe	32.5	33.0	33.4	33.4	32.0	32.3	32.8	32.8	32.4	32.3	33.0
S	67.5	67.0	66.6	66.6	68.0	67.7	67.2	67.2	67.6	67.7	67.0
Fe/S	0.481	0.492	0.501	0.501	0.471	0.478	0.487	0.489	0.478	0.478	0.492
<u>metals</u> S	0.494	0.499	0.506	0.511	0.481	0.490	0.493	0.494	0.488	0.486	0.501

Appendix 8. (cont.)

	DDH-13-20-1	DDH-13-20-2	DDH-13-20-3	DDH-13-20-4	DDH-13-20-5	DDH-13-20-6	DDH-13-20-7
Weight Percent							
Fe	46.20	43.94	46.01	45.71	45.21	45.20	45.55
S	53.70	53.34	52.89	53.30	53.34	53.30	52.30
Co	0.29	1.02	0.13	0.25	0.09	1.09	0.28
Mo	0.60	0.50	0.66	0.50	0.59	0.49	0.76
Ni	-	-	-	-	-	-	-
Mn	-	-	-	-	-	-	-
Cu	-	-	-	-	-	-	-
Ag	-	-	-	-	-	-	-
Total	100.79	98.80	99.69	99.76	99.35*	100.08	98.89
Atomic Percent							
Fe	33.1	32.1	33.3	33.0	32.7	32.7	33.3
S	66.9	67.9	66.7	67.0	67.3	67.3	66.7
Fe/S	0.494	0.473	0.499	0.492	0.487	0.487	0.500
<u>metals</u> S	0.501	0.487	0.505	0.498	0.491	0.501	0.508

*Total includes As 0.12

Wavelength dispersive analyses on the ARL probe at the University of Oregon by G. B. Sidder.
Conditions of operation as cited in Appendix 3.

APPENDIX 9

ELECTRON MICROPROBE COMPOSITIONS OF CUBANITE IN ORE

Appendix 9. Electron microprobe compositions of cubanite in ore.

	L-5-4	L-5-3	L-5-2	DDH-13-20-1	DDH-13-20-2	DDH-13-20-3	X-7-4	X-7-5
Weight Percent								
Fe	39.20	41.13	40.17	40.41	38.78	40.25	40.12	41.09
Cu	21.99	19.76	22.67	21.07	22.27	22.69	22.21	23.16
S	35.11	35.74	35.23	34.93	34.58	34.23	35.77	34.95
Ag	0.16	-	-	-	-	0.15	-	-
Ni	-	0.10	0.09	0.08	-	-	0.12	0.13
Co	0.11	0.10	0.12	0.09	0.10	0.07	0.07	0.06
Mn	0.03	-	-	-	-	0.03	0.03	0.04
Mo	-	-	-	0.21	-	-	-	0.22
Total	96.60	96.83	98.28	96.79	95.73	97.42	98.32	99.65
Atomic Percent								
Fe	32.8	34.1	33.1	33.7	32.7	33.6	32.9	33.6
Cu	16.1	14.4	16.4	15.5	16.5	16.6	16.0	16.6
S	51.1	51.6	50.5	50.8	50.8	49.8	51.1	49.8
Cu/Fe	0.493	0.422	0.496	0.458	0.505	0.495	0.487	0.495
$\frac{\text{Fe}+\text{Cu}}{\text{S}}$	0.957	0.940	0.979	0.969	0.969	1.010	0.957	1.009

Wavelength dispersive analyses on the ARL probe at the University of Oregon by G. B. Sidder.
Conditions of operation as cited in Appendix 3.

APPENDIX 10

ELECTRON MICROPROBE COMPOSITIONS OF PYRRHOTITE IN ORE

Appendix 10. Electron microprobe compositions of pyrrhotite in ore.

	X-7-1	X-7-2	X-7-3	L-5-6
Weight Percent				
Fe	58.31	60.65	60.27	60.16
S	37.52	38.27	38.51	37.99
Co	0.09	0.07	0.09	0.11
Mo	-	0.23	0.39	-
Ni	0.15	0.36	-	-
Mn	-	0.03	0.04	0.03
Cu	-	0.17	0.25	0.52
Ag	-	-	-	-
Total	96.07	99.78	99.55	98.81
Atomic Percent				
Fe	47.2	47.6	47.3	47.6
S	52.8	52.4	52.7	52.4
Fe/S	0.892	0.910	0.899	0.909
<u>metals</u>				
S	0.896	0.921	0.907	0.918

Wavelength dispersive analyses on the ARL probe at the University of Oregon by G. B. Sidder.
Conditions of operation as cited in Appendix 3.

APPENDIX 11

ELECTRON MICROPROBE COMPOSITIONS OF SCAPOLITE
IN THE PATAP GABBRO-DIORITES AND IN ORE

Appendix 11. Electron microprobe compositions of scapolite in the Patap gabbro-diorites and in ore.

	K-10-4	K-10-5	K-10-6	K-10-8	K-10-9	K-10-11	15-32-30-1	15-32-30-2	15-32-30-3	15-32-30-5
Weight Percent										
SiO ₂	55.49	56.10	56.77	56.04	56.15	57.34	57.01	57.57	55.09	54.10
Al ₂ O ₃	22.36	22.81	22.35	22.64	22.83	21.54	21.39	21.60	23.30	23.34
Fe ₂ O ₃ t	0.08	<0.06	<0.06	0.17	<0.06	<0.06	0.09	0.14	<0.06	0.23
CaO	6.98	7.08	6.56	6.98	7.27	5.62	5.66	5.71	8.19	8.16
Na ₂ O	9.75	9.72	10.31	9.61	9.69	10.22	10.14	10.42	8.93	8.83
K ₂ O	0.76	0.81	0.68	0.70	0.71	0.90	0.75	0.84	0.64	0.79
Cl	<u>3.14</u>	<u>2.98</u>	<u>3.27</u>	<u>3.15</u>	<u>2.84</u>	<u>3.59</u>	<u>3.42</u>	<u>3.42</u>	<u>2.75</u>	<u>2.71</u>
Total	98.56	99.50	99.94	99.29	99.49	99.21	98.46	99.69	98.90	98.16

Number of ions on the basis of 12 (Si+Al)

Si	8.137	8.113	8.197	8.129	8.113	8.318	8.321	8.320	8.008	7.955
Al	<u>3.863</u>	<u>3.887</u>	<u>3.803</u>	<u>3.871</u>	<u>3.887</u>	<u>3.682</u>	<u>3.679</u>	<u>3.680</u>	<u>3.992</u>	<u>4.045</u>
	12.000	12.000	12.000	12.000	12.000	12.000	12.000	12.000	12.000	12.000
Ca	1.097	1.097	1.015	1.085	1.125	0.874	0.885	0.884	1.276	1.285
Na	2.772	2.724	2.885	2.704	2.715	2.873	2.868	2.920	2.517	2.516
Fe ³⁺	0.008	0.000	0.000	0.018	0.000	0.000	0.010	0.016	0.000	0.026
K	<u>0.141</u>	<u>0.149</u>	<u>0.125</u>	<u>0.130</u>	<u>0.132</u>	<u>0.167</u>	<u>0.140</u>	<u>0.155</u>	<u>0.118</u>	<u>0.148</u>
	4.018	3.970	4.025	3.937	3.972	3.914	3.903	3.975	3.911	3.975
Cl	0.781	0.729	0.800	0.773	0.696	0.882	0.845	0.838	0.678	0.676
CO ₃ *	<u>0.244</u>	<u>0.226</u>	<u>0.219</u>	<u>0.207</u>	<u>0.257</u>	<u>0.112</u>	<u>0.142</u>	<u>0.187</u>	<u>0.259</u>	<u>0.296</u>
	1.025	0.955	1.019	0.980	0.953	0.994	0.987	1.025	0.937	0.972
Me**	27.4	27.6	25.2	27.7	28.3	22.3	22.7	22.3	32.6	32.5
EqAn***	28.4	28.7	26.0	28.6	29.6	22.7	22.6	22.7	33.1	34.8

*CO₃ calculated from charge balance

**Me = Ca/(Na+K+Ca) after Shaw (1960)

***EqAn = (Al - 3)/3 x 100 after Ellis (1978)

Appendix 11. (cont.)

	15-32-30-6	15-32-30-7
Weight Percent		
SiO ₂	56.60	57.65
Al ₂ O ₃	21.87	22.58
Fe ₂ O _{3t}	40.06	40.06
CaO	6.41	6.87
Na ₂ O	10.22	9.60
K ₂ O	0.74	0.71
Cl	<u>3.33</u>	<u>2.99</u>
Total	99.17	100.40*

Number of ions on the basis of 12 (Si+Al)		
Si	8.245	8.210
Al	<u>3.755</u>	<u>3.790</u>
	12.000	12.000
Ca	1.000	1.049
Na	2.886	2.650
Fe ³⁺	0.000	0.000
K	<u>0.137</u>	<u>0.129</u>
	4.023	3.828
Cl	0.821	0.722
CO ₃	<u>0.224</u>	<u>0.183</u>
	1.045	0.905
Me	24.9	27.4
EqAn	25.2	26.3

*Total includes S 0.14

Wavelength dispersive analyses on the ARL probe at the University of Oregon. Conditions as cited in Appendix 2.

APPENDIX 12

TRACE ELEMENT ANALYSES FOR ALL SAMPLES COLLECTED AT
THE MONTERROSAS MINE

Appendix 12. Trace element analyses for all samples collected at the Monterrosas Mine.

Table 12-A. Metal concentrations in samples collected from surface outcrops (in ppm).

	Cu	Mo	Pb	Zn	Co	Ag
<u>Ore</u>						
12-9-9	6900	60	6	12	30	3.1
12-2-17	2500	75	11	20	8	10.7
10-2-13	5670	3	20	35	≤5	3.5
8-2-14	1370	5	50	80	9	0.9
<u>The Patap Superunit</u>						
6-8-13	13	≤1	5	15	4	0.4
11-8-13	16	≤1	8	12	4	0.3
1-7-1	75	≤1	25	35	18	0.3
10-2-21	6	≤1	5	10	≤5	≤0.3
2-2-22	85	≤1	8	15	6	≤0.3
13-2-22	17	≤1	15	16	≤5	≤0.3
12-2-22	55	1	12	19	5	≤0.3
10-2-22	550	≤1	9	14	17	0.3
8-9-9	60	1	≤4	12	5	0.7
9-9-9	35	3	6	11	25	0.5
10-9-9	790	2	4	15	12	0.3
3-9-10	205	4	10	12	9	0.5
13-9-10	85	2	14	8	5	0.3
22-9-10	810	8	25	30	25	0.3
8-9-13	55	≤1	6	5	10	0.4
<u>The Linga Superunit</u>						
1-8-13	25	≤1	5	16	20	≤0.3
12-8-13	25	≤1	6	25	6	0.3
7-2-13	11	30	70	50	≤5	≤0.3
8-2-13	19	7	100	70	5	≤0.3
9-2-13	19	6	50	50	6	≤0.3
11-2-14	50	≤1	40	25	11	0.3
12-2-14	50	≤1	25	30	10	0.3
2-2-17	175	≤1	10	30	11	≤0.3
7-2-17	15	1	12	19	6	≤0.3
6-2-19	45	2	25	30	9	0.3
7-2-19	40	3	12	18	17	≤0.3
9-2-19	55	≤1	5	14	6	≤0.3
2-2-21	50	≤1	10	15	5	≤0.3
7-2-21	30	1	6	15	5	≤0.3
4-2-22	40	3	30	25	12	0.3
7-2-22	45	2	20	20	5	≤0.3
1-9-9	65	7	5	15	12	≤0.3
3-9-9	40	2	4	12	≤4	≤0.3
4-9-9	50	2	8	20	11	0.7

Appendix 12. (cont.)

Table 12-A. (cont.)

	Cu	Mo	Pb	Zn	Co	Ag
<u>The Linga Superunit</u>						
17-9-10	200	2	17	11	5	<0.3
2-9-11	55	4	15	14	11	0.5
2-9-12	45	2	6	12	5	<0.3
1-9-13	45	<1	5	11	<4	<0.3
2-9-13	100	<1	9	8	10	<0.3
3-9-13	200	<1	8	12	20	<0.3
4-9-13	115	<1	10	5	8	0.5
5-9-13	165	<1	10	8	15	0.3
12-9-13	20	<1	6	12	<4	<0.3
5-9-14	25	<1	9	10	8	0.3

Appendix 12. (cont.)

Table 12-B. Metal concentrations in samples collected from the 1132 Level (in ppm).

	Cu	Mo	Pb	Zn	Co	Ag
<u>Ore</u>						
12-32-30	3480	500	8	35	30	≤0.3
A-2	9900	20	18	20	165	2.5
C-3	9700	25	12	45	185	1.8
F-3	85000	100	12	40	55	8.0
H-7	26800	40	16	45	25	1.5
<u>The Patap Superunit</u>						
2-32-2	12	1	6	15	6	≤0.3
3-32-13	140	≤1	5	19	18	≤0.3
3-32-18	30	≤1	3	14	4	0.3
5-32-3	150	3	6	30	11	≤0.3
7-32-15	155	≤1	6	14	4	≤0.3
8-32-30	1100	4	12	45	16	≤0.3
A-1	100	3	25	18	11	0.8
A-5	1230	5	20	10	20	0.5
B-1	160	1	12	14	4	0.3
B-4	160	2	7	30	14	0.3
C-1	720	1	60	25	20	1.0
C-2	115	1	35	15	11	1.0
C-5	5200	17	11	17	17	1.3
C-6	45	1	8	20	6	≤0.3
C-8	140	3	14	12	4	1.5
D-1	295	2	14	60	25	0.7
E-2	1180	6	20	45	16	1.0
F-1	40	≤1	5	18	6	≤0.3
<u>The Linga Superunit</u>						
2-32-14	395	≤1	5	19	18	≤0.3
H-8	650	3	10	14	4	0.4
H-15	35	≤1	9	15	10	≤0.3
H-18	45	≤1	5	20	9	≤0.3

Appendix 12. (cont.)

Table 12-C. Metal concentrations in samples collected from the 1070 Level and from drill holes (in ppm).

	Cu	Mo	Pb	Zn	Co	Ag
<u>Ore</u>						
X-7	26300	7	7	20	530	5.8
M-5	42000	100	5	25	125	8.2
P-5	1350	60	4	13	40	1.0
DDH-13-20	680	225	16	40	630	0.3
<u>The Patap Superunit</u>						
1-21-70	30	41	7	19	14	0.3
1-70-18	35	3	5	14	5	0.3
2-70-18	450	41	3	25	9	0.4
2-70-20	14	41	4	16	5	0.3
3-70-18	35	41	6	20	4	0.3
6-70-20	130	41	15	16	5	0.3
R-4	1140	13	11	18	45	0.8
R-8	195	90	8	11	60	0.5
X-1	1420	10	5	35	40	0.7
X-6	1140	13	8	20	185	0.8
M-1	65	2	4	10	4	0.3
M-4	70	3	6	35	250	0.8
L-1	240	2	14	30	11	0.5
L-3	880	7	9	17	4	0.3
L-8	250	3	6	11	5	0.3
K-11	20	41	5	20	6	0.3
DDH-13-1	12	41	5	18	4	0.4
DDH-13-10F	30	41	5	20	4	0.3
DDH-13-10M	25	41	4	20	4	0.3
DDH-13-12	30	41	4	17	3	0.3
DDH-13-15	155	41	6	25	5	0.3
DDH-13-18	35	41	6	35	5	0.3
<u>The Linga Superunit</u>						
V-2	440	2	13	240	25	0.8
V-4	405	2	13	95	18	0.3
V-7	125	41	8	290	6	0.3
12-70-20	85	41	10	240	35	0.3
P-7	310	13	4	12	50	0.5
P-8	355	4	4	10	18	0.5
P-13	280	7	4	9	13	0.3